ATMOSPHERIC LIBRARY OF FAR AWAY WORLDS:

DEVELOPING A LIBRARY OF MODEL SIMULATIONS TO INTERPRET OBSERVATIONS OF EXOPLANET ATMOSPHERES

JAYESH MAHENDRA GOYAL

SUBMITTED BY JAYESH MAHENDRA GOYAL TO THE UNIVERSITY OF EXETER AS A THESIS FOR THE DEGREE OF DOCTOR OF PHILOSOPHY IN PHYSICS, JUNE 2019

THIS THESIS IS AVAILABLE FOR LIBRARY USE ON THE UNDERSTANDING THAT IT IS COPYRIGHT MATERIAL AND THAT NO QUOTATION FROM THE THESIS MAY BE PUBLISHED WITHOUT PROPER ACKNOWLEDGEMENT

I CERTIFY THAT ALL MATERIAL IN THIS THESIS WHICH IS NOT MY OWN WORK HAS BEEN IDENTIFIED AND THAT NO MATERIAL HAS PREVIOUSLY BEEN SUBMITTED AND APPROVED FOR THE AWARD OF A DEGREE BY THIS OR ANY OTHER UNIVERSITY

SIGNED: JAYESH MAHENDRA GOYAL

Front page figure : Artist's Impression of "Hot Jupiter" Exoplanets. NASA and ESA. STScI-PRC15-44a

Abstract

The number of exoplanets that have been discovered now exceeds 3500. This population of exoplanets contains a rich diversity, for example; hot Jupiters, warm Neptunes, super Earths and Earth-like planets, exhibiting variation in the planetary mass, radius, and distance from the host star. Moreover, the diversity of exoplanets is greatly multiplied by the potential variation in characteristics such as the internal and atmospheric composition. However, in terms of observing exoplanet atmospheres hot Jupiters are currently the best targets, due to their high temperatures and large atmospheric scale heights. This makes high spectroscopic signal-to-noise ratio (SNR) observations possible, using telescopes like the Hubble Space Telescope (HST), Very Large Telescope (VLT) and in the future the James Webb Space Telescope (JWST). Therefore, the major focus of this thesis has been to develop theoretical models to interpret the observations of exoplanet atmospheres, primarily hot Jupiters and warm Neptunes.

A given planet's observed transmission or emission is shaped by different physical and chemical processes occurring in the atmosphere. Forward models aid in the understanding of these processes when used in conjunction with observations. Therefore, in this thesis we explore hot Jupiter exoplanet atmospheres using 1D radiative-convective equilibrium models, and create an extensive publicly available library of simulations covering a variety of H_2/He dominated exoplanet atmospheres, termed as the "Atmospheric Library of Far Away Worlds".

In this thesis we present three different libraries of model simulations using high temperature line-lists. First, a planet specific library of transmission spectra and equilibrium chemical abundances for 117 observationally significant exoplanets for a range of temperatures, metallicity, C/O ratio, cloud and haze parameters, with isothermal Pressure-Temperature (P-T) profiles. Second, a generic library of transmission spectra and equilibrium chemical abundances, that can be scaled to a wide range of H_2/He dominated exoplanet atmospheres for all parameters considered in the first library, along with planetary gravity and a wider temperature range, again using isothermal P-T profiles. The first two libraries were developed using two approaches of condensation, local condensation and condensation with rainout. Finally, a library with self-consistent radiative-convective equilibrium (rce)

P-T profiles and corresponding equilibrium chemical abundances, transmission and emission spectra, and contribution functions, using condensation with rainout.

Transmission spectra observations have been extremely productive in identifying specific trace species in the atmospheres of some hot Jupiter planets. However, the transmission spectrum of a given planet is a combination of the effect of opacities due to all the species in its atmosphere. Given that the number of chemical species present can be considerable and each have different absorption cross-sections, it is challenging to determine which species is responsible for shaping features within the spectrum itself. Moreover, the opacities and the chemical composition of the atmosphere are a function of its pressure-temperature (P-T) structure, metallicity, carbon-to-oxygen ratio and the condensation processes occurring within the atmosphere. Therefore, a library of model transmission spectra and corresponding chemical abundances will therefore aid identifying the species contributing substantially to the transmission spectra and thereby help constrain the target atmospheric chemical composition. Recent transmission spectra observations of hot Jupiter exoplanet atmospheres have shown that their spectral features, especially H_2O, are smaller in amplitude than that expected for a clear atmosphere with solar metallicity. What causes these spectral features to mute is an open question, with the presence of clouds and haze as one possibility or high mean molecular mass. A transmission spectrum library can aid in identifying different mechanisms that could cause these spectral features to mute.

We have used the planet specific library of model simulations to interpret transmission spectra observations of twelve exoplanet atmospheres and characterise them. We also demonstrated the application of this library in conjunction with the JWST simulator `PandExo`, as a predictive tool to plan future observations. The planet specific library includes models with fixed gravity for a particular planet. Therefore, to make the library of models flexible enough to be adapted to any gravity values (different planets) and also to their updated values in the future, we developed the generic library of transmission spectra and derive a scaling relationship to scale them to a range of H_2/He dominated exoplanet atmospheres. The generic library spans a wider temperature range and is also not constrained by the planetary equilibrium temperature, unlike the planet specific library. Therefore, generic library can reveal important processes due to temperature anomalies, for example, the presence of VO without TiO , in the atmosphere of hot Jupiter WASP-121b.

The weather, climate and dynamics of a planetary atmosphere are governed by its pressure-temperature (P-T) structure. Therefore, it is necessary to constrain the P-T structure of a planet's atmosphere, to understand the various physical processes occurring within them. The presence of an atmospheric temperature inversion can also be determined by constraining the P-T structure. The P-T structure of the planetary atmosphere also governs its spectral signatures, when remotely observed. Transmission spectrum probe a very small vertical region and only the limb of the planetary atmosphere and cannot constrain its P-T structure. This can be overcome by measuring the emission spectrum of the planet, where the flux originates from much deeper in the planet's atmosphere as well as from the complete planetary hemisphere. Moreover, the emission spectrum can be used to constrain the P-T structure of the planetary atmosphere. Therefore, to overcome the limitations due to the assumption of isothermal P-T profiles, and also to generate planetary model emission spectra, we developed a third library with radiative-convective equilibrium P-T profiles. We investigated the effect of various model choices such as condensation methodology, treatment of line-wing profiles, source of line-lists, convection and the methodology to vary the C/O ratio, on the P-T profiles and thereby the spectra. We showed how thermal ionisation, H-, Fe and TiO/VO opacities shape the P-T structure of extremely irradiated hot Jupiters like WASP-121b. We investigated different mechanisms which act to form a temperature inversions and their observable signatures in the emission spectra. This library of model simulations with radiative-convective equilibrium P-T profiles has also been used to discover the temperature inversion for the first time in an exoplanet atmosphere in WASP-121b.

Simulated observations using theoretical forward models also aid in predicting scientifically important targets for characterisation, to use precious telescope time most efficiently. The launch of the JWST will enable probing exoplanet atmospheres from wavelengths of 0.6 µm all the way up to 28 µm. Therefore, all the libraries of models presented in this thesis will also be extremely valuable to select the best targets for characterisation using the JWST.

Contents

List of Figures

List of Tables

Declaration

The majority of the research presented in this thesis was performed by myself, in collaboration with Nathan Mayne, Benjamin Drummond, David Sing, David Amundsen, Pascal Tremblin, Hannah Wakeford and Tom Evans. Here is the breakdown of contributions for each chapter.

Chapter Three

The planet specific library of model simulations was developed by me with inputs from Nathan Mayne, David Sing and Benjamin Drummond, using the ATMO model which was originally developed by Wolfgang Hayek and later extensively modified by Pascal Tremblin, David Amundsen and Benjamin Drummond. I contributed to various developments in the code, such as the addition of opacity of various species, including H- opacity, multi-gas Rayleigh scattering, treatment of haze and clouds, contribution function, coupling the 1D Eddysed cloud model to ATMO and many other model improvements to develop the library of model simulations. I also contributed to testing and benchmarking the rainout condensation chemistry. The Pandexo Simulation of the model was performed by Aarynn Carter. Observational interpretation was guided by inputs from David Sing, Tom Evans, Jessica Spake and Nikolay Nikolov. Eric Hebrard helped in solving chemistry issues.

Chapter Four

The generic library of model simulations was developed by me with input from Hannah Wakeford, Nathan Mayne, Nikole Lewis, Benjamin Drummond and David Sing. Hannah Wakeford also contributed to the development of figures for this work.

Chapter Five

The library of self-consistent simulated exoplanet atmospheres was developed by me with inputs from Nathan Mayne, Benjamin Drummond, David Sing and Pascal Tremblin. Thermal Ionisation was included in the ATMO model by Benjamin Drummond. The computation for iron opacity was performed by Mark Phillips.

Acknowledgements

The most important person I would like to thank without whom this PhD would not have been possible is my PhD supervisor Nathan Mayne. Nathan has been an extremely supportive supervisor not just in research but throughout my PhD journey, helping me in solving various problems, making career decisions, motivating when in need and even disagreeing on many things, especially the word "probe"!!!. He has also been very supportive during tough times for me in the final year, for which I am very grateful to him. I learnt, how do research as a theorist from him, most importantly to include rigour in my research work. I would also like to thank Nathan to take out his precious time to review all my writings from research papers to thesis, job applications and even paper review reports. The second important person I would like to thank is Ben Drummond, who basically was by third supervisor and officially became my second supervisor when David left Exeter. I have learnt all the basics of ATMO from Ben and troubled him a lot with all my questions, each time knocking his office door. Ben has been extremely helpful during whole my PhD, clearing my doubts, giving support when in need and always helping me in improving and correcting my work. David Sing my official second supervisor for first 3 years gave me an observational perspective, thus keeping me to ground when theory could predict anything!!! Working with David, I got amazing opportunity to work with observers and use the models directly to interpret observations which was very exciting and also helped developing strong collaborations with observers. I got to learn how to understand the simple physics behind observations from him.

I am also grateful to Tom Evans, Nikolay, Jess and Aarynn to give me amazing opportunity to work with them in interpreting their observations, which gave me new insights. Working with Tom on series of WASP-121b papers has been very exciting. I am also grateful to Hannah Wakeford and Nikole Lewis for giving me opportunity to visit STScI thus resulting in the development of generic library. Hannah has been very supportive. I would especially like to thank David Amundsen, since a lot of work in this thesis is based on the developments made by him. James and Pascal for answering all of my queries concerning radiative transfer and ATMO, I could rely on them to answer all my doubts.

I would like specially thank Sam for answering and solving all my computa-

tional questions and Alison for writing the thesis at almost the same time!!! Moreover, these long years of PhD went with ease because of Jess, since we started PhD together, discussing literally everything from science to philosophy, and supporting each other. I would like to thank the Exeter Astrophysics group to be so inclusive with all the social events like, tea breaks, pub nights, movie nights, journal club etc., this really helped me to blend in the department, arriving from a completely different country and made this PhD journey much easier.

My family has been extremely supportive and patient during whole of my PhD even though I have been thousands of miles away. I am especially grateful to my mother who had to go through tough times without me being there with her for a long time, still she was very supportive. My father, elder aunt, brother Aayush and sister Archita who supported me to finish this. I am very grateful to my brother Aayush, without him I don't think I would have been able to leave our family home. I would like to thank all my friends for their continuous support.

Jayesh Goyal
17th June 2019

Chapter 1

Introduction

> “The Universe is a pretty big place. If it’s just us seems like an awful waste of space.”
>
> — Carl Sagan

1.1 Exoplanets

Looking at the stars for hundreds of years humans have always wondered about the existence of other worlds like our own and civilisations on other planets. Although, the existence of planets other than Earth in our solar system has been known for a long time to our ancestors on Earth, no one knew whether the stars that they see in the night sky have any planets. However, for the first time in human history we have the technological capability to find planets around other stars. Over the last ∼25 years we have been on the path of revolution in astronomy and astrophysics, and this revolution has been the discovery of exoplanets. Basically, any planet outside our solar system is termed an “Exoplanet”. Discovery of exoplanets has opened an entire new paradigm to explore the Universe. The question “Are we alone in the Universe?” is one of the most fundamental question for humanity and the discovery of Exoplanets has the potential to answer this question. It is not just this fundamental question, but many other exciting questions like, what are the varieties of different exoplanets out there? Are Earth like planets common in our galaxy or in the Universe? How do these planets form? What is the composition of their atmospheres? What kind of planets can form around binary stars? (Is it really like Tatooine?) and the list goes on. It is only in the last ∼25 years that we have actually begun our true journey to explore distant worlds, far beyond our own, by exploring exoplanets. This all started with the discovery of first planetary mass body outside our solar system around a pulsar in 1992 (Wolszczan et al. 1992), followed by the first unambiguous detection of an exoplanet in 1995, named 51 Pegasi b, around a main sequence star (Mayor et al. 1995). This discovery brought exoplanet in the mainstream research, leading to many more discoveries in the subsequent years.

Due to ambiguities in the definition of a planet, especially at the extremities, like for Jupiter size or bigger planets, the International Astronomical Union (IAU) 2003 extra-solar planet working group recommends following definition (Perryman 2014),

“Objects with true masses below the limiting mass for thermonuclear fusion of deuterium (currently calculated to be 13M_j for objects of solar metallicity) that orbit stars or stellar remnants are planets (no matter how they formed). The minimum mass required for an extrasolar object to be considered a planet should be the same as that used in the solar system.”

However, there have been many objections to this definition (Chabrier et al. 2014; Soter 2006; Hatzes et al. 2015).

As of May 2019, the number of exoplanets that have been detected has reached a staggering number of ∼4000, and is increasing basically everyday. Most of these detections have been possible because of the Kepler spacecraft (Borucki et al. 2011). This number is also now dramatically increasing after the launch of the Transiting Exoplanet Survey Satellite (TESS) mission (Ricker et al. 2014).

Since size and mass are the two main parameters currently determined for exoplanets using transit and radial velocity techniques, respectively, they are mainly classified as below:

Planet Size - For transiting planets, as adopted in Borucki et al. (2011)

- Earth-size, or terrestrial planets (< 1.25 R_E)
- super-Earth-size ($1.25 - 2$ R_E)
- Neptune-size ($2 - 6$ R_E)
- Jupiter Size ($6 - 15$ R_E)

Planet Mass - For radial velocity or micro-lensing planets as adopted in Stevens et al. (2013)

- sub-Earths, or terrestrial planets (10^{-8} M_E – 0.1 M_E)
- Earths (0.1 M_E – 2 M_E)
- super-Earths (2 M_E – 10 M_E)
- Neptunes (10 M_E – 100 M_E)
- Jupiters (100 M_E – 10^3 M_E)
- super-Jupiters (10^3 M_E – 13 M_J)

- brown dwarfs (13 M_E – 0.07 M_S)
- stellar companions (0.07 M_E – 1 M_S)

1.2 Exoplanet Population

There is no simple physical principle that can be used to determine whether planets are rare or very common in the Universe. Therefore, before the discovery of exoplanets there was ample room for speculation about their occurrence rates. However, with the recent discoveries of exoplanets it is now clear that planets are ubiquitous, with $11 \pm 4\%$ Sun like stars predicted to host Earth like planets (Petigura et al. 2013), dropping down to $\sim$1% for hot Jupiter exoplanets (Howard et al. 2012b; Wright et al. 2012). Now the next question that arises is the variety in the exoplanet population. The exoplanets that have been detected span a large range of radii and orbital distance from their host stars, as shown in Figure 1.1. As classified earlier, the variety of exoplanets that have been discovered is astonishing, there are hot Jupiters, cold gas giants, warm Neptunes, mini-Neptunes, super-Earths which might be ocean worlds or ice giants, and finally there are many planets similar to Earth's size, which might be rocky planets or lava worlds. Among the confirmed planets a large number of them are giant planets (see Figure 1.2) which can be attributed to bias in observations, as it is easier to detect large radius short orbital distance exoplanets, using the transit method. Many multi-planet systems have also been detected like the famous Trappist-1 system of planets (Gillon et al. 2017). Due to their short orbits many of these detected exoplanets are predicted to be tidally locked which means their revolution time around their host star is equal to their rotation time. For e.g. moon is tidally locked to Earth, since its rotation period of 28 days is equal to its revolution period around the Earth.

1.3 Detection Techniques

Currently there are several techniques to detect exoplanets. However, most of the exoplanets have been detected by two of the main techniques, radial velocity and transit, explained in detail below.

1.3.1 Radial Velocity

This is the technique by which the first exoplanet around a sun like star, 51 Pegasi b was detected (Mayor et al. 1995). The planetary motion around the host star under the influence of gravity causes the stellar motion about the star-planet barycentre (centre of mass). This motion results in the doppler shift of the host star's radiation

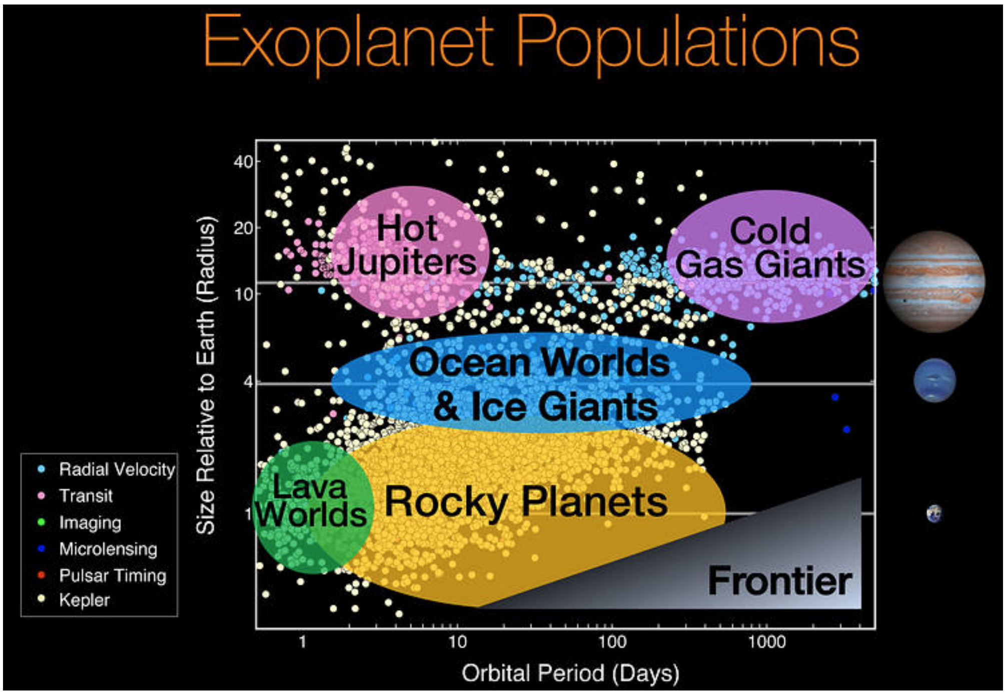

Figure 1.1: Exoplanet Population as in August 2017. (Source : NASA https://www.nasa.gov/image-feature/ames/kepler/exoplanet-populations)

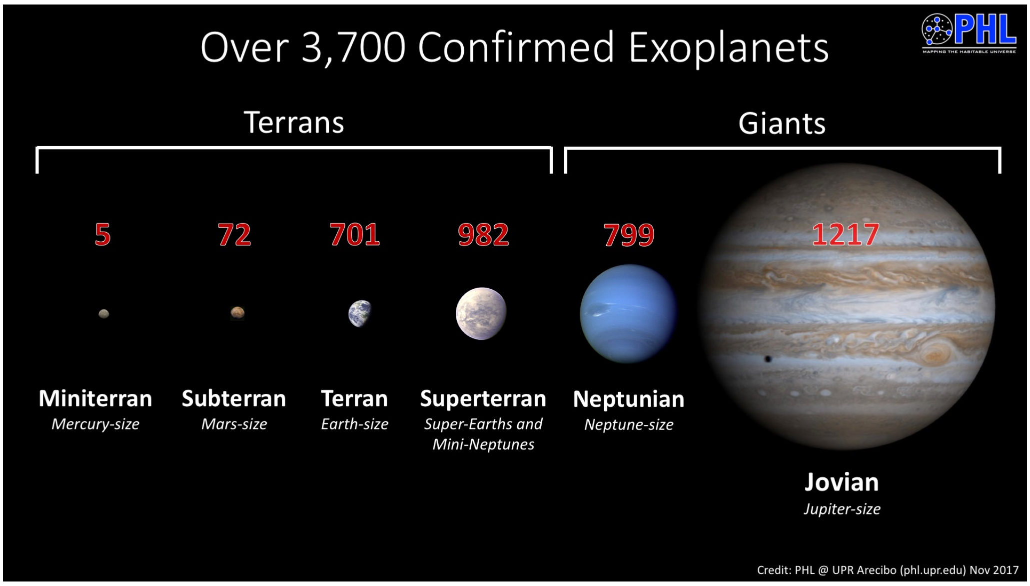

Figure 1.2: Figure showing approximate number of different types of exoplanets detected. (Source : PHL @ UPR Arecibo)

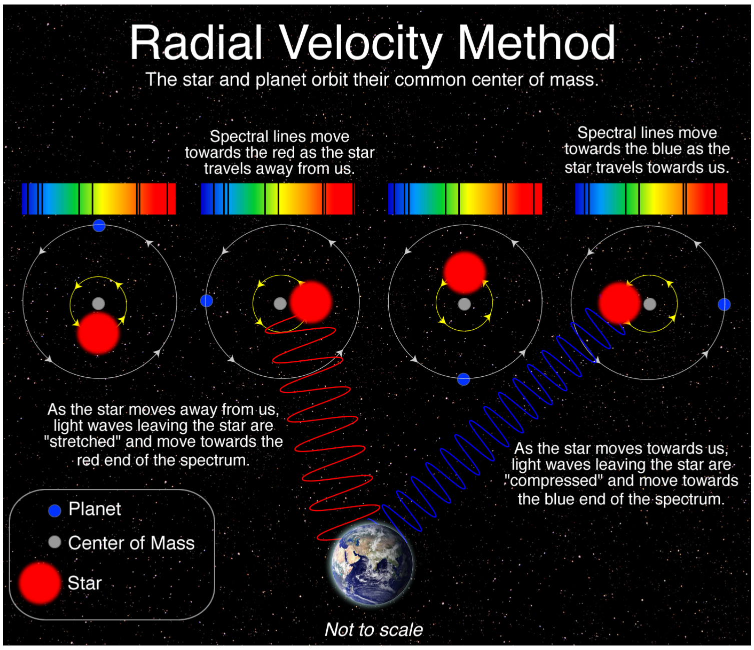

Figure 1.3: Figure illustrating radial velocity technique. Credit: Las Cumbres Observatory

measured on Earth, blue-shifted when moving towards Earth and red-shifted when moving away as shown in Figure 1.3. This doppler shift is dependent on the mass of the orbiting planet. Therefore, the radial velocity semi-amplitude (K_*) of the host star enables us to determine a lower limit on the planet's mass (M_p) using:

$$k_* = \left(\frac{2\pi G}{P}\right)^{1/3} \frac{M_p \sin i}{(M_p + M_*)^{2/3}} \frac{1}{(1-e^2)^{1/2}} \tag{1.1}$$

where M_* is the mass of the host star, G is gravitational constant, P is the planet's orbital period, e is the orbital eccentricity and i is the orbital inclination, such that $i = 90^\circ$ is edge-on and $i = 0^\circ$ is face-on along the line of sight of the observer. It gives only the lower limit on M_p, as inclination cannot be determined by using the radial velocity technique and we can only compute $M_p sini$. This technique can constrain the planet's mass but not the planet's radius. The accuracy of radial velocity instruments is determined using the radial velocity semi-amplitude K_*. The host star's K_* is typically around $100m/s$ for close in hot Jupiter exoplanets, for Jupiter around the Sun $K_* = K_j = 12.5m/s$ and for Earth around Sun $K_* = K_E = 0.09m/s$. Some of the best radial velocity surveys like the HARPS can reach accuracies of 1 ms^{-1} (Mayor et al. 2003).

1.3.2 Transit Photometry

The first transit of an extrasolar planet was observed in 1999, during the photometric monitoring of the then known close in hot Jupiter system HD 209458 (Henry et al. 2000). This was quickly followed by various ground and space based surveys. Currently, this is the technique by which most of the exoplanets have been detected, primarily due to Kepler mission (Borucki et al. 2011), Wide Angle Survey of Planets (WASP) (Pollacco et al. 2006) and ongoing Transiting Exoplanet Survey Satellite (Ricker et al. 2014) mission. In this technique the planet is detected when it transits the host star, leading to a decrease in the brightness of the host star as shown in Figure 1.4. This effect is repeated at the orbital period of the planet. The transit probability for eccentric orbit is given by $p = \frac{R_*}{a_p(1-e^2)}$, where R_* is the stellar radius, a_p is the semi-major axis of the planet and e is the planet orbital eccentricity (Borucki et al. 1984; Barnes 2007). This equation shows that planets with eccentric orbits are more likely to transit than equivalent planets with the same semi-major axis, but circular orbits ($e = 0$). The observational quantity measured during transit observations is transit depth δF, defined as the ratio of planetary disc area to stellar disc area during occultation, i.e $\delta F = \left(\frac{R_p}{R_*}\right)^2$. A Jupiter-like planet orbiting a Sun-like star produces a flux variation or transit depth of the order of 1%, on the other hand an Earth-like planet around a Sun-like star produces a flux variation of the order of 0.01%. However, depths of up to ~7-13% can be expected for planets in the super-earth to mini-Neptune regime, around M dwarfs, the most common stars in the Milky way and with large lifespan. Variable atmospheric extinction makes ground based photometry to better than ~0.1 % accuracy very difficult. Therefore, space based observatories for transit method are particularly important, where continuous long uninterrupted observations can be made above Earth's atmosphere.

One of the most important effects to be considered while measuring the transit depths is the stellar limb darkening effect. Limb darkening refers to the decrease in intensity of the stellar image, moving from the centre of the star to the limb due to combined effects of changing optical depth with decreasing star density and temperature with radius. It is represented as a function of $\mu = cos\theta$, where θ is the angle between normal to the stellar surface and line of the sight of the observer. Thus, limb darkening is minimum at the stellar centre, that is when $\theta = 0$ and $\mu = 1$. The effect of limb darkening results in the curvature of the light curves as shown in Figure 1.4, in contrast to the sudden drop in the flux as soon as the transit begins.

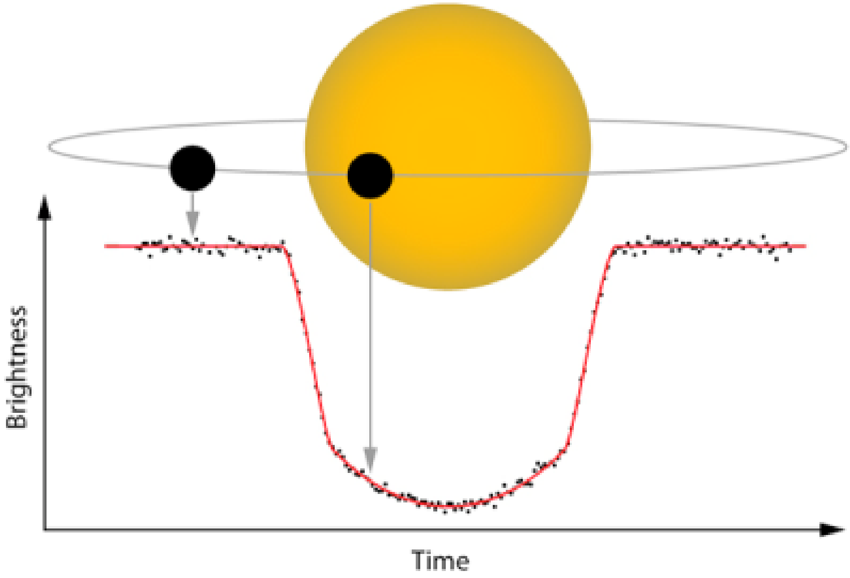

Figure 1.4: Figure showing transit technique. Credit: ESO

1.3.3 Other Methods

Apart from radial velocity and transit technique explained above, direct imaging, micro-lensing and astrometry are the other most promising techniques to detect exoplanets.

Direct Imaging

Direct imaging simply is the technique to directly observe emission from the planets. Direct imaging is technically very challenging, both from ground and space, due to very small angular separation between planets and their host stars and as the planetary emission is swamped by the bright stellar glare. Therefore, this technique is particularly suitable for the planets that orbit at considerably large distances from their host star with typical angular separations of $\sim$0.1-0.5 arcsec, so that the planetary signature can be disentangled (spatially resolved) from their host star signal. Direct detections typically need contrast ratios of 10^{-9} to 10^{-10} at separations of 0.01 to 1 arcsec with current instruments. The two main requirements for this technique are high spatial resolution and high contrast. One of the methods of achieving high contrast is by using a coronagraph in telescopes, as it masks the host stellar disk, allowing the observer to disentangle the planetary signature mainly in the infrared part of the electromagnetic spectrum as seen in Figure 1.5, which shows the existence of four directly image planets around their host star.

Although technically challenging, direct imaging offers many benefits scientifically. The first being the direct confirmation of existence of the exoplanets detected by other techniques. The ability to detect planets at large orbital distances from

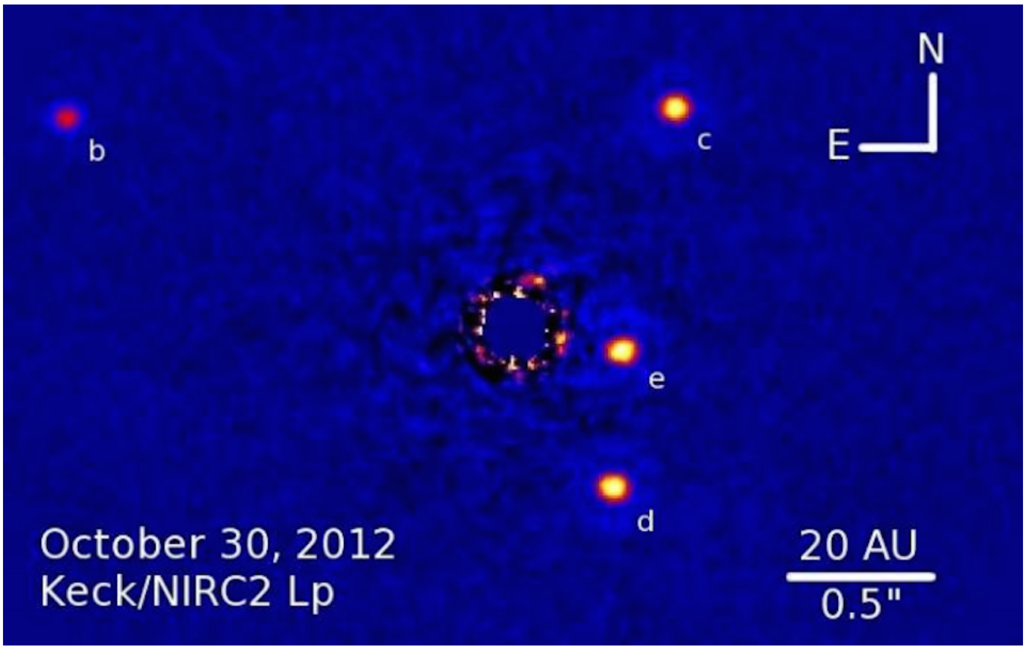

Figure 1.5: Figure showing direct imaging planets of the HR-8799 system (Marois et al. 2010).

their host stars is very beneficial and complementary to transit detection which is biased more towards close in planets. This technique also provides a first step to achieve the future goal of directly imaging an exoplanet surface.

Microlensing

In this technique an exoplanet is detected using the effect of gravitational lensing as shown in Figure 1.6. Unlike other techniques, this technique is very fruitful in detecting planets as far away from us as the centre of our galaxy ∼22000 light years away (Beaulieu et al. 2006) and even in other galaxies. Gravitational lensing as predicted by Einstein's theory of relativity refers to bending of light rays of a background light source by a foreground mass. Specifically, gravitational microlensing refers to the magnification of the background light due to foreground mass, as the background light bends and creates two distorted unresolved images. In this phenomena, background light acts as a source and the foreground mass as a lens. Therefore, for a single star without a planet this micro-lensing event will lead to magnification for a certain time during the micro-lensing event as shown on the extreme left plot of Figure 1.6. However, if there is a planet orbiting a star, for a certain time duration, there will be spike in the magnification due to planet mass, in a particular geometrical alignment, as shown in the rightmost plot of Fig. 1.6, thus leading to detection of the planet.

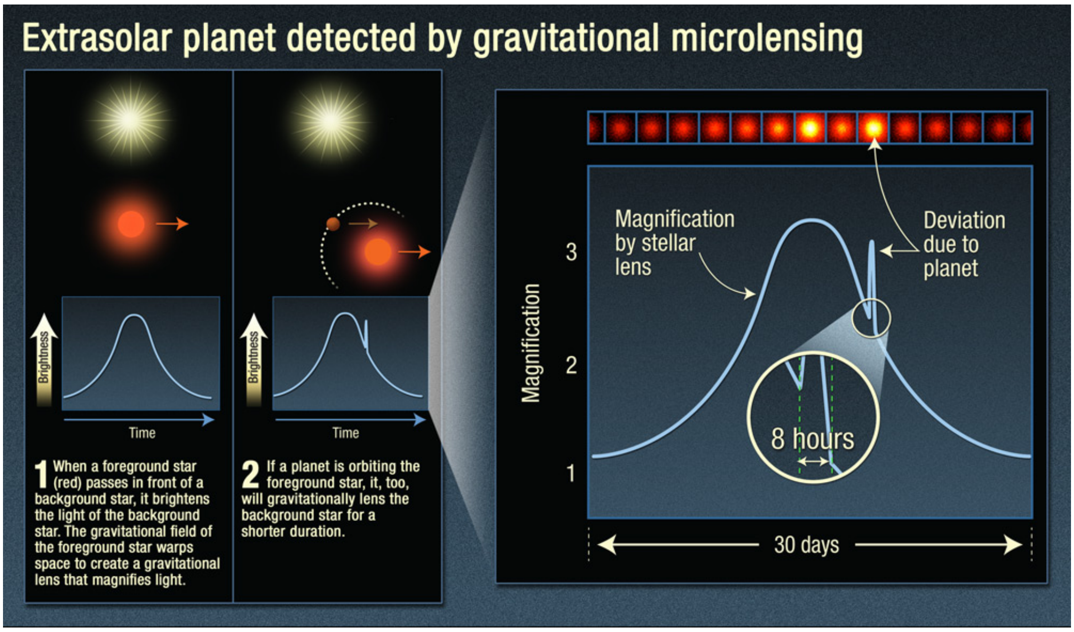

1 When a foreground star (red) passes in front of a background star, it brightens the light of the background star. The gravitational field of the foreground star warps space to create a gravitational lens that magnifies light.

2 If a planet is orbiting the foreground star, it, too, will gravitationally lens the background star for a shorter duration.

Figure 1.6: Figure illustrating micro-lensing technique. Credit: NASA, ESA, and K. Sahu (STScI)

Astrometry

The astrometry technique similarly to the radial velocity technique, uses the fundamental principle of the revolution of the host star around the common centre of mass (barycentre) of the star and the planet or the planetary system, but instead of doppler shift it measures actual movement of the star in the sky, relative to the telescope. A star with a planet will exhibit oscillating motions in the sky, which can be detected only by very high precision measurements, due to the required precision of the order of few micro arc-seconds.

Any stellar motion in our galaxy when measured from Earth is a combination of three motions, first the motion of Earth around the Sun, second the motion of star around the centre of the galaxy and third the motion of the star due to the gravitational pull of the planet. The combined motion due to all three motions is measured using the Astrometry technique by missions such as GAIA (Gaia Collaboration et al. 2016). Thus by subtracting the other two motions the motion due to planet can be detected, thus constraining planetary mass.

1.4 Observations of Exoplanet Atmospheres

The field of exoplanet atmosphere characterization has been primarily driven by advances in observational techniques in the recent years. The area covered by the atmosphere of a planet is very thin in comparison to the bulk planet, therefore it is extremely difficult observationally to probe their atmospheres. In this section I discuss some of the most fruitful techniques used to probe exoplanet atmospheres.

1.4.1 Transmission Spectroscopy

In the transit technique the planet is detected when it transits the host star, leading to a decrease in the brightness of the host star, thus allowing us to measure its radius. This size/radius of the planet also includes its atmosphere. However, the thickness of the planetary atmosphere is dependant on its composition and its Pressure-Temperature (P-T) structure. This thickness also varies depending on the absorption characteristics of the atmospheric gases and particles, thus leading to a wavelength dependant total planetary radius. Therefore, measuring the radius of the planet as a function of wavelength can reveal the characteristics of its atmosphere. This is the fundamental principle behind transmission spectroscopy.

In this technique the transit depth of the planet is measured at different wavelengths as shown in Figure 1.7. During the transit, a fraction of the stellar light passes through the narrow annulus of the planet's atmosphere surrounding its limb. Therefore, at wavelengths where the planetary atmosphere absorbs this light, the transit depth increases. This wavelength dependant transit depth and hence the apparent planet radius, effectively leads to observed transmission spectrum. This transmission spectrum when interpreted using atmospheric models can give a wealth of information about the planetary atmosphere such as the dominant absorbing gases, Rayleigh scattering, presence of aerosols, clouds, limb temperature etc. The inferred abundances of the absorbing gases based on the size of the spectral features can then be used to constrain the metallicity and C/O ratio of the planetary atmosphere. It must however be noted that transmission spectrum only provides the information about the limb of the planetary atmosphere, which may or may not be extended to the entire atmosphere. The detailed numerical derivation of the transmission spectrum that can be used in atmosphere models is shown in 2.10 in Chapter 2 with its analytical solution given in Lecavelier Des Etangs et al. (2008). As shown in Section 1.3.2, even for transmission spectroscopy transit depth δF is measured, but in different wavelength bands given by $\delta F(\lambda) = \left(\frac{R_p(\lambda)}{R_*(\lambda)}\right)^2$, where λ is the wavelength of electromagnetic radiation.

Various species have been detected on various planets using transmission spectroscopy. Alkali metal elements like sodium and potassium have been detected in the atmospheres of various exoplanets, for example HD 209458b (Charbonneau et al. 2002; Sing et al. 2008; Redfield et al. 2008; Snellen et al. 2008; Sing et al. 2016) and XO-2b (Sing et al. 2011). Water has also been detected in many hot Jupiter atmospheres, (e.g Deming et al. 2013; Wakeford et al. 2013; Stevenson et al. 2014).

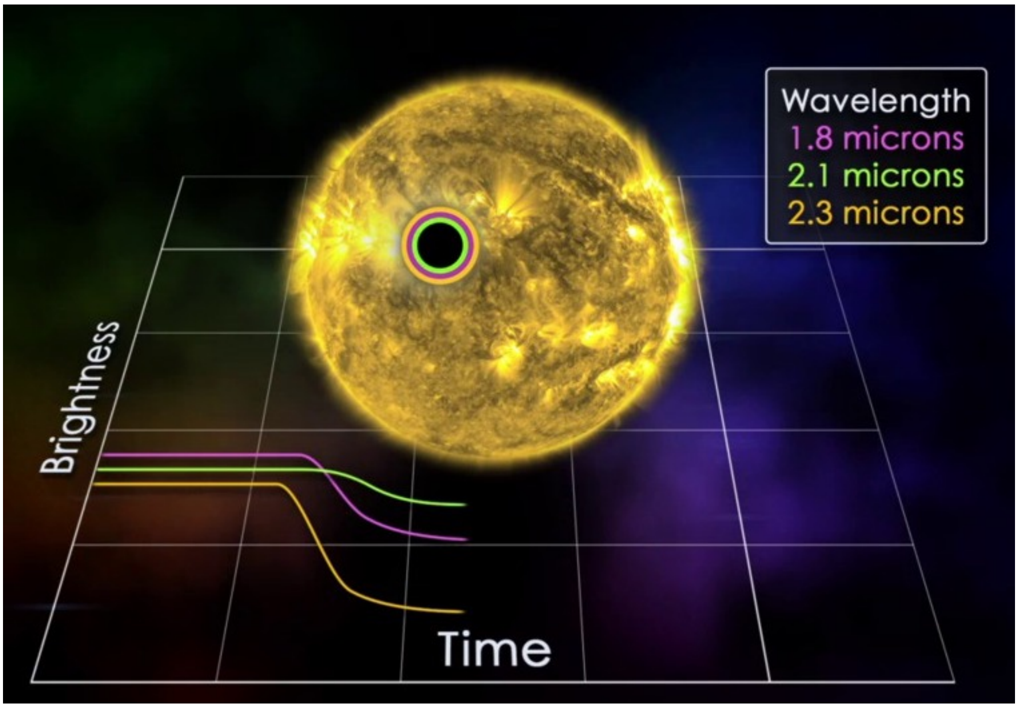

Figure 1.7: Figure illustrating transmission spectroscopy. Credit: NASA

Additionally, Kreidberg et al. (2014) and Sing et al. (2016) highlighted the possibility of clouds and hazes in some of these planets. A strong constraint on the water abundance was placed using three distinct water features by Wakeford et al. (2018). Helium was detected in the atmosphere of WASP-107b for the first time by Spake et al. (2018). Sodium was detected with its pressure broadened wings for the first time using ground based Very Large Telescope (VLT) in the atmosphere of WASP-96b (Nikolov et al. 2018), the exoplanet with potentially the clearest atmosphere.

In transmission spectroscopy we measure the stellar light attenuated by the planet's atmosphere and thereby infer the atmospheric properties. During the primary transit, stellar light traverses the planet's atmosphere transversely. Therefore, the large geometrical column along the chord leads to a large path length, which is extremely beneficial in the detection of trace species in the atmosphere, one of the primary advantages of transmission spectroscopy. However, due to large tangential path length, the atmosphere becomes optically thick along the line of sight as we go deeper, making this technique limited to upper (low pressure) atmospheres (∼1 mbar). Therefore, a very small part of the overall atmosphere is probed using transmission spectroscopy. Moreover, it is only the limb of the planetary atmosphere that is probed using this technique.

1.4.2 Emission Spectroscopy

For transmission spectroscopy, the observations are taken while the planet is passing in front of the host star, also called the primary eclipse. However, for emission spectroscopy the observations are taken while the planet is passing behind the host star, also called the secondary eclipse as show in Fig. 1.8. Emission spectroscopy overcomes several limitations of transmission spectroscopy. In this technique, the light emanating radially from the atmospheric interior is probed, indirectly. Therefore, deeper (high pressure) levels of the planetary atmosphere can be probed, depending on the atmospheric composition. Moreover, the day side of the planetary atmosphere is probed in emission spectroscopy. Therefore, it is worth noting that transmission and emission spectroscopy probe different regions of the whole 3D planetary atmosphere.

To obtain the emission spectrum of the planet during secondary eclipse, the total stellar plus planet flux is measured just before the secondary eclipse, followed by just the stellar flux during eclipse as shown in Figure 1.8. Therefore, subtracting the stellar flux from the combined planetary and stellar flux, results in just the flux of the planet, given by eclipse depth, D_{ecl}

$$D_{ecl} = \frac{R_p}{R_*}^2 \left(\frac{F_*(\lambda) + F_p(\lambda)}{F_*(\lambda)} - 1 \right) \tag{1.2}$$

where R_p and R_* are planetary and stellar radius, respectively. $F_*(\lambda)$ is the stellar flux and $F_p(\lambda)$ the planetary flux.

This methodology exploits the fact that the planetary spectrum deviates from that of a blackbody, because of the wavelength dependant opacity and vertical P-T profile. Therefore, this methodology also allows constraining the P-T profile of the planetary atmosphere, thus revealing the bulk atmospheric structure. For example, the detection of an inversion layer in the atmosphere of WASP-121b using emission spectroscopy (Evans et al. 2017). It also allows probing much deeper atmospheres in the spectral window regions.

1.4.3 Phase Curves

Outside of the transit and eclipse phases, the flux of the star-planet system over the full orbital period can give the planetary emission and even planetary albedo at different phase angles as shown in Figure 1.10. This phase curve measurement can be an important diagnostic to understand the overall dynamics of the atmosphere, presence of winds, day-night temperature energy transport etc.

The sub-stellar point is the position on the planet where the centre of star's disc appears exactly overhead and in the absence of any winds this will also be the region

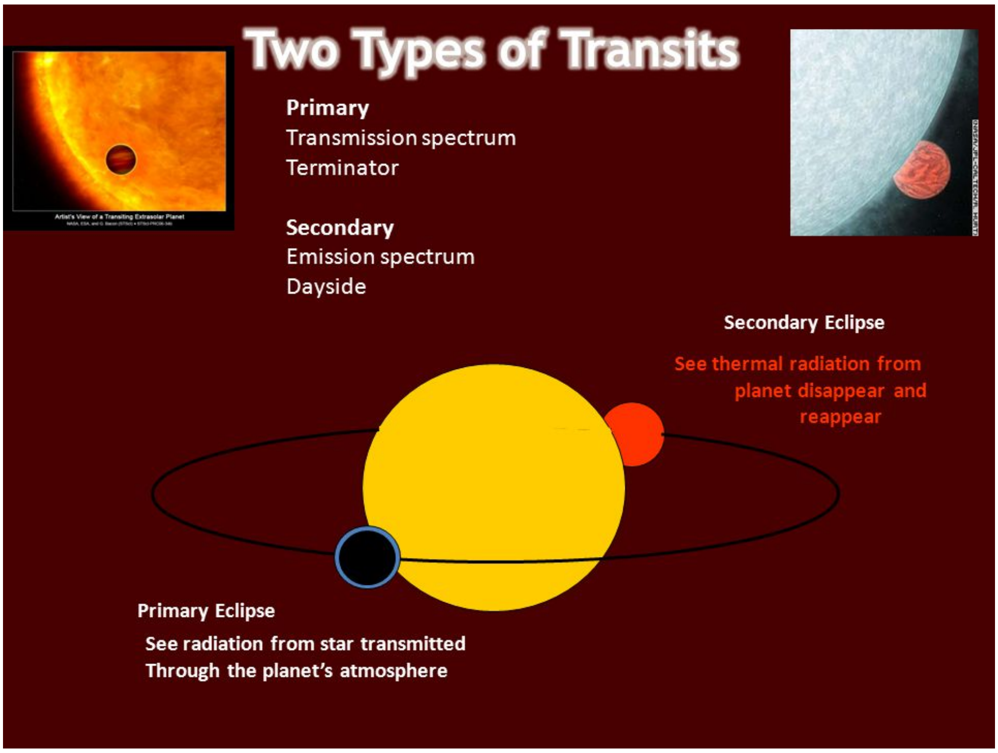

Figure 1.8: Figure illustrating primary and secondary eclipse. Image Credit: Angelle Tanner, Mississippi State University

of highest temperature (brightest) on the planet. However, the observations of the orbital phase curve of HD189733b (Knutson et al. 2007) using the InfraRed Array Camera (IRAC) 8 micron infrared channel onboard the Spitzer space telescope, revealed a shift in this point of highest temperature towards eastwards longitudes, for the first time, as shown in Figure 1.10. This concluded the presence of winds on this planet as predicted by 3D simulations and also an efficient redistribution of energy via jets leading to small day/night temperature contrasts. This, along with more observations later for HD-209458b (Zellem et al. 2014) and WASP-19b (for e.g Zellem et al. 2014; Wong et al. 2016) motivated further development of 3D General Circulation Models (GCM) to understand the dynamics and the weather on these tidally locked hot Jupiter exoplanets.

However, at optical wavelengths some hot Jupiters have been found to show westward shift in the brightest point with respect to the sub-stellar point, such as Kepler-7b (Demory et al. 2013) and Kepler-41b (Shporer et al. 2015). The presence of inhomogeneous reflective clouds in optical on the westside of the sub-stellar point has been theorised as the potential reason for this westward shift (Demory et al. 2013; Shporer et al. 2015).

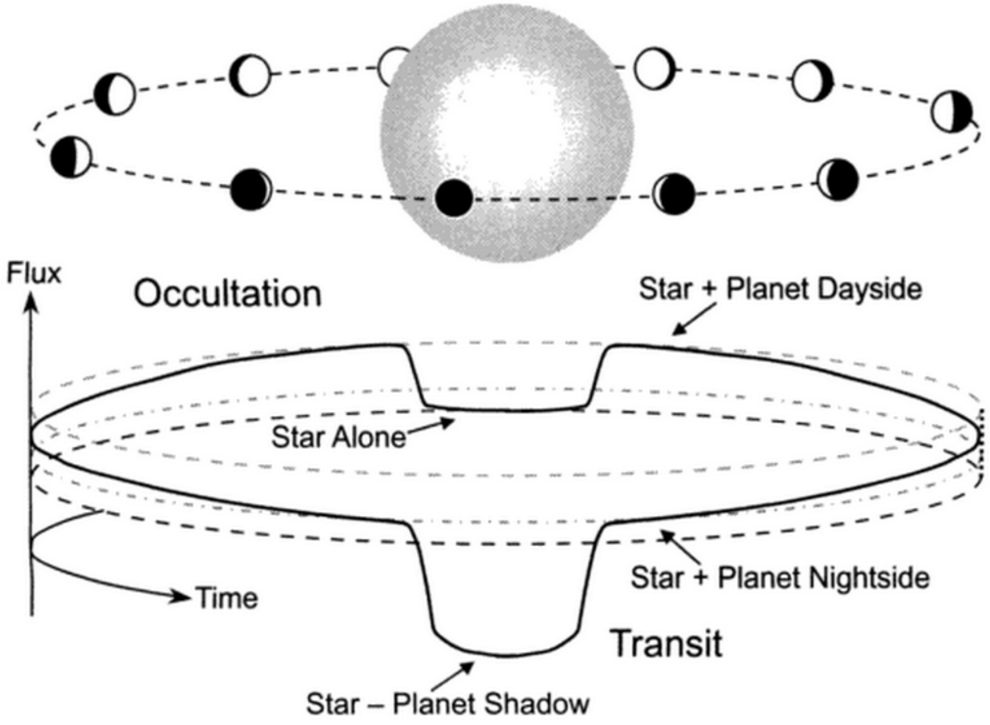

Figure 1.9: Figure showing flux for different phases of an exoplanet, including primary and secondary eclipse. Image Credit : Josh Winn.

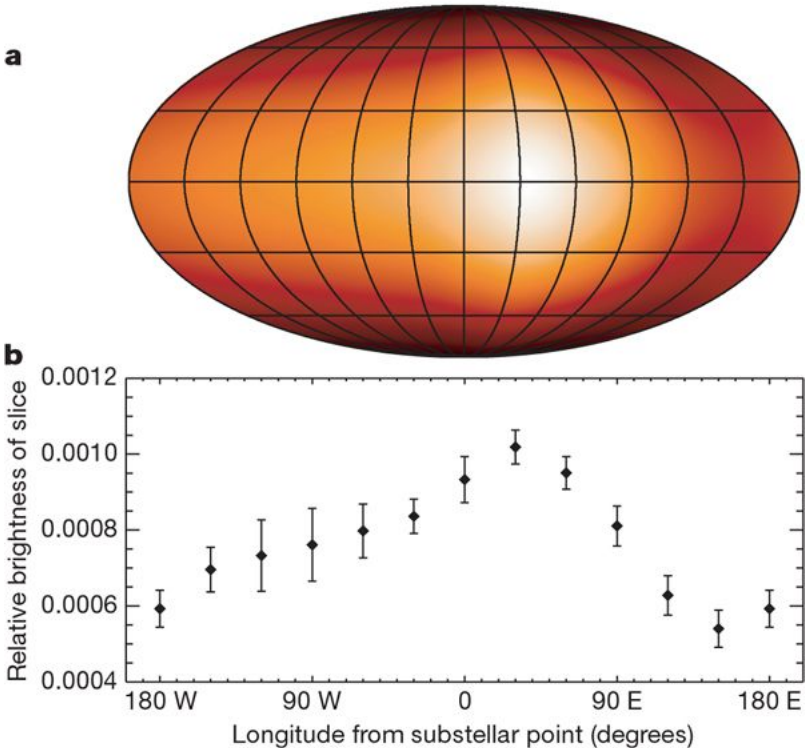

Figure 1.10: Figure showing shift of point of highest temperature by winds observed using phase curves (Knutson et al. 2007).

1.4.4 Direct Imaging

The technique used to directly detect exoplanets at sufficiently large distances from their host star, as explained in Section 1.3.3 can also be used to study their atmospheres. This can be particularly applicable in determining the atmospheric composition of young luminous planets, at a distance of more than 10s of AU from the host star. However, the low SNR for such planets makes it extremely difficult for current instruments. Nonetheless, instruments such as the Gemini Planet Imager (GPI) and the SPHERE onboard the VLT have been able to detect atmospheric features in some of the directly imaged planets (Currie et al. 2013; Macintosh et al. 2015). Currie et al. (2013) observed β Pic b using combined photometric observations from GPI and VLT. Atmospheric models with large dust grains failed to reproduce the planet's spectrum, but the models with thick clouds and small grain size particles were consistent with observations for this planet. Macintosh et al. (2015) discovered the planet 51 Eri b using the GPI. Near-infrared observations of this planet show a spectrum with strong methane and water-vapor absorption features. Using the planetary atmosphere and evolution models, the effective temperature of this planet was constrained to be 750 K with a radius of 0.76R_J

Direct imaging spectroscopy is the most promising technique to probe deeper levels of terrestrial exoplanet atmospheres and even their surface in the future, with bigger and better telescopes, even Earth like planets.

1.4.5 High Resolution Doppler Spectroscopy

In Section 1.1 we discussed how the radial velocity technique can be used to detect exoplanets, using the doppler shift in the host star's emission. However, the gravitational pull of the host star imparts a significantly larger orbital velocity on the planet, than the planet does on the star. Therefore, the planet has a substantially larger radial velocity semi-amplitude signal (K_p) ranging from 30 km/s for the Earth-sun system, up-to hundreds of km/s for the close-in hot Jupiters (Birkby 2018), than the star. Consequently, the doppler shift of the planetary spectral features are much larger than that of their host star. Moreover, any contamination from the telluric lines in the Earth's atmosphere, when observing from the ground, also appears essentially stationary in wavelength. Therefore, these large wavelength shifts of the planet's spectrum during its orbit can be used to disentangle it from the host star spectrum and that from the Earth's atmosphere. To achieve this, high resolution time series spectroscopy is performed, where the Doppler shift of the planet is sufficiently sampled along the orbit, i.e long enough to detect notable wavelength shifts in the planet's spectrum. This wavelength shift is set by the resolution of the spectrograph, with typically shifts of $>$ 10 pixels of the detector during the time series (Snellen et al. 2010; Birkby 2018). Initial attempts to use high resolution spectroscopy to study exoplanet atmospheres proved unsuccessful mainly because long exposure times are required, making the technique particularly susceptible to poor observing conditions but also due to instrumental limitations. Snellen et al. (2010) reported the first robust detection of a molecule (Carbon monoxide) in the atmosphere of HD 209458b using this technique but during its transit, using the high-resolution (R=100,000) CRyogenic InfraRed Echelle Spectrograph (CRIRES) at ESO's Very Large Telescope (VLT) (Wiedemann 1996). Brogi et al. (2012) reported the discovery of CO in the atmosphere of τ Bootis b in the thermal dayside spectrum using this technique. Therefore, high resolution spectroscopy can be used to detect molecular features and constrain the planetary orbital velocity. Moreover, after subtracting the shift due to planetary orbital velocity, the remaining shift (if any) can be attributed to winds in the planetary atmosphere as shown in Snellen et al. (2010). Therefore, high resolution spectroscopy can also be used to constrain winds in the planetary atmosphere, using the measurements for sufficiently long time, albeit over a narrow wavelength range in any phase (transit or any other phase giving thermal dayside spectrum), that could produce doppler shifts in the absorption line of the molecule

1.5 Modelling of Exoplanet Atmospheres

The modelling of exoplanet atmospheres can be broadly divided into two categories, first those termed forward models and second the retrieval (inverse) models, explained in detail below.

1.5.1 1D Forward Models

The forward modelling approach basically means modelling using first principles. This approach represents our understanding of the process or a system, which in this case is a planetary atmosphere. For a planetary atmosphere model the fundamental laws of radiative transfer, chemistry, dynamics etc. are employed under various constraints such as the hydrostatic equilibrium, radiative-convective equilibrium, total energy and mass balance, chemical equilibrium etc.. These all processes and constraints are explained in detail in Chapter 2. Moreover, forward models can be used to create simulated observations which can be both used to interpret existing observations but also aid in choosing scientifically important targets for characterisation, to use precious telescope time most efficiently. These models are generally independent of observations, however they evolve as our understanding of planetary atmospheres evolve through observations. The construction of forward atmospheric models is essentially an iterative process.

The forward modelling approach has varying levels of sophistication, depending on the availability of computation time. 1D forward atmospheric models reduce the complexity arising due to 3D nature of the atmospheres by performing calculations in the 1D column of the atmosphere. This assumption is fairly reasonable when there are fewer observational constraints and the 3D structure of the atmosphere is still unresolved, which is currently the situation for exoplanet atmospheres. However, some of the 3D effects can be taken into consideration in 1D models via parameterisation as shown in Chapter 2.

The forward modelling approach for exoplanet and brown dwarf atmospheres lies at the frontier of astronomy and planetary sciences. Therefore, some of the initial theoretical investigations of these atmospheres, like the modelling of brown dwarf Gliese 229B, trace their origin from the studies of Titan and Earth (Marley et al. 1996), while some used modified stellar atmosphere codes (Allard et al. 1996). The stellar approach uses opacities from various different sources and includes species expected to be in the gas phase only at high temperatures such as TiO (Titanium Oxide) and VO (Vanadium Oxide), however, the planetary approach uses opacities from standard HITRAN database (Rothman et al. 2009) and includes low temperature species, for e.g., PH_3 (Phosphine) and H_2S (Hydrogen Sulphide). Moreover, radiation schemes in models developed using stellar approaches are usually well tested and suitable for spectroscopic studies of exoplanetary atmospheres, as compared to Earth (Solar System) based models. However, stellar models lack robust cloud formation schemes which are well tested for Earth based models. So both approaches have advantages and disadvantages. So the best methodology while modelling brown dwarf and exoplanet atmospheres is to include the advantages of both approaches in a single model, which was generally adopted in subsequent studies.

Burrows et al. (1997) provided a theoretical basis for understanding the spectral features of exoplanet and brown dwarf atmospheres. Seager et al. (2000) and Brown (2001) and Hubbard et al. (2001) all predicted forward model transmission spectra for HD 209458b which later led to the detection of a sodium feature in its atmosphere (Charbonneau et al. 2002). Sudarsky et al. (2003) presented a systematic exploration of model spectra. Fortney et al. (2010) provided a detailed analysis of the effect of temperature, surface gravity and metallicity on transmission spectra for various hot Jupiter planets. More recently, Mollière et al. (2015) developed a generalised grid of forward model emission spectra for a range of planetary gravity values and other planetary characteristics without focusing on specific planets and Mollière et al. (2016) presented a grid of emission and transmission spectra for 18 important JWST targets, with a sophisticated cloud scheme included in their model. More recently Malik et al. (2017) and Gandhi et al. (2017) presented self-consistent forward models with varying levels of complexity. Goyal et al. (2018) presented an extensive publicly available grid of model transmission spectra for 117 observationally significant hot Jupiter exoplanet atmospheres, assuming two different condensation approaches, explained in detail in Chapter 3. Goyal et al. (2019b) presented a generic grid of model transmission spectra that can be scaled to a wide range of hot Jupiter planets, explained in detail in Chapter 4.

The 1D Forward model termed “ATMO ” is primarily used in this thesis. ATMO is a 1D-2D radiative-convective equilibrium model for planetary atmospheres (Tremblin et al. 2015; Tremblin et al. 2016; Amundsen et al. 2014; Drummond et al. 2016; Goyal et al. 2018). It has been applied to interpret observations of several exoplanets both as a forward and retrieval model (for e.g Evans et al. 2017; Nikolov et al. 2018; Goyal et al. 2019b). It solves the radiative transfer equation for a given set of opacities, P-T profile and chemical abundances in equilibrium as well dis-equilibrium, all described in detail in Chapter 2.

1.5.2 Retrieval Models

As explained in the previous section, in forward models physical constraints are imposed depending on our understanding of the process in a system. For example, 1D atmospheric forward models assume the atmosphere is in radiative-convective-chemical equilibrium. Therefore, the accuracy of forward models is reliant on both the validity of the assumed constraints, and the completeness of the physical description developed. Retrieval models approach the problem differently by limiting the number of assumed physical constraints and modelled processes, restricting, predominantly, to only radiative transfer. For example, most of the exoplanet atmosphere retrieval models do not conserve energy locally and globally. The aim of the retrieval models is predominantly to match the observational spectra as accurately as possible, by relaxing physical constraints and identify the spectral features. Therefore, retrieval models also termed inverse models as they are driven by observations, while forward models are generally developed under physical constraints, independent of observations, although they evolve with observations. Although quite new in the field of exoplanet atmospheres, retrieval methods have been used for a long time in the Earth and solar system science community (Irwin et al. 2008), primarily due to the abundance of Earth and solar system observational data.

The forward problem involves solving a set of coupled equations, beginning with a initial condition and iterating to convergence, thereby generating simulated observations using the model, to explain real observations. However, with highly detailed observations the problem can be reversed and planetary characteristics derived using the retrieval process. Therefore, retrieval models for exoplanet atmospheres have some-kind of simple forward models in their backend, with varying levels of imposed constraints and parameterisations, depending on computational resources.

An atmospheric retrieval code primarily consists of two components: 1. a parametric or a forward model to compute the atmospheric spectrum for given atmospheric parameters, 2. an optimisation algorithm, analogous to a statistical inference method to sample the model parameter space given the data. The goal of this optimisation algorithm is to sample the high dimensional parameter space extensively and efficiently, and find a model solution space to explain the given data (Madhusudhan 2018).

These optimisation algorithms have evolved substantially for exoplanet atmospheres. The first step started with a simple grid based search retrievals, with optimisation using the χ^2 minimisation (Madhusudhan et al. 2009). This was followed by a Bayesian inference methods, used in various other areas of astronomy. Different retrieval codes use different Bayesian inference techniques such as Markov Chain Monte Carlo (MCMC) (Madhusudhan et al. 2011; Benneke et al. 2012; Evans et al. 2017), Optimal Estimation (Irwin et al. 2008; Lee et al. 2012a; Line et al. 2013) and Nested sampling (Benneke et al. 2013).

The optimal estimation (OE) method allows specification of priors for the parameters in the cost function to be minimised. Here, prior refers to the best initial guess of the parameters and cost function refers to the difference between the model spectra and observational spectra. This leads to faster convergence with high resolution and high signal to noise ratio (SNR) data. Therefore, this method has been widely used in the Earth and solar system science community, due to availability of strong priors from in-situ or high resolution observations (Irwin et al. 2008). However, the OE method can be inaccurate for low-resolution low SNR data, as available for exoplanet atmospheres, due to multi-modal parameter space with strong degeneracies, leading to weak priors.

The MCMC method is the most widely used optimisation algorithm in retrieval models. In this method the parameter space exploration starts at an initial guess and progresses as a "random walk", where any given step in the chain depends only on the previous step. This method allows efficient and extensive sampling of the posterior distribution. However, the MCMC method is not optimised for calculating the evidence or likelihood function ($\mathcal{L}$), making it challenging to conduct model comparisons when multiple models are the possible solution (Madhusudhan 2018; Trotta 2017).

Nested sampling overcomes the limitations of the OE and MCMC method. This method starts with a given number of points in the parameter space randomly drawn from the prior distribution (Feroz et al. 2009). In each step the point with the lowest likelihood $\mathcal{L}_{min}$ is discarded and replaced by another point from the prior distribution with $\mathcal{L} > \mathcal{L}_{min}$, where the new point is within the iso-likelihood contour of $\mathcal{L}_{min}$.

1.5.3 3D Models

Real planetary atmospheres have a three dimensional structure. Therefore, even though we can get a rough estimate of the planetary properties using 1D and 2D models, the most accurate simulations can only be performed using 3D models. The models that are generally used for studying the weather and climate of the earth as a whole are called as General Circulation Models (GCMs). These models are the most sophisticated physical and numerical models of the atmosphere and for the case of Earth even coupled with ocean and land models. 3D models take into consideration all the dynamical effects like horizontal and vertical advection, transport of chemical species etc. Many recent observations of the shift of hot spot on hot Jupiter exoplanets due to strong winds have also motivated the development of 3D models. However, 3D models are computationally expensive so it is hard to use them to explore a large parameter space.

GCMs basically involves a dynamic core which solves the approximate versions of the Navier stokes equation, a radiation scheme that calculates heating rate as explained earlier, cloud parameterisation schemes etc. All these elements are then discretised over a grid, often in latitude, longitude and vertical coordinates, although other options exist. The Navier Stokes equations can be simplified by adopting a number of approximations depending on the nature of the atmosphere in question. Most of the initial works solved the primitive equations under the assumption of hydrostatic equilibrium with constant gravity (Showman et al. 2002; Showman et al. 2009; Menou et al. 2009; Heng et al. 2011). However, since the radius of hot Jupiter atmospheres are relatively larger, some of the recent works started to solve full non-hydrostatic equations with varying gravity (Mayne et al. 2013, 2014; Amundsen et al. 2014). 3D models for hot Jupiter planets have been increasing in sophistication in the recent years, with fully coupled hydrodynamics, equilibrium chemistry and non-grey radiative transfer (Drummond et al. 2018a) and with fully coupled cloud model (Lines et al. 2018a; Lines et al. 2018b).

1.6 Aims of this thesis

- 1) To characterise the atmospheres of hot Jupiter and warm Neptune exoplanets using their observations and 1D atmosphere models.
- 2) To understand the most dominant physical and chemical processes that shape the transmission and emission spectra of hot Jupiter and warm Neptune exoplanet atmospheres.
- 3) To identify key physical parameters that effect the spectra and thereby use them to predict observations for a range of exoplanet atmospheres, to choose the best scientific targets and plan future observations.
- 4) To develop a library of models and use them for interpreting the observations of Exoplanet atmospheres.
- 5) To identify key molecular features in exoplanet atmospheres.
- 6) To determine the Pressure-Temperature structure of the exoplanet atmospheres.
- 7) Provide a publicly available library of simulated observations for community to use, for choosing best targets for observations using the JWST, as well as a useful complementary tool for interpretation, alongside atmospheric retrieval analysis.

Chapter 2

Modelling Planetary Atmospheres

> "No matter what you look at, if you look at it closely enough, you are involved in the entire universe."
>
> — Michael Faraday

2.1 Constructing a 1D atmosphere model

The basic ingredients required to construct a 1D atmosphere model are chemistry, radiative transfer, opacity database, convective parameterisation and a numerical solver to solve the equations under various physical constraints. Such a model could then be improved by implementing more physical schemes for missing processes such as photodissociation, vertical mixing, clouds, haze etc. or improving on the existing parameterised schemes. Moreover, the ability to calculate synthetic observations (e.g. transmission spectra) from the atmospheric structure could also be included in such a model. In this chapter I delve into the details and formulation of radiative transfer, opacity database, chemistry, convective parameterisation, cloud and haze parameterisation, as well as the generation of synthetic observations for planetary atmospheres.

2.2 Radiative Transfer

There are many books explaining the fundamentals of radiative transfer at different levels of complexity, focusing primarily on either stellar or planetary atmospheres. Here, I show the derivation and physical meaning of the radiative transfer equation and its solution for a planetary atmosphere, a description which has been formulated using a number of sources (Chandrasekhar 1960; Rybicki et al. 1986; Thomas et al. 2002; Seager 2010).

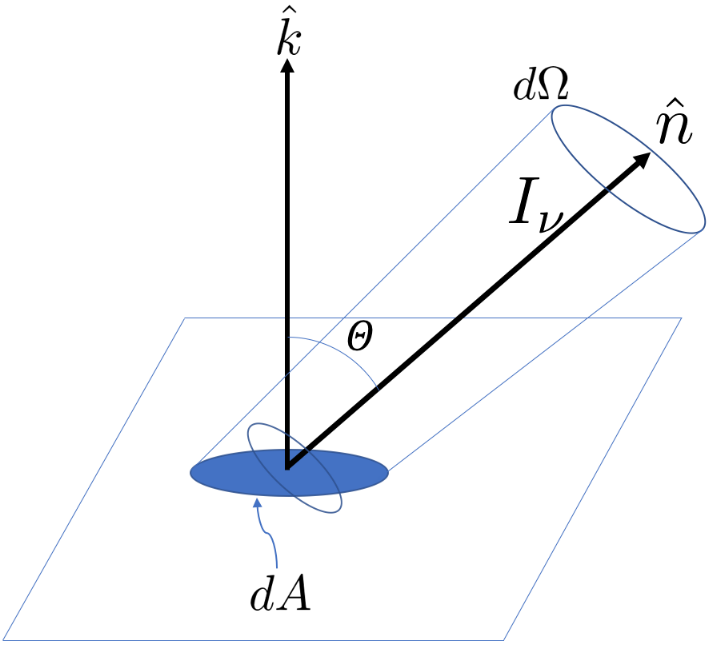

Figure 2.1: Illustrative figure to define intensity.

2.2.1 Basic Terminologies

The most basic quantity that is measured by the instruments to quantify radiation is energy flux, defined as the energy received by the unit area of a detector in the unit time in a frequency interval. However, to model the transport of radiation in a star or a planetary atmosphere a quantity called specific intensity (spectral radiance in Earth science) I for a pencil of radiation as shown in Figure 2.1 is used. Specific intensity is defined as the amount of energy dE passing through a surface element of area dA whose normal $\hat{k}$ is inclined at an angle of Θ with respect to the direction of propagation of the radiation $\hat{n}$, through small element of solid angle $d\Omega$ in the direction of propagation, per unit time interval dt, per unit frequency interval $d\nu$ (can also be wavenumber or wavelength) at any location x given by,

$$I(x,\hat{n},\nu,t) = \frac{dE}{dA\cos\Theta d\Omega dt d\nu} \qquad [ergcm^{-2}sr^{-1}s^{-1}Hz^{-1}] \tag{2.1}$$

It must be noted that although directionality is implied by I it is a scalar quantity. The mean intensity $J(x,\nu,t)$ is defined as the intensity averaged over the solid angle given by

$$J(x,\nu,t) = \frac{1}{4\pi}\int_\Omega I(x,\hat{n},\nu,t)d\Omega. \qquad [ergcm^{-2}s^{-1}Hz^{-1}] \tag{2.2}$$

$J(x,\nu,t)$ is also called the zeroth moment of intensity and is also a scalar, as it is mean intensity. This quantity is particularly useful to formulate emission due to scattering as explained in the next section.

The first moment of intensity is the flux $F(x, \nu, t)$ (irradiance in Earth science) obtained by integrating the intensity of radiation over the solid angle $d\Omega$

$$F(x, \nu, t) = \int_{\Omega} I(x, \hat{n}, \nu, t) \hat{n} d\Omega \qquad [ergcm^{-2}s^{-1}Hz^{-1}] \tag{2.3}$$

It must be noted that the flux is a vector quantity having directional dependance. Physically, F conveys the cumulative effects of all angular beams in different directions, while I precisely describes each angular beam or a pencil of radiation. Therefore, F changes as we move away (as distance increases) from the source of radiation, however the intensity remains constant. For example, intensity measured at a distance of Earth from the Sun is same as that on the surface of the Sun, but the flux is reduced to $\frac{1}{r_{es}^2}$ times the flux value at the Sun's surface, where r_{es} is the distance between Earth and Sun. This is because the Sun subtends a smaller solid angle at the distance of Earth as compared to that at its surface. The dependance of intensity on solid angle makes it independent of distance unlike flux, since the distance is actually embedded in the solid angle. Since the variation of stellar flux with time is negligible for the timescales we consider, we formulate for the static case and drop the variation with time for all further equations. We neglect the effect due to starspots and flares in this work. However, it has to be noted that intensity and therefore all its moments deal with energy flow per unit time. It is obvious that all the variables I, J and F are dependant on position vector x so we also drop the notation x in the list of variables for these quantities (in brackets).

J when computed is integrated over a solid angle as shown in Eq. 2.2. In spherical geometry specified by polar angle θ with azimuthal symmetry this becomes

$$J(\nu) = \frac{1}{4\pi} \int_0^{2\pi} \int_{-1}^{1} I(\nu, \mu) d\mu d\phi = \frac{1}{2} \int_{-1}^{1} I(\nu, \mu) d\mu, \tag{2.4}$$

where $\mu = \cos\theta$. The flux in this case is given by

$$F(\nu) = \int_0^{2\pi} \int_{-1}^{1} I(\nu, \mu) \mu d\mu d\phi = 2\pi \int_{-1}^{1} I(\nu, \mu) \mu d\mu. \tag{2.5}$$

2.2.2 Formulating transport of radiation in a planetary atmosphere

Radiative transfer fundamentally deals with transport of energy using electromagnetic radiation. In the plane parallel approximation, the planetary atmosphere can be divided into multiple plane parallel layers as shown in Figure 2.2 with homogeneous properties such as temperature (T), pressure (P) and density (ρ) defined for each layer. The radiative transfer equation can then be solved for each layer and radiative flux in each layer can be computed. It must be noted that the plane parallel approximation is valid when the radial depth of the modelled atmosphere is much smaller than the bulk radius. The most basic form of the radiative transfer equation for a plane parallel atmosphere in local thermodynamic equilibrium (LTE) condition with isotropic and coherent scattering (no change in frequency like Raman scattering) can be written as,

$$\mu\frac{dI(\nu,\mu,\phi)}{ds} = -\alpha(\nu)I(\nu,\mu,\phi) - \sigma(\nu)I(\nu,\mu,\phi) + \sigma(\nu)J(\nu) + \alpha(\nu)B(\nu,T) \tag{2.6}$$

where, $\mu = \cos\theta$ and θ is the polar angle of radiation beam, ϕ is the azimuthal angle, ν is the frequency of the radiation, $I(\nu,\mu,\phi)$ is the intensity, ds is the thickness of the layer, $J(\nu)$ is the mean intensity defined earlier (can be thought as emission intensity due to scattering), T is the temperature of the layer, $B(\nu,T)$ is the thermal emission intensity often called the Planck function, $\alpha(\nu)$ is the absorption coefficient $[m^{-1}]$ and $\sigma(\nu)$ $[m^{-1}]$ is the scattering coefficient. Absorption and scattering coefficients physically represent the relative loss of intensity per unit length due to absorption and scattering, respectively from the pencil of radiation. Absorption cross-section κ^a, the quantity computed using line-lists described in detail in Section 2.4 is related to absorption coefficient via the number density n such that,

$$\kappa^a(\nu,T,P) = \sum_j \kappa^a_j(\nu,T,P) = \sum_j\sum_i n_{ji}(T,P)\alpha_{ji}(\nu,T,P) \tag{2.7}$$

where, j refers to different molecular or atomic species and i refers to energy level populations (atomic or molecular states) of those species (if there are more than one). The similar relationship can be applied between scattering coefficient and scattering cross-section (see Section 2.6 for details).

As shown in Figure 2.2, for 1D models assuming azimuthal symmetry, only the variation in θ directions is considered through μ (μ is a variable for all beams, not to be confused with the zenith angle, which is the angle of incident irradiation). Therefore, the dependance on ϕ can be omitted and we get

$$\mu\frac{dI(\nu,\mu)}{ds} = -\alpha(\nu)I(\nu,\mu) - \sigma(\nu)I(\nu,\mu) + \sigma(\nu)J(\nu) + \alpha(\nu)B(\nu,T), \tag{2.8}$$

$$\text{where, for azimuthal symmetry,} \tag{2.9}$$

$$J(\nu) = \frac{1}{2}\int_{-1}^{1} I(\nu,\mu)d\mu,$$

Physically, Eq. 2.8 computes the change in the intensity of radiation $I(\nu,\mu)$ as it traverses the atmospheric layer of thickness ds entering at an angle of θ with

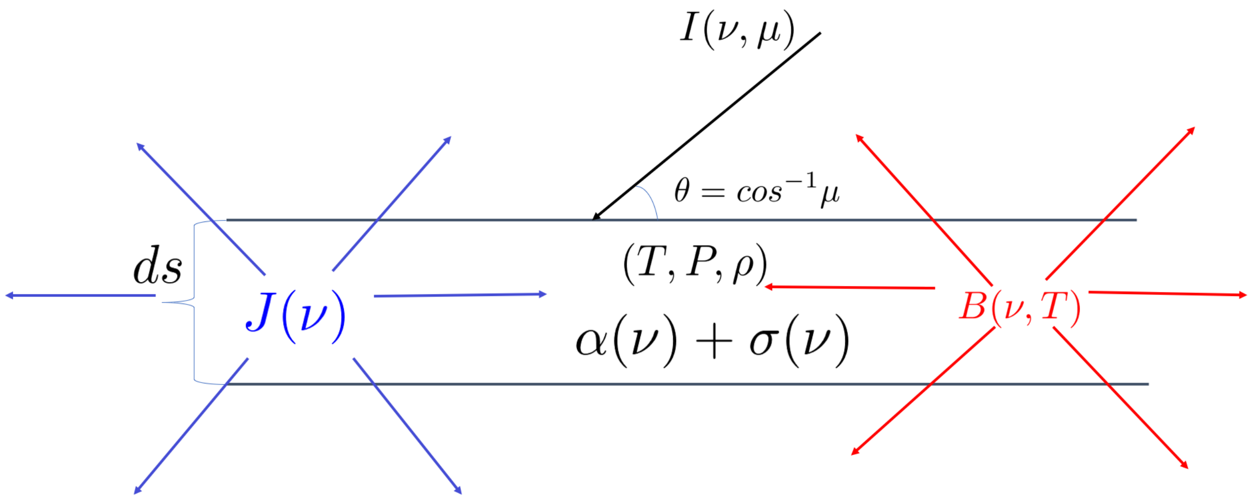

Figure 2.2: Illustrative figure to formulate radiative transfer equation. Blue arrows show scattered beams and red shows Planck emission beams.

respect to normal specified by $\mu = \cos\theta$ as shown in Figure 2.2. This change in intensity is the combined effect of absorption, scattering and emission in the layer. The first term on the right hand side (rhs) represents the loss (therefore negative) in intensity due to true absorption by gases which is dependant on $\alpha(\nu)$. The second term represents loss due to scattering, dependant on the scattering coefficient $\sigma(\nu)$ which is computed based on the type of scattering process (see Section 2.6.1 for Rayleigh scattering cross-section calculation). The scattering of radiation in a true sense does not result in loss but is just redirected in different directions based on the property of the gases/particles. However, there is also a gain in the given pencil of radiation due to scattering from other pencils/beams of radiation. This gain in intensity (therefore addition) is given by the third term (also called emission due to scattering) again dependant on scattering coefficient $\sigma(\nu)$ and $J(\nu)$. Physically, $J(\nu)$ determines the addition of intensity in the considered pencil of radiation from all the other directions. It must be noted that $J(\nu)$ is a function of $I(\nu,\mu)$ as defined in 2.4. The reason why emission due to scattering for an isotropically scattering atmosphere is equal to $J(\nu)$ is derived below.

Emission due to scattering $E_{scatt}(\nu,\mu)$ is given by,

$$E_{scatt}(\nu, \mu) = \frac{1}{2}\int_{-1}^{1} p^{(0)}(\mu, \mu')I(\nu, \mu)d\mu', \tag{2.10}$$

where

$$p^{(0)}(\mu, \mu') = \frac{1}{2\pi}\int_{0}^{2\pi} p(\mu, \phi, \mu', \phi')d\phi', \tag{2.11}$$

where $p(\mu, \phi, \mu', \phi')$ is the single scattering phase function representing contribution of scattered pencil of radiation from direction (μ', ϕ') into direction (μ, ϕ) (Chandrasekhar 1960). The phase function in general represents the angular distribution of the scattered radiation. For isotropic scattering and azimuthal symmetry $p^{(0)}(\mu, \mu') = \frac{1}{2\pi}\int_0^{2\pi} p(\mu, \phi, \mu', \phi')d\phi' = 1$ which makes Eq. 2.10 equivalent to taking mean of intensity over all solid angles via μ and ϕ. Therefore, the emission intensity due to scattering is equal to J. It must be noted that even if we consider isotropic scattering, the variation in the pencil of radiation due to variation in μ still remains, as each pencil of radiation depending on its orientation (angle), traverses a different distance through the atmosphere.

The last term on the rhs of Eq. 2.8 is the thermal emission (addition to the beam) term dependant on the absorption coefficient $\alpha(\nu)$ and Planck thermal emission function $B(\nu, T)$ which is always isotropic. The dependance on $\alpha(\nu)$ is a result of Kirchhoff's law of radiation which states that under LTE conditions the emissive properties of a gas are related to its absorption properties, such that the thermal emission coefficient is simply equal to the absorption coefficient.

Separating absorption and emission terms we get,

$$\mu\frac{dI(\nu, \mu)}{ds} = -\alpha(\nu)[I(\nu, \mu) - B(\nu, T)] - \sigma(\nu)[I(\nu, \mu) - J(\nu)] \tag{2.12}$$

Here we define a quantity called the source function $S(\nu, \mu)$, by combining the emission terms and normalising by $\alpha(\nu) + \sigma(\nu)$ to simplify the equation. Thus giving,

$$\mu\frac{dI(\nu, \mu)}{ds} = [\alpha(\nu) + \sigma(\nu)][-I(\nu, \mu) + S(\nu, \mu)], \tag{2.13}$$

where

$$S(\nu, \mu) = \frac{\alpha(\nu)B(\nu, T) + \sigma(\nu)J(\nu)}{\alpha(\nu) + \sigma(\nu)}$$

Absorption and scattering coefficients can be combined together as the total extinction coefficient $\kappa(\nu)$ given by $\kappa(\nu) = \alpha(\nu) + \sigma(\nu)$. Moreover, since the distance travelled by the light in a medium is dependant on total opacity, rather than the path s, a more useful quantity to measure the distance travelled by light is the optical depth given by

$$d\tau_\nu = \kappa(\nu)ds, \tag{2.14}$$

where $d\tau$ is the change in the optical depth over distance ds. Therefore, rearranging Eqs. 2.13 and using 2.14 we get the simplest form of the radiative transfer equation for a plane parallel atmosphere with isotropic and coherent scattering,

$$\mu\frac{dI(\nu,\mu)}{d\tau_\nu} = -I(\nu,\mu) + S(\nu,\mu). \tag{2.15}$$

The other quantity generally used in these equations is the single scattering albedo $\omega_o = \frac{\sigma(\nu)}{\alpha(\nu)+\sigma(\nu)}$, describing the fraction of light lost from the pencil of radiation due to scattering. Therefore, the source function can also be written as $S(\nu) = (1-\omega_o)B(\nu) + \omega_o J(\nu)$. Thus Eq. 2.15 can also be written as

$$\mu\frac{dI(\nu,\mu)}{d\tau_\nu} = -I(\nu,\mu) + (1-\omega_o)B(\nu,T) + \omega_o J(\nu), \tag{2.16}$$

$$\text{where} \qquad J(\nu) = \frac{1}{2}\int_{-1}^{1} I(\nu,\mu)d\mu.$$

2.2.3 Solving the radiative transfer equation and computing radiative flux in ATMO

For irradiated exoplanets, radiation is the primary mode by which energy is received from their host star and propagated through the atmosphere, thus playing a dominant role in governing the behaviour of the atmosphere. The first step in solving for the impact of the radiation on the atmosphere is to compute the energy received from the host star at the top of the atmosphere. Consider a host star emitting radiation from its surface at intensity $I_{star}(\nu)$ with radius R_{star}, so the flux at the top of the planet's atmosphere F_{TOA} at a distance (semi-major axis) of a at a given time t is,

$$F_{TOA}(\nu,t) = \frac{R_{star}}{a}^2 \int_0^{2\pi}\int_0^{\pi/2} I_{star}(\upsilon,\phi,\nu,t)\cos\upsilon\sin\upsilon d\upsilon d\phi, \tag{2.17}$$

where υ and ϕ are the co-latitude (complimentary angle of latitude) and longitude of the star, respectively. Assuming uniform stellar intensity across star's surface, we get

$$F_{TOA}(\nu,t) = (R_{star}/a)^2\pi I_{star}(\nu,t). \tag{2.18}$$

However, $\pi I_{star}(\nu,t) = F_*(\nu,t)$, where F_* is the flux at the surface of the star,

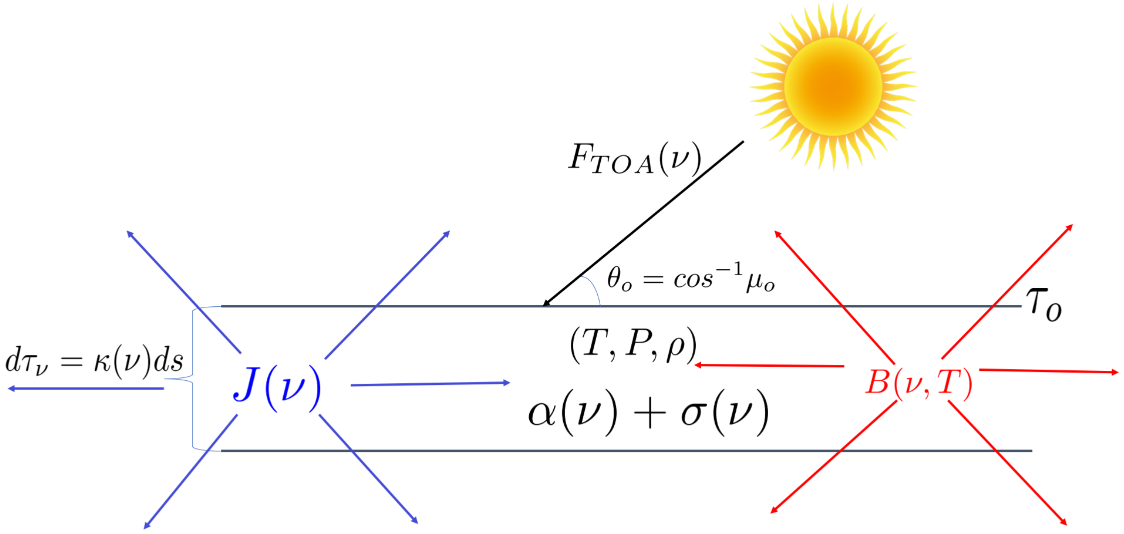

Figure 2.3: Illustrative figure for solving radiative transfer equation, showing the distribution of intensity via different terms of the equation.

since it is the intensity integrated over the entire solid angle of the sphere. Therefore,

$$F_{TOA}(\nu, t) = (R_{star}/a)^2 F_*(\nu, t). \tag{2.19}$$

Now here $F_{TOA}(\nu, t)$ is the flux at one specific point, the sub-stellar point at the top of the planet's atmosphere. It must be noted that from the modelling perspective we are interested in calculating the total incident energy received by the planet per unit time. Therefore, the flux received on the entire dayside hemisphere has to be integrated. This cannot be achieved by just multiplying the planet hemispherical surface area $2\pi R_p^2$, as the flux received at different locations (latitude and longitude) of the planet will be different. The total flux on the dayside is therefore computed by integrating $F_{TOA}(\nu, t)$ over the entire hemisphere. In the 1D models we are however just concerned with the intensity at one specific point in the atmosphere, therefore the variation of flux/intensity due to location on the planet is accounted for using the angle of incidence θ_o via $\mu_o = \cos\theta_o$. Since the variation of stellar flux with time is negligible for the timescales we consider, we drop the variation with time as before.

Eq. 2.16 shows the general form of radiative transfer equation which is an integro-differential equation. Similarly, most of the radiative transfer equations with different assumptions/approximations are of this form with varying degrees of complexity. If we consider an hypothetical atmosphere without any scattering, then in that case ω_o will be 0, leaving just the Planck emission $B(\nu, T)$ in the source term.

In that case, the solution becomes quite simple given by,

$$I(\tau_\nu,\nu,\mu) = -I_o(\nu,\mu_o)e^{\frac{-(|\tau_\nu-\tau_o|)}{\mu}} + \int_{\tau_o}^{\tau_\nu} \frac{1}{\mu}B(\nu,T)e^{\frac{|\tau_\nu-\tau_\nu'|}{\mu}}d\tau_\nu' \tag{2.20}$$

where, $I_o(\nu,\mu_o)$ is the incident intensity at the top of the atmosphere entering at an angle of θ_o as shown in Figure 2.3 and τ_o is the optical depth at the top of the atmosphere. It must be noted that the temperature dependance of B is communicated through τ_ν, therefore indirectly B is a function of optical depth. However, scattering cannot be neglected while solving the radiative transfer equation, as it contributes substantially in transferring energy which we can realise by looking at the blue sky of the Earth primarily due to Rayleigh scattering by gases in the atmosphere. Since, scattering adds a substantial amount of mathematical complexity and also computational expense while solving radiative transfer equations, various mathematical as well as numerical methods have been developed to tackle this problem (see Chandrasekhar 1960; Thomas et al. 2002, for details).

In ATMO the radiative flux/intensity is divided into two parts named direct and diffuse while solving. This division is mathematically beneficial while solving the radiation transfer equation, especially for adopting suitable physically motivated boundary conditions (Thomas et al. 2002). The direct flux Eq. 2.21 simply deals with the extinction of host star flux entering the atmosphere as it traverses different layers of optical depth τ_ν. The scattering due to this direct flux acts as a source term for diffuse flux/intensity equation as shown in Eq. 2.22. Therefore, at first the direct flux equation is solved and then using the flux that has survived extinction, the diffuse equation is solved.

The direct flux/intensity equation simply follows the extinction law (Beer-Lambert's law) given by

$$F_{rad,dir}(\nu) = F_{TOA}(\nu)e^{\frac{-\tau_\nu}{\mu_o}}, \tag{2.21}$$

where, $F_{rad,dir}(\nu)$ is the direct stellar flux that has survived extinction in each layer of the atmosphere, therefore acts as a source term for diffuse flux/intensity equation given by

$$\mu\frac{dI(\nu,\mu)}{d\tau_\nu} = -(I(\nu,\mu)+(1-\omega_o)B(\nu,T)+\omega_oJ(\nu))+\omega_o\frac{F_{rad,dir}(\nu)}{4\pi}p^{(0)}(\mu,\mu_o), \tag{2.22}$$

where $p^{(0)}(\mu,\mu_0)$ is the phase function as defined earlier representing scattering from μ_o into μ. However, since we assume isotropic scattering $p^{(0)}(\mu,\mu_0) = 1$. The Eq. 2.22 is similar to Eq. 2.16 with an additional source term due to scattering of the direct flux. Simply this can be written as,

$$\mu \frac{dI(\nu,\mu)}{d\tau_\nu} = -I(\nu) + S_d(\nu), \tag{2.23}$$

$$\text{where,} \tag{2.24}$$

$$S_d(\nu) = (1-\omega_o)B(\nu,T) - \omega_o J(\nu)) - \omega_o \frac{F_{rad,dir}(\nu)}{4\pi}. \tag{2.25}$$

The Eq. 2.23 is solved using the discrete ordinate method in ATMO by sampling ray directions (μ) using Gauss-Legendre quadrature. The solution for this equation is of the form similar to Eq. 2.20 but with all the scattering terms embedded in the source term given by

$$I(\tau_\nu,\nu,\mu) = -I_o(\nu,\mu_o) e^{\frac{-(|\tau_\nu - \tau_o|)}{\mu_o}} + \int_{\tau_o}^{\tau_\nu} \frac{1}{\mu} S(\tau_\nu,\nu,\mu) e^{\frac{-(|\tau_\nu - \tau'_\nu|)}{\mu}} d\tau'_\nu, \tag{2.26}$$

$$\text{where,} \tag{2.27}$$

$$S_d(\nu,\mu) = (1-\omega_o)B(\nu,T) - \omega_o J(\nu)) - \omega_o \frac{F_{rad,dir}(\nu)}{4\pi}, \tag{2.28}$$

where the incident radiation $I_o(\nu,\mu_o)$ at the top of the atmosphere can be computed using $I_o(\nu) = \frac{F_{TOA}(\nu)}{\mu_o}$ because,

$$F_o(\mu,\nu) = \int_{-1}^{0} I_o(\nu)\mu\delta(\mu-\mu_o)d\mu = \mu_o I_o(\nu), \tag{2.29}$$

where $F_o = F_{TOA}$ is the incident stellar flux and $\delta(\mu-\mu_o)$ is the dirac-delta function indicating intensity is 0 everywhere except in the direction of μ_o (where it is infinite). Thus, Eq. 2.26 is solved for $I(\nu,\mu)$ for each layer of the atmosphere to obtain the diffuse radiative flux $F_{rad,diff}(\nu) = 2\pi \int_{-1}^{1} I(\nu,\mu)\mu d\mu$ following the definition of flux, (see Eq. 2.3) and assuming azimuthal symmetry with variation only in μ. The full radiative transfer equation in its integral form is solved in ATMO following the method of Trujillo Bueno et al. (1995), using a Gauss-Siedel type Λ acceleration scheme for scattering. Therefore, we obtain the the total radiative flux F_{rad} in each layer of the atmosphere given by

$$F_{rad} = \int_{0}^{\infty} \big(F_{rad,dir}(\nu) + F_{rad,diff}(\nu)\big) d\nu. \tag{2.30}$$

2.3 Recirculation factor

In a planetary atmosphere advection due to winds is one of the major processes responsible for transporting energy. To incorporate the 3D effect of advection in 1D models as adopted by Fortney et al. (2007), we simply reduce the incoming flux in the 1D column of the atmosphere by a factor called the "recirculation factor", hereafter termed "rcf". It parameterises the redistribution of input stellar energy in the planetary atmosphere, by the dynamics, where a value of 1 equates to no redistribution, while 0.5 represents efficient redistribution. The value of 0.5 rcf indicates 50% of the total incoming stellar energy is advected to the night side (the side of the planet facing away from the star), while 0.25 rcf indicates 75% of the total incoming stellar energy is advected to the night side. It must also be noted that an additional factor, the incidence angle θ_o also contributes to the reduction in this total incoming stellar energy. $\theta_o = 60°$ equating to the dayside (the side of the planet facing towards the star) average is the most commonly adopted value of incidence angle, contributing to 50% reduction in the total incoming stellar energy, since $\cos 60° = 0.5$.

2.4 Absorption Cross-sections

As described in the previous section, solving the radiative transfer equation requires the absorption and scattering properties of gas in each layer. The bulk absorption properties of gaseous species due to all transitions can be represented by the absorption cross-section $[\kappa^a(\nu, T, P)]$ as shown in Eq. 2.7. Even the general opacity computations for any gaseous species require computation of wavelength dependant absorption cross-sections. These absorption cross-sections are computed using line list databases from various sources such as HITRAN (High Resolution TRANsmission) (Rothman et al. 2013) and Exomol (Tennyson et al. 2016). The line lists available from various sources primarily consists of line intensities directly, or Einstein coefficients or oscillator strengths which can be then used to compute line intensities. In this section we cover the details required to calculate absorption cross-sections, for detailed derivations of equations and basic theory refer Rybicki et al. (1986), Hubeny et al. (2014), and Amundsen (2015)

2.4.1 Einstein Coefficients

To describe the interaction of radiation with an atomic system, Einstein considered a simple case of two discrete energy levels (Rybicki et al. 1986). The first level of energy E (lower) and the second of energy E + $h\nu_0$ (upper), where h is the Planck's constant, c is the velocity of light in vacuum and ν_0 is the frequency of emission/absorption of electromagnetic radiation. There are three processes that can happen in this system described by Einstein coefficients which are:

Spontaneous Emission - When the system makes a transition from upper to lower level it emits a photon, which can even happen in the absence of a radiation field. This process is represented by Einstein A coefficient A$_{ul}$ (upper to lower), defined as the transition probability per unit time for spontaneous emission (s^{-1}).

Absorption - When the system makes a transition from lower to upper level by absorbing a photon of energy hν_0, which requires the presence of a radiation field, therefore is also dependant on the energy density of the radiation field. It must also be noted that, the energy differences between the two levels are not infinitely sharp and therefore are described by a line profile function sharply peaking at ν_0. The likelihood of the frequencies in the vicinity of ν_0 to cause transitions is described by this line profile function. This process is represented by Einstein B coefficient B$_{lu}$ (lower to upper), defined as the transition probability per unit time per unit energy density of the radiation field for absorption. This can be represented in various units.

Stimulated Emission - When the system makes a transition from upper to lower level by emitting a photon, due to the presence of the radiation field. This process is represented by another Einstein B coefficient B$_{ul}$ (upper to lower), defined as the transition probability per unit time per unit energy density of the radiation field for stimulated emission.

All the Einstein coefficients are related to each other by following two equations (Šimečková et al. 2006; Rybicki et al. 1986)

$$g_l B_{lu} = g_u B_{ul}, \tag{2.31}$$

$$A_{ul} = 8\pi h \nu_o^3 B_{ul}, \tag{2.32}$$

where g$_l$ and g$_u$ are the statistical weights or degeneracies of lower and upper levels, respectively, h is the Planck's constant and c is the velocity of light. Eq. 2.32 is only valid when B$_{ul}$ is in the units of transition probability per unit time per unit energy density per unit frequency $s^{-1}J^{-1}cm^3Hz$. When B$_{ul}$ is in the units of transition probability per unit time, per unit energy density per unit wavenumber $s^{-1}J^{-1}cm^3cm$ it becomes

$$A_{ul} = 8\pi hc\tilde{\nu}^3 B_{ul}, \tag{2.33}$$

where $\tilde{\nu}$ is the wavenumber of the of the electromagnetic radiation. Wavenumber is more often used in spectroscopy because energy levels are conveniently proportional to wavenumber (or frequency) as compared to wavelength. Moreover, spectrometers are often calibrated in wavenumber because it is independent of the

the fundamental constants c and h (Seager 2010). Henceforth, wavenumber will be used throughout this section.

Due to this temperature independent relationship between Einstein coefficients, knowing any one of them is sufficient for computing line intensities as shown later. The temperature independence of Eqs. 2.31 and 2.33, also makes them valid when atoms are not in thermodynamic equilibrium.

2.4.2 Oscillator Strengths

Some line-lists provide oscillator strengths (gf values) instead of Einstein coefficients to compute line intensities. For example, the VALD line-list database[1] (Heiter et al. 2008). However, the oscillator strength is directly related to the Einstein A coefficient by

$$g_u A_{ul} = \frac{8\pi^2 e^2 \tilde{\nu_o}^2}{m_e c} g_l f_l u, \tag{2.34}$$

where e is the electron charge in CGS units, m_e is the mass of the electron, ν_o is the wavenumber of the transition and $f_l u$ is the oscillator strength of the transition. Thus this equation provides a relationship between Einstein A coefficient and oscillator strength.

2.4.3 Line Intensities

The transition of an electron between lower and upper states i and j results in the emission or absorption of a photon of energy $\delta E = E_i - E_j$. The spectral line intensity of the transition is then given by,

$$S_{i,j} = I_a \frac{A_{ij}}{8\pi c \tilde{\nu_{i,j}}^2} \frac{g' e^{(} -c_2)E''/T(1 - e^{-c_2 \tilde{\nu}_{i,j}/T})}{Q(T)}, \tag{2.35}$$

where spectral line intensity $S_{i,j}$ is weighted by the natural terrestrial isotopic abundances I_a (more generally isotopic abundance of mixture). A_{ij} is the Einstein coefficient for spontaneous emission, $\tilde{\nu}_{i,j}$ is the wavenumber, g' is the statistical weight or degeneracy of the upper level, c_2 is hc/k, where k is the Boltzmann Constant, E'' is the energy of the lower level, T is the temperature and $Q(T)$ is the partition function at temperature T. This equation also provides the relationship between line intensity and Einstein coefficient (A_{ij}). As mentioned earlier some line-lists provide line intensities directly at a particular reference temperature, while some provide Einstein coefficients and oscillator strengths, which can then be used to compute line intensities.

---

[1] `http://vald.astro.uu.se/`

The HITRAN (High Resolution TRANsmission) database (Rothman et al. 2013) is the most widely used line-list source in various atmospheric models, most accurate specifically for Earth's atmosphere. This database is established at a reference temperature of 296 K (Rothman et al. 2010) with line intensities accurate up-to ∼400 K. The high temperature version of HITRAN called as HITEMP (Rothman et al. 2010) is also established at a reference temperature of 296 but the calculations have been performed up-to temperatures of ∼4000 K, only for certain molecules.

HITRAN provides spectra line intensity $S_{i,j}(T_{ref})$ data as a function of wavenumber $\tilde{\nu}_{i,j}$ for a transition from $\delta E = E_i - E_j$, at a reference temperature of $T_{ref} = 296\ K$ and therefore the line intensity $S_{i,j}T$ at various temperatures can be calculated using

$$S_{i,j}T = S_{i,j}(T_{ref}) \frac{Q(T_{ref})}{Q(T)} \frac{exp(-c_2 E''/T)}{exp(-c_2 E''/T_{ref})} \frac{[1 - exp(-c_2 \tilde{\nu}_{ij}/T)]}{[1 - exp(-c_2 \tilde{\nu}_{ij}/T_{ref})]}, \tag{2.36}$$

where $Q(T_{ref})$ and $Q(T)$ are partition functions at reference temperature T_{ref} and required temperature T provided in the HITRAN database. E'' is the lower state energy of transition and c_2 is hc/k, where k is the Boltzmann Constant.

Partition functions are generally provided with line-list data. However, they can also be computed using

$$Q(T) = \sum_{i=0}^{\infty} g_i e^{\frac{-E_i}{k_B T}}, \tag{2.37}$$

where the sum is over all the levels from i to ∞, g_i is the statistical weight (degeneracy) of the level, which is generally equal to $2J + 1$ where J is the total angular momentum quantum number (Rybicki et al. 1986) and E_i is the energy of the ith level.

Expected temperatures on hot Jupiter exoplanets can be substantially higher than 296 K, for example WASP-107b has an equilibrium temperature (T_{eq}) of 770 K while that of WASP-12b is 2580 K (see Appendix B.1). In such high temperature conditions, higher energy levels can also be populated than those occupied at 296 K. In such conditions, the HITRAN low temperature line lists can underestimate the absorption of radiation by several orders of magnitude. Therefore, high temperature line lists such as ExoMol[2] (Tennyson et al. 2016) are used to overcome the limitations of HITRAN. Exomol line-lists also provide Einstein coefficients which can be converted to line intensities using Eq. 2.35.

---

[2] `www.exomol.com`

2.4.4 Line Broadening

In nature, the observed absorption or emission lines are never monochromatic. They are constantly influenced by various external or internal factors, leading to broadening of these lines. The absorption/emission lines of various species are broadened by different physical processes in the planetary atmosphere. This effect of broadening is communicated to absorption cross-section via the line profile as in Eq. 2.41. The three major broadening processes are natural broadening, doppler broadening and pressure broadening.

Natural broadening arises as a direct consequence of Heisenberg's uncertainty principle. Emitted photons during transitions will not have definite energy but a distribution of energies about some mean. This leads to natural broadening, but this is very small compared to pressure and doppler broadening for atmospheres of hot Jupiter's, so we neglect it.

All the particles in a planetary atmosphere are in thermal motion while they are emitting or absorbing photons, this leads to a shift in the observed wavenumber, since particles are emitting or absorbing in their own frame of reference. This combined effect leads to broadening of the lines, known as doppler broadening. Doppler broadening can be easily computed using the analytical equation from Thomas et al. (2002) given by

$$\alpha_n(\tilde{\nu}) = \sqrt{\frac{m_z}{2\pi k_B T}} \int_{\infty}^{\infty} dv_x e^{-{v_x}^2/{v_0}^2} \alpha'_n(\tilde{\nu} + v_x \tilde{\nu}_0/c), \tag{2.38}$$

where, α_n is the absorption cross-section with doppler broadening, α'_n is the absorption cross-section without doppler broadening, m_z is the mean particle mass of the species, v_x is the thermal velocity along the line of sight, $\tilde{\nu}$ is the shifted wavenumber of the absorbed photon, $\tilde{\nu_0}$ is the rest frame wavenumber of the absorbed photons, T is the temperature, k_B is the Boltzmann constant and c is the velocity of light. Doppler broadening is a strong function of temperature and becomes significant in low pressure and high temperature environments.

Including the effect of pressure broadening while computing absorption coefficients for different planetary atmospheres is one of the most significant challenges facing the exoplanet modelling community. This broadening is a result of interaction of molecules with other molecules in the atmosphere. Collisions between particles effectively reduce the lifetime of the upper and lower state of transitions, resulting in the broadening of the line. Pressure broadened line width is given by

$$\alpha_L^p(P_p, T) = \alpha_L^p(P_0, T_0) \left(\frac{T_0}{T}\right)^{n_p} \frac{P_p}{P_0}, \tag{2.39}$$

where, α_L^p is the pressure broadened width for perturbing species p, T_0 and P_0

are reference temperature and pressure respectively, P_p is the partial pressure and n_p the temperature exponent. The pressure broadening is also linearly dependent on the partial pressure of perturbing species given by,

$$\alpha_L = \sum \alpha_L^p(P_p, T) \tag{2.40}$$

where, α_L is the total pressure broadened width due to all the species. Therefore, the pressure broadened width will be dominated by the most abundant species in the atmosphere. Hot Jupiter atmospheres are hydrogen and helium dominated, so the effect of broadening due to these abundant species is required to calculate accurate pressure broadening. Published data on broadening of different molecules due to H_2 and He is very sparse, so wherever possible we take H_2 and He broadening, while for other molecules we use air and self broadening parameters as given by HITRAN. The table for broadening parameters and temperature exponents used for different molecules can be found in (Amundsen et al. 2014; Goyal et al. 2018).

It is also important to note that at higher metallicities, the atmospheric abundance of species other than H_2 and He such as CO, H_2O, CO_2, H_2S, etc., become significant. In such conditions, the effect of broadening due to all major species on all the other radiatively important species should be taken into account. It is difficult to accurately comment on the effect of pressure broadening at high metallicities since no study has been done in that area according to our knowledge, although the need for laboratory measurements in this region of the parameter space has been highlighted by Fortney et al. (2016).

2.4.5 Equation for Absorption Cross-section

Using line intensities, absorption cross-sections of each species as a function of wavelength can be obtained using,

$$\kappa^a_{\tilde{\nu},T,p} = S_{i,j}T\phi(\tilde{\nu}) \tag{2.41}$$

where $\kappa^a_{\tilde{\nu},T,p}$ is the absorption cross-section as a function of wavenumber, temperature and pressure and $\phi(\tilde{\nu})$ is the line profile. The effects of the broadening explained in detail in the previous section is included in the absorption cross-section computation via the line profile. These absorption cross-sections are calculated at a resolution of $\Delta\tilde{\nu} = 0.001cm^{-1}$ in ATMO, which is basically equivalent to a line-by-line computation (Garland et al. 2019).

This line profile can be assumed to be of different shapes, e.g., Gaussian, Lorentz or the convolution of the two, called the Voigt profile. For more details see HITRAN documentation[3] and Amundsen (2015). Absorption cross-sections can also be calculated using standard codes such as ExoCross[4].

It must be noted that absorption cross-sections that need to be calculated for different types of atmospheres might be different. For example, the absorption cross-section of H_2O calculated for a hot Jupiter with a H_2-He dominated atmosphere will not be accurate for a Earth like planet with a nitrogen dominated atmosphere, due to difference in sources of broadening.

2.5 Correlated-K Methodology

Once absorption cross-sections are computed they can be used in radiative transfer models to compute absorption/emission of radiation due to different molecules in the atmosphere. Subsequently, this can be used to compute heating rates, P-T profiles, synthetic spectrum etc. in the forward models. Moreover, inverse (retrieval) models use these cross-sections to constrain the molecular abundances in the planetary atmospheres (Irwin et al. 2008; Line et al. 2015; Evans et al. 2017), based on observed data. Therefore, small errors in including these cross-sections accurately in retrieval models can have far reaching effects on the retrieved posterior probability distribution functions of various molecular species (Garland et al. 2019). However, absorption cross-sections include a large number of transitions as a function of wavenumber, temperature and pressure for each molecule, making them computationally expensive when included in the radiative transfer models, directly at their original wavenumber resolution, a method termed the line-by-line method. At sufficiently high resolution there is no difference between high resolution and line-by-line method cross-section ($\Delta\nu = 0.001cm^-1$). The line-by-line method is the most accurate technique adopted in models, but is computationally expensive. Therefore, some kind of binning technique is needed to increase the efficiency of these absorption cross-section calculations, while including them in the atmospheric models.

One of the most common methods adopted is to bin at a particular wavenumber resolution ($\Delta\tilde{\nu} = 10, 1\,cm^{-1}$) from the original line-by-line resolution, by preserving the area (MacDonald et al. 2017). The other method commonly adopted in stellar atmosphere models is the opacity sampling method (see Hubeny et al. 2014, for details), where the line opacity is sampled on a fine grid of wavenumber points such as $1\,cm^{-1}$, as adopted in Line et al. (2015). However, combining cross-sections of different gases at this reduced resolution can lead to substantial errors, due to insufficient resolution as discussed by Garland et al. (2019). Accuracy of the opac-

---

[3] https://hitran.org/docs/definitions-and-units/

[4] https://github.com/Trovemaster/exocross

ities after binning or sampling line-by-line cross-sections ($\Delta\nu = 0.001cm^{-1}$) at the resolution of $\tilde{\nu} = 10, 1cm^{-1}$ has been questioned by Garland et al. (2019).

The most widely adopted method in various planetary atmosphere models and even the Earth GCM models is the correlated-k technique (Lacis et al. 1991), because of the combination of accuracy and computational efficiency that can be achieved using this technique. Line-by-Line (LbL) absorption cross-sections calculated in previous section can have similar values at several wave-numbers. Therefore, combining the radiative transfer (transmission/absorption) calculations for all these wave-numbers can potentially lead to a significant decrease in the computational time, by decreasing the number of monochromatic calculations. This is the basic principle behind the correlated-k method. The correlated-k approximation is a standard approach used in many Earth based atmospheric models, both 1D and 3D (Goody et al. 1989; Lacis et al. 1991; Edwards et al. 1996) and also many of the forward models developed for exoplanet atmospheres (Fortney et al. 2010; Mollière et al. 2015; Malik et al. 2017).

In radiative transfer calculations as explained in Section 2.2 we deal with computation of transmission/absorption of radiation through a layer of atmosphere. Consider a spectral interval $\Delta\tilde{\nu} = \tilde{\nu}_1 - \tilde{\nu}_2$, the beam transmittance $T_b(u)$ along a mass path (column density) u in this spectral interval is then given by

$$T_b(u) = \frac{1}{\delta\tilde{\nu}} \int_{\tilde{\nu}_1}^{\tilde{\nu}_2} d\tilde{\nu} e^{-k(\tilde{\nu})u}, \tag{2.42}$$

where, $k(\tilde{\nu})$ is the wavenumber dependant cross-section. The LBL method, requires calculation of $k(\tilde{\nu})$ at a very high spectral resolution such that $k(\tilde{\nu})$ is essentially constant over the interval $\Delta\tilde{\nu}$, typically of the order of $0.001cm^{-1}$. This has to be repeated for a range of u, temperature and pressure encountered in the atmosphere, making it computationally very expensive.

To overcome this limitation, we transform Eq. 2.42 by using the fact that the similar values of k will be encountered many times in the spectral interval. Therefore, by binning all the different values of k in different groups (by calculating their probability distributions) and computing transmittance only once for each group we can reduce the total number of monochromatic calculations. Doing this grouping over the entire spectrum from optical to infrared is also not practical as we loose the wavenumber information during this grouping process as explained further, therefore the first step in the correlated-k method basically involves dividing absorption cross-sections over the entire spectrum as calculated in the previous section in different spectral (we use wavenumber for ATMO) bands, depending on the required accuracy and application. For example, for ATMO correlated-k opacity files are computed at 3 different spectral resolutions, the lowest resolution with 32 bands, medium resolution with 500 bands and highest resolution with 5000 bands, each suited for different applications explained later in this section.

Following this, within each band with the spectra interval $[\tilde{\nu}_2, \tilde{\nu}_1]$, $k(\tilde{\nu})$ are arranged/grouped in the monotonically increasing order and divided into n subintervals (bins). Thus following Lacis et al. (1991) the frequency (probability) distribution of absorption cross-sections $f(k)$ is obtained by binning and summing wavelength subintervals $\Delta\tilde{\nu}_j$, which have absorption cross-sections within a specified range (k_i, $k_i + \Delta k_i$) using

$$f(k) = \frac{1}{\tilde{\nu}_2 - \tilde{\nu}_1} \sum_{1}^{j} \left| \frac{\Delta\tilde{\nu}_j}{\Delta k_i} \right| W(k_i, k_i + \delta k_i) \tag{2.43}$$

where j is the number of wavenumber sub-intervals, $W(k)$ is the window function that is zero everywhere except between k_i and $k_i + \delta k_i$. The absolute value of $\frac{\Delta\tilde{\nu}_j}{\Delta k_i}$ used in the equation accounts for the change in sign due to increasing or decreasing cross-sections within the interval $\Delta\tilde{\nu}_j$. This then transforms Eq. 2.42 into finite sum given by

$$T_b(u) = \sum_{j=1}^{N} \Delta k_j f(k_j) e^{-k_j u} \tag{2.44}$$

where N is the total number of monotonic subintervals over the range of k values in the band. This in the integral form can be written as

$$T_b(u) = \int_{k_{min}}^{k_{max}} dk f(k) e^{-ku} \tag{2.45}$$

where k_{min} and k_{max} are the minimum and maximum values of k in the band. Now, the sum of $f(k)$ over all the values of k is unity, that is $\int_{k_{min}}^{k_{max}} dk f(k) = 1$. Therefore, the cumulative k-distribution can be defined as $g(k) = \int_0^k dk' f(k')$ a process known as converting to g-space (Cumulative probability space). Each band is then further divided into n subintervals in the cumulative probability space as shown in the Figure 2.4. Following this, by fitting transmission for all the subintervals in single exponential for the set of required column densities, k-coefficient for that particular subinterval is generated along with their corresponding weight. However, the optimum number of subintervals (k-coeffcients) to be used is still unknown. Therefore, to determine the number of k-coefficients in each band, an error calculation is done between the fitted transmission and the line by line transmission for a set of required column densities in each band, starting with number of sub-intervals (k-coefficients) equal to one. When the error reaches acceptable limits (typically 10^{-4} from Amundsen (2015)), the total number of sub-intervals (k-coefficients) in each band is obtained. This process is followed for each temperature, pressure and band

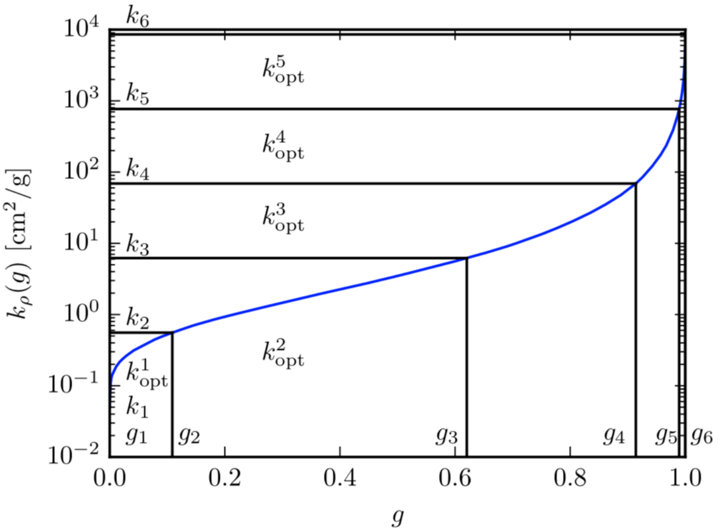

Figure 2.4: Figure from Amundsen (2015) illustrating exponential sum fitting of transmissions (ESFT) to calculate k-coefficients for each sub-interval within a band. Horizontal axis shows "g" (Cumulative probability) of cross-sections within each band. Vertical axis shows absorption cross-sections (κ_ρ) as a function of "g".

for a particular species of gas. However, the spacing between the sub-intervals and consequently the number of k-coefficients and their weights would remain the same at a different temperature and pressure for a given species. A look up table is generated for different species at different temperature, pressure and wavelength bands including corresponding weights in each band for each species. All these calculations are done offline, meaning beforehand, not when the model is running and only the look up table is used while running the radiative transfer model. In this way the correlated-k method can reduce thousands of absorption line calculations to a few band calculations and thereby reducing computational requirements drastically.

The differences in absorption cross-sections using the LBL and correlated-k method with 500 bands ($\Delta\tilde{\nu} = 100cm^{-1}$) is shown in Figures 2.5a and 2.5b, respectively. It can be seen that there is a tendency to loose detailed features, but is not a problem when just heating rates are being computed, which are accurate even with just 32 correlated-k bands. However, this can be overcome by using high resolution (more bands) correlated-k tables, for instance to compute synthetic spectra in ATMO 5000 correlated-k bands ($\Delta\tilde{\nu} = 10cm^{-1}$) are used.

Amundsen et al. (2014) created a correlated-k opacity database for ATMO based on the methodology adopted within the Met Office SOCRATES radiative transfer model (Edwards et al. 1996). This database has been updated for this analysis with more species, all of them listed in Table 3.1. This database is on a pressure and temperature grid which extends from 70 K to 3000 K and 10^{-4} to 10^8 Pa (10^{-9} to 10^3 bar) with 20 and 40 points, respectively, giving a total of 800 points for each species and each band, covering the complete range of temperatures and

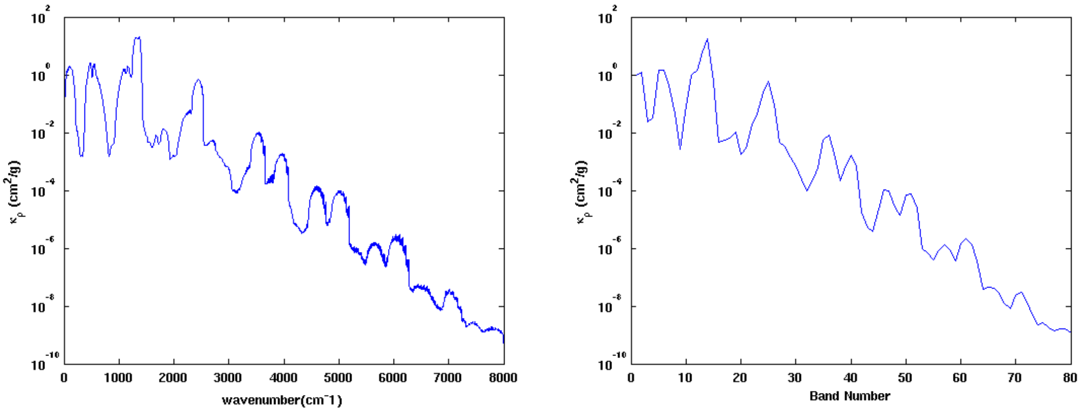

(a)

(b)

Figure 2.5: **(a)** Figure showing absorption cross-section of SO_2 using Line-by-Line (LBL) method. **(b)** Figure showing absorption cross-section of SO_2 using correlated-$k$method at 500 band resolution (100 cm^{-1}) equally spaced between 1 and 50000 cm^{-1}.

pressures expected in exo-planetary atmospheres. These correlated-k opacity files are at 3 different spectral resolutions, the lowest resolution with 32 bands, medium resolution with 500 bands and highest resolution with 5000 bands. The 500 and 5000 bands are evenly spaced in wavenumber between 1 cm^{-1} and 50000 cm^{-1}. The lowest resolution 32 band files are used for generating consistent radiative-convective equilibrium P-T profiles, since the model has to iterate numerous times between radiative transfer and chemistry at each level, making it computationally expensive. 500 and 5000 band files are used to generate the transmission and emission spectra of a planet. Most of the spectra in this thesis have been calculated using 5000 bands, which corresponds to R∼5000 at 0.2 µm while decreasing to R∼100 at 10 µm.

As described earlier, k-coefficients for each gaseous species included in the model are computed, for a range of temperatures and pressures. Depending on the chemical composition of the atmosphere these opacities of individual species are combined together, to obtain a total opacity. Many studies currently use pre-mixed opacities, where opacities are computed for a particular atmospheric composition (generally solar metallicity) (Morley et al. 2015). However, chemical composition will be different for different planets, and will also change with parameters such as temperature, metallicity and C/O ratio. Therefore, using pre-mixed opacities is not flexible, and is accurate only for a particular atmospheric composition (Amundsen et al. 2017). Therefore, combining k-coefficients of different gases to obtain the total opacity of the atmosphere is crucial for flexibility and accuracy with different compositions, so that the dependance on chemical composition need not be considered beforehand. `ATMO` adopts the random overlap method with resorting and re-binning

(Lacis et al. 1991; Amundsen et al. 2017) to combine k-coefficients "on the fly" depending on the chemical composition, temperature and pressure at each atmospheric level, for each spectral band, during each iteration. Random overlap methods assumes that the absorption cross-sections of all the gases are uncorrelated, which is considered to be good assumption (Lacis et al. 1991). This assumption simplifies the total transmission of the gas mixture to a scalar multiplication of the transmission due to individual gas species. However, this includes monochromatic calculation for all the k-coefficients for all the gases in the mixture, which is computationally very expensive. To circumvent this, Lacis et al. (1991) resorted the k-coefficients and re-binned them for the mixture "on the fly", reducing the computation time. Therefore, using the technique of random overlap allows us to simulate atmospheres for a certain range of temperatures, metallicities and C/O ratio. This "on the fly" combination of k-coefficients using the random overlap technique also makes the model physically consistent, which means that the opacities, and thereby the P-T structure, are consistent with the chemical composition of the atmosphere at any given iteration.

2.6 Scattering Cross-sections

2.6.1 Multi-gas Rayleigh Scattering

Rayleigh scattering is one of the most important process affecting the radiation budget and the albedo of the planetary atmosphere from ultraviolet to visible wavelengths. Rayleigh scattering due to any of the species present in the atmosphere is given by

$$\sigma_{\mathrm{n}}^{\mathrm{RAY}}(\lambda) = \frac{32\pi^3(m_{\mathrm{r}}-1)^2}{3\lambda^4 n^2} f(\rho_{\mathrm{n}}), \tag{2.46}$$

where λ is wavelength in cm, $\sigma_n^{\mathrm{RAY}}(\lambda)$ is Rayleigh scattering cross section in cm^2, m_{r} is the (real) refractive index for that particular gas, n is the number density in cm^{-3} (Liou 1980). To consider the anisotropy of scattering particles, a correction factor $f(\rho_n)$ is applied given by

$$f(\rho_{\mathrm{n}}) = \frac{6+3\rho_{\mathrm{n}}}{6-7\rho_{\mathrm{n}}}, \tag{2.47}$$

where ρ_n is the depolarisation factor. Additionally, being additive in nature, the total Rayleigh scattering in the atmosphere will be the sum of the scattering due to individual species.

In H_2 and He dominated atmospheres with solar metallicity, it is only the Rayleigh scattering due to H_2 and He that is significant. However, with an increasing metallicity of the planetary atmosphere, the abundance of other gases such as CO_2, CO, H_2O and CH_4 start increasing substantially (although the atmosphere remains H_2 and He dominated for metallicities $\leq 200\times$ solar) (Moses et al. 2013b). In such cases, Rayleigh scattering due to these other species also become significant. Therefore, we have included multi-gas Rayleigh scattering, due to the species CO, N_2, CH_4, NH_3, H_2O, CO_2, H_2S and SO_2, in addition to H_2 and He in the `ATMO` model. The H_2 refractive index is adopted from Leonard (1974) and that of He from Mansfield et al. (1969). Depolarisation factors for both are taken from Rayleigh (1919) and Penndorf (1957). The source of refractive index and depolarisation factor for CO, N_2, CH_4 and CO_2 is Sneep et al. (2005), for NH_3 and H_2O is Cox (2000) and for H_2S and SO_2 is the National Physical Laboratory (NPL[5]) database. The wavelength dependance of the refractive index is neglected in our calculations.

2.6.2 Haze and Cloud Treatment

In `ATMO` the opacity of haze, small scattering aerosol particles suspended in the atmosphere, is implemented as a parameterised enhanced Rayleigh scattering. This can be represented by $\sigma(\lambda) = \alpha_{\text{haze}}\sigma_0$ where $\sigma(\lambda)$ is the total scattering cross-section with haze, α_{haze} is the haze enhancement factor and $\sigma_0(\lambda)$ is the scattering cross-section due to all other gases (since `ATMO` considers multi-gas scattering), and is computed using Eqs. 2.46 and 2.47.

Clouds are treated as large particles with grey opacity. Therefore, we use a simple treatment of clouds similar to Benneke et al. (2012) and Sing et al. (2016). In this treatment, clouds are primarily scattering in nature thus decreasing the amount of radiation received by the observer at Earth when the exo-planetary limb is being observed in transmission. The result of significant cloud opacity on transmission spectra is, obscured or muted molecular absorption features depending on the cloud strength, which is governed by the particle size, chemical and radiative properties of the particles. Since, at this stage it is extremely difficult to constrain the type of aerosol particles in exoplanetary atmospheres (Wakeford et al. 2015), we simply tune the strength of grey scattering to represent clouds. Therefore, the size of any absorption features is a function of the strength of grey scattering, representing the cloud deck. This can be represented by $\kappa(\lambda)_c = \kappa(\lambda) + \alpha_{\text{cloud}}\kappa_{H_2}$, where $\kappa(\lambda)_c$ is the total scattering opacity in cm^2/g, $\kappa(\lambda)$ is the scattering opacity due to nominal Rayleigh scattering in similar units, α_{cloud} is the variable cloudiness factor governing the strength of grey scattering and κ_{H_2} is two times the scattering opacity due to H_2 at 350 nm which is $\sim 2.5 \times 10^{-3}\text{cm}^2/\text{g}$. This value is calculated using Eqs. 2.46 and 2.47 for the scattering cross-section in cm^2 and divided by the mass of the H_2

---

[5] `http://www.kayelaby.npl.co.uk/general_physics/2_5/2_5_7.html`

molecule in *grams* to obtain scattering opacity in cm^2/g, assuming a completely H_2 atmosphere (that is H_2 mole fraction abundance of 1).

2.7 Convection

In the previous sections we discussed about the transport of energy via radiation. The other such dominant mode of energy transport in a planetary atmosphere is convection. Convection is the transport of energy by the bulk motion of matter in the atmosphere in the vertical direction. It is driven by the temperature gradient. The macroscopic movement of matter results in energy flow from hotter to cooler regions. The rising hot air parcels that can lead to formation of thunderstorms, boiling water etc. are common examples of convection. Numerical treatment of convection in atmosphere models is computationally very intensive. In 3D, convection requires high spatial resolution, since it generally occurs on a spatial scale much smaller than the large-scale flow. In 1D it is difficult to include because of the conservation of mass issues, a limitation of 1D column. Therefore, different types of parameterisations are used to represent convection in the models.

In ATMO, Mixing length theory is used to compute convective flux. The mixing length is conceptually analogous to mean free path in thermodynamics. A fluid parcel will conserve its properties for a characteristic length l called the mixing length, before mixing with the surrounding fluid. As presented by Henyey et al. (1965) convective flux is given by

$$F_{\mathrm{conv}} = \frac{1}{2}\rho C_p T v_{conv} \frac{l}{H_p} \frac{\Gamma}{\Gamma + 1} (\nabla_T - \nabla_{ad}), \tag{2.48}$$

where $\nabla_T = \partial log(T)/\partial log(P)$, ∇_{ad} is the adiabatic gradient, C_p the specific heat at constant pressure, H_p the pressure scale height, v_{conv} the convective velocity, Γ the efficiency parameter and $l = \alpha H_p$ the mixing length, where α is the mixing length parameter. The details of the computation of v_{conv} and Γ can be found in (Gustafsson et al. 2008).

It must be noted that for irradiated hot Jupiter's the contribution of convective flux is almost negligible in the part of the atmosphere probed by current observations, as radiative flux overwhelms the convective flux in this region. However, it might become important for planets with temperature less than ~1000 K, with low irradiation.

2.8 Atmospheric Chemistry

Chemistry governs the atmospheric composition and therefore its interaction with radiation, and other properties such as the mean molecular mass, and heat capacity. Chemistry of the atmosphere can be broadly classified in two types. The first is driven by the thermal energy of the atmosphere called as the thermochemical equilibrium (equilibrium chemistry), for example in the high temperature environments ($\sim> 1000\,K$) such as hot Jupiters or the deep interior atmosphere of planets. The second is the dis-equilibrium/non-equilibrium chemistry driven by external energy sources, like the ozone formation in the Earth's atmosphere due to solar UV radiation or advection, explained briefly in Section 2.8.2.

For Earth and solar system planets, we are able to obtain in-situ measurements of their chemical composition using various instruments and interplanetary space probes. However, for exoplanet atmospheres we rely predominantly on models. Therefore, for hot Jupiter exoplanets, as a first step in forward models, the atmospheric chemical composition is determined by the equilibrium chemical abundances (i.e assuming thermochemical equilibrium), calculated using various techniques.

Chemical reactions involve exchange of mass as well as the energy. Enthalpy of formation, H, is a convenient measure of the energy content of a molecule. Therefore, a chemical reaction proceeds spontaneously to a state where it will have lowest energy. Indeed, in a static state the laws of mechanics require that the physical system be in a state of minimum energy. However, in a dynamical system containing many gas molecules, the system is also governed by the principle of maximum entropy, or the tendency of the system to reach maximum disorder. The entropy of the molecule, S, is the measure of the number of states available to the molecule. The combination of these two principles, minimum energy and maximum entropy are combined together as Gibbs free energy (G) given by:

$$G = H - TS \tag{2.49}$$

where T is the temperature. Thus for a closed thermodynamic system, the equilibrium state is reached when G is minimum.

For example, consider a following chemical reaction from Yung et al. (1999)

$$\mathrm{H_2 + M \longrightarrow H + H + M} \tag{2.50}$$

At 300 K (representative of the Earth's atmosphere) the change in G from left to right side is 97 kcal mole^{-1}. Therefore, equilibrium favours the molecular form, H_2. However, at 6000 K (representative of solar atmosphere), the change in Gibbs free energy is -37.4 kcal mole^{-1}. Equilibrium now shifts to the right, favouring H.

This explains why H_2 is more stable form of hydrogen in planets, whereas in the solar atmosphere H atoms dominate over H_2.

While computing G for this reaction, the energy term H is more important than the entropy term TS at 300 K, but the reverse is true at 6000 K. Enthalpy is a measure of the energy involved in making or breaking chemical bonds, basically internal energy, which to a first order is dependant on the electronic configuration of the molecules and is independent of the external parameters. In contrast, the entropy part of G is proportional to temperature, which is a macroscopic property of the gas (note that H is indirectly dependant on temperature). The Gibbs energy principle provides a connection between microscopic properties of the individual molecules and the macroscopic properties of the gas as a whole.

In ATMO, the equilibrium chemical abundances are computed by using the technique of Gibbs energy minimisation. To calculate abundances by minimising Gibbs energy, the Gibbs energy of formation for each chemical species need to be computed. This is tabulated in JANAF database (Chase 1986) for most of the chemical species as a function of temperature, and for the remaining species can be computed using the equilibrium constant for the reaction that includes the required species from Tsuji (1973). However, the data in the JANAF database is tabulated at specific intervals of temperature which is not sufficient to compute equilibrium chemical abundances at a range of temperatures as required in the atmosphere models. Therefore, Gordon et al. (1994) have generated polynomial fits to compute Gibbs energy of formation as a function of temperature using the JANAF database and tabulated fit coefficients for various species. We use this tabulated database of fit coefficients from Gordon et al. (1994) to compute equilibrium chemical abundances in ATMO. The exact methodology and implementation details of the equilibrium schemes are explained in Drummond et al. (2016).

The Gibbs energy minimisation scheme follows the method of Gordon et al. (1994), with the thermochemical data for each species taken from McBride et al. (1993) and McBride et al. (2002). Any gaseous species tend to condense in the atmosphere when the temperature is below the condensation temperature of the species, thus depleting the elemental species that form the condensate species and drastically affecting the atmospheric structure and the spectra. Therefore, treatment of condensation while computing the equilibrium chemical abundances also becomes important.

`ATMO` considers three options when calculating the chemical equilibrium abundances:

1) Gas-phase only - Only gas phase species are included and condensed phase species assumed to be negligible.

2) Local condensation - Condensed species are allowed to form, depleting the gas-

phase abundance of the elements locally but each model level is independent and has the same elemental abundance.
3) Rainout condensation - Condensed species are allowed to form and the elemental abundance of the elements within those condensed species are progressively depleted along the P-T profile from high to low pressure in the atmosphere, as derived in Section 2.8.1 in Chapter 2.

The gas-phase only approach (1) is likely to be valid for very hot atmospheres where the temperature is above the condensation temperature of most condensate species. The local condensation option (2) assumes that the formation of condensates in one model level does not effect the availability of elements in other model levels. Finally, the rainout condensation approach (3) assumes that once condensates are formed the particles sink in the atmosphere and the elements that comprise that condensate are depleted stoichiometrically from the layers above (e.g Barshay et al. 1978; Burrows et al. 1999; Mbarek et al. 2016).

To compute equilibrium chemical abundances in the local condensation approach, Gibbs energy is minimised for all the gaseous and condensation species combined together, at a particular temperature and pressure (model level). The methodology for the rainout condensation approach is described in the next section.

2.8.1 Rainout Condensation

The Gibbs energy minimisation (chemical equilibrium) calculation requires elemental abundances as an input, which in the model are defined as

$$B_i = \frac{n_i^{atom}}{n^{atom}}, \tag{2.51}$$

where n_i^{atom} is the number density of atoms of the element i , n^{atom} is the total number density of atoms and B_i is the mole fraction of the input elemental species. Number density is defined as the number of atoms of a particular element or chemical species per unit volume of the mixture.

However, equilibrium chemical abundances when computed, are the mole fraction of the output product species defined as.

$$f_j = \frac{n_j}{n}, \tag{2.52}$$

where f_j is the mole fraction of the species j, n_j is the number density of the species and n is the total number density of gas, using the ideal gas law.

The differences in the quantities, the mole fraction of the input elemental species and output product species defined in Eq. 2.51 and Eq. 2.52, respectively is clarified using the following example. Suppose we have a box containing one molecule of H_2 and one atom of He. In this case, the mole fraction of the element species H and He are $\mathrm{B_H} = 2/3$ and $\mathrm{B_{He}} = 1/3$, respectively, since there are two atoms of H, one atom of He and three atoms in total. The mole fraction of the output product species are $\mathrm{f_{H_2}} = 1/2$ and $\mathrm{f_{He}} = 1/2$, since there is one molecule of H_2, one atom of He and two particles (one molecule plus one atom) in total.

The rainout process in the model is treated by depleting the elemental abundances sequestered by the condensate species, from all of the model layers above (i.e toward lower pressure) using,

$$B_i^k = B_i^{k-1} - \sum_j a_{ij} f_j^{k-1} \frac{n}{n^{atom}}, \tag{2.53}$$

for $k \geq 2$, where the sum is over the number of *condensed species* only. a_{ij} is the number of atoms of element i in species j. We note that $B_i^{k=1}$ corresponds to initial input elemental abundances. We further note that the model level $k = 1$ denotes the "bottom" model level (i.e the highest pressure/lowest altitude). Eq. 2.53 is dealing with the change in the mole fractions of the input elemental species. Thus the second term on the right in Eq. 2.53 is appropriately scaled by using the term $\frac{n}{n^{atom}}$, so it returns the elemental species mole fraction for each element, from the mole fraction of the output product species. We have validated this rainout computation by comparing the initial model input elemental abundances, with the final total element abundances sequestered in various chemical species, which are conserved.

2.8.2 Chemical Kinetics

Although the assumption of chemical equilibrium is a good starting point for hot Jupiter exoplanet atmospheres (Madhusudhan et al. 2016b), there are many physical processes such as horizontal and vertical mixing, photochemistry etc., that can perturb the atmosphere out of equilibrium. Moreover, dis-equilibrium chemistry plays an important role in governing the atmospheric abundances of cooler planets (Equilibrium temperature < ∼1000 K), more likely in the super-Earth or Earth like regime. In-fact Earth's atmosphere is the perfect example of how the dis-equilibrium chemistry can dramatically alter the primordial atmosphere and can also lead to emergence of life. In ATMO, dis-equilibrium chemistry is computed using a chemical kinetics scheme which directly deals with chemical reactions. To obtain dis-equilibrium chemical abundances, the continuity equation given by

$$\frac{\delta n_i}{\delta t} = P_i - n_i L_i - \frac{\delta \Phi_i}{\delta z}, \tag{2.54}$$

is solved for chemical steady state, i.e $\frac{\delta n_i}{\delta t} \sim 0$, where n_i is the number of moles of the species and t is the time. P_i and L_i are chemical production and loss terms, respectively, computed from the system of chemical reactions in a chemical network. The term $\frac{\delta \Phi_i}{\delta z}$ represents the vertical mixing, where Φ_i is the vertical transport flux and z is the vertical distance co-ordinate. Since this is a 1D model, horizontal mixing is neglected. More details about the dis-equilibrium chemistry implementation in ATMO can be found in Drummond et al. (2016), with a more general description of chemical kinetics in Moses (2014). In this thesis, all the results are with equilibrium chemistry, leaving dis-equilibrium chemistry investigations for the future.

2.8.3 Metallicity

Metallicity is one of the most common terminologies used in astrophysics to describe elemental abundances of a system. In general terms it is defined as the mass fraction of the elements heavier than helium. which can be represented by,

$$Z = \sum_{i>He} \frac{m_i}{M}, \tag{2.55}$$

where Z is the metallicity, m_i is the total mass of each element i heavier than helium and M is the total mass of the system. Alternatively, this can also be defined as the ratio of number of atoms of each element and the number of atoms of hydrogen per unit volume. However, another commonly used terminology for metallicity in the astrophysics community is [Fe/H] defined as,

$$[Fe/H] = log\left(\frac{N_{Fe}^{atoms}}{N_{H}^{atoms}}\right) - log\left(\frac{N_{Fe}^{atoms}}{N_{H}^{atoms}}\right)^{Sun} \tag{2.56}$$

where N_{Fe}^{atoms} is the number density (number of atoms per units volume) of Iron (Fe) in the mixture/star, N_{H}^{atoms} is the number of atoms of hydrogen. The same quantities with superscript “Sun”, denote the quantities in the Sun. Therefore, in this case the metallicity is defined with respect to the solar metallicity. By assuming that other heavy elements scale uniformly with Fe, this can be generalised for any element heavier than hydrogen and helium and written as [M/H], where,

$$[M/H] = log\left(\frac{N_{M}^{atoms}}{N_{H}^{atoms}}\right) - log\left(\frac{N_{M}^{atoms}}{N_{H}^{atoms}}\right)^{Sun}$$
$$[M/H] = log\left(\frac{N_{M}^{atoms}/N_{H}^{atoms}}{N_{M}^{atoms,sun}/N_{H}^{atoms,sun}}\right)$$

After, rearranging the terms we get,

$$\frac{N_M^{atoms}}{N_H^{atoms}} = \left(\frac{N_M^{atoms}}{N_H^{atoms}}\right)^{Sun} 10^{[M/H]} \tag{2.57}$$

[M/H] of 0 corresponds to solar metallicity and [M/H] of 1 corresponds to 10 times solar metallicity, where all the heavy elemental abundances other than hydrogen and helium are 10 times more than that in the Sun.

2.8.4 C/O Ratio

The Carbon to Oxygen ratio or C/O ratio is one of the most common parameters used in the literature to constrain the chemical composition of a planetary atmosphere (Seager et al. 2005; Kopparapu et al. 2012; Madhusudhan 2012; Moses et al. 2013a; Mollière et al. 2015; Goyal et al. 2018; Drummond et al. 2019) and also as an indicator of the formation location of the planet in the protoplanetary disk (Öberg et al. 2011; Madhusudhan et al. 2016a). There are three methodologies used to vary this ratio, first by varying C/H without varying O/H (Moses et al. 2013a), second by varying O/H without varying C/H abundances (Moses et al. 2013b; Goyal et al. 2018) and third by varying abundance of both C/H and O/H (see Drummond et al. 2019, for details of all 3 methodologies). In Chapters 3 and 4 we adopt the methodology of varying O/H without varying C/H to investigate the change in chemical abundances due to change in C/O ratio. However, in Chapter 4 we use both, first and second methods to investigate the effect of changes in the C/O ratio. The C/O ratio governs which species will dominate the planetary atmosphere, for e.g, H_2O, CH_4 etc. Therefore, C/O ratio plays an important role in governing the atmospheric structure and the observational spectra, explained in detail in the further chapters.

2.9 Computing P-T profiles in Radiative-Convective equilibrium

In the previous sections we discussed the details of radiative transfer and absorption cross-section calculations, chemistry and convection, all contributing to the computation of P-T profiles. We here discuss the basic methodology used in ATMO to compute P-T profiles in radiative-convective equilibrium, consistently with equilibrium chemistry. At first, we initialise the model with initial guess P-T profile which can even be isothermal, although this will take more iterations to converge, as it is farther away from the true solution. Chemical equilibrium abundances are then calculated for this P-T profile as explained in Section 2.8. Using these abundances along with the absorption cross-sections of different chemical species, in the form of k-coefficients, (since we use correlated-k technique) total opacity is calculated for each layer of the atmosphere. Following this, the radiative transfer equation is solved to compute incoming and outgoing radiative fluxes for each layer of the atmosphere as described in Section 2.2. The same approach is followed for convective flux as explained in Section 2.7. This is then checked for energy flux balance in each layer of the atmosphere as well as the atmosphere as a whole, using Eq. 2.58 for energy conservation and Eq. 2.59 for hydrostatic equilibrium. If the condition for energy conservation and hydrostatic equilibrium is not satisfied within the required numerical accuracy, corresponding to error in flux balance (typical value of $\sim 10^{-}3$), the P-T profile is perturbed within minimum and maximum step sizes ($\sim$0.1-0.9) for the next iteration. This step size is basically the multiplying factor to the temperature perturbation while the model is iterating to obtain a converged solution. These all previous steps are repeated for each iteration, until a P-T profile that satisfies hydrostatic equilibrium and conservation of energy is obtained, consistent with equilibrium chemistry and corresponding opacities, for a given set of planetary characteristics. Energy conservation is given by the following equation

$$F_{\mathrm{rad}} + F_{\mathrm{conv}} - \sigma T_{\mathrm{int}}^4 = 0, \tag{2.58}$$

where F_{rad} the radiative flux and F_{conv} is the convective flux as derived in Sections 2.2 and 2.7, respectively. T_{int} represents the internal temperature of planet or the temperature at which the planet is cooling.

The constraint of hydrostatic equilibrium which defines pressure structure as a function of altitude is implemented using

$$\frac{d}{dz}(P_{gas} + P_{turb}) - \rho g = 0, \tag{2.59}$$

where P_{gas} is pressure due to gaseous species, P_{turb} is turbulent pressure, z is altitude, ρ is density and g is gravity.

Figure 2.6 shows radiative-convective equilibrium P-T profiles with and without temperature inversion. Dominant physical processes in different parts of the atmosphere can also be noticed in this figure. Convection plays important role only in the deepest parts of the irradiated hot Jupiter atmospheres ($>$ 100 bar), which current observations cannot probe. Radiation governs the P-T structure across wide range of pressures. Radiative diffusion leads to isothermal structure in the deep atmosphere as shown in Figure 2.6, primarily because high opacity in this region decreases mean free path for the photons as in stellar atmospheres (Rybicki et al. 1986). The interplay between absorption of stellar radiation due to optical opacities and planetary emission due to infrared opacities, governs the P-T profile in the

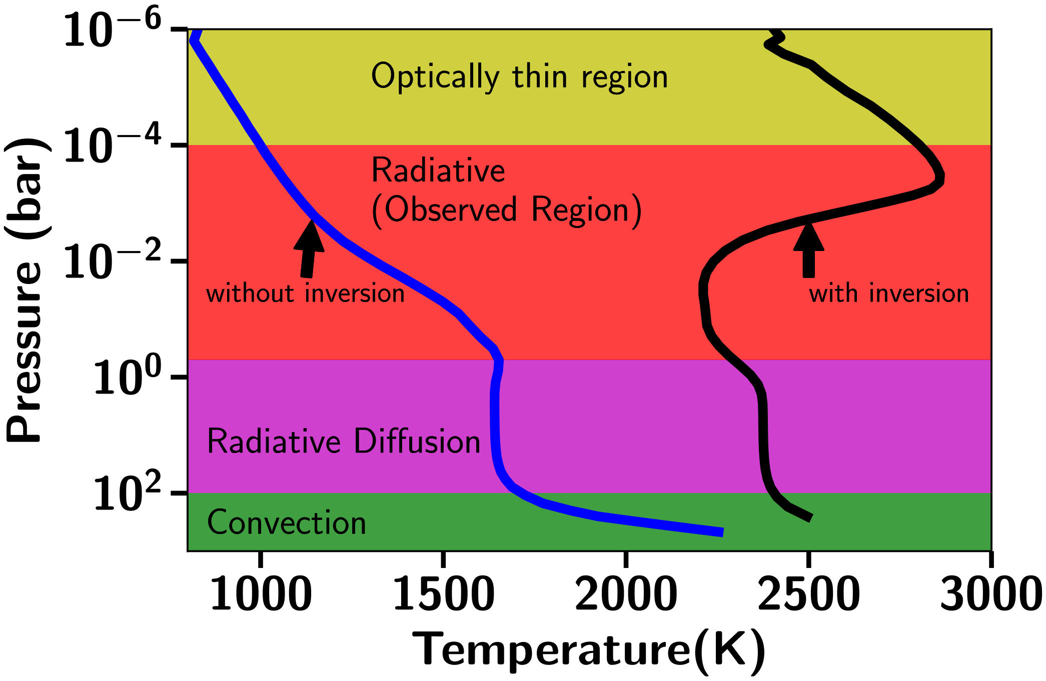

Figure 2.6: Illustrative figure to show dominant processes in different parts of a hot Jupiter atmosphere with radiative-convective equilibrium P-T profiles, with (black) and without inversion (blue).

radiative region between ~1 bar to 0.1 millibar, which is the only region probed by current observations , either using transmission or emission spectra. Sufficiently high optical opacity can lead to temperature inversion in this observed radiative region. At the top where pressure becomes less than ~ 0.1 millibar the atmosphere becomes optically thin and most of the radiation penetrates this part of the atmosphere.

2.10 Computation of Transmission Spectra

The computation of transmission spectra fundamentally involves computing the spectral radius of the planet, which is dependant on the atmospheric structure and its composition. Therefore, to compute transmission spectra it is required to solve the radiative transfer equation in the tangential geometry (instead of radial) as shown in Figure 2.60.

Transmission spectra in `ATMO` are computed as shown in schematic Figure 2.7 using the equation

$$R^2_{\rm p,eff}(\lambda) = R^2_{\rm p,opq}(\lambda) + 2\int_{R_{\rm p,opq}}^{R_{\rm p,TOA}} b\,{\rm d}b(1 - e^{-\tilde{\tau}(b,\lambda)}), \qquad (2.60)$$

where $R_{\rm p,eff}(\lambda)$ is the wavelength dependent effective planetary radius including the atmosphere, $R_{\rm p,opq}(\lambda)$ is the radius below which the atmosphere is optically

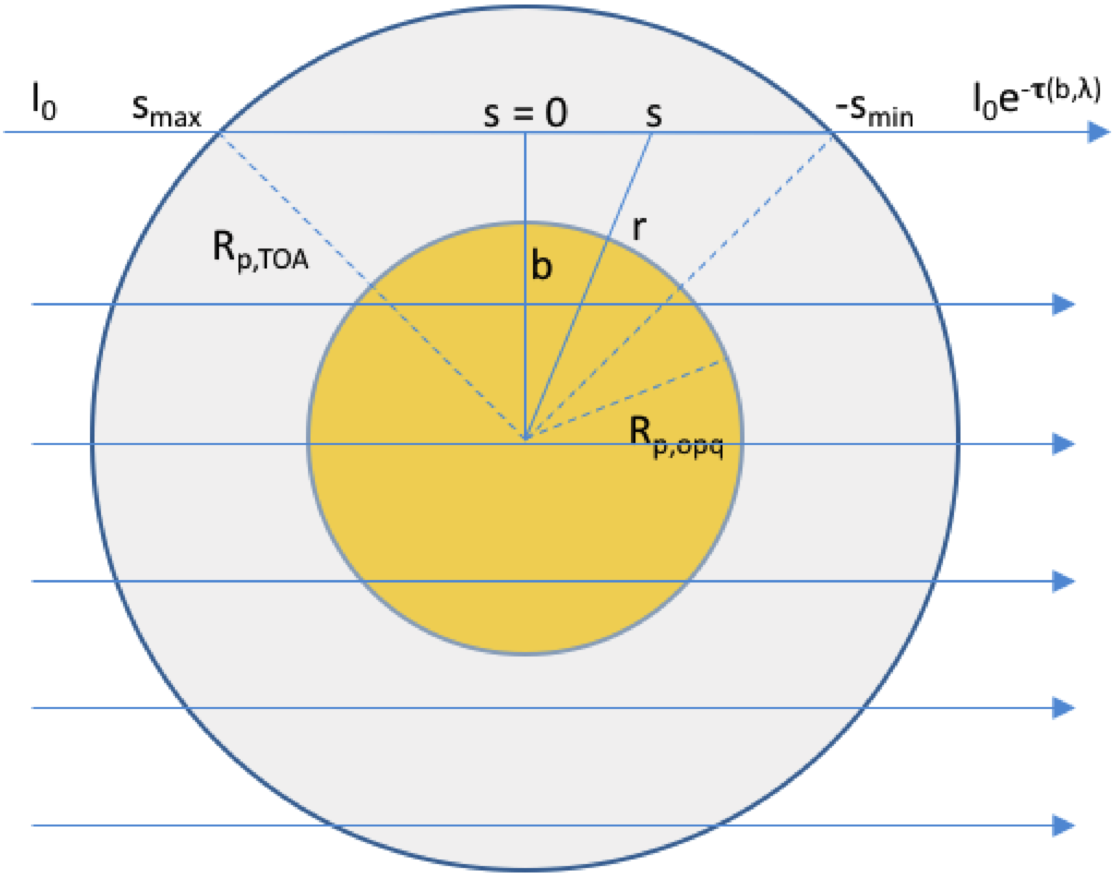

Figure 2.7: Geometry of transmission spectrum computation. I_0 is the incoming stellar radiation, $R_{\mathrm{p,eff}}(\lambda)$ is the wavelength dependent effective planetary radius including the atmosphere, $R_{\mathrm{p,opq}}(\lambda)$ is the radius below which the atmosphere is optically thick, $R_{\mathrm{p,TOA}}$ is the radius at the top of the atmosphere, b is the impact parameter, $\tilde{\tau}(b, \lambda)$ is the atmospheric optical depth, s is the ray path coordinate.

thick, $R_{\mathrm{p,TOA}}$ is the radius at the top of the atmosphere, b is the impact parameter which is the perpendicular distance of the radiation beam from the the planet centre as shown in Figure 2.7, all in cm. $\tilde{\tau}(b,\lambda)$ is the atmospheric optical depth which for a 1D P-T profile is spherically symmetric and independent of ϕ but is a function of impact parameter b and given by

$$\tilde{\tau}(b,\lambda) = \int_{-s_{\mathrm{min}}}^{s_{\mathrm{max}}} \mathrm{d}s\kappa_{\rho}(\lambda,s)\rho(s), \tag{2.61}$$

where s_{min} is the minimum path coordinate of the ray as it leaves the atmosphere as illustrated in Figure 2.7, while s_{max} is the maximum path coordinate where the ray enters the atmosphere both in cm, $\rho(s)$ is the density in g/cm^3 at path s given by $\sqrt{r^2-b^2}$ in cm and $\kappa_{\rho}(\lambda,s)$ is the opacity as a function of wavenumber and path s in cm^2/g. This gives the effective radius of the planet as a function of wavelength which represents the model transmission spectra of the planet. It is worth noting that the chemical and the thermodynamic structure of the atmosphere imprint their signature in the transmission spectra via ρ and κ variables. We note that we assume single scattering and neglect refraction while computing our transmission spectra.

2.11 Contribution Function

Emission spectrum represents the top of the atmosphere (TOA) flux at different wavelengths for a given planet. However, this is a combination of flux from the different layers of the atmosphere. To identify the levels of the atmosphere contributing the most to this top of the atmosphere (TOA) emission spectra, the Contribution function (CF) (Chamberlain et al. 1987; Knutson et al. 2009; Drummond et al. 2018b) is calculated given by,

$$CF = B(\nu,T)\frac{d(e^{-\tau_\nu})}{d(ln(P))}, \tag{2.62}$$

where ν is the frequency, T is the temperature, $B(\nu,T)$ is the Planck emission, τ_ν is the optical depth and P is the pressure at each level of the atmosphere. The vertical P-T profile and the wavelength dependent optical depth, are the primary quantities required to calculate the contribution function. Optical depth is a function of transmittance which decreases as we go deeper in the planet's atmosphere. Therefore, the CF is higher in the region where there is a larger change in the optical depth or transmittance for a unit change in the pressure (altitude) over the same region. In simpler terms, the CF peaks in the region where the wavelength dependent optical depth is one, when planet is being probed from the top of the atmosphere.

Chapter 3

Planet Specific Library of Forward Model Transmission Spectra

> "Hesitating to act because the whole vision might not be achieved, or because others do not yet share it, is an attitude that only hinders progress."
>
> — Mahatma Gandhi

Simulated exoplanet transmission spectra are critical for planning and interpretation of observations and to explore the sensitivity of spectral features to atmospheric thermochemical processes. Although HST observations have led to the detection of several species (Sing et al. 2013; Sing et al. 2016), it is limited by its wavelength coverage (0.2 to 1.7 μ m). The launch of the James Webb Space Telescope (JWST) in 2018 will enable probing exoplanet atmospheres from wavelengths of 0.6 all the way up-to 28 μ m (Beichman et al. 2014; Greene et al. 2016). Therefore, it will be extremely valuable for the detection of species with signatures in the mid to near-infrared, which can provide constraints on various physical parameters such as the temperature, C/O ratio and metallicity. In this chapter we present a grid of forward model transmission spectra for 117 exoplanets that are scientifically important targets for characterisation. The grid for each target consists of a range of variables; atmospheric temperature, metallicity, C/O ratio, haziness and cloudiness (described in Section 3.3.2). This grid is publicly available online[1,2], and we encourage the community to use it as a tool to assist them in planning future observations, such as with JWST, HST and various ground based telescopes, along-with interpreting existing datasets. It can provide a useful complement for interpretation,

---

[1] https://bd-server.astro.ex.ac.uk/exoplanets/

[2] https://drive.google.com/drive/folders/1Yz94usAAiXtnLR0yoq-qkuhegRrI4u4B

alongside atmospheric retrieval analysis.

In Section 3.1 the input parameters and schemes, including the opacity sources and their implementation, and chemistry setup is described. In Section 3.2 the validation of chemistry scheme with local and rainout condensation is shown. In Section 3.3 we describe the basis for the selection of planets in the current grid and the model setup, along-with the description and justification of the chosen parameter space. In Section 3.4 we present a comparison between spectra derived from isothermal and radiative-convective equilibrium pressure-temperature profiles (hereafter termed “isothermal P-T profiles” and “consistent P-T profiles”, respectively). Decoupled transmission spectrum is shown and described in Section 3.5 to identify major spectral features in transmission spectra by using HD 2094588b as an example. In Section 3.6 we provide the analysis of the model simulations over the entire parameter space for a subset of planets. In Section 3.7 we present an interpretation of the observations from Sing et al. (2016), and the inferred best fit characteristics. In Section 3.8 we demonstrate the application of the grid to plan observations, by using one of our simulations as an input to the JWST simulator `PandExo` (Batalha et al. 2017). Finally, we summarise this chapter in Section 3.9.

3.1 Input Schemes, Data and Parameters

3.1.1 Opacity Setup for the Grid

Hot Jupiter exoplanets are expected to be H_2 and He dominated. Therefore, pressure broadening due to H_2 and He species has to be taken into account for each radiatively important gaseous species in the model (see Amundsen et al. 2014; Hedges et al. 2016, for details). However, HITRAN only provides air and self pressure broadened line widths for various gases which will not be accurate for hot Jupiter exoplanets. We include an up-to-date set of opacities for high temperature exoplanet atmospheres in `ATMO` primarily from ExoMol (Tennyson et al. 2016), with H_2 and He broadening taken into account for the species where data are available, otherwise we use the air broadening parameters from HITRAN. Table 3.1 shows the updated source of line lists compared to Amundsen et al. (2014), for various molecules and the corresponding partition functions used in `ATMO`. Updated pressure broadening parameters for each molecule are also documented in Table 3.2. We note that we exclude CrH opacities in the current model simulations, due to non availability of thermochemical constants to compute equilibrium chemical abundances of CrH.

At higher metallicities, atmospheric abundance of species other than H_2 and He such as CO, H_2O, CO_2, H_2S, etc., become significant. In such conditions, the effect of broadening due to all major species on all the other radiatively important species should be taken into account. It is difficult to accurately comment on the effect of pressure broadening at high metallicities since no study has been done in that area according to our knowledge, although the need for laboratory measurements in this region of the parameter space has been highlighted in Fortney et al. (2016). However, equilibrium chemistry calculations show that even at 200 times solar metallicity the composition remains H_2 and He dominated, allowing us to perform simulations up-to this upper limit of metallicity. Since absorption coefficient calculations are sensitive to atmospheric composition, one of the future goals of our research is to generate an opacity database for a larger range of compositions.

We have considered only those opacities making a significant contribution to the derived spectra in our analysis. For example, C_2H_2 and C_2H_4 have almost overlapping absorption peaks throughout the spectrum except between 10 to 12 µm. However, C_2H_2 opacity dominates over C_2H_4 opacity. Also equilibrium chemistry dictates that if C_2H_4 is present in the atmosphere C_2H_2 will also be present (Moses et al. 2011) with almost equal or higher concentrations, even at high C/O ratios. Therefore, we have included only C_2H_2 in our current analysis, since C_2H_2 will effectively mask the features of C_2H_4.

3.1.2 Chemistry Setup for the grid

`ATMO` can employ two chemistry schemes, a Gibbs energy minimisation scheme following Gordon et al. (1994) used for equilibrium chemistry calculations and a chemical kinetics scheme that currently adopts the chemical network of Venot et al. (2012). The exact methodology and implementation details of both schemes are explained in Drummond et al. (2016). The chemical kinetics scheme can also be used to simulate non-equilibrium physical processes like vertical mixing and photochemistry. The coupling of the radiative-convective scheme with the chemistry (equilibrium and non-equilibrium) scheme also allows fully consistent modelling, where both the P-T profile and the chemical abundances are solved for simultaneously. Therefore, it provides a final P-T and chemical abundances profiles which are physically consistent with each other. However, as a grid for a range of planets requires extensive computational resources, we restrict ourselves to equilibrium chemistry for this work. Using equilibrium chemistry, to model hot Jupiter atmospheres is also a reasonable assumption, due to high temperature of these planets.

For this particular analysis, a total of 258 chemical species comprising of both gaseous and condensate species were included. The 23 elements included in the model to form these 258 species are H, He, C, N, O, Na, K, Si, Ar, Ti, V, S, Cl, Mg, Al, Ca, Fe, Cr, Li, Cs, Rb, F and P. Local chemical equilibrium abundances are computed by minimising the Gibbs energy independently on each model level.

Molecule	Line list	Partition Function
H_2O	Barber et al. (2006)	Barber et al. (2006)
CO_2	Tashkun et al. (2011)	Rothman et al. (2009)
CO	Rothman et al. (2010)	Rothman et al. (2009)
CH_4	Yurchenko et al. (2014)	Yurchenko et al. (2014)
NH_3	Yurchenko et al. (2011)	Sauval et al. (1984)
Na	VALD3[1]	Sauval et al. (1984)
K	VALD3[1]	Sauval et al. (1984)
Li	VALD3[1]	Sauval et al. (1984)
Rb	VALD3[1]	Sauval et al. (1984)
Cs	VALD3[1]	Sauval et al. (1984)
TiO	Plez (1998)	Sauval et al. (1984)
VO	McKemmish et al. (2016)	Sauval et al. (1984)
FeH	Wende et al. (2010)	Wende et al. (2010)
CrH[2]	Tennyson et al. (2012)	Burrows et al. (2002)
PH_3	Sousa-Silva et al. (2014)	Sousa-Silva et al. (2014)
HCN	Harris et al. (2006)	Harris et al. (2006)
	Barber et al. (2014)	Barber et al. (2014)
C_2H_2	Rothman et al. (2013)	Rothman et al. (2013)
H_2S	Rothman et al. (2013)	Rothman et al. (2013)
SO_2	Underwood et al. (2016)	Underwood et al. (2016)
H_2-H_2 CIA	Richard et al. (2012)	N/A
H_2-He CIA	Richard et al. (2012)	N/A

Table 3.1: Molecular line lists used in `ATMO` and their sources.
[1] Heiter et al. (2008) (`http://vald.astro.uu.se/~vald/php/vald.php`).
[2] Note : CrH opacities are not included in the grid (see Section 3.1.1).

Molecule	Broadener	Line Width Source	Exponent Source
H_2O	H_2	Gamache et al. (1996)	Gamache et al. (1996)
	He	Solodov et al. (2009) and Steyert et al. (2004)	Gamache et al. (1996)
CO_2	H_2	Padmanabhan et al. (2014)	Sharp et al. (2007)
	He	Thibault et al. (1992)	Thibault et al. (2000)
CO	H_2	Régalia-Jarlot et al. (2005)	Le Moal et al. (1986)
	He	BelBruno et al. (1982) and Mantz et al. (2005)	Mantz et al. (2005)
CH_4	H_2	Pine (1992) and Margolis (1993)	Margolis (1993)
	He	Pine (1992)	Varanasi et al. (1990)
NH_3	H_2	Hadded et al. (2001) and Pine et al. (1993)	Nouri et al. (2004)
	He	Hadded et al. (2001) and Pine et al. (1993)	Sharp et al. (2007)
Na	H_2	Allard et al. (1999), Allard et al. (2003), and Allard et al. (2007)	Sharp et al. (2007)
	He	Allard et al. (1999), Allard et al. (2003), and Allard et al. (2007)	Sharp et al. (2007)
K	H_2	Allard et al. (1999), Allard et al. (2003), and Allard et al. (2007)	Sharp et al. (2007)
	He	Allard et al. (1999), Allard et al. (2003), and Allard et al. (2007)	Sharp et al. (2007)
Li, Rb, Cs	H_2	Allard et al. (1999)	Sharp et al. (2007)
	He	Allard et al. (1999)	Sharp et al. (2007)
TiO, VO	H_2	Sharp et al. (2007)	Sharp et al. (2007)
	He	Sharp et al. (2007)	Sharp et al. (2007)
FeH, CrH	H_2	Sharp et al. (2007)	Sharp et al. (2007)
	He	Sharp et al. (2007)	Sharp et al. (2007)
PH_3	H_2	Bouanich et al. (2004)	Levy et al. (1994)
	He	Salem et al. (2005)	Levy et al. (1994)
HCN	H_2	Landrain et al. (1997)	Sharp et al. (2007)
	He	Landrain et al. (1997)	Sharp et al. (2007)
C_2H_2,H_2S, SO_2	Air	Rothman et al. (2009)	Rothman et al. (2009)

Table 3.2: Type and source of pressure broadening for all opacities used in `ATMO`.

This scheme has been validated by reproducing the results of the TECA chemical equilibrium code (Venot et al. 2012), as well as the analytical solutions to chemical equilibrium by Burrows et al. (1999) and Heng et al. (2016). For more details on the chemistry schemes see Drummond et al. (2016). The list of all gaseous and condensate species used for equilibrium chemistry computation in this analysis is given below:

H_2, O-3P, O-1D, CO, C, CH, $3CH_2$, $1CH_2$, H_2O, O_2, H_2O_2, CH_4, H_2CO, CH_3OH, CO_2, CH_3OOH, C_2H_2, C_2H_4, C_2H_6, CH_2CO, CH_3CHO, C_2H_5OH, C_2H_5OOH, CH_3COOOH, C_3H_8, C_4H_8Y, C_4H_10, C_2H_5CHO, C_3H_7OH, C_2H_6CO, C_2H_8CO, C_2H_3CHOZ, cC_2H_4O, H, C_7H_8, OH, OOH, CH_3, HCO, CH_2OH, CH_3O, CH_3OO, C_2H, C_2H_3, C_2H_5, CHCO, CH_2CHO, CH_3CO, C_2H_5O, C_2H_4OOH, C_2H_5OO, CH_3COOO, $1C_3H_7$, $1C_4H_9$, CH_3OCO, CO_2H, $2C_2H_4OH$, $1C_2H_4OH$, $2C_3H_7$, $2C_4H_9$, N_2, He, Ar, N-4S, N-2D, NH, NH_2, NH_3, NNH, NO, NO_2, N_2O, NCN, HNO, CN, HCN, H_2CN, HCNN, HCNO, HOCN, HNCO, HON, NCO, HNO_2, HONO, NO_3, $HONO_2$, CH_3ONO, CH_3NO_2, CH_3NO, C_3H_7O, C_4H_9O, cC_6H_6, N_2O_3, NH_2OH, N_2O_4, N_2H_2, N_2H_3, N_2H_4, HNNO, HNOH, HNO_3, H_2NO, CNN, H_2CNO, C_2N_2, HCNH, Na, NaH, NaO, NaOH, NaCl, K, KH, KO, KOH, KCl, HO2, SO, SO_2, Cl, HCl, ClO, Cl_2, Ti, TiO, V, VO, Si, SiH, S, SH, H_2S, Mg, MgH, MgS, Al, AlH, AlOH, Al_2O, Al_2O_3, Fe, FeH, Cr, CrN, CrO, Ca, F, HF, Li, LiCl, LiH, LiF, Cs, CsCl, CsH, CsF, Rb, RbCl, RbH, RbF, P, PH, PH_3, PO, P_2, PS, PH_2, P_4O_6, Ca(a), Ca(b), Ca(l), Ti_3O_5(a), Ti_3O_5(b), Ti_3O_5(l), Ti(a), Ti(b), Ti(l), TiO(a), TiO(b), TiO(l), V(cr), V(l), VO(s), VO(l), V_2O_3(s), V_2O_3(l), V_2O_4(a), V_2O_4(b), V_2O_4(l), V_2O_5(s), V_2O_5(l), Cr(a), Cr(b), Cr(l), Na_2S(a), Na_2S(b), Na_2S(l), K_2S(a), K_2S(b), K_2S(c), K_2S(l), KCl(l), KCl(s), Na(l), Na(cr), K(l), K(cr), S(l), S(cr1), S(cr2), NaCl(l), NaCl(s), $MgSiO_3$(a), $MgSiO_3$(b), $MgSiO_3$(c), $MgSiO_3$(l), Mg_2SiO_4(s), Mg_2SiO_4(l), $MgAl_2O_4$(s), $MgAl_2O_4$(l), Al_2O_3(a), Al_2O_3(l), SiO_2(hqz), SiO_2(l), $NaAlSi_3O_8$(s), Na_2O(l), Na_2O(a), Na_2O(c), $NaAlSiO_4$(s), $KAlSi_2O_6$(s), Fe(a), Fe(b), Fe(c), Fe(d), Fe(l), FeS(a), FeS(b), FeS(c), FeS(l), H_2O(l), H_2O(s), NH_3(l), NH_3(s), Cr_2O_3(a), Cr_2O_3(b), Cr_2O_3(c), Cr_2O_3(d), Cr_2O_3(l), $LiAlO_2$(s), $LiAlO_2$(l), CsCl(a), CsCl(b), CsCl(l), RbCl(cr), RbCl(l), H_3PO_4(l), H_3PO_4(cr).

where species with brackets indicate condensate species and cr stands for crystalline, l for liquid, s for solid and a,b,c represent different states. O-3P and O-1D are allotropes of atomic Oxygen, similarly N-4S, N-2D are allotropes of Nitrogen. Prefix "c" before Carbon species denote cyclic molecule.

As described in Chapter 2 Section 2.8, there are three options to compute equilibrium chemical abundances in ATMO, namely, gas-phase, local condensation and rainout condensation. All the model simulations in the grid are performed using the equilibrium chemistry scheme including both, local condensation and condensation with rainout. Condensation with rainout mechanism is implemented differently in

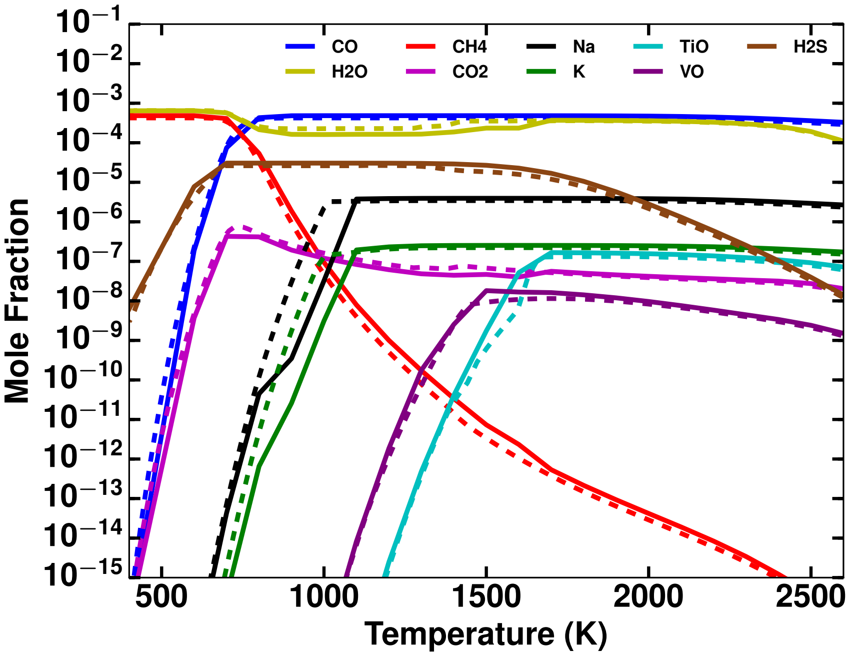

Figure 3.1: Figure showing equilibrium chemical abundances from `ATMO` (solid lines) and GGchem (Woitke et al. 2018) (dashed lines) for a range of temperatures for CO, H_2O, CH_4, CO_2, Na, K, TiO, VO and H_2S at 1 millibar pressure level in the atmosphere. Horizontal axis shows temperature in K and vertical axis shows the mole fraction (dimensionless) of the chemical species. **(b)** Same as 1a but for C_2H_2, NH_3, HCN, SO_2, FeH, Li, Rb and PH_3.

different planetary atmospheric models (Burrows et al. 1999; Lodders et al. 2006a; Fortney et al. 2008; Mbarek et al. 2016), explained in detail in the next section.

The solar elemental abundances are adopted from Asplund et al. (2009). In a particular simulation, the elemental abundances are then adjusted for the set metallicity and C/O ratio parameters. The metallicity is taken into account by multiplying the abundances of the elements (except H, He and O) by the appropriate factor, and then re-normalising such that the sum of the fractional abundances is equal to unity. We note that the oxygen abundance is set via the carbon abundance and the prescribed C/O ratio following Moses et al. (2011), and the C/O ratio refers to total elemental abundance across gas and condensate phase.

3.2 Validating the Chemistry Scheme

3.2.1 Equilibrium chemistry with local condensation

The chemical abundances of different output species in a chemical equilibrium model is dependant on the method of equilibrium scheme, source of input solar elemental abundances, list of species considered for equilibrium chemistry computation and the thermodynamic data of the chemical species. Therefore, to validate the chemistry

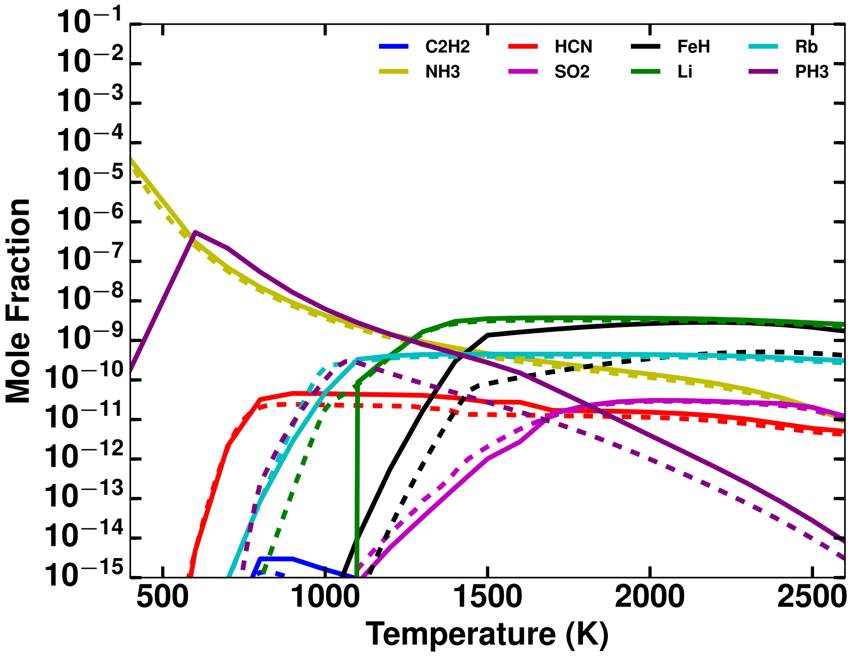

Figure 3.2: Same as 3.1 but for C_2H_2, NH_3, HCN, SO_2, FeH, Li, Rb and PH_3.

scheme as well as the model choices made for the grid, we compare with the output of other published models to compute equilibrium chemical abundances.

Figure 3.1 and 3.2 present chemical abundances derived using `ATMO` (solid lines) compared against those derived using the GGchem chemical model (Woitke et al. 2018), for all the species for which we included opacities in Goyal et al. (2018), except Caesium (Cs), which is not included in GGchem chemical model. For this comparison we adopt local condensation (without rainout) and the solar elemental abundances of Lodders (2003) for both models, and the condensate list for ATMO matches that of Goyal et al. (2018). The major differences between the GGchem and the `ATMO` model choices used in Goyal et al. (2018, 2019a) are the included element and condensate species, the methodology to compute equilibrium chemical abundances and the source of thermodynamic data. Figure 3.1 and 3.2 shows that the agreement for most of the species is very good, except for a substantial difference in PH_3 and to a lesser extent for FeH and Li. The differences in PH_3 abundances, between ATMO and GGchem, is likely due to differences in the list of condensate species included and the source of thermodynamic data. However, doubt on the accuracy of thermodynamic data of various phosphorous species which affect the PH_3 abundances, contained in the JANAF database (Chase 1986), has been raised by Lodders et al. (2002b), suggesting we cannot perform an accurate benchmarking for this species. Since thermodynamic data for FeH is not available in the JANAF database, we estimate it using the equilibrium constant for the reaction, Fe + H <=> FeH from Tsuji (1973) in `ATMO`. However, the GGChem model adopts the thermodynamic data from Barklem et al. (2016), thus offering a potential reason

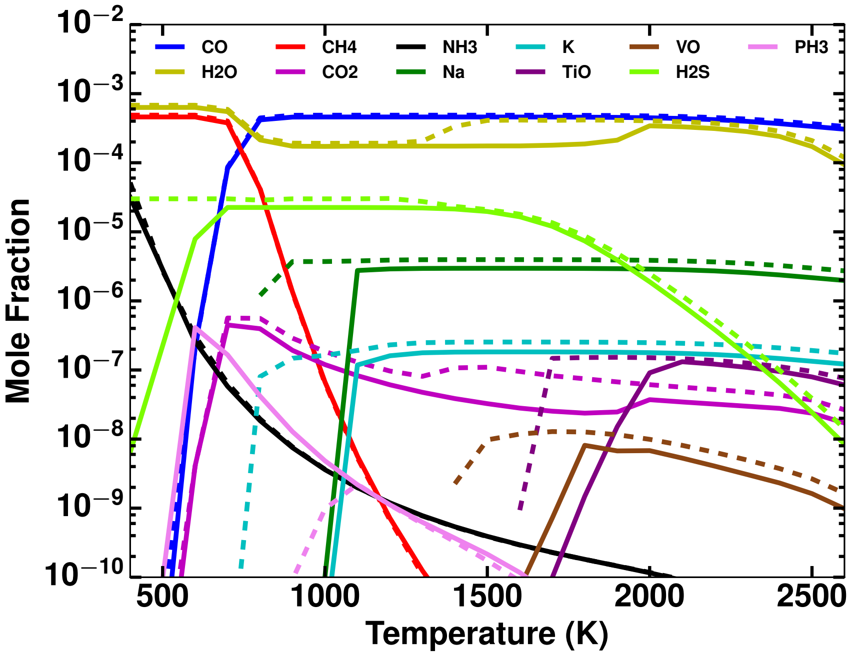

Figure 3.3: Figure showing equilibrium chemical abundances with condensation and rainout following the isothermal P-T profile from `ATMO` (solid lines) with same model inputs as used in the library and Exo–transmit (Kempton et al. 2017) (dashed lines) for a range of temperatures for various important chemical species (in terms of opacity contribution at solar metallicity and solar C/O ratio) at 1 millibar pressure level in the atmosphere. Horizontal axis shows temperature in K and vertical axis shows the mole fraction (dimensionless) of the chemical species.

for the differences in FeH. The sudden drop in Li abundances for temperatures less than 1100 K in `ATMO` can be attributed to differences in the condensate list between `ATMO` and GGchem. However, this is observationally insignificant due to its low abundances. Aside from PH_3, FeH and Li, Figure 3.1 and 3.2 validates the ATMO equilibrium chemistry scheme including local condensation against one of the most up to date and well tested open source chemical equilibrium models available.

3.2.2 Equilibrium chemistry with rainout condensation

To validate the `ATMO` equilibrium chemistry scheme under the assumption of rainout condensation, we compare with the chemical abundances obtained from Exo–transmit (Kempton et al. 2017; Mbarek et al. 2016). Figures 3.3 and 3.4, show the equilibrium abundances for the main species (in terms of abundance and opacity contribution at solar metallicity and C/O ratio), derived using ATMO and Exo-transmit. For this comparison `ATMO` has been setup to include condensation with rainout, the solar elemental abundances of Asplund et al. (2009) (as used in Goyal et al. 2018) and the same list of condensates as Goyal et al. (2018). For Exo-transmit, the default values from Lodders (2003) have been used for the solar el-

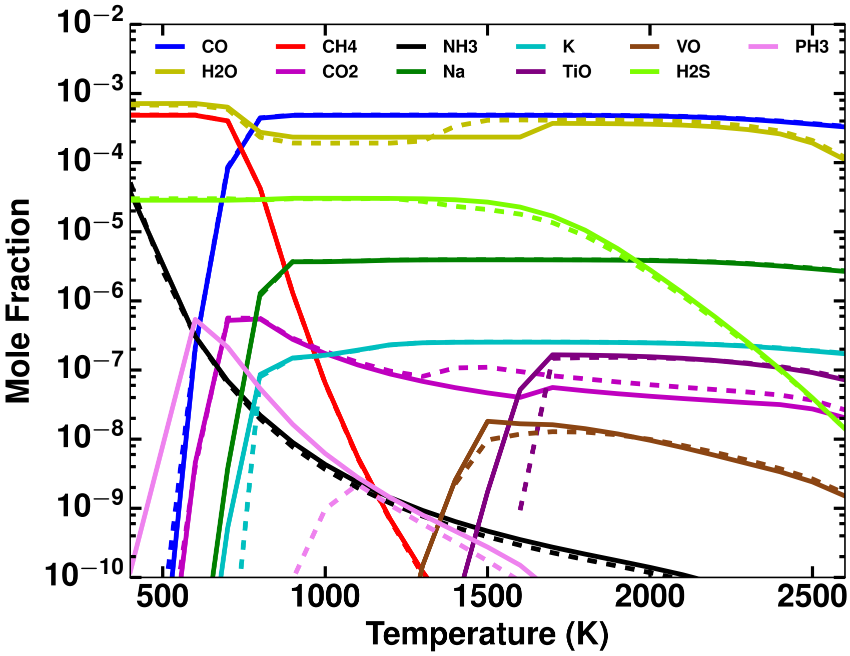

Figure 3.4: Same as 3.3 but with sequential rainout approach along constant pressure and solar elemental abundances from Lodders (2003) in `ATMO`

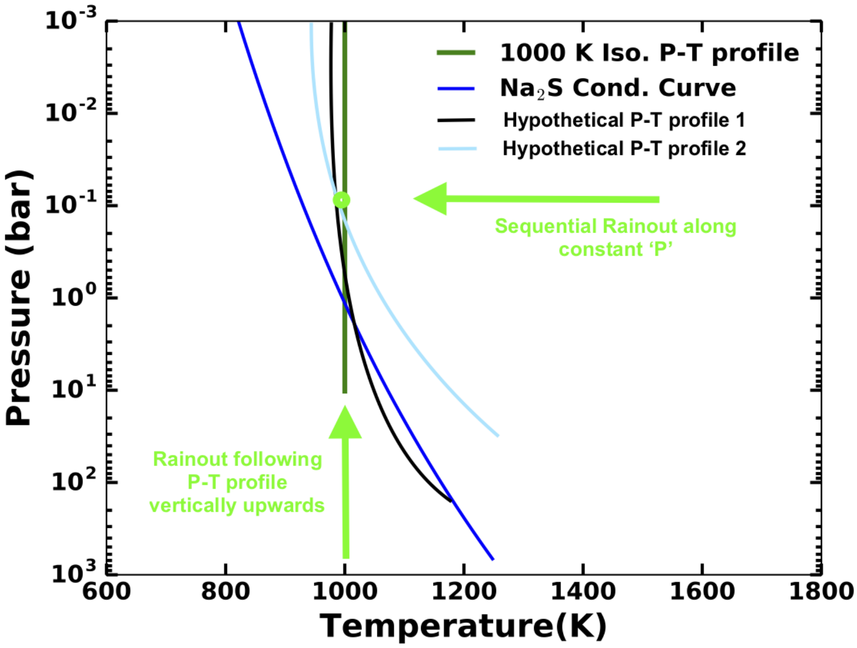

Figure 3.5: Schematic figure explaining two different rainout techniques, one following the constant temperature from high to low pressure as in `ATMO` and the other sequential rainout technique, following the constant pressure path from high to low temperature, as adopted in Exo-transmit.

emental abundances. Figure 3.3 shows a rapid decrease in the abundances of certain species as a function of temperature, caused by condensation and subsequent rainout, at markedly different temperatures between `ATMO` and Exo–transmit. The main cause of this difference is the numerical technique employed, combined with the assumption of an isothermal temperature–pressure profile. In `ATMO` the atmospheric chemistry is calculated first at highest pressures, and then following the temperature–pressure profile towards lower pressures. When a given species condenses, the elements that form that condensate are removed from the atmospheric column for all levels at lower pressures, i.e. rainout. However, in Exo–transmit, for a given temperature and pressure, the chemical mixture is calculated by moving, at constant pressure, from 3000 K toward the required temperature. Similarly, once a condensate is formed it is removed from the atmosphere for subsequent steps. Figure 3.4 shows a comparison where the `ATMO` calculation has been adapted to replicate the rainout technique adopted in Exo–transmit, along-with the use of solar elemental abundances from Lodders (2003) matching Exo–transmit. The very good agreement in chemical abundances, for almost all species, seen in Figure 3.4 reveals that the differences apparent in Figure 3.3 are primarily due to model choices. The differences in PH_3 abundances seen here can again be attributed to differences in list of condensate species and thermodynamic data, as seen previously when comparing with the GGchem model.

The two different rainout approaches adopted by ATMO and Exo-transmit, are shown in schematic form in Figure 3.5. Figure 3.5 shows the condensation curve for Na_2S species, and two hypothetical P-T profiles, alongside an isothermal one. The chemical mixture at the point marked by the green dot, on the isothermal profile (a simplified assumption for two hypothetical P-T profiles) is dependent on the method employed. In `ATMO`, we follow the isothermal atmospheric P-T profile vertically (i.e. from high to low pressures), performing sequential condensation and rainout to reach the green dot, while Exo–transmit iterates from high to low temperatures, at constant pressure, sequentially condensing species (and raining them out) along this path to reach the green dot. For the first hypothetical profile, which crosses the Na_2S condensation curve[3] at high pressures, the `ATMO` approach will result in a closer agreement between the isothermal and first hypothetical P-T profile, whereas the Exo–transmit method will be in disagreement. For the second hypothetical P-T profile, which does not cross the Na_2S curve, the Exo–transmit approach will result in a better match between the isothermal and hypothetical P-T profile, under the assumption of rainout. In summary, the differences in the calculated chemical abundances between `ATMO` and Exo–transmit can be largely explained by

---

[3] The condensation in both models is calculated using Gibbs energy minimisation, so the condensation curves are purely illustrative

both a choice of condensation/rainout approach and adopted solar elemental abundances. However, neither model approach to condensation is demonstrably more accurate, and as shown schematically in Figure 3.5 both can lead to errors under the assumption of an isothermal profile.

3.3 Numerical setup for the Grid

We use 50 vertical model levels with minimum and maximum optical depths of 10^{-7} and 10 at 1 µm, respectively. This covers the atmospheric region that is characterised via transmission spectra (∼0.1-100 millibar), with reasonable computational time for each model run. However, when we compute *P*-*T* profiles as performed in model validation Section 3.4, our maximum optical depth limit is 2×10^5 at 1 µm, since we need to compute temperatures even in the higher pressure region (~ 10 bar). Also to standardise the comparison of transmission spectra for a range of variables, we set the pressure at which the radius of the planet is defined at 1 millibar (Lecavelier Des Etangs et al. 2008). We note that there exists a degeneracy between reference transit radius and associated reference pressure as highlighted by Lecavelier Des Etangs et al. (2008) and Heng et al. (2017). Transmission spectra probes the atmospheric region around ∼0.1-100 millibar, therefore we restrict our upper atmosphere model boundary pressure to 10^{-6} bar. The input stellar spectra for each planetary model grid are taken from the BT-Settl[4] models (Allard et al. 2012; Rajpurohit et al. 2013). These stellar spectra are selected according to closest obtained host star temperature, gravity and metallicity from the TEPCAT database (Southworth 2011a). All the parameters required for model initialisation like stellar radius, planetary radius, planetary equilibrium temperature, surface gravity and semi-major axis are also adopted from TEPCAT[5] database, along with observational parameters like stellar V_{mag} and K_{mag} for target selection (see Appendix B.1).

3.3.1 Target Selection

An order of magnitude estimate of the observable transit signal can be calculated using basic geometry (Winn 2010), by using planet parameters and taking the ratio of the annular area of the planetary atmosphere to that of the stellar surface area given by

$$OTS = \frac{2R_{\mathrm{p}}H}{R_*^2}10^6, \tag{3.1}$$

---

[4] https://phoenix.ens-lyon.fr/Grids/BT-Settl/AGSS2009/SPECTRA/

[5] http://www.astro.keele.ac.uk/jkt/tepcat/allplanets-ascii.txt

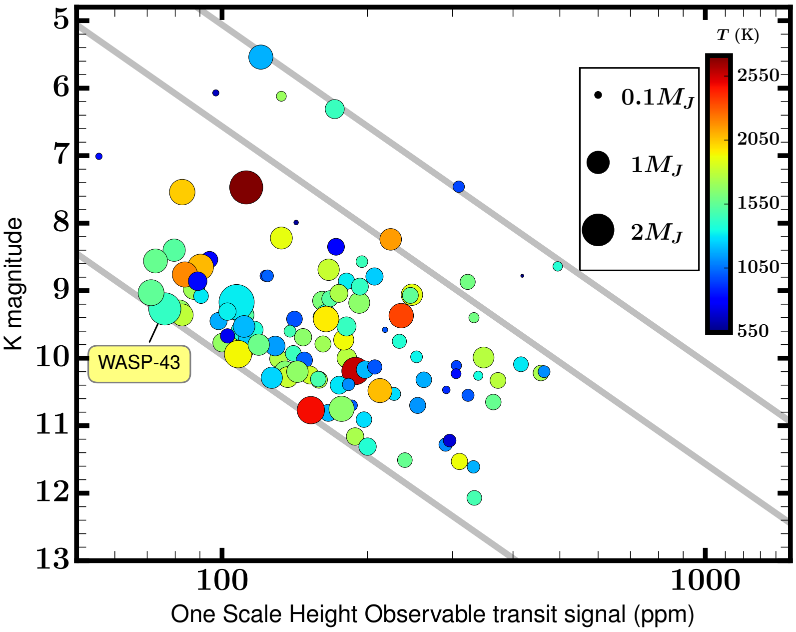

Figure 3.6: Figure showing host star K magnitude vs. one atmospheric scale height observable transit signal in parts per million (ppm) for all the planets selected in the grid. Colours indicate the temperature of the planet based on the scale, and the size shows the planet mass relative to the mass of the Jupiter. Grey lines indicate contours at theoretical relative signal to noise (SNR) ratio values of 20, 10 and 2.1 (for WASP-43b) from top to bottom.

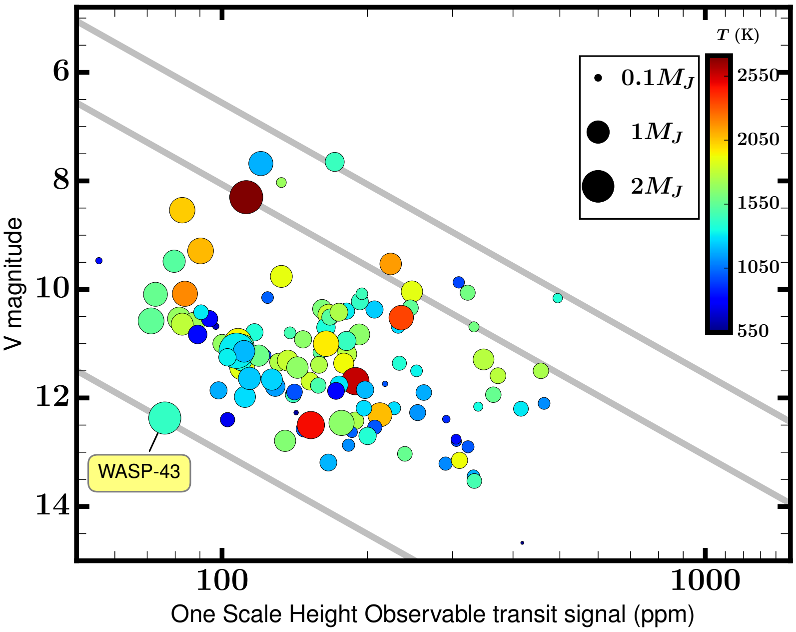

Figure 3.7: Same as 3.6 but for V magnitude and SNR contours of 20, 10 and 1 (for WASP-43b) from top to bottom.

where OTS is the observable transit signal for one scale height of the atmosphere in parts per million (ppm), H is scale height given by $KT/\mu g$, where K is the Boltzmann constant, T is the planetary equilibrium temperature, μ is the mean molecular weight of the planetary atmosphere which in this case is for a H_2 and He dominated atmosphere, g is the planetary surface gravity, R_p is the planetary radius within which the planet is optically thick at all wavelengths and R_* is the stellar radius, all in CGS units. The OTS for each planet and their host star V_{mag} and K_{mag} are plotted in Figure 3.6, along with contours, at a particular relative theoretical signal to noise ratio (SNR) given by

$$SNR_{\rm c} = SNR_{\rm ref}\frac{OTS_{\rm c}}{OTS_{\rm ref}}10^{\frac{-(V_{\rm c}-V_{\rm ref})}{5}}, \tag{3.2}$$

where $SNR_{\rm c}$ is the theoretical relative signal to noise ratio of the contour, $SNR_{\rm ref}$ is the same for the reference planet, OTS_c are the range of one scale height observable transit signal plotted in the contours, while $OTS_{\rm ref}$ is the OTS for the reference planet, V_c and $V_{\rm ref}$ are the V magnitudes in the contours and reference planet host star, respectively. In our case we have taken WASP-12b as our reference to plot SNR contours in Figure 3.6 and 3.7. This SNR for WASP-12b is calculated with five scale height transit depth value and the average noise calculated from Mandell et al. (2013) for one transit. These contours are used to select observationally significant atmospheres of exoplanets as shown in Figure 3.6 and 3.7.

We select the planets with theoretical relative SNR greater than that of WASP-43b in V_{mag} and K_{mag} as shown in Figure 3.6 and 3.7. We have deliberately chosen to make this grid planet specific, rather than exploring the huge parameter space of mass, radius, gravity etc., which would have increased the size of the grid substantially. Making it planet specific is also very helpful to directly use it for observational proposals and interpretation without interpolation. All the planets with their parameters and references, selected in our current grid of model simulations from TEPCAT database (Southworth 2011a), are shown in Appendix B.1.

3.3.2 Parameter Space Selection

This section describes in detail, the parameter space of the grid for which model transmission spectra are generated. These parameters have been selected based on the most important physical parameters affecting the transmission spectra and the computational feasibility of running the simulations for a range of planets. For each planet, five major parameters are varied and are listed in Table 3.3. The first parameter is the temperature of the planet, which is not a well constrained parameter observationally, since it is dependent on various other properties of the atmosphere. However, it has a profound effect on the transmission spectra of a planet (Fortney

Temperature (K)	Metallicity (x solar)	C/O-ratio	Haze enhancement factor (α_{haze})	Grey cloudiness factor (α_{cloud})
T_{eq} - 300	0.005	0.15	1 (No Haze)	0 (No Cloud)
T_{eq} - 150	0.1	0.35	10	0.06
T_{eq}	1	0.56	150	0.2
T_{eq}+ 150	10	0.70	1100	1
T_{eq} + 300	50	0.75		
	100	1		
	200	1.5		

Table 3.3: Table showing the entire parameter space of the grid. The temperature is with respect to the planetary equilibrium temperature (T_{eq}). The C/O ratio of 0.56 is solar value. The haze enhancement factor is with respect to gaseous Rayleigh scattering. The grey cloudiness factor is with respect to H_2 scattering cross-section at 350 nm.

et al. 2010). The zeroth order T_{eq} calculated based on the distance of the planet from the host star is the only known parameter. When computing transmission spectra we are concerned with the temperature approximately around the 1 millibar pressure region of the atmosphere. Therefore, T_{eq} is used as a first guess. We vary the temperature of the planetary atmosphere in increments of 150 K to a maximum of ±300 K, with respect to the T_{eq} of the planet, giving a total of 5 temperature grid points per planet as shown in Table 3.3. The selection of 150 K increment is based on the typical temperature uncertainty in the observational transmission spectra (Lecavelier Des Etangs et al. 2008). The selection of maximum variation of ±300 K is based on a compromise between computational feasibility and accuracy required to capture major spectral features. The metallicity of a planet is a parameter which indirectly determines the chemical composition of its atmosphere, thereby affecting its observable signatures in the transmission spectra. The metallicity is varied from sub-solar to super-solar values: 0.005, 0.5, 1, 10, 50, 100 and 200 times solar.

Öberg et al. (2011) and Madhusudhan et al. (2016a) provided evidence of utilising C/O ratios to constrain the location of planetary formation in the debris disk. Its effect on the exoplanet atmospheric chemistry has been studied extensively by Seager et al. (2005), Kopparapu et al. (2012), Madhusudhan (2012), and Moses et al. (2013a). In particular, Mollière et al. (2015) developed a very extensive grid for various C/O ratios and analysed its effect on the emission spectrum. The C/O ratios are selected here based on the current important transition values guided by previous studies. Our selection of lower C/O ratios (0.15 and 0.35) was guided by model fitting to observations, since some of the observations were consistent with very low C/O ratio (see Section 3.7). Therefore, our parameter space contains C/O ratios of 0.15, 0.35, 0.56, 0.7, 0.75, 1 and 1.5. The solar C/O ratio is ∼0.56 (Caffau et al. 2011).

Sing et al. (2016) presented a comparative planetology of various exoplanets that highlighted the importance of haze and clouds in understanding and characterising exoplanet atmospheres using transmission spectra. Lecavelier Des Etangs et al. (2008) and Sing et al. (2015) and Sing et al. (2016) highlighted the effect of haze in muting the spectral features in transmission spectra. Therefore, haze in the form of Rayleigh scattering having variable strengths with respect to the nominal multi-gas Rayleigh scattering has been included in the grid as a fourth parameter. α_{haze}, the haze enhancement factor, explained in Section 2.6.2 is varied in the grid in steps such that it leads to approximately one scale height change in the transmission spectrum, where the Rayleigh scattering dominates, which leads to multiplication factors 1, 10, 150, 1100 times nominal multi-gas Rayleigh scattering in the grid.

A grey scattering opacity representing clouds of different scattering cross-sections is used as a fifth parameter. We use a grey cloud strength factor (α_{cloud}) (see Section 2.6.2) of 0.06, 0.2 and 1 corresponding to scattering opacity (κ) of $\sim 1.5 \times 10^{-4}$, 5×10^{-4} and 2.5×10^{-3} cm^2/g, respectively in the grid. $\alpha_{\mathrm{cloud}} = 0$ corresponds to clear sky scenario. These factors were chosen based on the change in the 1.4 μm H_2O spectral feature due to addition of grey clouds, particularly for the test case of HD 189733b (McCullough et al. 2014; Sing et al. 2016; Heng et al. 2017). However, since these factors correspond to fixed values of scattering opacity, they are independent of planetary parameters. The factors 0.06, 0.2 and 1 led to the transit radius ratio of this 1.4 μm feature being reduced to ~66%, 33% and 15%, respectively, compared to clear atmosphere case (see Figure 3.26 discussed in Section 3.6.4). In `ATMO`, clouds can be specified at any level in the atmosphere. However, we specify clouds throughout the atmosphere (all 50 levels), while changing its scattering strength to represent the degree of cloudiness.

3.4 Validation of Transmission Spectra using Isothermal P-T profile with those using radiative-convective equilibrium profile

In Goyal et al. (2018) we calculated transmission spectra adopting isothermal P-T profiles. In this section we explain the differences between transmission spectra computed using isothermal P-T profiles and those using consistent radiative-convective equilibrium P-T profiles. We note that model transmission spectra with isothermal P-T profiles have been shown sufficient to explain the observations (see Fortney 2005; Heng et al. 2017).

To quantify the effect of assuming an isothermal P-T profile as opposed to cal-

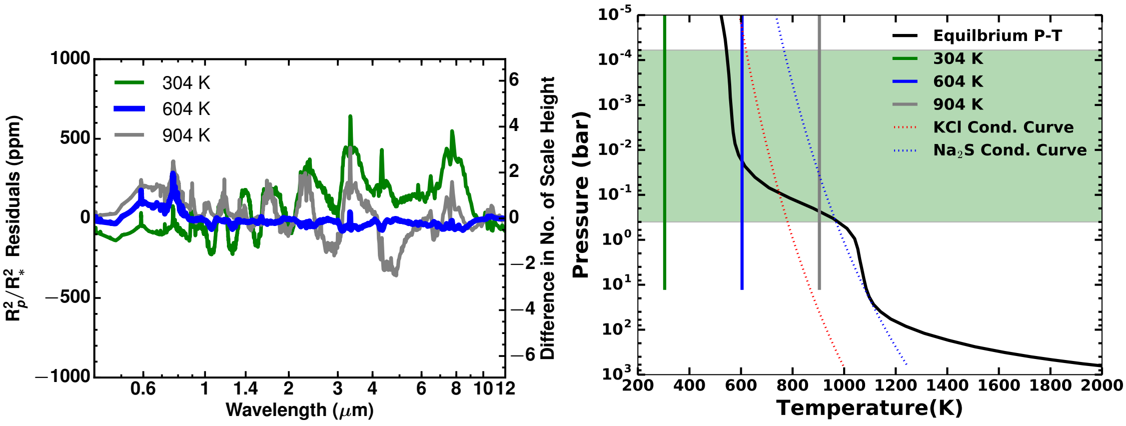

(a) (b)

Figure 3.8: **(a)** Figure showing differences (residuals) in transit depth ($R_\mathrm{p}^2/R_\star^2$) generated using radiative-convective equilibrium P-T profiles and isothermal P-T profile (in the sense consistent minus isothermal) for the isothermal temperatures in our parameter space for GJ 3470b which are 304 K (green), 604 K (blue) and 904 K (grey). Thicker line in blue for 604 K shows minimum residuals and green line for 304 K shows maximum residuals. Spectra with equilibrium P-T profile is using the recirculation factor of 0.5. Residuals are shown both in transit depth in parts per million (ppm) on left and number of scale heights on right Y-axis. X-axis shows wavelength in µm. **(b)** Figure showing radiative-convective equilibrium P-T profiles for a recirculation factor of 0.5 (black), and isothermal P-T profiles in our parameter space for GJ 3470b which are 304 K (green), 604 K (blue) and 904 K (grey). The condensation curves for KCl and Na_2S are also shown with dotted lines in red and blue respectively. Shaded green region highlights the atmospheric pressures (altitude) probed using the transmission spectra. X-axis shows temperature in Kelvin and Y-axis shows pressure in bar. Lower boundary pressure for isothermal P-T profiles has been restricted to 10 bar compared to 10^3 bar adopted earlier in Goyal et al. (2018).

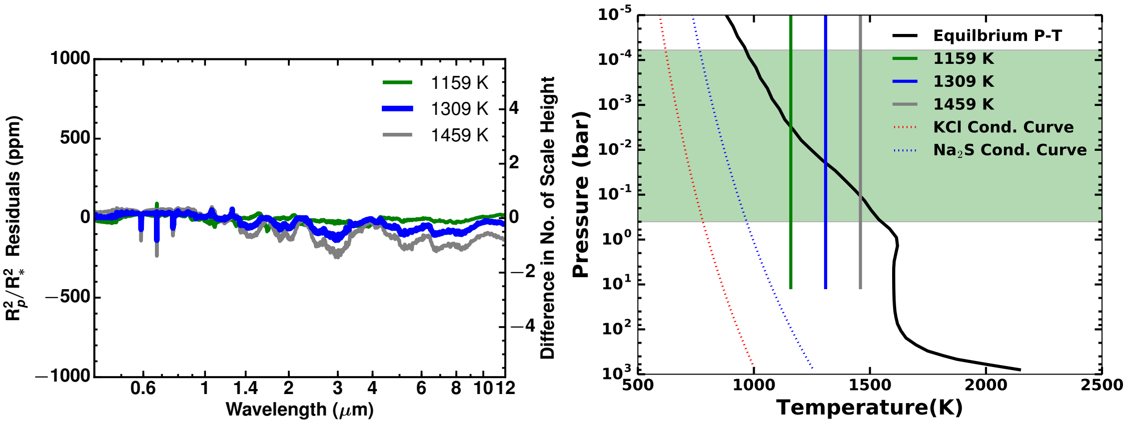

(a) (b)

Figure 3.9: **(a)** Figure showing residuals similar to Figure 3.8a, but for hotter planet, HD 209458b (T_{eq} = 1459 K) at 1159 K (green), 1309 K (blue) and 1459 K (grey). Thicker line in blue for 1309 K shows minimum residuals and green line for 1159 K shows maximum residuals. **(b)** Figure similar to Figure 3.8b, but for HD 209458b showing radiative-convective equilibrium *P*-*T* profiles for a recirculation factor of 0.5 (black), and isothermal *P*-*T* profile at 1159 K (green), 1309 K (blue) and 1459 K (grey).

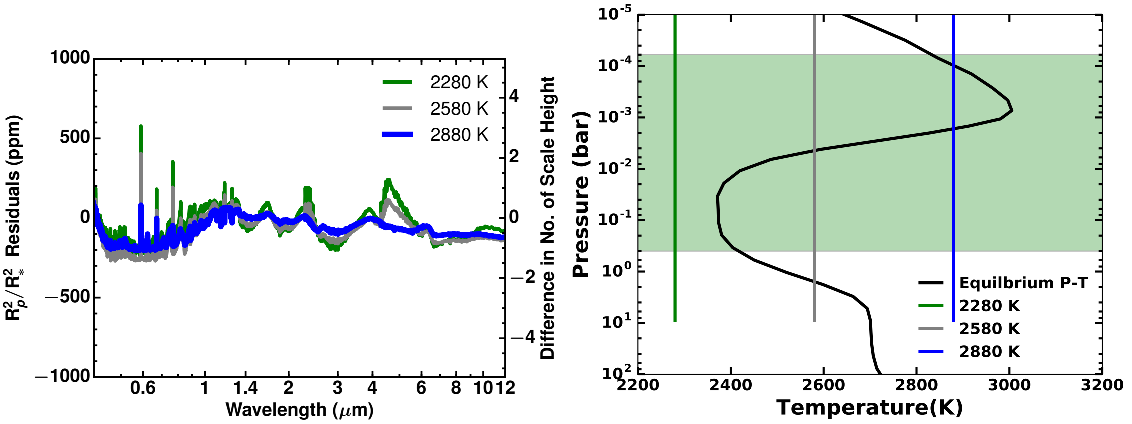

(a) (b)

Figure 3.10:]

(a) Figure showing residuals similar to Figure 3.8a, but for a hotter planet WASP-12b (T_{eq} = 2580 K) at 2580 K (green), 2730 K (grey) and 2880 K (blue). Thicker line in blue for 2880 K shows minimum residuals and green line for 2280 K shows maximum residuals. **(b)** Figure similar to Figure 3.8b but for WASP-12 showing radiative-convective equilibrium *P*-*T* profiles for a recirculation factor of 0.5 (black), and isothermal *P*-*T* profile at 2280 K (green), 2580 K (grey) and 2880 K (blue).

culating a *P*-*T* profile consistent with radiative-convective equilibrium, we compared the two approaches for planets spanning a wide range of T_{eq}. Namely, GJ 3470b ($T_{eq} = 604\,K$), HD 209458b ($T_{eq} = 1459\,K$) and WASP-12b ($T_{eq} = 2580\,K$). Computing a *P*-*T* profile consistent with radiative-convective equilibrium requires adoption of an angle of incidence (θ) for the radiative flux, and a "recirculation factor" (treated as a reduction in incoming flux as in Fortney et al. 2007). The recirculation factor simulates the redistribution of input stellar energy in the planetary atmosphere, by the dynamics, where a value of 1 equates to no redistribution, while 0.5 represents efficient redistribution. Simulations adopting solar metallicity, solar C/O ratio, without cloud or haze, were then performed for the consistent case, adopting $\theta = 60°$ (equating to the dayside average) and a recirculation factor of 0.5, and compared to each of the counterpart different temperature isothermal simulations in our grid.

The differences (residuals) between simulated spectra derived from the consistent simulations and their isothermal counterparts at three different temperatures adopted in the grid are shown for GJ 3470b, HD 209458b and WASP-12b in Figures 3.8a, 3.9a and 3.10a, respectively. Figures 3.8b, 3.9b and 3.10b show the derived consistent (equilibrium) *P*-*T* profiles and the adopted isothermal profiles for these simulations, alongside the condensation curves of KCl and Na_2S. Figures 3.8a, 3.9a and 3.10a include both examples of the largest and smallest residuals, and reveal that the differences are all less than ∼1 scale height for the closest matching isothermal spectrum at all the wavelengths. Therefore, very high precision measurements (e.g ∼150 ppm for HD 209458b) would be needed to detect temperature variations via altitude-dependent scale height differences in the transmission spectra probed region.

In the case of GJ 3470b, residuals within ∼1 scale height are seen for the isothermal temperature of 604 K in Figure 3.8a since this temperature is closest to the consistent *P*-*T* profile in the transmission spectra probed region, which is almost isothermal, as shown in Figure 3.8b. The residuals are largest for the coolest isothermal simulation at 304 K, since it is substantially different from the consistent *P*-*T* profile. For HD 209458b and Wasp-12b, the residuals of the closest matching isothermal spectrum are again within ∼1 scale height, despite the *P*–*T* profile being far from isothermal. For optical wavelengths large residuals can be seen, for the coolest isothermal temperature, at the core of the strong Na lines for HD 209458b and TiO/VO lines for WASP-12b. For HD 209458b this large difference is caused by the condensation of Na_2S which occurs, as shown in Figure 3.9b, in the coolest isothermal simulation, at pressures above 10^2 Pa (where the Na_2S condensation curve intersects the temperature of 1159 K), but not in the consistent version. In our model we assume efficient settling of condensates i.e. "rainout", which as described in Section 2.8.1, depletes the atmosphere above the condensation point of the constituent species. This leads to the absence of Na features in the spectrum derived from the coolest isothermal simulation, and thus, large residuals when compared to the radiative-convective equilibrium version. A similar effect is found for WASP-12b, but due to condensation of TiO/VO bearing species in the coolest isothermal simulation as shown in Figure 3.10a. However, additionally, there is substantial deviation of coolest isothermal P-T profile from that of consistent profile, as seen in Figure 3.10b, increasing the residuals. It is important to note that the residuals found between the spectra derived from the isothermal and consistent P-T profile simulations are also a function of the recirculation factor adopted in the latter. As the recirculation factor is an unconstrained parameter this introduces uncertainties into the consistent calculation thereby effecting the match with the isothermal spectra.

In summary, for all the test case planets from our grid shown in Figures 3.8a, 3.9a and 3.10a, the assumption of an isothermal atmosphere leads to observationally negligible differences for the closest matching, most appropriate isothermal temperature, except where the temperatures are cool enough for condensation and subsequent rainout to occur (as is the case for lowest isothermal temperature for these planets). In practice, different isothermal temperatures can be used for different altitudes, as was done for for the Na line in HD 189733b (Huitson et al. 2012), which would avoid this issue.

As described in Section 3.1.2 we assume efficient settling of condensed species (rainout) as one of the approaches while computing the equilibrium chemistry in our current simulations, which is a widely adopted assumption in the literature (Burrows et al. 1999; Lodders et al. 2006a; Fortney et al. 2008; Mbarek et al. 2016). Without a sophisticated cloud model, calculating whether a given condensate will be present in the atmosphere or settle is not possible, so the best that can be done are the two limiting cases of efficient settling (rainout) and efficient vertical lofting (local condensation or no-rainout). Therefore, we develop our grid of models using this two extreme assumptions of local condensation and rainout condensation.

3.5 Decoupled Transmission Spectra

Transmission spectra are shaped by the total opacity due to various molecular species. Therefore, here we show the major spectral features in the transmission spectra of hot Jupiter exoplanets across a wide wavelength regime. Figures, 3.11 and 3.12 show the transmission spectra with opacities of just individual species included in the simulation. All the individual opacity model runs are for HD 209458b with 1609 K equilibrium temperature, solar metallicity, solar C/O ratio and a clear atmosphere. We omit Rayleigh scattering to avoid absorption features being masked

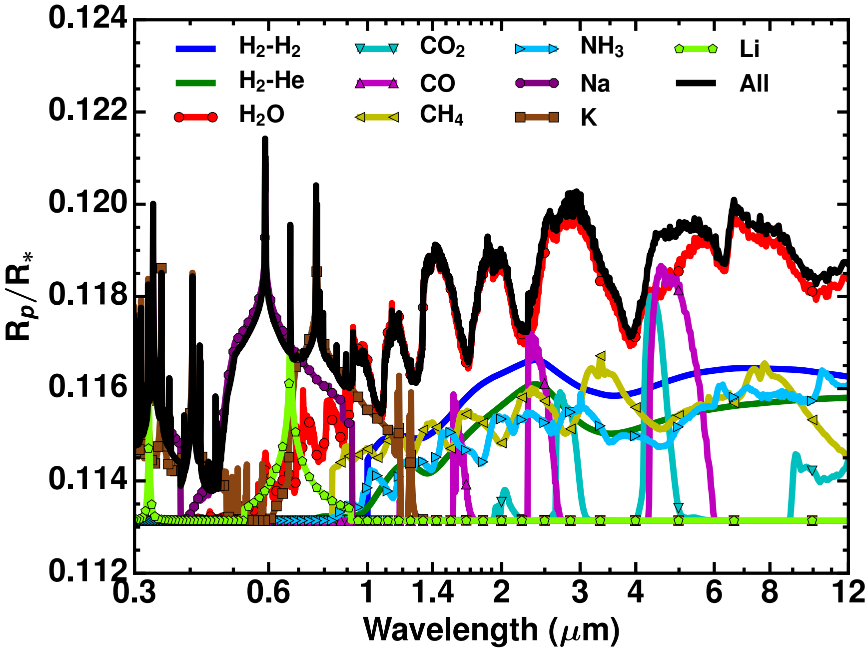

Figure 3.11: Figure showing transmission spectra features of each individual molecule used in `ATMO` (1 to 10) for HD 209458b with 1609 K equilibrium temperature, solar metallicity, solar C/O ratio and a clear atmosphere. H_2-H_2 (blue), H_2-He (green), H_2O (red), CO_2 (cyan), CO (magenta), CH_4 (yellow), NH_3 (lightblue), Na (purple), K (brown), Li (lightgreen) and all 20 opacities (black). No $R_\mathrm{p}/R_\star$ offset was applied while plotting. Rayleigh scattering is switched off to avoid absorption features being masked at optical wavelengths. Individual simulations are divided into blocks of 10 while plotting for clarity.

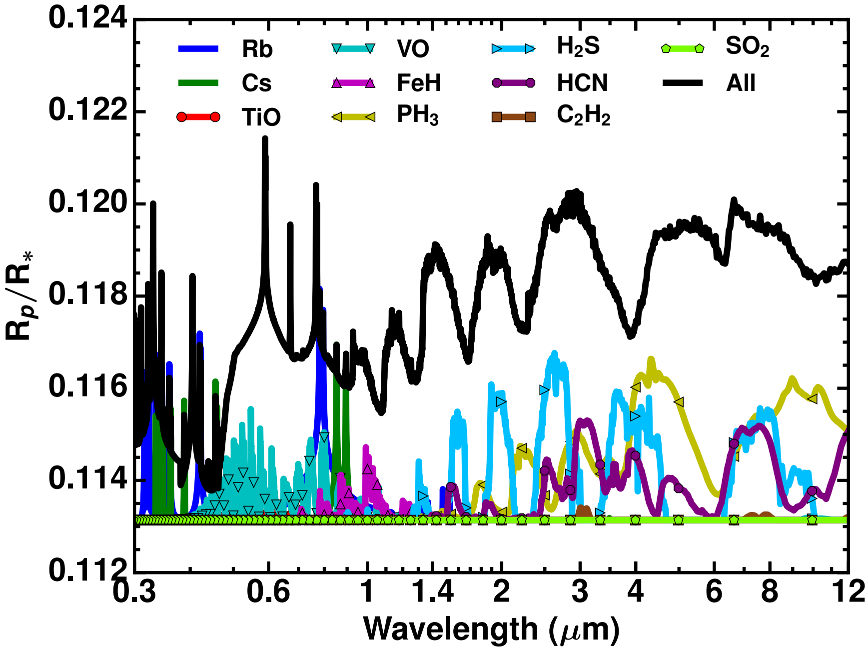

Figure 3.12: Same as Figure 3.11 but for Rb (blue), Cs (green), TiO (red), VO (cyan), FeH (magenta), PH_3 (yellow), H_2S (lightblue), HCN (purple), C_2H_2 (brown), SO_2 (lightgreen) and all 20 opacities (black)

at optical wavelengths. The simulation depicted in black in both the figures include all the 20 opacities in the `ATMO`, hereafter termed “all opacity simulation”. This allows identification of major species which contribute to final transmission spectra.

With just H_2-H_2 or H_2-He collision induced absorption (CIA) opacities included in the simulation, shown in blue and green, respectively in Figure 3.11, we mainly see broad band collision induced signatures of absorption, primarily in the near infrared regions. The simulation with just water (H_2O) in red (Figure 3.11), leads to spectral features in almost all parts of the spectrum, one of the major ones being at 1.4 µm, which has been detected in many exoplanet atmospheres. Comparing the all opacity simulation in black, and the simulation in red with just H_2O opacity we can clearly see that H_2O dominates the final transmission spectra at solar metallicity. This changes with change in metallicity and C/O ratio, as explained in detail in Sections 3.6.2 and 3.6.3. Carbon dioxide (CO_2) also has many significant features with the strongest one at ∼4.2 µm. Carbon monoxide (CO) has extremely large spectral signatures at around 1.6 µm, 2.2-2.8 µm and a wide-band 4 to 6 µm feature. The comparison with the all opacity simulation also shows the substantial contribution of CO to the final planetary transmission spectrum, especially in the 4-6 µm region. Except in the optical, methane (CH_4) also has many important features similar to H_2O , with major features in the 1.2-1.3, 1.7-1.8, 2-2.8, 3-4 and 7-9 µm bands. Depending on the C/O ratios, infrared spectra can either be H_2O dominated or CH_4 (carbon species) dominated (Kopparapu et al. 2012; Madhusudhan 2012; Moses et al. 2013a; Venot et al. 2015; Mollière et al. 2015). Moreover, since the primary absorption features between 1 to 5 µm region, alternate between H_2O and CH_4 as a function of wavelength, they are in principle readily distinguishable. Ammonia (NH_3) has some wide band spectral features, but smaller than H_2O and CH_4. Sodium (Na) has one of the strongest signature in hot Jupiter spectra at around 0.58 µm and has been detected conclusively in many of these planets. Potassium (K) is the other alkali metal with very strong spectral features, the strongest being at 0.76 µm along with many narrow features which are extremely difficult to resolve with current instruments. We can also see from Figure 3.11, the all opacity simulation matches the individual Na and K model spectra around 0.58 µm and 0.76 µm, respectively, demonstrating their dominance at these wavelengths.

Alkali metal elements like Lithium (Li) (shown in Figure 3.11), Rubidium (Rb) and Cesium (Cs) (shown in Figure 3.12) have very narrow features in the all opacity simulation, making it challenging to detect them observationally. However, broadband features can be seen in the optical wavelengths in the individual spectra of these species, at high pressure levels (deeper) in the atmosphere, making them important opacity sources to obtain accurate heating rates (depending on their abundances) and thereby P-T profiles.

Titanium oxide (TiO) and vanadium oxide (VO) don't have any major features at temperatures of 1600 K due to their low concentrations. However, at very high temperatures, above 2200 K, TiO and VO dominate the visible region of the spectrum suppressing the Na and K features, as seen in Figure 3.17. Due to their high optical opacity, their presence could lead to a thermal inversion in the planetary atmosphere (Spiegel et al. 2009; Evans et al. 2017). Iron Hydride (FeH) features are also visible only at high temperatures similar to TiO/VO. Phosphine (PH_3) has its primary features in the infrared with the major one between 4 to 5 µm. Hydrogen sulphide (H_2S) and hydrogen cyanide (HCN) also have many strong spectral features especially in the infrared. Equilibrium chemistry calculations show H_2S is a quite abundant species for all temperature and metallicity regimes when rainout condensation is included (see Section 3.6.1, 3.6.2, 3.6.3), therefore its primary spectral peaks at 1.5, 2 µm and between 2.5 to 3, 3.3 to 5, 6 to 10 µm will be interesting to observe with JWST. The detection of H_2S in Jupiter (Niemann et al. 1998), emphasised the importance of condensation with rainout, since without condensation FeS takes up all sulphur inhibiting H_2S formation. At higher metallicities, HCN becomes important due to an increase in its concentration. This leads to many HCN features around 1.1µm, 1.4 to 1.5 µm , 2.5 to 2.7 µm and 3 to 3.2 µm along with a possible broadband feature between 6 and 9 µm. Acetylene (C_2H_2) features are negligible at solar metallicity but increase substantially at higher metallicities due to an increase in its concentration. Sulphur dioxide (SO_2) tends to become important at higher metallicities (See Section 4.3 for details). We note that this analysis is based on a particular planet and specific parameters, therefore the strength of the features might change with change in planetary and grid parameters (basically changing chemistry). However, the position of peaks in wavelength will remain unchanged since they are inherent characteristics of each species/molecule.

3.6 Transmission Spectra: variation with parameters

The major spectral features of various species in the transmission spectrum of exoplanets are described in Section 3.5. In this section, we explore the parameter space for a subset of planets, to demonstrate their effect on the transmission spectra. For brevity, we select three planets with different equilibrium temperatures covering our target range. The effect on the transmission spectra of these planets over the entire parameter space is investigated, along with their physical interpretation. The three planets for which we present the analysis are, HAT-P-12b, WASP-17b and WASP-12b, with equilibrium temperatures of 960 K, 1755 K and 2580 K, respectively. These

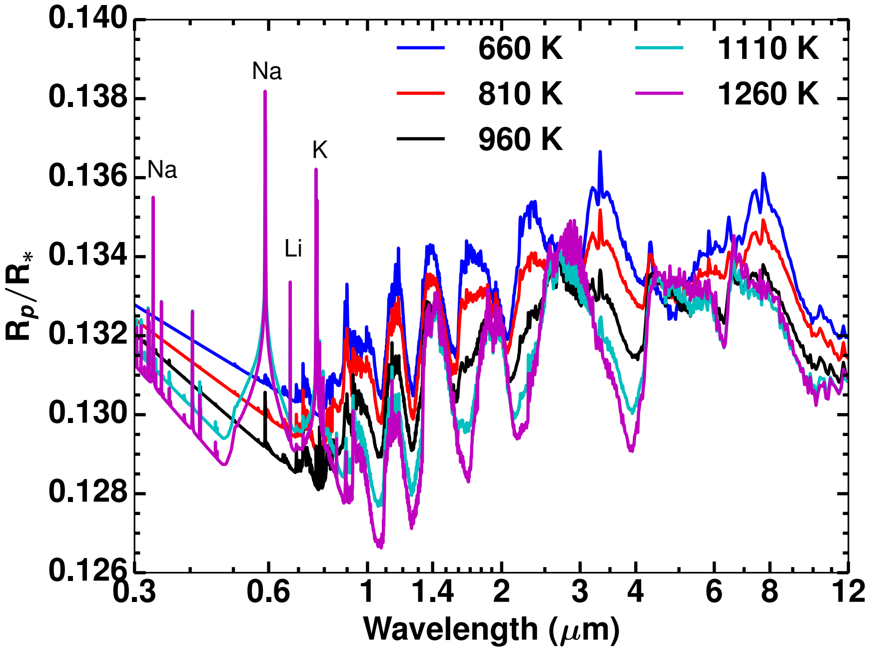

Figure 3.13: Figure showing HAT-P-12b transmission spectra for a range of temperatures (in Kelvin) at solar metallicity, solar C/O ratio and clear atmosphere. X-axis is wavelength in µm and Y-axis transit radius ratio ($R_\mathrm{p}/R_\star$).

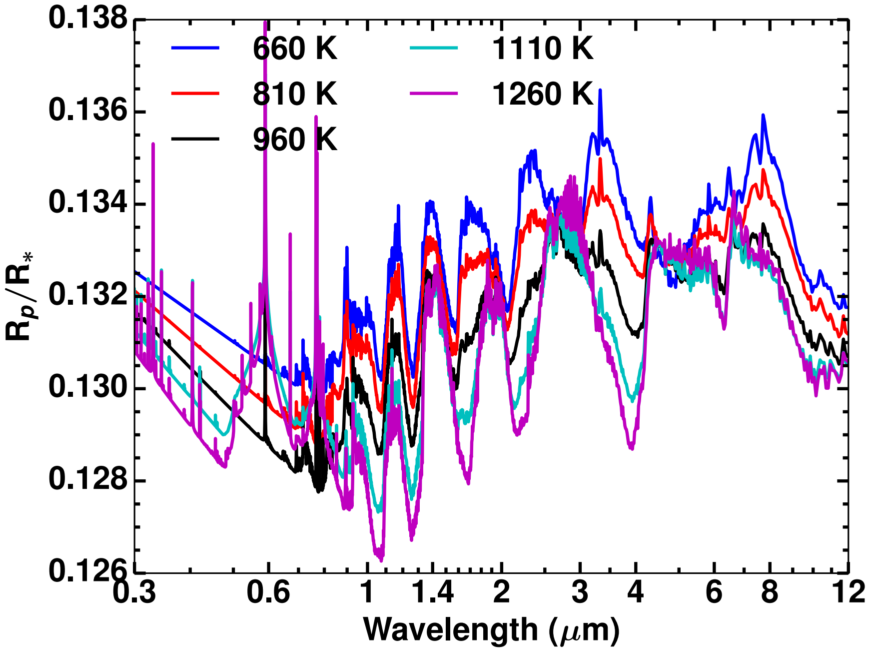

Figure 3.14: Same as Figure 3.13 but with local condensation approach.

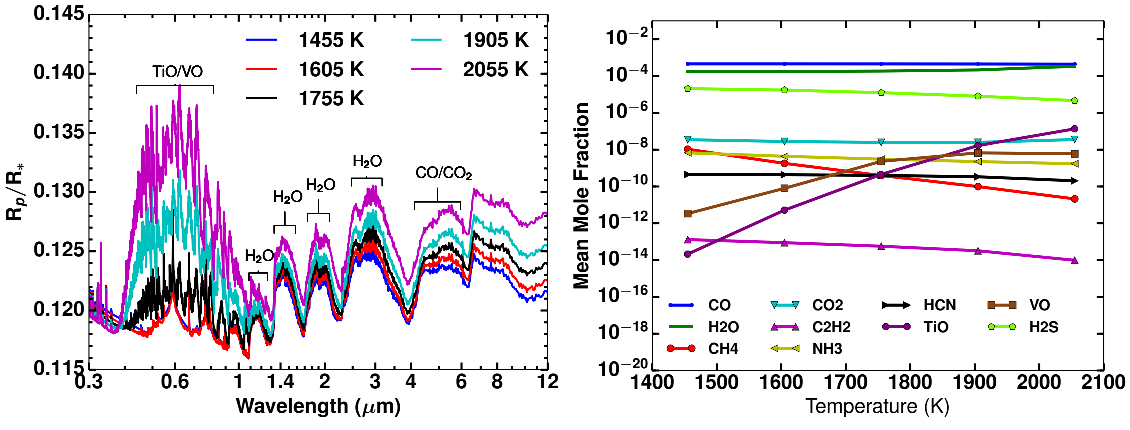

(a) (b)

Figure 3.15: **(a)** Figure showing WASP-17b transmission spectra for a range of temperatures, similar to Figure 3.13, with major molecular features shown at equilibrium temperature (1755 K). **(b)** Figure showing change in mean chemical abundances between 0.1 and 100 millibar for various molecules, with change in temperature for WASP-17b at solar metallicity, solar C/O ratio and clear atmosphere. X-axis is temperature in Kelvin while Y-axis shows mean abundances in units of mole fraction.

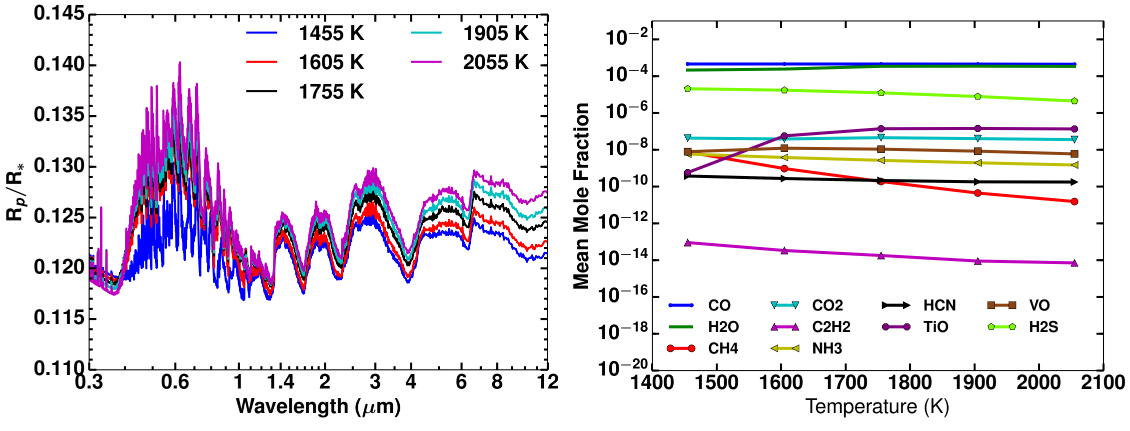

(a) (b)

Figure 3.16: **(a)** Same as Figure 3.15a but with local condensation approach. **(b)** Same as Figure 3.15b but with local condensation approach.

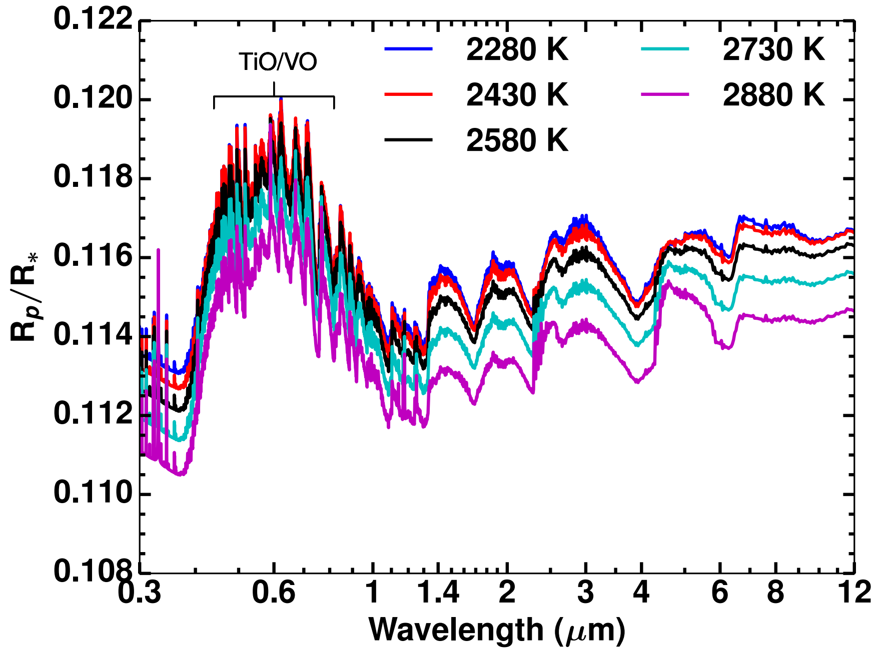

Figure 3.17: Figure showing WASP-12b transmission spectra for a range of temperatures, similar to Figure 3.13

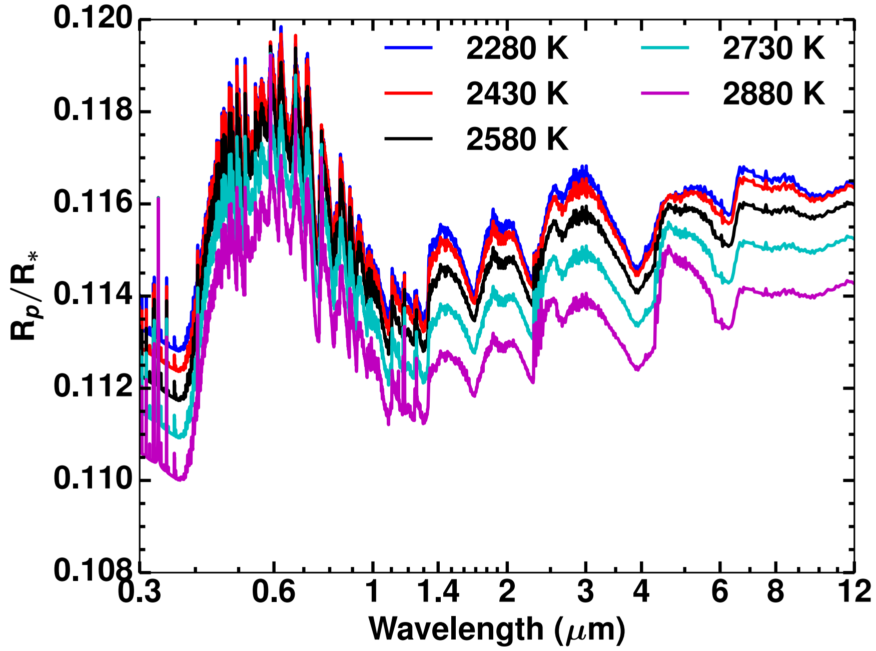

Figure 3.18: Same as Figure 3.17 but with local condensation approach

three different planets cover the full range of currently observed hot Jupiter planets.

3.6.1 Effect of Temperature

The temperature structure of the planet governs the most important physical and chemical mechanisms in a planetary atmosphere. The isothermal temperature we adopt, is indicative of the temperature at the ∼1 millibar pressure level. The metallicity and C/O ratio were fixed to solar values to explore the effect of temperature, without any changes due to other parameters.

Changes in the transmission spectral features for a range of temperatures for HAT-P-12b with an equilibrium temperature of 960 K are shown in Figure 3.13. As the temperature increases from 660 K to 1260 K, the dominant spectral features vary substantially. For temperatures from 660 K to 960 K, the spectra are dominated by CH_4 without any Na, K or other alkali metal features. However, at a temperature of 1110 K we see a strong Na feature at 0.589 µm, a K feature at 0.76 µm, a Li feature at 0.67 µm and most importantly H_2O features start to dominate spectra over those of CH_4. The alkali metal features of Li, Rb and Cs also start showing their signatures at this temperature. Moreover, spectral features of CO also appear for $T>960$ K, between 4 to 6 µm. The spectra with local condensation approach as shown in Figure 3.14 is also very similar, except larger features of alkali species as they are not removed from the atmosphere as in the rainout condensation approach. Moreover, small features of TiO/VO can be seen at temperatures of 1260 K absent in the rainout scenario, as they are sustained in the atmosphere.

The change in transmission spectral features for a range of temperatures for WASP-17b with an equilibrium temperature of 1755 K are shown in Figure 3.15a. The features become stronger with the increase in temperature, because the scale height increases, implying hot planets are the best targets for transmission spectroscopy as found in previous studies (Fortney et al. 2010).

To understand the change in equilibrium chemical abundances with temperature, we calculate the simple linear mean abundances for some spectrally important species in the transmission spectra probed region (0.1-100 millibar). Figure 3.15b shows these mean abundances for WASP-17b. CO is the most abundant chemical species after H, H_2 and He (not shown here). Surprisingly, H_2S is also as abundant as H_2O, but with a weak spectral signature, therefore it has not yet been detected in any exoplanet atmosphere. However, H_2S abundances decrease with increasing temperature while that of H_2O increases, especially after 1900 K. The drop in CH_4 abundances with increase in temperature is substantial, going from 10^{-8} to 10^{-11} mole fraction as temperature goes from 1455 K to 2055 K. HCN and C_2H_2 abundances are almost constant with increase in temperature but decreases after 1900 K.

We note that the H_2O mole fraction is 3.1×10^{-4} at 1500 K with solar metallicity and solar C/O ratio, when only gas phase chemistry is considered, dropping to 2.4×10^{-4} with local and rainout condensation chemistry, which is the case for this entire grid, as some of the oxygen is taken up by condensate species reducing elemental oxygen available to form H_2O (Moses et al. 2011).

With the increase in temperature there is a gradual increase in the concentration of both TiO and VO and their features become increasingly significant for WASP-17b, as seen in Figure 3.15b . The spectra with local condensation approach as shown in Figure 3.16a is particularly different at lower temperatures (1455 and 1605 K), since the abundance of TiO and VO becomes spectrally important even at ∼1450 K in this case as compared to ∼1700 K with rainout condensation approach.

Figure 3.17 shows spectra for WASP-12b with an equilibrium temperature of 2580 K. Here we clearly see the gradual increase in the TiO/VO features as we increase the temperature from 2280 to 2880 K, with the spectra substantially dominated by TiO/VO with extremely large effective $R_\mathrm{p}/R_\star$ in the optical. This shows that the presence of TiO/VO in these high temperature planetary atmospheres leads to a substantial signature in transmission spectra in agreement with previous studies (Burrows et al. 1999; Fortney et al. 2010). It is also important to note that TiO/VO features develop around Na and K features, thereby masking them. We would expect Na and K to be ionised as such high temperatures, but we currently don't include ionisation in our model. We also see that the ratio of optical and near-infrared bands $R_\mathrm{p}/R_\star$ change with changing temperature. The spectra with local condensation approach as shown in Figure 3.18 is almost similar, except with larger features due to slightly higher abundances.

3.6.2 Effect of Metallicity

Figure 3.19a, 3.20a and 3.21a show changes in the transmission spectra with changes in metallicity for HAT-P-12b, WASP-17b and WASP-12b, respectively. Additionally, their corresponding mean chemical abundances are shown in 3.19b, 3.20b and 3.21b, respectively. These simulations are at planetary equilibrium temperature, solar C/O ratio and do not include any haze or clouds. At optical wavelengths, for HAT-P-12b as shown in Figure 3.19a, we see the change in the Rayleigh scattering strength as we go from sub-solar metallicities to super-solar metallicities. This is a direct result of inclusion of multi-gas Rayleigh scattering, explained in Section 2.6.1. The larger spectral features (higher $R_\mathrm{p}/R_\star$) at higher metallicities for all wavelengths can be attributed to an increase in opacity (Fortney et al. 2010). In the infrared and near infrared we see a trend where increasing metallicity leads to an increase in the strength of spectral features. However, there is a substantial change

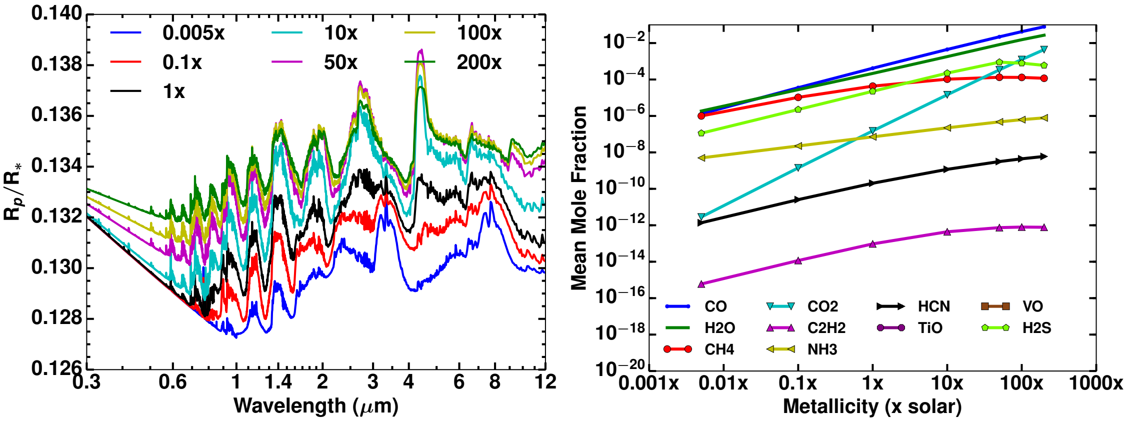

(a) (b)

Figure 3.19: **(a)** Figure showing HAT-P-12b transmission spectra for a range of metallicity (times solar) at its equilibrium temperature, solar C/O ratio and clear atmosphere. X-axis is wavelength in µm and Y-axis transit radius ratio ($R_\mathrm{p}/R_\star$). **(b)** Figure showing change in mean chemical abundances between 0.1 and 100 millibar for various molecules, with change in metallicity for HAT-P-12b. X-axis is metallicity (× solar) while Y-axis shows mean mole fraction.

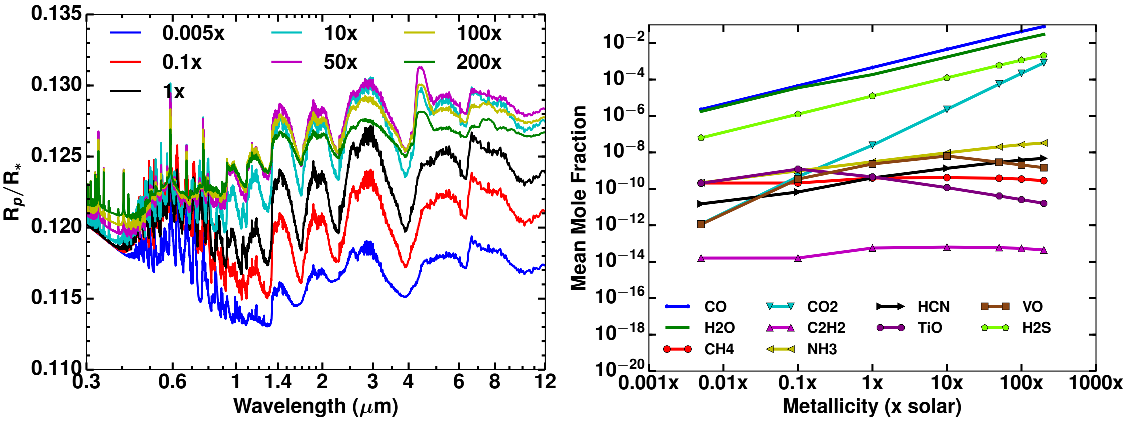

(a) (b)

Figure 3.20: **(a)** Figure showing WASP-17b transmission spectra for a range of metallicity (times solar), similar to Figure 3.19a, with major molecular features shown at highest metallicity (200x). **(b)** Figure showing change in mean chemical abundances between 0.1 and 100 millibar for various molecules, with change in metallicity for WASP-17b, similar to Figure 3.19b.

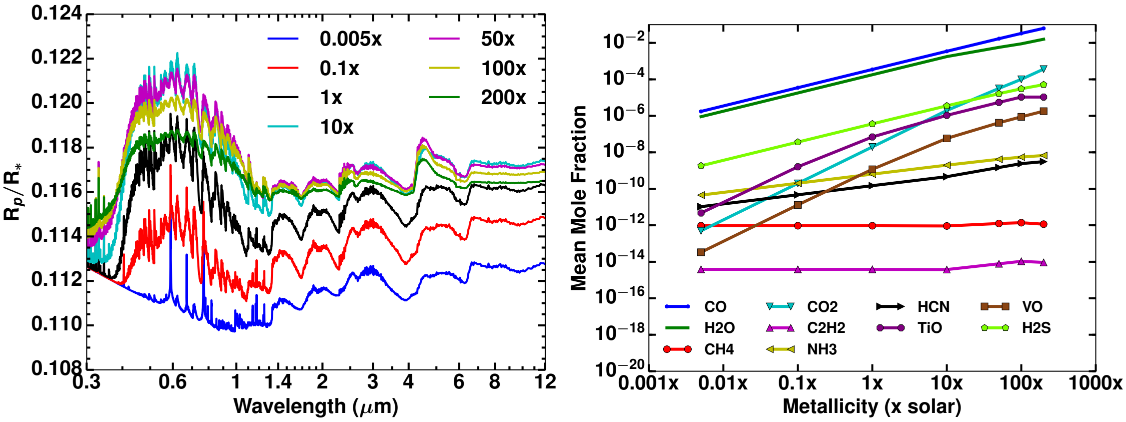

(a)

(b)

Figure 3.21: **(a)** Figure showing WASP-12b transmission spectra for a range of metallicity (times solar), similar to Figure 3.19a. **(b)** Figure showing change in mean chemical abundances between 0.1 and 100 millibar for various molecules, with change in metallicity for WASP-12b, similar to Figure 3.19b.

in the features at 50 times solar metallicity. This can be attributed to a increase in H_2O and CO_2 abundances and a corresponding decrease in CH_4 abundances shown in Figure 3.19b for HAT-P-12b.

For WASP-17b, one of the major effects is the transition from TiO/VO dominated optical spectra to spectra with Na and K features as we go from sub-solar to super-solar metallicities. There is also a substantial change in the spectra for metallicities greater than 10 times solar, primarily due to rapid increase in CO_2 abundances.

Figure 3.21a shows the change in transmission spectra with changes in metallicity for WASP-12b, with equilibrium temperature of 2580 K. At extremely sub-solar metallicity, TiO/VO features are absent, due to their low abundances as seen in Figure 3.21b. This is in complete contrast to effect of metallicity for WASP-17b, indicating how different temperature regimes can result in varying effects of metallicity. However, the strength of TiO/VO spectral features increase with increasing metallicity reaching its peak at solar metallicity, before decreasing again. This decrease in spectral feature size is primarily due to decrease in scale height of the atmosphere as metallicity increases.

3.6.3 Effect of C/O ratio

Figures 3.22a, 3.23a and 3.24a show changes in the transmission spectra resulting from the changes in the C/O ratio for HAT-P-12b, WASP-17b and WASP-12b, respectively. Additionally, the mean chemical abundances are shown in 3.22b, 3.23b and 3.24b, respectively. These simulations are at planetary equilibrium temperature,

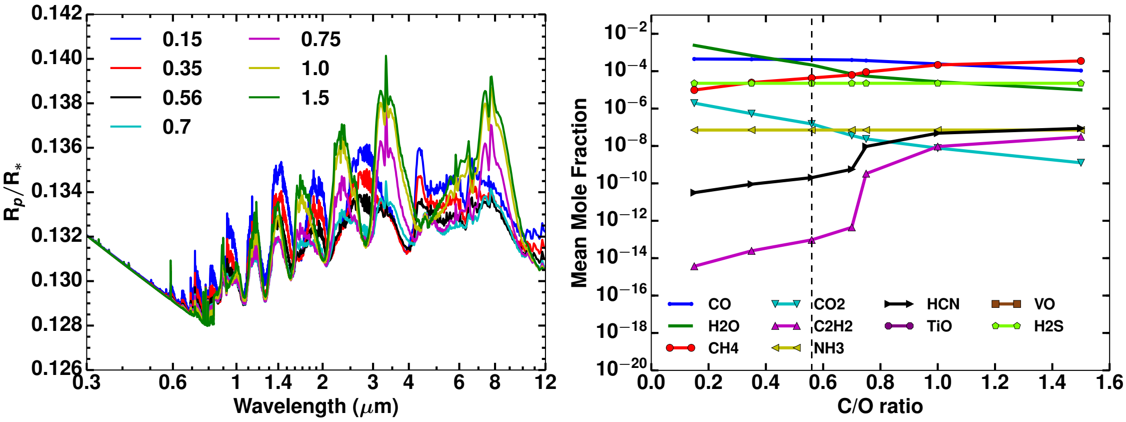

(a) (b)

Figure 3.22: **(a)** Figure showing HAT-P-12b transmission spectra for a range of C/O ratio at its equilibrium temperature, solar metallicity and clear atmosphere. X-axis is wavelength in µm and Y-axis transit radius ratio $(R_\mathrm{p}/R_\star)$. **(b)** Figure showing change in mean chemical abundances between 0.1 and 100 millibar for various molecules, with change in C/O ratio for HAT-P-12b, X-axis is C/O ratio and Y-axis is mean abundances in units of mole fraction. Dashed line indicates solar C/O ratio.

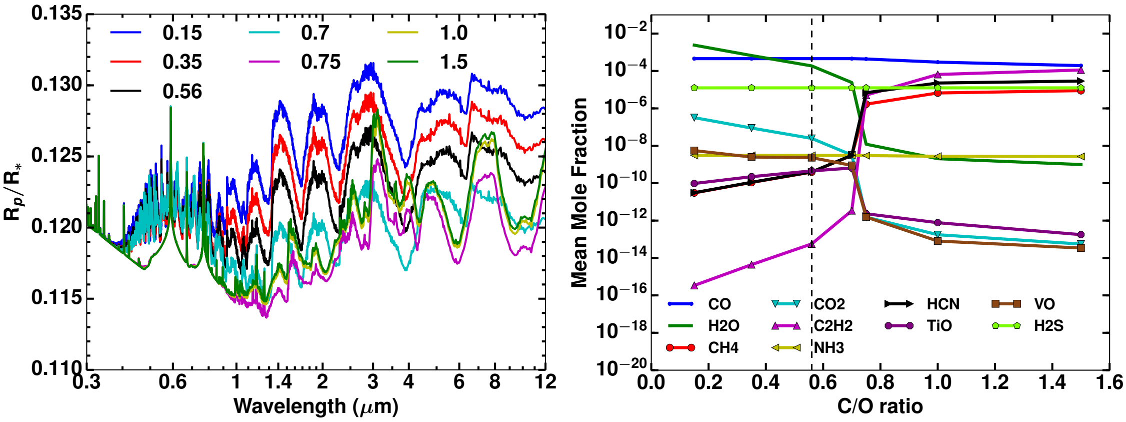

(a) (b)

Figure 3.23: **(a)** Figure showing WASP-17b transmission spectra for a range of C/O ratio, similar to Figure 3.22a. **(b)** Figure showing change in mean chemical abundances between 0.1 and 100 millibar for various molecules, with change in C/O ratio for WASP-17b, similar to Figure 3.22b.

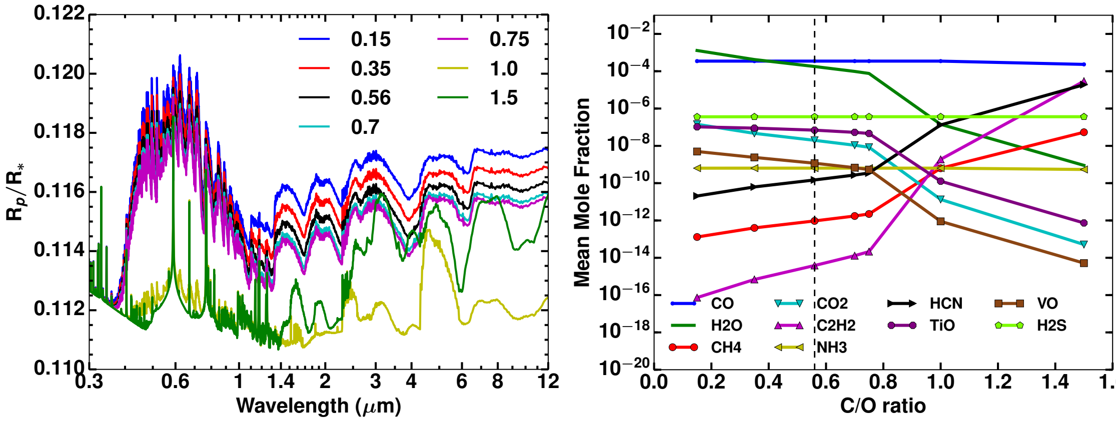

(a) (b)

Figure 3.24: **(a)** Figure showing WASP-12b transmission spectra for a range of C/O ratio, similar to 3.22a. **(b)** Figure showing change in mean chemical abundances between 0.1 and 100 millibar for various molecules, with change in C/O ratio for WASP-12b, similar to Figure 3.22b.

solar metallicity, and do not include any haze or clouds.

For HAT-P-12b, as the C/O ratio increases CH_4 features start dominating over the H_2O features, with C/O ratio of ~0.7 being the transition value, as seen in Figure 3.22a. Interestingly, Figure 3.22b shows that H_2O and CH_4 abundances are almost equal at the C/O ratio of ~0.7 (solar). However, H_2O dominates below ~0.7 and CH_4 above it. Note that for lower C/O ratios, oxygen-bearing species such as CO and CO_2 dominate, but are replaced by other carbon-bearing species such as HCN and C_2H_2 as the C/O ratio increases, thereby changing the spectra drastically.

In the case of WASP-17b, as shown in Figure 3.23a, a transition can again be seen from a H_2O to a CH_4 dominated infrared spectrum as the C/O ratio increases. However, in this case the transition occurs at a higher C/O ratio of ~0.75 (compared to ~0.7 for HAT-P-12b), implying that planets with higher equilibrium temperature have higher transition C/O ratios, in agreement with previous studies (Kopparapu et al. 2012; Madhusudhan 2012; Moses et al. 2013a; Venot et al. 2015; Mollière et al. 2015). Figure 3.23b shows the change in mean abundances with C/O ratio for WASP-17b. Here, the transition from H_2O to CH_4 dominated chemistry occurs at higher C/O ratio compared to HAT-P-12b. It can also be seen that C_2H_2 and HCN abundances slightly increase even more than CH_4 for WASP-17b, for a C/O ratio of 0.75 and higher. This results in a drastic change in transmission spectra, at a C/O ratio of 0.75.

Figure 3.24a shows spectra for WASP-12b at solar metallicity at various C/O ratios with a clear atmosphere. Figure 3.24a demonstrates an evolution in the TiO/VO features with C/O ratio. For a C/O ratio up to ~0.75, TiO/VO features

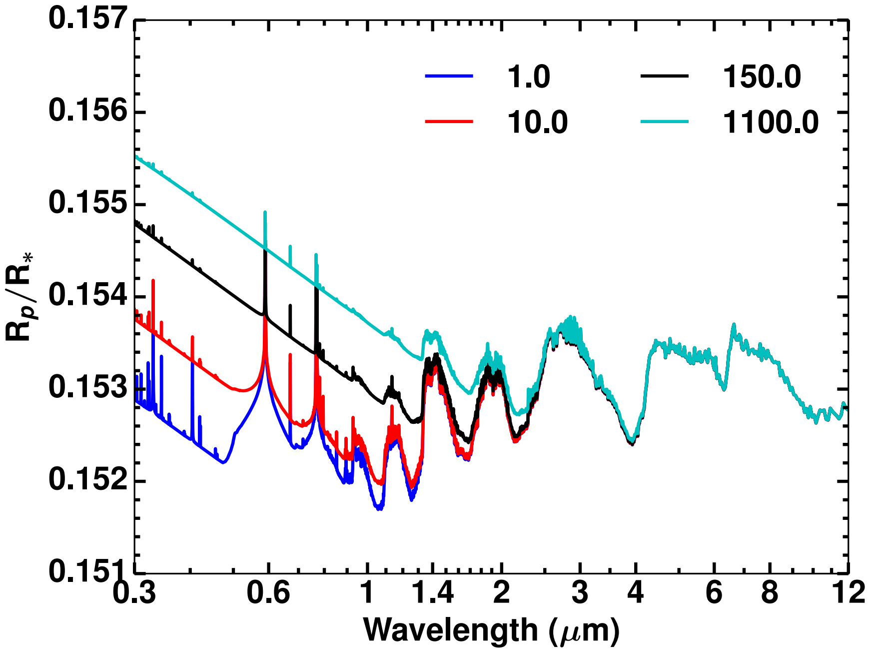

Figure 3.25: Figure showing HD 189733b transmission spectra for a range of haze enhancement factor at its equilibrium temperature, solar C/O ratio, solar metallicity and no clouds. X-axis is wavelength in µm and Y-axis transit radius ratio ($R_\mathrm{p}/R_\star$).

are dominant but decline thereafter, becoming almost absent by a C/O ratio of 1 and completely absent by 1.5. This is caused by the depletion of oxygen, and subsequent depletion of TiO/VO, as shown in Figure 3.24b. As found for cooler planets there is a clear transition in the spectra with C/O ratio, as shown in Figure 3.24b. However, this transition occurs at a higher C/O ratio, ∼1-1.4, compared to that found in lower temperature planets (e.g., HAT-P-12b at a C/O ratio of ∼0.7). Furthermore, the transition in cooler planets is simply between a H_2O and CH_4 dominated infrared spectrum, whereas in this hotter case HCN and C_2H_2 also become more abundant, and therefore spectrally important alongside CH_4 at higher C/O ratios. Therefore, HCN may well be detectable using the NIRSPEC G395 grism onboard JWST, which could also aid constraining planetary atmospheric C/O ratio. We also performed additional tests adopting radiative-convective equilibrium P-T profiles for some planets, to explore whether our conclusions relating to the C/O transition values are robust, and find they remain unchanged, in agreement with previous works (Kopparapu et al. 2012; Madhusudhan 2012; Moses et al. 2013a; Venot et al. 2015; Mollière et al. 2015).

3.6.4 Effect of Haze and Clouds

Haze can be an important source of scattering in planetary atmospheres. Figure 3.25 shows the effect of our haze treatment on the transmission spectra of HD 189733b.

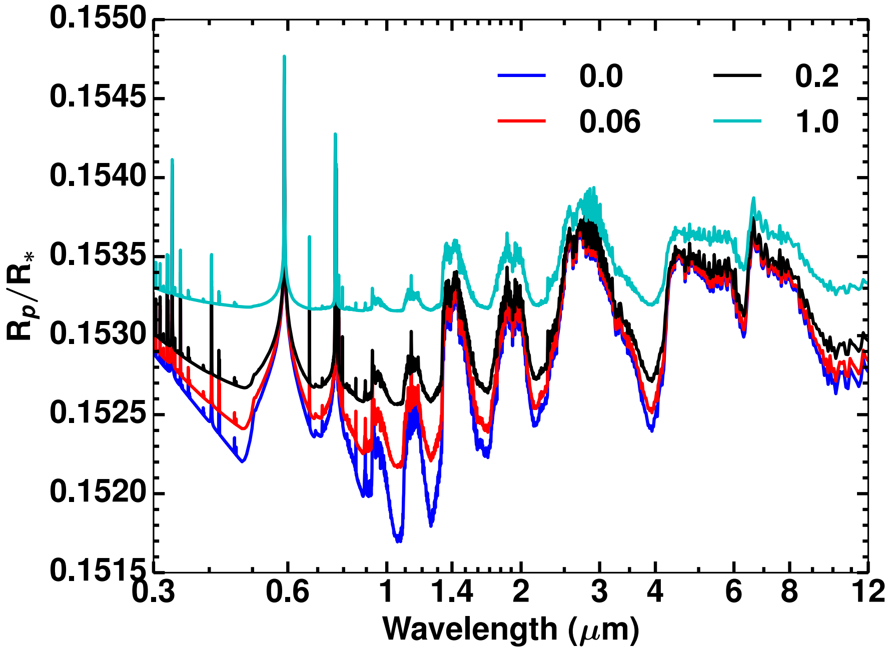

Figure 3.26: Figure showing HD 189733b transmission spectra for a range of grey cloud enhancement factor at its equilibrium temperature, solar C/O ratio, solar metallicity and no haze. X-axis is wavelength in µm and Y-axis transit radius ratio ($R_\mathrm{p}/R_\star$).

It shows that as the amount of haze is increased in the atmosphere there is an increase in the amplitude of Rayleigh scattering slope and tendency to mute features, especially at very high values of haze enhancement factor. Haze pre-dominantly effects the optical part of the spectrum due to its scattering nature.

Figure 3.26 shows the effect of our cloud treatment on the transmission spectra of HD 189733b. An increase in cloud strength (α_haze) from 0 which indicates no clouds, to 1 which corresponds to grey scattering opacity of $2.5 \times 10^{-3}\mathrm{cm}^2/\mathrm{g}$ (explained in detail in Section 3.3.2), increasingly mutes the absorption features at all wavelengths in the transmission spectra. Essentially, increasing cloud cover tends to flatten the spectra. However, interestingly for very hot planets like WASP-12b, the TiO/VO features are so large that even the maximum cloud strength in our parameter space is not able to mute them completely. We note that our model simulations can be used to produce a spectrum that represents patchy clouds using a linear combination of clear and cloudy models (e.g Line et al. 2016).

3.7 Interpretation of Observations

In this section we interpret the observations of ten hot Jupiter exoplanets from Sing et al. (2016), using model spectra from our grid. The best fitting planetary characteristics are determined for each planet, using transmission spectra in chemical

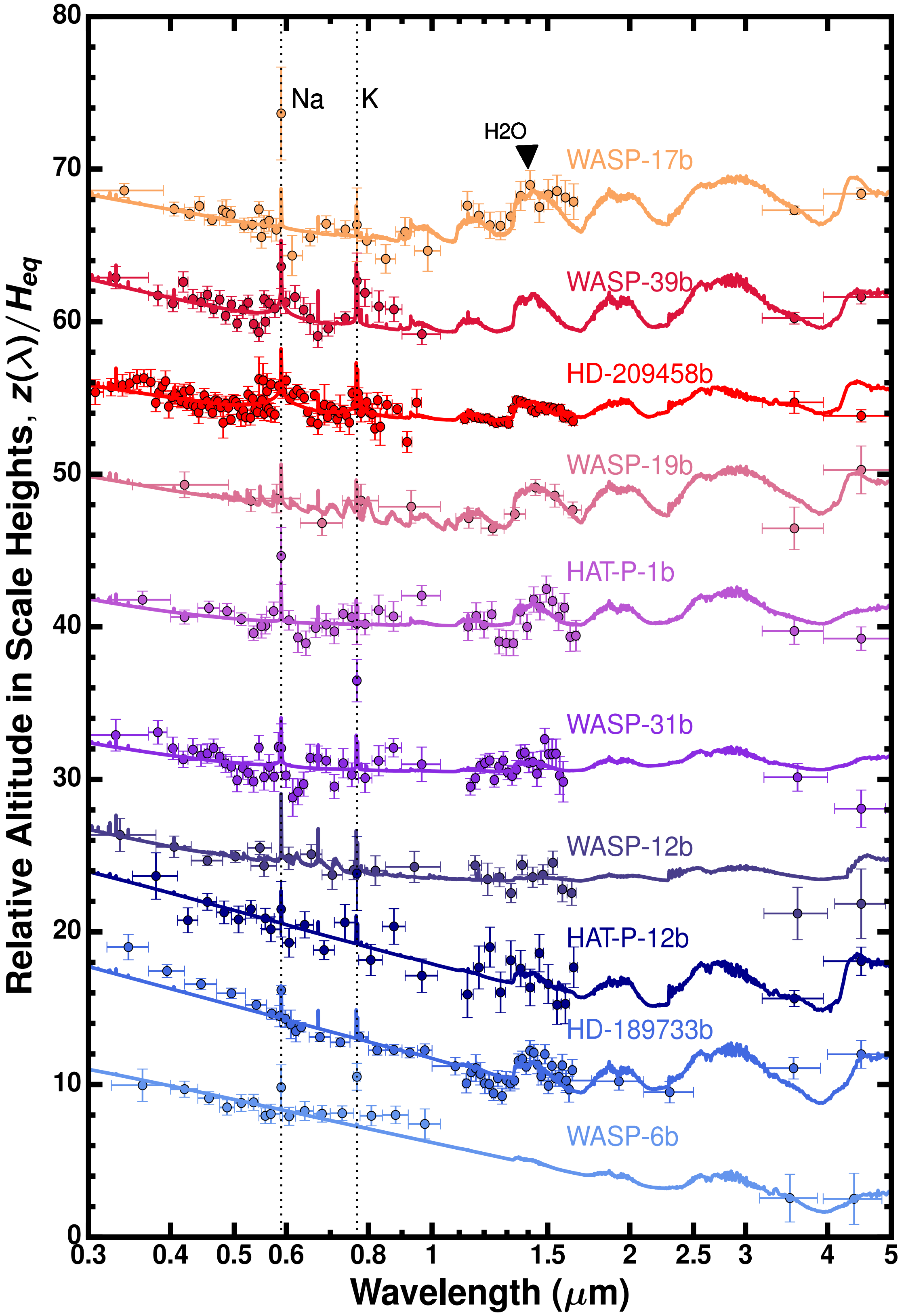

Figure 3.27: Figure showing the ATMO forward model grid with rainout condensation applied to observations of 10 exoplanets from Sing et al. (2016). The Y-axis shows relative altitude in scale height. Solid lines show best fit forward models and filled circular markers show HST observations with error-bars. Planet names are placed above their respective spectra. Dashed lines indicate expected Na and K features. Comparatively clear atmospheres at the top have strong H_2O and alkali features. The strength of these features decreases from top to bottom as planets become more hazy and cloudy.

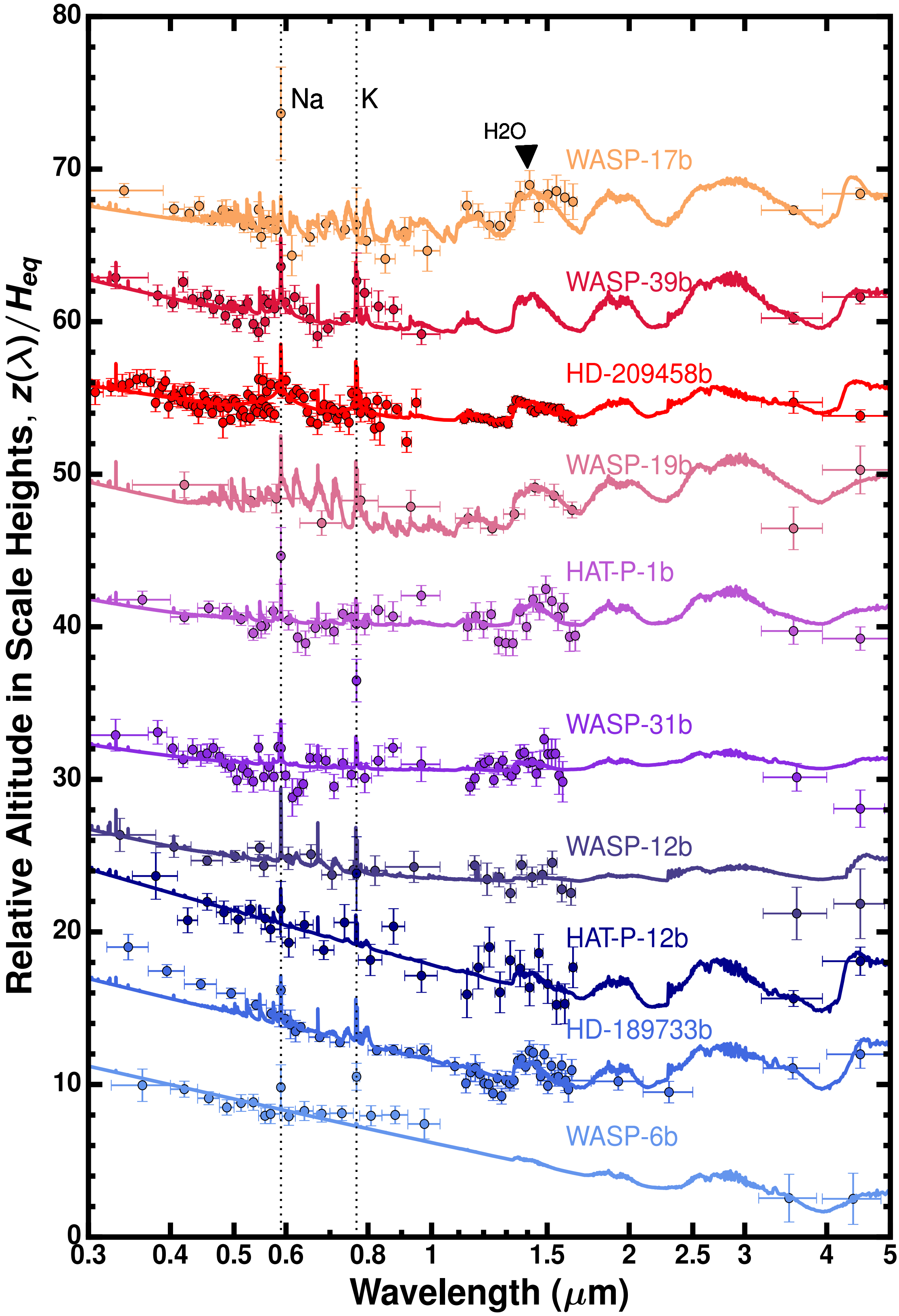

Figure 3.28: Figure showing the ATMO forward model grid with local condensation applied to observations of 10 exoplanets from Sing et al. (2016). The Y-axis shows relative altitude in scale height. Solid lines show best fit forward models and filled circular markers show HST observations with error-bars. Planet names are placed above their respective spectra. Dashed lines indicate expected Na and K features. Comparatively clear atmospheres at the top have strong H_2O and alkali features. The strength of these features decreases from top to bottom as planets become more hazy and cloudy.

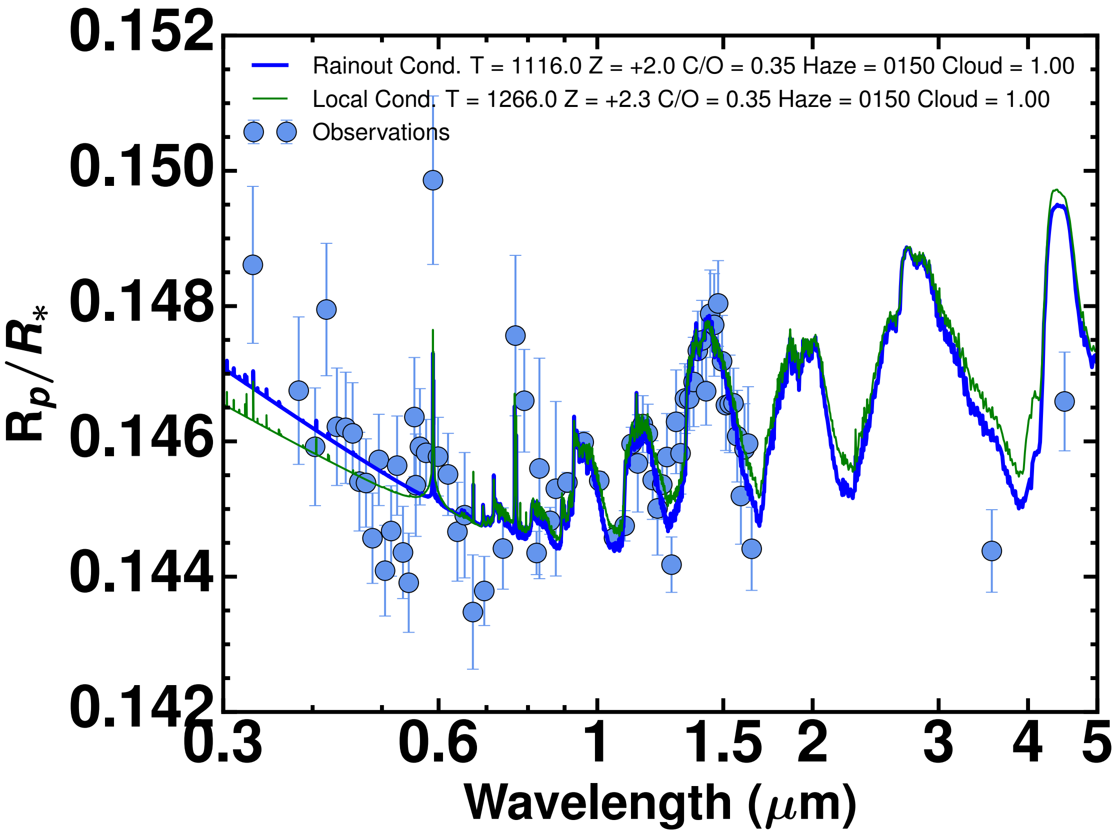

Figure 3.29: WASP-39b data from Wakeford et al. (2017) fitted to local and rainout condensation grid from Goyal et al. (2018).

Planet	T_{eq} (K)	$T_{bestfit}$ (K)	Metallicity (x solar)	C/O	Haze (α_{haze})	Cloud (α_{cloud})	χ^2	DOF	Reduced χ^2	Data Source
WASP-17b	1755	1605	10	0.35	150	1.0	32.44	38	0.853	Sing et al. (2016)
WASP-39b	1116	1266	1	0.56	10	0.2	40.18	34	1.181	Fischer et al. (2016) and Sing et al. (2016)
HD-209458b	1459	1159	1.0	0.7	10	0.2	210.47	123	1.711	Sing et al. (2016)
WASP-19b	2077	1777	10	0.56	150	0	7.79	13	0.60	Huitson et al. (2013) and Sing et al. (2016)
HAT-P-1b	1322	1322	0.1	0.15	10	1.0	49.37	41	1.2	Wakeford et al. (2013) and Nikolov et al. (2014)
WASP-31b	1575	1425	0.005	0.35	1	0.06	82.89	60	1.38	Sing et al. (2015) and Sing et al. (2016)
WASP-12b	2580	2880	0.1	0.56	150	1	21.35	23	0.928	Sing et al. (2013) and Sing et al. (2016)
HAT-P-12b	960	1260	10	0.7	1100	0.2	27.25	30	0.908	Sing et al. (2016)
HD-189733b	1191	1491	0.1	0.56	150	0	85.88	52	1.65	Pont et al. (2013), McCullough et al. (2014), and Sing et al. (2016)
WASP-6b	1184	1184	0.005	0.15	1100	0	29.1	18	1.616	Nikolov et al. (2015) and Sing et al. (2016)
WASP-96b	1285	1585	0.1	0.7	1	0	47.44	48	0.99	Nikolov et al. (2018)
WASP-121b	2358	2208	100	0.35	1	0.2	116.18	74	1.57	Evans et al. (2018)

Table 3.4: Table showing best fit planetary characteristics for all the observed exoplanets from Sing et al. (2016) with rainout condensation chemistry. The C/O ratio of 0.56 is solar value. The haze enhancement factor is with respect to gaseous Rayleigh scattering. The grey cloudiness factor is with respect to H_2 scattering cross-section at 350 nm. DOF refers to degrees of freedom applied to best fit.

Planet	T_{eq} (K)	$T_{bestfit}$ (K)	Metallicity (x solar)	C/O	Haze (α_{haze})	Cloud (α_{cloud})	χ^2	DOF	Reduced χ^2	Data Source
WASP-17b	1755	1455	10	0.15	150	0.06	50.24	38	1.322	Sing et al. (2016)
WASP-39b	1116	1266	1	0.56	10	0.2	39.42	34	1.16	Fischer et al. (2016) and Sing et al. (2016)
HD-209458b	1459	1159	10	0.7	10	0.2	211.1	123	1.72	Sing et al. (2016)
WASP-19b	2077	2227	0.005	0.15	1.0	0	13.51	13	1.039	Huitson et al. (2013) and Sing et al. (2016)
HAT-P-1b	1322	1322	0.1	0.15	10	1.0	49.81	41	1.214	Wakeford et al. (2013) and Nikolov et al. (2014)
WASP-31b	1575	1275	0.005	0.35	1	0.06	85.16	60	1.42	Sing et al. (2015) and Sing et al. (2016)
WASP-12b	2580	2880	0.1	0.56	150	1	21.48	23	0.934	Sing et al. (2013) and Sing et al. (2016)
HAT-P-12b	960	1260	10	0.7	1100	0.2	27.43	30	0.914	Sing et al. (2016)
HD-189733b	1191	1341	0	0.7	150	0	106.43	52	2.047	Pont et al. (2013), McCullough et al. (2014), and Sing et al. (2016)
WASP-6b	1184	1184	0.005	0.15	1100	0	29.55	18	1.64	Nikolov et al. (2015) and Sing et al. (2016)
WASP-96b	1285	1435	0	1.5	1	0	45.15	48	0.94	Nikolov et al. (2018)
WASP-121b	2358	2058	0.005	0.15	1	0.2	105.85	74	1.43	Evans et al. (2018)

Table 3.5: Table showing best fit planetary characteristics for all the observed exoplanets from Sing et al. (2016) with local condensation chemistry. The C/O ratio of 0.56 is solar value. The haze enhancement factor is with respect to gaseous Rayleigh scattering. The grey cloudiness factor is with respect to H_2 scattering cross-section at 350 nm. DOF refers to degrees of freedom applied to best fit.

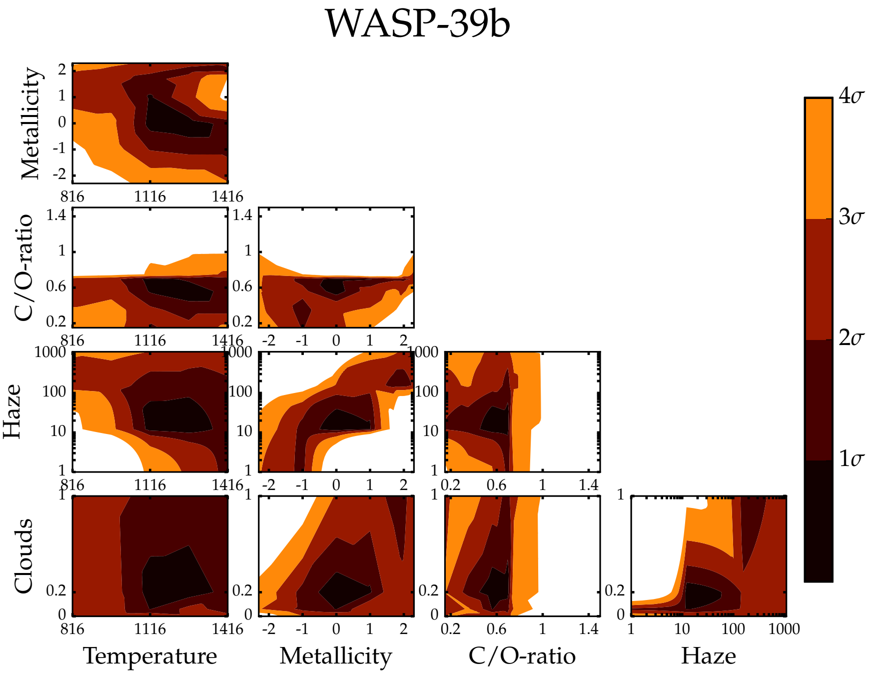

Figure 3.30: Figure showing χ^2 map for WASP-39b using data from Sing et al. (2016). Contours of χ^2 are shown for all the combinations of grid parameters. Axis for cloud and haze factors are log-scaled. Metallicity is also log-scaled, 0 being solar metallicity and 2 being 100 times solar metallicity. Colours indicate confidence intervals as shown in colormap to the right.

equilibrium and the standard technique of χ^2 minimisation, where the only free parameter is a vertical offset between the data and model. We have also compared our physical interpretations with previous studies. Degrees of Freedom (DOF) is equal to number of data points minus 1, due to free vertical offset (R_p/R_*) parameter.

Figure 3.27 shows the best fitting model spectra with observations for all the planets, using the rainout condensation approach and the Figure 3.28 shows a similar plot, but adopting the local condensation approach. These figures can be directly compared to Figure 1 of Sing et al. (2016). However, in this thesis the best fit transmission spectra come from a homogenous set of forward models from our grid, compared to a combination of different models shown in Sing et al. (2016). The best fitting planetary characteristics along with their χ^2 values are shown in Table 3.4. We also present the χ^2 maps (Madhusudhan et al. 2009), to demonstrate how the physical parameters are constrained for each planet, in Figure 3.30 for WASP-39b and in Figures A.1a to A.5a in Appendix A.1 for all the other planets. For this, χ^2 is computed for each model simulation. Then we fix values of a pair of parameters whilst allowing all others to be free. This is repeated for all pair combinations and all the possible combinations of grid parameters. The resulting χ^2 space is mapped along with confidence intervals, which are obtained under the assumption of a χ^2 distribution with two degrees of freedom, since there are two unconstrained variables for each plot on the map.

3.7.1 WASP-17b

The best fit WASP-17b forward model (topmost) in Figure 3.27 shows that the data are consistent with 10 times solar metallicity and sub-solar C/O ratios as shown in Table 3.4. The best fitting model gives a reduced chi square value of 0.85 which can be considered to be an excellent fit for a purely forward model. It also shows signature of haze due to Rayleigh scattering of the order of $\alpha_{\text{cloud}} = 150$. The data are also consistent with cloudiness factor of $\alpha_{\text{cloud}} = 1$. However, the Na feature in our best fit model is not as strong as in the observations. The reason for this is unclear and retrieval models are also not able to explain this strong feature as shown in Barstow et al. (2017). The χ^2 map for WASP-17b is shown in Figure A.1a in Appendix A.1. It shows that the data are consistent with the lowest possible C/O ratio in our parameter space. Therefore, current observations do not show clear features indicative of carbon bearing species. This finding was also one of the initial motivations to expand our parameter space to C/O ratio as low as 0.15. The best fit model also shows that H_2O features dominate the infrared spectra.

With the local condensation approach the best fit temperature is lower at 1455 K along with lower cloudiness factor. Even the fit is not as good as the rainout approach and the primary reason for this are the small TiO/VO features in the spectra, which arise at this temperature only for the case of adopting the local condensation approach.

3.7.2 WASP-39b

For WASP-39b shown in Figure 3.27, the data are consistent with $\alpha_{\mathrm{haze}} = 10$ and $\alpha_{\mathrm{cloud}} = 0.2$ with solar metallicity and solar C/O ratio. The data for this planet shows one of the clearest atmosphere of the set as concluded by Fischer et al. (2016), but our results also show weak haziness and cloudiness. Figure 3.30 shows the χ^2 map for WASP-39b, revealing that except the temperature all other values are very well constrained for this planet. The 1σ credible range for the temperature of the planet is higher than the upper limit of our parameter space. The metallicity of the planet is well constrained between solar and slightly sub-solar values, while the C/O ratio is well constrained near a solar C/O ratio. The data are also consistent with the presence of Na and K, albeit at a low significance.

In Wakeford et al. (2017) the observational data for WASP-39b was improved substantially by three more transit observations, using the Hubble WFC3 instrument. Therefore, we reinterpreted the spectra with both the approaches rainout and local condensation as shown in Figure 3.29. The best fit models give a reduced χ^2 value of 1.56 and 1.57 for rainout and local condensation case, respectively, with 69 DOF. The updated data is consistent with super-solar metallicity but with extremely low C/O ratio for both the condensation approaches, which is a direct result of detection (addition) of two more water features in the new dataset. These three water features help in placing a precise constraint on the water abundances (Wakeford et al. 2017) and therefore also favours a low C/O ratio, due to absence of features of any carbon bearing molecules. The best fit model also shows substantial amount of haziness and cloudiness for this planet. We also note that the fit in the original paper (Wakeford et al. 2017) is different from the fit presented here, because of the presence of the rainout bug in the earlier version of ATMO.

3.7.3 HD 209458b

HD 209458b is the best observationally constrained planet in our sample. We find that the data are consistent with solar metallicity and a combination of Rayleigh haze and grey clouds, with muted H_2O, Na and K features. However, a rise in the $R_{\mathrm{p}}/R_{\star}$ values between 0.3 and 0.4 µm in the Rayleigh slope part of the spectrum is still not explained by the model. This may be due to thermospheric effects or missing opacity. The χ^2 map of HD 209458b is shown in Figure A.1b in Appendix A.1. It demonstrates that the best fit values of HD 209458b are very well constrained with 4σ confidence. This is mainly due to the high wavelength resolution in observations compared to any other planet. However, it is interesting to see that some of the parameters like metallicity have a bi-modal structure in the maps. Therefore, although observations are consistent with a 10 times solar metallicity model, a 0.1 times solar metallicity model can also explain the observations, with the corresponding decrease in haziness, cloudiness and temperature. With the local condensation approach, data is consistent with a slightly super-solar metallicity. The data is also consistent with a C/O ratio of 0.7 using both the approaches, hinting at the features of carbon bearing species in the spectra.

3.7.4 WASP-19b

WASP-19b is the planet with least observational data points, posing a challenge to accurately constrain its characteristics. This can be seen in the χ^2 map plot for WASP-19b in Figure A.2a in Appendix A.1. Temperature, clouds and haze are the least constrained, while the C/O ratio is constrained to values less than solar, and metallicity between 0.1 to 1 times solar, considering 1σ confidence intervals. However, data are consistent with 10 times solar metallicity and solar C/O ratio with haze, but no grey clouds. The H_2O feature is clearly visible in the model and observations, muted by haze, all in agreement with Huitson et al. (2013). The best fit forward model also suggests a weak narrow Na feature for WASP-19b, which has not been detected in the observations due to lack of sufficient data points. TiO/VO features can also be seen as expected at these temperatures but muted by haze.

3.7.5 HAT-P-1b

The HAT-P-1b data are consistent with 0.1 times solar metallicity, sub-solar C/O ratio of 0.15, $\alpha_{\text{haze}} = 10$ and substantial grey cloudiness factor of $\alpha_{\text{cloud}} = 1$. They are consistent with H_2O features similar to Wakeford et al. (2013) but are strongly muted, which can be attributed to the extreme cloudiness. One of the most important discrepancies between the data and the model, is that the best fit forward model in chemical equilibrium predicts a very weak, narrow Na feature, compared to a larger feature in the observations implying that it might have enhanced (non-solar or disequilibrium) Na concentration in agreement with Nikolov et al. (2014). The χ^2 map for HAT-P-1b is shown in Figure A.2b in Appendix A.1. It demonstrates that similar to WASP-17b, the HAT-P-1b data are consistent with the lowest considered C/O ratio in our parameter space, i.e. C/O=0.15. Interpreted characteristics of this planet are very similar to that of WASP-17b, but with more cloudiness. The best fit local condensation model is also exactly the same as the rainout condensation model for HAT-P-1b.

3.7.6 WASP-31b

The WASP-31b data are consistent with a 0.005 times solar metallicity and the C/O ratio of 0.35 with no enhanced Rayleigh scattering, but a grey cloud enhancement factor $\alpha_{\text{cloud}} = 0.06$. One of the important discrepancies between the data and the model, is that the observations suggest a possible K feature without any Na feature, which none of the forward models in our parameter space for this planet are able to reproduce. Na and K have very similar condensation curves so they are both expected in the spectrum in chemical equilibrium conditions (see 3.7.8 for the exception). Sing et al. (2015) interpreted a strong haze and cloud deck with K feature, but our best fit forward model in chemical equilibrium suggests a more clear atmosphere, with a very weak K feature and extremely sub-solar metallicity. This discrepancy points towards a sub-solar Na/K abundance in agreement with Sing et al. (2015). It also highlights the degeneracy existing between the effect of metallicity and clouds/haze on spectral features and can be seen in χ^2 map for WASP-31b in Figure A.3a.

3.7.7 WASP-12b

WASP-12b has the highest equilibrium temperature among our observed targets. Madhusudhan et al. (2011) concluded a high C/O ratio and weak thermal inversion for this planet based on Spitzer infrared measurements. However, HST WFC3 optical observations from Sing et al. (2016) show a completely flat spectra with just a Rayleigh scattering slope. The data from Sing et al. (2016) are consistent with an extremely hazy and cloudy atmosphere. They show evidence for aerosols and small TiO/VO features in the model. The best fit values reach the upper edge of our parameter space for clouds ($\alpha_{cloud=1}$) along with haziness factor of $\alpha_{\text{haze}} = 150$, sub-solar metallicity and solar C/O ratios. The χ^2 map of WASP-12b is shown in Figure A.3b in Appendix A.1. It shows that many of the parameters are unconstrained, which is mainly due to the feature-less spectrum. At such high temperatures very few chemical species can condense, therefore it can be seen that the rainout and local condensation, both approaches lead to same best fit model. However, Kreidberg et al. (2015) obtained more precise data between 0.8 and 1.6 µm with 6 HST transits along with detection of a H_2O feature. When data from Kreidberg et al. (2015) are used along with the data from Sing et al. (2016), they are consistent with an equilibrium temperature of 2280 K, extremely sub-solar metallicity, C/O ratio of 0.15, haze factor of $\alpha_{\text{haze}} = 10$ and cloud factor of $\alpha_{\text{cloud}} = 0.06$. It is also consistent with the 1.4 µm H_2O feature. Since our best fit model suggests a C/O ratio of 0.15, ruling out carbon-rich spectra, it is in agreement with retrieval results of Kreidberg et al. (2015), within the 1σ uncertainties.

3.7.8 HAT-P-12b

The data for HAT-P-12b are consistent with a strong enhanced Rayleigh scattering, $\alpha_{\rm haze} = 1100$, reaching the upper limit of parameter space, but without any grey clouds. The best-fit model shows evidence for K, but not Na. Interestingly, this particular scenario, where a K feature is present but Na is not, is produced in our model simulations for HAT-P-12b shown in Figure 3.13. However, this scenario is not in agreement with other spectral features, therefore, is not selected as best fit model. However, the temperature required to obtain K features without any Na features lie within 2 σ uncertainties of best fit temperature values. Figure A.4a in Appendix A.1 shows χ^2 map for HAT-P-12b, which also suggests extremely high haziness for this planet is well constrained.

3.7.9 HD 189733b

HD 189733b is the planet with the second highest number of observations of our targets and has one of the strongest enhanced Rayleigh scattering signatures in agreement with Pont et al. (2013). The data shows H_2O and Na feature as found in McCullough et al. (2014) and Sing et al. (2016). They are consistent with $\alpha_{\rm haze} = 150$, solar metallicity and solar C/O ratio, shown in Figure 3.27 and Table 3.4. However, the forward model also predicts a Na feature which is not seen in the observations. The χ^2 maps show that most of the model parameters are well constrained as seen in Figure A.4b in Appendix A.1. Only the temperature of the planet tends to hit the upper edge of our parameter space.

3.7.10 WASP-6b

WASP-6b has very few observations similar to WASP-19b making it very difficult to constrain its physical parameters. There is a strong signature of haze with $\alpha_{\rm haze} = 1100$ also in agreement with Nikolov et al. (2015), but no Na or K signature, tentatively seen in observations. The χ^2 map for WASP-6b in Figure A.5a in Appendix A.1 also do not not show strong constraints on any other parameters except haze.

3.7.11 WASP-96b

WASP-96b is a hot Saturn type exoplanet with the equilibrium temperature of 1285 K. In Nikolov et al. (2018) we detected the deep sodium wings in the atmosphere of an exoplanet (WASP-96b) for the first time as shown in Figure 3.31 and 3.32. Figure 3.31 shows the best fit model for WASP-96b data from Nikolov et al. (2018), using the rainout and local condensation grid. Both the best fit models don't need

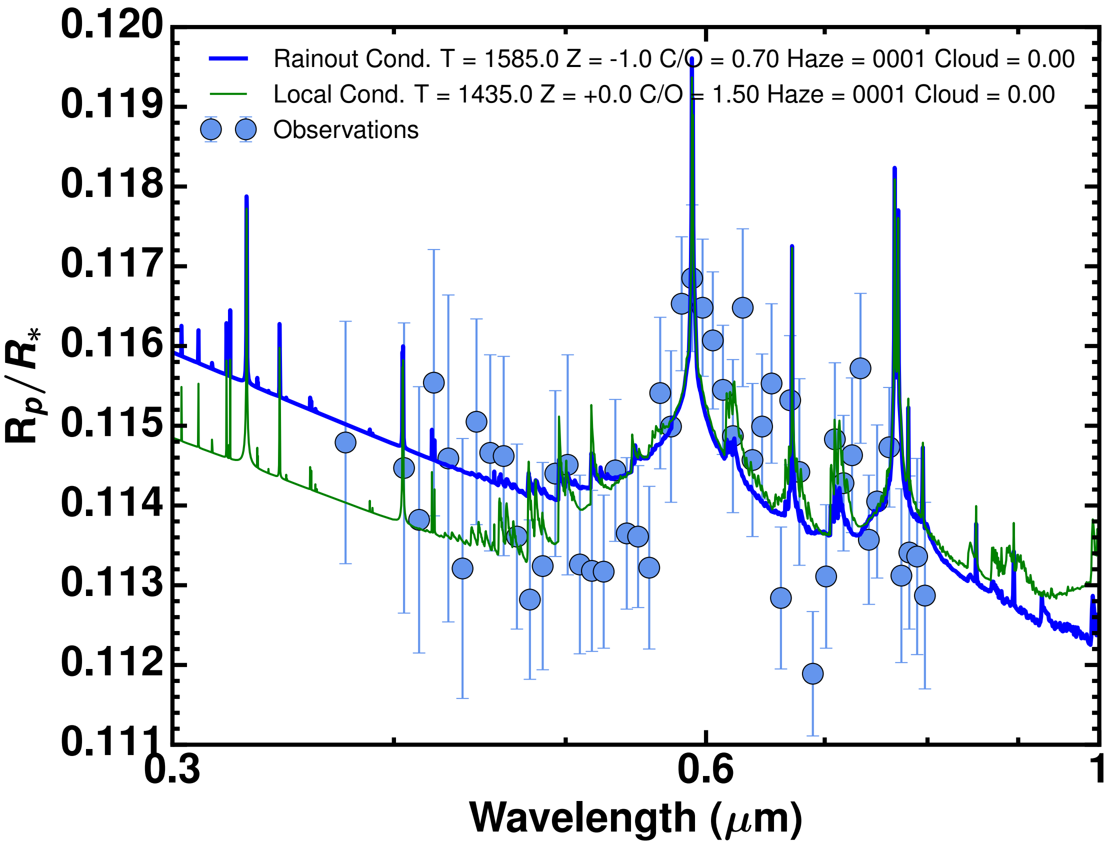

Figure 3.31: WASP-96b data from Nikolov et al. (2018) fitted to local and rainout condensation grid from Goyal et al. (2018).

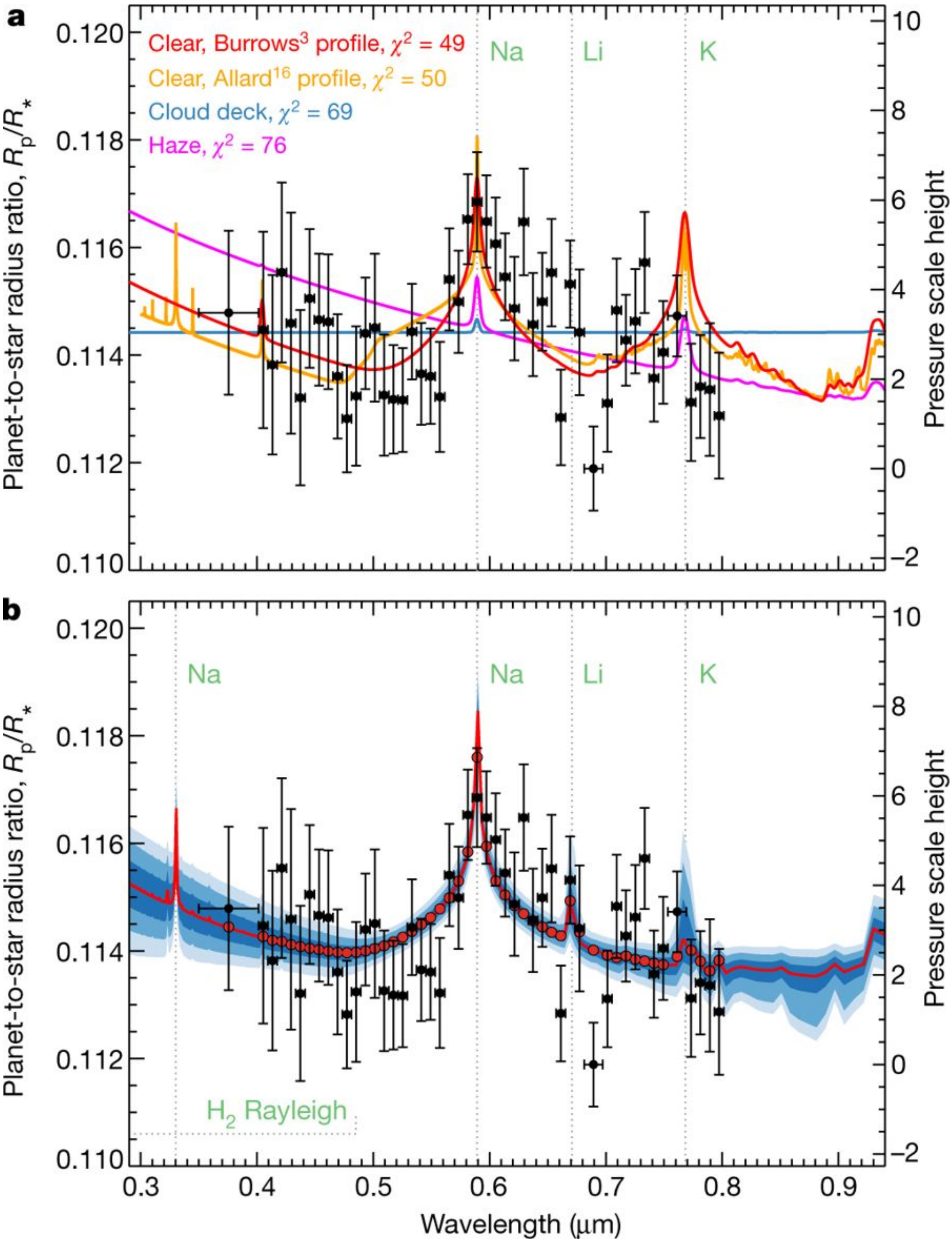

Figure 3.32: (a) Comparison of the FORS2 observations (black dots with 1σ vertical error bars; the horizontal bars indicate spectral bin widths) with clear, cloudy and hazy one-dimensional forward atmospheric models at solar abundance(continuous lines). The two best-fit models assume a clear atmosphere with different line broadening shapes for Na and K. Models with hazes or clouds (magenta and blue) predict much smaller and narrower absorption features (Nikolov et al. 2018). (b) Similar to a, but showing the best-fit model obtained from the retrieval analysis(red line) binned to the data resolution (red dots), with the 1σ, 2σ and 3σ confidence intervals (dark blue to pale blue regions). Both figures are adopted from (Nikolov et al. 2018), Nature.

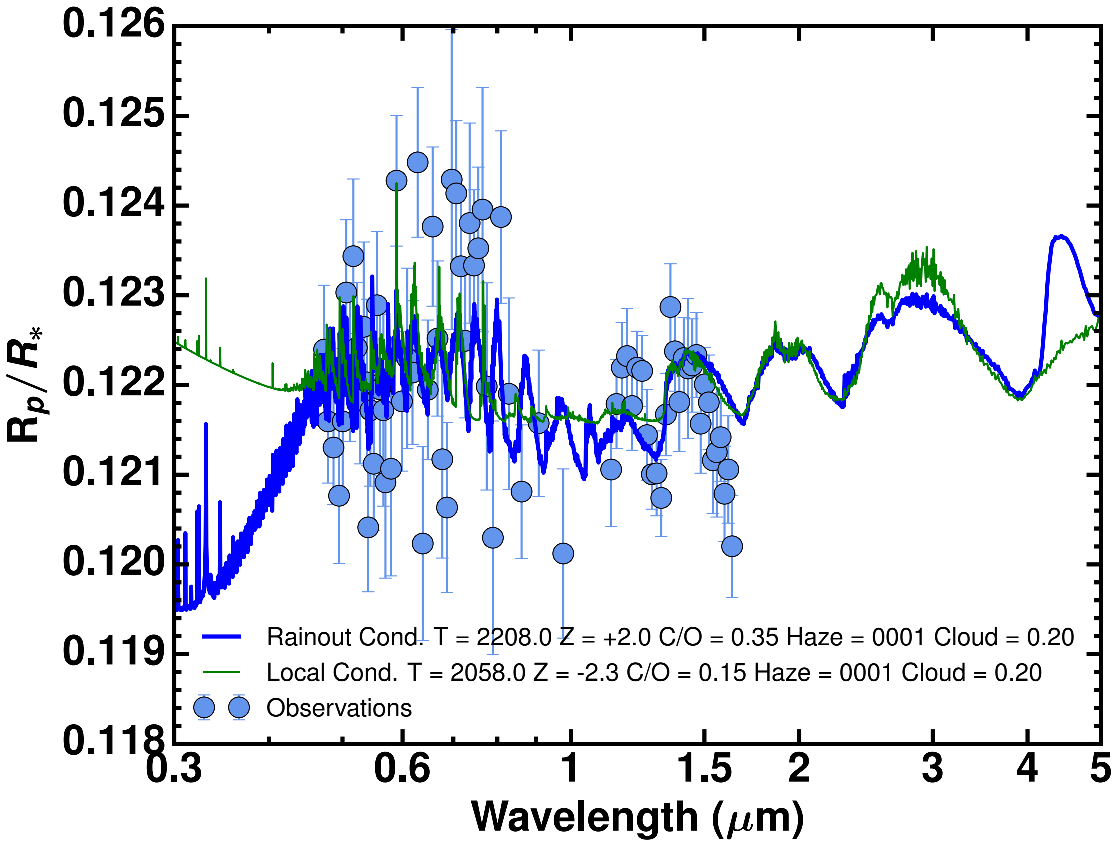

Figure 3.33: WASP-121b data from Evans et al. (2018) fitted to local and rainout condensation grid from Goyal et al. (2018).

any clouds or haze to explain the observations, making the atmosphere of WASP-96b one of the clearest yet seen in transmission spectrum, for an exoplanet. Metallicity is close to solar value. The lack of H_2O as well as features of any carbon bearing species, leaves C/O ratio unconstrained, thus giving drastically different C/O ratios with local and rainout condensation. This observation used the FORS2 instrument on VLT, thus also providing a high resolution spectra compared to space based instruments such as WFC3 onboard HST. The previous observations of other planets revealed only the narrow absorption line cores of Na and K, which could have been obscured by clouds or hazes. However, the clear atmosphere of WASP-96b allows us to probe deeper in the atmosphere (i.e to higher pressures) revealing the absorption line wings of Na for the first time and allowing to place strong constraint on the Na abundances. In this work we also used two different line wing profiles for Na and K, while testing which of the profiles provide a better fit to observations. As seen from Figure 3.32, the Burrows profile (Burrows et al. 2000) just provides a slightly better fit than Allard profile (Allard et al. 2003), indicating that even current observations from VLT FORS2 cannot distinguish between these two line shapes.

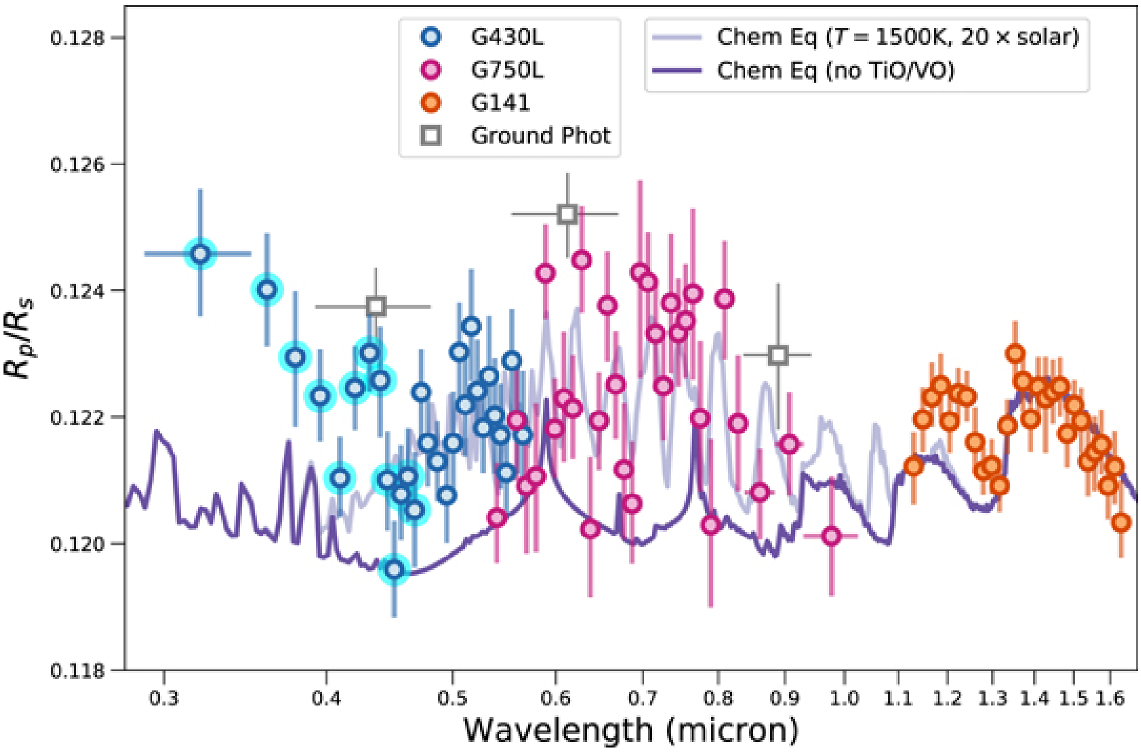

Figure 3.34: Transmission spectrum for WASP-121b from Evans et al. (2018). Two forward models assuming chemical equilibrium are shown, both with a temperature of 1500 K and 20Œsolar metallicity. One model includes TiO/VO opacity (light purple line) and the other does not include TiO/VO opacity (dark purple line). Figure adopted from Evans et al. (2018), AJ.

3.7.12 WASP-121b

WASP-121b is a extremely irradiated hot Jupiter with the dayside equilibrium temperature of about 2358 K. This is also the first planet with strong evidence of an inversion layer (Evans et al. 2017). At first the library of models developed in Goyal et al. (2018) was used to interpret the transmission spectra observations of WASP-121b from Evans et al. (2018). However, we have excluded the data short-ward of 0.47 μm while performing the fitting, since the steep slope in this region is not explained by Rayleigh scattering and is potentially due to SH molecule (Evans et al. 2018), currently not included in the ATMO modelFigure 3.33 shows the best fit local condensation and rainout condensation model, from the library of models for WASP-121b. The best fit models give a reduced χ^2 value of 1.57 and 1.43 for rainout and local condensation case, respectively, with 74 DOF. Both models show TiO/VO features in the optical along with 1.4 µm H_2O feature and have sub-solar C/O ratios. However, they both differ substantially in the metallicity, haze and cloud values, which highlights a strong degeneracy between these three parameters when interpreting observations. In Goyal et al. (2018) we restricted the isothermal temperature for the models to $T_{eq} = \pm 300$ K for both, local and rainout condensation cases. However, as discussed in Chapter 4 the TiO/VO features can become prominent in the spectra at substantially different temperatures for local and rainout condensation approaches. Moreover, only VO can become prominent in the certain temperature range (see Section 4.3.4 in Chapter 4 for details). Therefore, in Evans et al. (2018) we interpreted the transmission spectra observations of WASP-121b as shown in Figure 3.34, without anchoring the temperatures to equilibrium temperatures for the local condensation case. We developed a small grid of aerosol-free atmosphere models across a range of temperature and metallicity, assuming isothermal P-T profiles and chemical equilibrium abundances, similar to (Goyal et al. 2019b). This grid consisted of models with temperatures ranging from 1000 K to 2700 K with increments of 100 K, each computed for metallicities of 0.1x, 1x, 10x, 20x, 30x, 40x and 50x solar. The opacities used in this model simulation was similar to those used in (Goyal et al. 2019b) plus the Iron (Fe) opacity. The model setup was similar to that used in (Goyal et al. 2019b). However, only local condensation was used to compute chemical abundances, where the abundances on each level are independent of the other levels and just dependant on the pressure and temperature on that level. Apart from a uniform vertical offset, no other correction was applied to the model while comparing with observations. However, the data short-ward of 0.47 µm was not used while interpreting observations in Evans et al. (2018) with ATMO forward model grid due to large slope in this region possibly due to SH (see Evans et al. (2018) for details), currently not included in ATMO.

The model with 1500 K and 20x solar metallicity ((light purple line)) is the best fit model as shown in Figure 3.33 with reduced χ^2 of 1 for 69 degrees of freedom. However, models with 10x and 20x solar metallicity at 1500 K also provide a good fit to the observed spectra. The model without TiO/VO opacity (dark purple line) is also shown in the figure, clearly showing the importance of these opacities to explain the current observations. Figure 3.34 shows the best fit model decoupled into different opacities and their corresponding mixing ratios in the left panel. Apart from H_2-H_2 and H_2-He collision induced absorption (CIA), and Rayleigh scattering opacity (not shown in the plot), the dominant molecular opacities are Na and VO in the optical and H_2O in the near infrared wavelengths. Surprisingly, TiO opacities are not as dominant as the VO opacities even though the solar elemental abundance of Ti is about an order greater than that of V (Asplund et al. 2009). This is because at 1500 K a large amount of Ti is condensed in Ti_3O_5(s) as compared to V in V_2O_3, thus leading to more VO in gas phase as compared to TiO. Therefore. VO dominates the spectrum (see Goyal et al. 2019b, for more details).

It can however be noticed that the best fit forward model is not able to explain the observations short-ward of 0.47 µm and the bump between 1.15-1.3 µm. The observations short-ward of 0.47 µm have been speculated to be due to SH absorption, currently missing in our models due to uncertainty in the electronic transitions of SH molecule (Zahnle et al. 2009). The bump between 1.15-1.3 µm can either be explained by VO or FeH opacity. However, the abundance of FeH required to produce this bump is 5 orders of magnitude larger than 20x solar metallicity model, as obtained using retrieval analysis (not in chemical equilibrium) in Evans et al. (2018), which is considered implausible. The other candidate is VO but this requires increasing the abundance which is incompatible with the optical spectrum in the retrieval analysis. Thus, this bump between 1.15-1.3 µm still remains a mystery.

3.8 Simulating JWST observations using the library

The James Webb Space Telescope (JWST) is an infrared space telescope with a 6.5-metre primary mirror scheduled for launch in 2021. The high sensitivity of JWST and its suite of instruments (NIRCam, NIRSpec, NIRISS and MIRI) spanning 0.6-28.3 µm provide the potential to revolutionise our understanding of the atmospheres of extrasolar transiting planets. In preparation for its launch Batalha et al. (2017) have developed a noise simulator, called `PandExo`[6], which creates observation simulations of all observatory-supported time-series spectroscopy modes.

We present `PandExo` simulations of the transmission spectra of WASP-17b for the NIRISS SOSS, NIRSpec G395H and MIRI LRS modes shown in Figure 3.35 using

---

[6] http://pandexo.science.psu.edu:1111/#

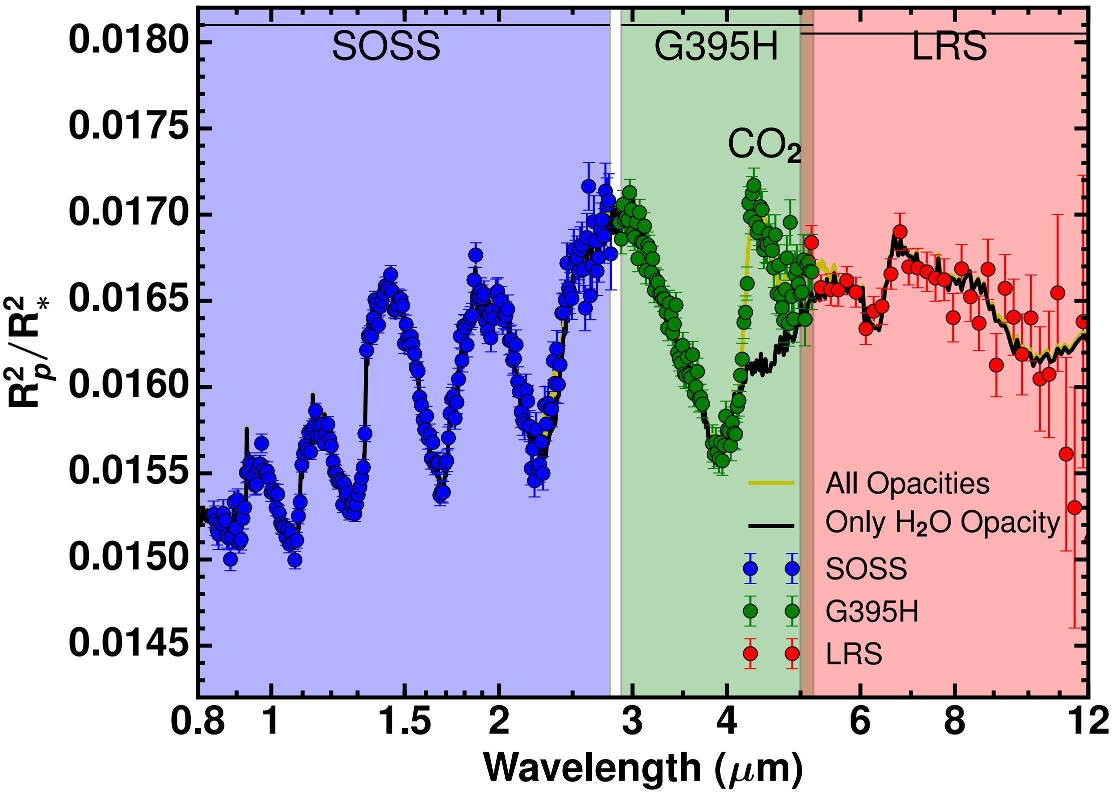

Figure 3.35: Figure showing ATMO best fit model transmission spectrum (transit depth) for WASP-17b simulated with `PandExo` for JWST observations. Model spectrum with all opacities is shown in yellow, which for most of the spectrum is hidden behind only H_2O opacity spectrum shown in black. CO_2 (carbon dioxide) feature is marked. Shaded regions and corresponding coloured markers indicate different JWST instrument modes, red indicates NIRISS SOSS mode, blue indicates NIRSpec G395H mode and green indicates MIRI LRS mode. X-axis is wavelength in µm and Y-axis transit depth ($R_\mathrm{p}^2/R_\star^2$).

the `ATMO` model simulation which best-fits the current HST data shown in Figure 3.27 and best fit values given in Table 3.4. We also over-plotted this simulation with only H_2O opacity model spectrum, which shows H_2O features explain the spectrum almost completely. Interestingly, between 4 and 6 µm, the model spectrum created by only the H_2O opacity deviates from that generated when including all the opacity sources, which we find is due to CO features, even though this spectrum is for a very low C/O ratio of 0.15. This highlights the capability of JWST to detect CO in exoplanet atmospheres and also possibly constrain their C/O ratio.

The `PandExo` simulation in Figure 3.35 was performed for a single occultation with an equal fraction of in to out of transit observation time, a noise floor of 20 ppm was set for all observation modes and detector saturation was set at 80% full well. The stellar and planetary parameters necessary for the simulation were retrieved from the TEPCAT database and the stellar spectrum used was identical to the one used for the WASP-17b model grid from the BT-SETTL stellar models. All instrument related parameters, such as subarrays and readout patterns, were kept at the `PandExo` defaults. The maximum resolution of the `ATMO` model grid spectrum currently provided is not strictly as high as the achievable resolution of the NIRSpec G395H, however binning of the data will be typically necessary to improve the signal to noise and make resolving certain spectral features possible. As such we do not expect the current model resolution to negatively affect either the current `PandExo` simulations or any future data analysis. It is evident from these simulations that JWST is likely to provide a dramatic improvement in data quality and wavelength coverage, and the model atmospheres presented, in conjunction with `PandExo`, are an excellent predictive tool for the planning of future observations.

3.9 Summary

We have created an extensive grid[7] (∼920,000 simulations) of forward model transmission spectra with corresponding chemical abundances for 117 observationally significant exoplanets (7840 simulations per planet). The simulated spectra and abundances were produced using a 1D radiative–convective–chemical equilibrium model termed `ATMO` (described in Tremblin et al. 2015; Tremblin et al. 2016; Drummond et al. 2016), under the assumption of an isothermal P-T profile and including local condensation and rainout condensation, varying temperature, metallicity, C/O ratio, haziness and cloudiness. The opacity database used for the simulation (Amundsen et al. 2014) is one of the most up-to-date for high temperature planets, including H_2 and He broadening wherever possible. The selection of the planets to be modelled was based on their observational transit signal and signal to noise ratio

---

[7] `https://bd-server.astro.ex.ac.uk/exoplanets/`

(SNR) in V_{mag} and K_{mag}.

In this chapter, we explored the validity of the assumption of an isothermal atmosphere, by comparing our simulations with versions including a P-T profile in radiative-convective and chemical equilibrium. For a test planet (HD 209458b), we demonstrated that the difference in the transmission spectra between the isothermal and consistent P-T profile were small in most cases, except in the temperature regime where spectrally important species condense and potentially rain out of the atmosphere (for example, Na).

We used our set of model simulations to interpret observations of ten exoplanet atmospheres from Sing et al. (2016). We see a continuum from clear to hazy/cloudy atmospheres as found by Sing et al. (2016). The data for all the ten planets are consistent with sub-solar to solar C/O ratio, 0.005 to 10 times solar metallicity and a water, rather than a methane dominated atmosphere. The data for WASP-17b, HAT-P-1b and WASP-6b are consistent with the lowest C/O ratio in out parameter space (0.15), implying the current observations of these planets do not show any clear features, indicative of carbon bearing species. The data for HAT-P-12b and WASP-6b are consistent with extremely high haziness, but without any grey clouds. The data for WASP-12b show extremely muted H_2O features leading to the most hazy and cloudy planet of all, while the data for WASP-17b, WASP-39b, WASP-19b and WASP-31b are consistent with a comparatively clear atmosphere. The χ^2 map for WASP-31b also highlighted the degeneracy existing between the effect of metallicity and clouds/haze on spectral features. The χ^2 map for HD 209458b revealed a bimodal structure in metallicity, again highlighting the degeneracy between metallicity and all other considered parameters.

We described the variation in transmission spectra with the grid parameters, specifically, temperature, metallicity, C/O ratio, haziness and cloudiness. We also explored the change in the chemical equilibrium abundances with respect to these parameters in the transmission spectra probed region ($\sim$ 0.1 to 100 millibar). We highlighted spectral features of various chemical species across a range of wavelengths, useful for identifying their signatures in JWST or HST transmission spectra. CO remains the most abundant chemical species between $\sim$0.1 to 100 millibar, apart from H, H_2 and He in all the temperature regimes, except below 800 K, where H_2O and CH_4 are more abundant than CO.

CO also remains the most abundant chemical species apart from H, H_2 and He in all the metallicity regimes. CO abundances also increase substantially with increasing metallicity. There are changes in the spectral features with change in metallicity, first due to change in chemical composition and second due to change in atmospheric scale height, which decreases with increase in metallicity for a given temperature. We find the transition C/O ratio, from H_2O to CH_4 (carbon species) dominated spectra increases with increasing temperature in agreement with previous studies (Kopparapu et al. 2012; Madhusudhan 2012; Moses et al. 2013a; Venot et al. 2015; Mollière et al. 2015), but spanning a larger range, with values as low as ~0.7 for low equilibrium temperature (960 K) planets like HAT-P-12b and ~1-1.3 for very high equilibrium temperature (2580 K) planets like WASP-12b, where even HCN and C_2H_2 can become more abundant than CH_4.

We also demonstrated the application of our set of model simulations in conjunction with JWST simulator `PandExo`, as a predictive tool to plan future observations.

We note some of the other major limitations of the current grid. Only the terminator region of the planetary atmosphere is probed using transmission spectra. Therefore, it may not be the representative of the entire planetary atmosphere. The assumption of equilibrium chemistry becomes less accurate with the decrease in the equilibrium temperature and non-equilibrium effects such as vertical mixing in 1D might become important (Drummond et al. 2016). Current treatment of clouds and haze in our model is very simple without considering any type, shape or distribution of particles which might effect transmission spectra (Wakeford et al. 2015; Morley et al. 2015). 1D model is also limited by the absence of various 3D effects like spatial variability, 3D cloud structure, dynamics including horizontal and vertical advection with quenching etc., which can have dramatic effects on observable signatures (Agúndez et al. 2014; Zellem et al. 2014; Kataria et al. 2016).

JWST is expected to constrain the atmospheric P-T structure os some exoplanets motivating our upcoming work to publish an extended set of model simulations, comprising of transmission spectra, emission spectra and contribution functions with consistent radiative-convective equilibrium P-T profiles and equilibrium chemistry. A next step is also to include non-equilibrium chemistry and more realistic clouds, however the computational feasibility is still to be established. The current grid is publicly available online[8] and will continuously evolve with the discovery of new observationally significant exoplanets. We encourage the community to use it as a tool to assist them in planning future observations, such as with JWST, HST and various ground based telescopes, along-with interpreting existing datasets. It can provide a useful complement for interpretation, alongside atmospheric retrieval analysis.

---

[8] `https://bd-server.astro.ex.ac.uk/exoplanets/`

Chapter 4

Fully Scalable Forward Model Grid of Exoplanet Transmission Spectra

> “A theory is the more impressive the greater the simplicity of its premises, the more different kinds of things it relates, and the more extended its area of applicability.”
>
> — Albert Einstein

Planning and interpretation of exoplanet atmospheric characterisation observations necessarily relies on theoretical spectra generated from atmospheric models. There currently exist several exoplanet atmospheric forward model grids and simulators providing publicly available theoretical transmission spectra (e.g. Fortney et al. 2010; Mollière et al. 2016; Kempton et al. 2017; Goyal et al. 2018) all of which make specific choices about the atmospheric physics, chemistry, radiative transfer and spectroscopic line lists incorporated into their models. However, intercomparisons between these modeling frameworks still prove difficult. Many of the exoplanet spectral databases produced to date cover very specific non-overlapping parts of exoplanet atmospheric phase space. Often choices made by specific teams concerning the underlying spectroscopic line lists and physical processes like condensation and rainout are not clearly outlined, which can lead to disagreements and confusion when the models are applied by scientists outside the team. Furthermore, the sensitivity of these theoretical spectra to these specific physics choices are often not explored. Publicly accessible databases that provide representative theoretical spectra for exoplanet atmospheres spanning a broad range of atmospheric properties and physical assumptions are necessary to determine the validity of our understanding of these distant worlds to our theoretical constructs. These grids also provide a straight forward way to test spectral sensitivity both within a given modeling framework and across modeling frameworks.

Transmission spectra observations of exoplanet atmospheres have been increasing in quality and resolution since the commissioning of the Wide Field Camera 3 (WFC3) instrument on board the Hubble Space Telescope (HST) (e.g. Deming et al. 2013; Kreidberg et al. 2014; Wakeford et al. 2016; Sing et al. 2016; Evans et al. 2016b; Evans et al. 2017; Wakeford et al. 2018) and FORS2 on the Very Large Telescope (VLT) (Nikolov et al. 2018). This increase in data fidelity has also motivated development of grids of models covering fine variations of model parameters, especially those that alter the chemistry most significantly.

In this chapter we present a publicly available[1] new generic grid of forward model simulations that can be scaled to a wide range of star-planet pairs for atmospheric transmission spectra. We provide a user-friendly generic grid of simulated transmission spectra to interpret observations, where the word "generic" implies a grid of models that can be scaled to a wide range of H_2/He dominated exoplanet atmospheres. We also derive and present scaling equations which can be used with this grid, for a wide range of planet-star combinations. We highlight the sensitivity of our model transmission spectra to choices in atmospheric physics, such as condensation schemes. We also provide comparisons between our scalable grid and planet specific grid as well as spectra generated by other atmospheric modelling frameworks. These comparisons critically highlight how choices made in generating atmospheric models influence our interpretation of the underlying physics captured by observations. In Section 4.1 we first detail the model, its setup for the grid and treatment of condensation. In Section 4.2 we describe the parameter space of the grid. In Section 4.3 we present the scientific results obtained from the grid by detailing the effects of sensitivity tests on atmospheric chemical composition and the resultant transmission spectra. In Section 4.4 we detail how the models can be scaled to any planet-star combination and compare them with other published model grids in the literature for validation. In Section 4.5 we discuss the application of the grid with specific reference to the transmission spectral index established in Sing et al. (2016) and finally this chapter is summarised in Section 4.6.

4.1 Model Setup for Generic Grid

We use `ATMO`, a 1D-2D radiative-convective equilibrium model for planetary atmospheres (Tremblin et al. 2015; Tremblin et al. 2016; Amundsen et al. 2014; Drummond et al. 2016; Tremblin et al. 2017; Goyal et al. 2018) to compute a grid of generic forward models, which can be scaled to represent a wide range of H_2/He dominated atmospheres. For this work we use isothermal P-T profiles under the

---

[1] https://drive.google.com/open?id=1ZFbkPdqg37_Om7ECSspSpEp5QrUMfA9J

assumption of chemical equilibrium. We include H_2-H_2 and H_2-He collision induced absorption (CIA) opacities. We also include opacities due to H_2O, CO_2, CO, CH_4, NH_3, Na, K, Li, Rb, Cs, TiO, VO, FeH, CrH, PH_3, HCN, C_2H_2, H_2S and SO_2. The source of these opacities and their pressure broadening parameters can be found in Amundsen et al. (2014) and Goyal et al. (2018). We note that in this work we adopt Na and K pressure broadened line profiles as derived in Burrows et al. (2000), instead of Allard et al. (2003), adopted for planet specific grid presented in Goyal et al. (2018). This was motivated by the results of Nikolov et al. (2018) where the profiles of Burrows et al. (2000) had a slightly better fit to observations than that of Allard et al. (2003), although the final results were statistically inconclusive while comparing these different pressure broadened profiles.

This grid of model simulations is baselined for a Jupiter radius planet (1 R_J at 1 millibar pressure) around a Solar radius star (1 R_{sun}). Our isothermal P-T profiles extend from 10^{-6} bar at the top of the atmosphere to 10 bar at the bottom, with the radius of the simulated planet that is 1 R_J, defined at the 1 millibar pressure level, which approximates the region of the atmosphere probed with transmission spectra (Lecavelier Des Etangs et al. 2008). The upper and the lower boundary conditions of the atmosphere, for the equilibrium chemical abundances calculation are set by the input pressure grid. We use 50 model levels for each isothermal P-T profile, which are evenly spaced in log(P) space. Over a large pressure range the assumption of an isothermal atmosphere is an extreme assumption, especially for isothermal P-T profiles with rainout (see Section 3.4 in Chapter 3). Therefore, we set the bottom of the atmosphere pressure to 10 bar, approximately similar to previous works (e.g Fortney et al. 2010).We compute transmission spectra in 5000 correlated-k bins, evenly spaced in wavenumber, which corresponds to R$\sim$5000 at 0.2 µm while decreasing to R$\sim$100 at 10 µm (see Goyal et al. 2018, for details).

4.2 Grid Parameter Space

The aim is to produce a forward model grid which can be scaled to any planet-star pair for both, local condensation and rainout condensation cases. The grid requires a sizeable number of parameters which must be sampled with sufficient fineness to allow accurate interpolation. For each of the two treatments of condensation we compute 28,160 forward models over a range of 22 planetary equilibrium temperatures (400, 600, 700, 800, 900, 1000, 1100, 1200, 1300, 1400, 1500, 1600, 1700, 1800, 1900, 2000, 2100, 2200, 2300, 2400, 2500, 2600; all listed in K), four planetary surface gravities (5, 10, 20, 50; all listed in ms^{-2}), five atmospheric metallicities (1, 10, 50, 100, 200; all in × solar), four C/O ratios (0.35, 0.56, 0.7, 1.0), four scattering haze parameters (1, 10, 100, 1100× standard Rayleigh-scattering) and four uniform cloud parameters (0, 0.06, 0.2, 1). Haze is treated as a small scattering aerosol particles and implemented as a parameterized enhanced multi-gas Rayleigh scattering, while clouds are treated as large particles with grey opacity. Haze parameterisation is implemented via the equation $\sigma(\lambda) = \alpha_{haze}\sigma_0(\lambda)$ where $\sigma(\lambda)$ is the total scattering crossection with haze, α_{haze} is the haze enhancement factor and $\sigma_0(\lambda)$ is the scattering crossection due to all other gases. The cloud parameterization is implemented vi the equation $\kappa(\lambda)_c = \kappa(\lambda) + \alpha_{\text{cloud}}\kappa_{H_2}$, where $\kappa(\lambda)_c$ is the total scattering opacity in cm^2/g, $\kappa(\lambda)$ is the scattering opacity due to nominal Rayleigh scattering in same units, α_{cloud} is the variable cloudiness factor governing the strength of grey scattering and κ_{H_2} is the scattering opacity due to H_2 at 350 nm which is $\sim 2.5 \times 10^{-3}\text{cm}^2/\text{g}$ (see Goyal et al. 2018, for more details) and Chapter 3.

We do not extend the grid to sub-solar metallicities and limit the high metallicity end to 200× solar. Above 200× solar the atmosphere becomes abundant in species other that H_2 and He, such as CO_2, H_2O, CO etc. This would require the inclusion of pressure broadening effects due to these species, and no existing studies have solved this problem due to lack of lab-based observational data (Fortney et al. 2016). The choice of C/O ratios in the grid is guided by important transition regimes as found by previous studies (Madhusudhan 2012; Mollière et al. 2015; Goyal et al. 2018). Each of the cloud and haze parameters apply a scaling from 0.0 or 1×, respectively, up to extreme values of almost total obscuration (1.0) for uniform clouds and 1100× the scattering parameter for haze.

4.3 Sensitivity Analysis of the Grid

This model grid explores a wide range of giant planet parameter space across temperatures and chemical abundances, for two different condensation regimes. Therefore, we detail the sensitivity of spectra to different parameter and physics choices in this section. We show a subset of our simulations for both local condensation (left) and rainout condensation (right) in Fig. 4.1, demonstrating the changes with temperature (top), metallicity (middle) and C/O ratio (bottom). For the same 3 grid parameters, we also show the changes in the mean chemical abundances of various spectrally important species in Fig. 4.2.

4.3.1 Impact of changing temperature

Changes in temperature have a more profound impact on the transmission spectrum compared to any other parameter, as the chemical composition is strongly dependent on the temperature, under the assumption of chemical equilibrium (Burrows et al. 1999). To demonstrate the impact of temperature on the transmission spec-

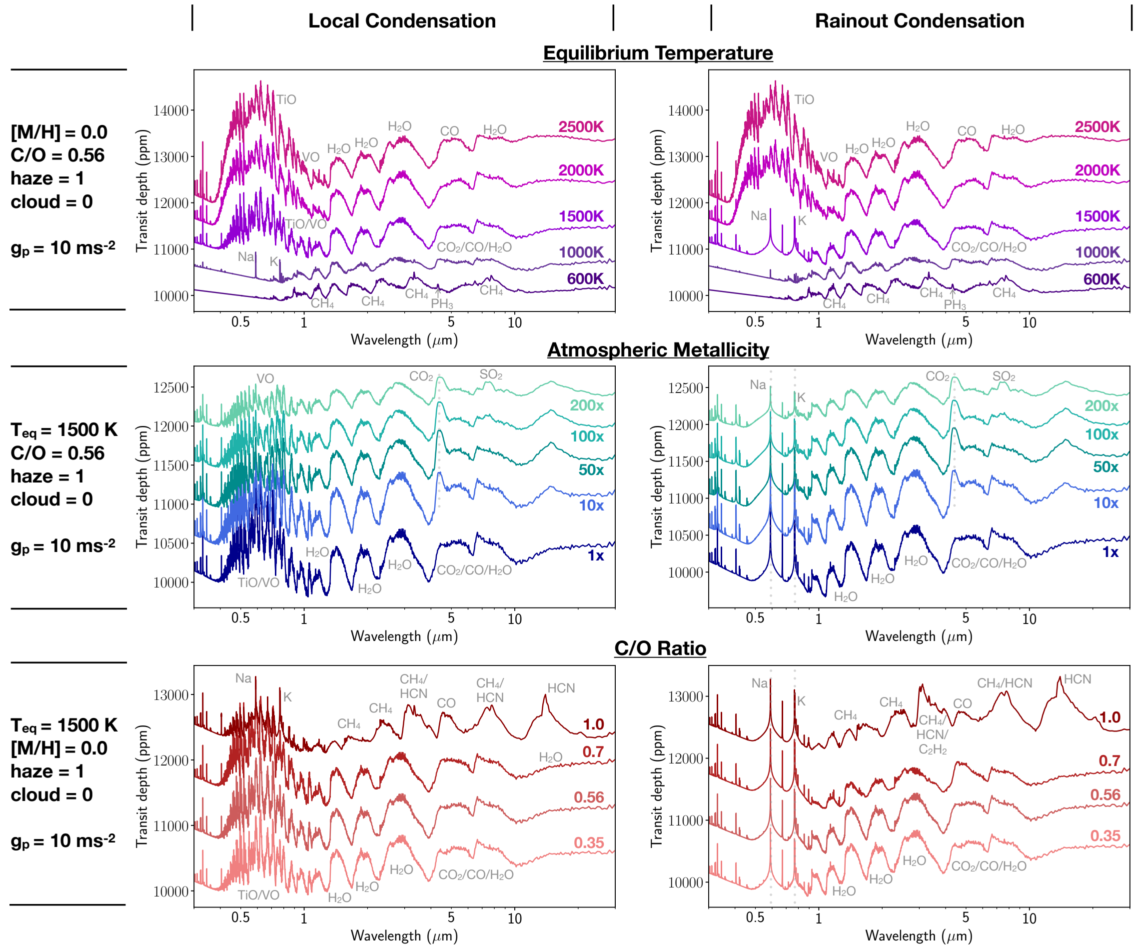

Figure 4.1: Figure showing transmission spectra with the effects of local condensation (left) and rainout condensation (right). We show the effects of varied temperature (top row) with a fixed metallicity and C/O ratio set to solar, varied metallicity (middle row) with a fixed $T_{eq} = 1500\,K$ and C/O at solar, varied C/O ratio (bottom row) with a fixed $T_{eq} = 1500\,K$ and solar metallicity.
In each case we consider a clear atmosphere with haze and cloud parameter set to 1.0 and 0.0, respectively, for a planet with radius 1 R_J around a star with radius 1 R_{sun} and g_p=10 ms^{-2}. An offset in transit depth has been added to each spectrum for clarity.

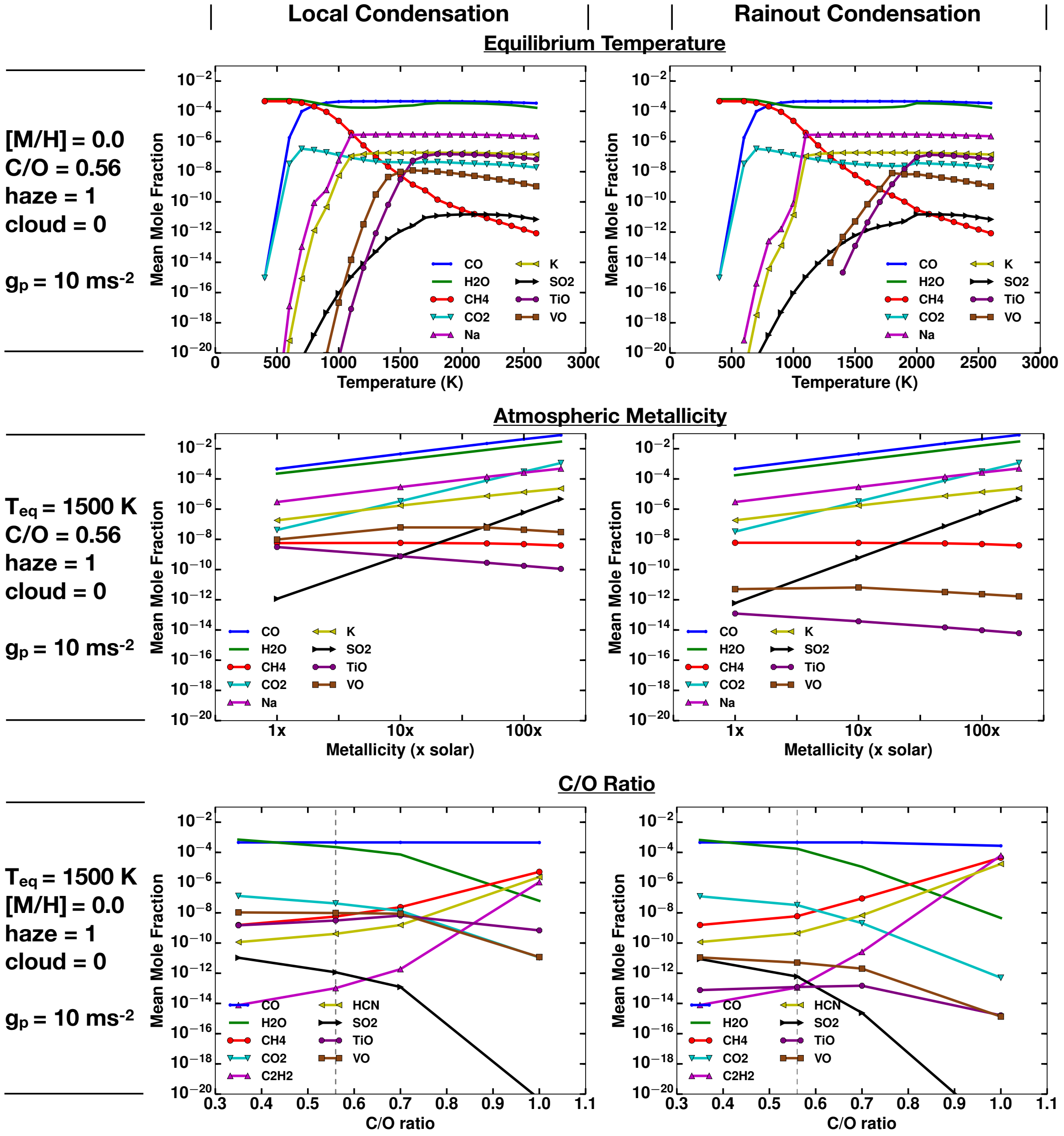

Figure 4.2: Figure showing change in mean chemical abundances between 0.1 and 100 millibar for various molecules for the same model simulations as in Fig. 4.1. Changes in mean chemical abundances due to local condensation (left) and rainout condensation (right) for varied temperature (top row) with a fixed solar metallicity and C/O ratio, varied metallicity (middle row) with a fixed $T_{eq} = 1500\,K$ and solar C/O ratio, and for varied C/O ratios with a fixed $T_{eq} = 1500\,K$ and solar metallicity (bottom row)].

trum we fix the metallicity and C/O ratio to solar value and use a clear atmospheric (haze and cloud parameters of 1.0 and 0.0, respectively) spectrum for a planetary gravity of 10 ms^{-2}, as shown in Fig. 4.1(top row). In both condensation cases, at low temperatures <1000 K the spectra are dominated by CH_4 with minor contributions from H_2O. Above ∼1000 K the spectra are dominated by H_2O absorption with contributions in the IR from CO and CO_2. This can also be noticed in Fig. 4.2 bottom row, where the CH_4 abundance drops dramatically after ∼1000 K. The main difference between the two condensation cases can again be seen in the optical. In the local condensation case TiO/VO absorption is expected at temperatures above ∼1400 K, while in rainout condensation, absorption by TiO/VO is suppressed until ∼1700 K. This implies that the atomic Na and K line absorption is only apparent in the local condensation grid between ∼ 800–1400 K. In the rainout condensation grid, the presence of Na and K is also impacted by condensation, therefore Na and K features are only expected between ∼ 1100–1700 K

4.3.2 Impact of changing metallicity

The effects of metallicity are shown for a clear atmosphere at an equilibrium temperature of 1500 K, solar C/O ratio(0.56) and gravity of 10 ms^{-2}. Generally, it can be seen that all the spectral features tend to be reduced in amplitude with increase in metallicity as seen in Fig. 4.1 (middle row), although the abundance of all the spectrally important species increase, as seen in Fig. 4.2. This is caused by the increasing metallicity leading to a reduction in the scale height of the atmosphere, as the mean molecular weight increases. With increase in metallicity, there is also increase in CO_2 abundance (Moses et al. 2013b) as seen in Fig. 4.2, which can also be noticed by rise in strong CO_2 feature at 15 µm.

In the local condensation case, the strength of TiO/VO features in the optical decreases with increasing metallicity at 1500 K, which is a combination of decrease in TiO/VO abundance as well as muting of the features due to increased molecular weight of the atmosphere. In contrast, rainout condensation entirely removes TiO and VO features at 1500 K due to condensation and removal of the species deeper in the atmosphere, leading to their lower abundances. The lower abundances of TiO and VO, leaves the atomic lines of Na and K as the dominant transmission features in the optical. There is, however, little difference (between rainout and no-rainout) in the infrared (IR) with only moderate changes in the absolute abundance of the oxygen based species due to condensate formation. The IR spectra are mainly dominated by H_2O features. However, CO and CO_2 features can be seen between 4 and 5 µm.

Additionally, there is a SO_2 feature between 7 to 8 µm which first appears in the 100× solar metallicity models, with a stronger feature at 200× solar metallicity. The presence of SO_2 can possibly be used to constrain the metallicity of exoplanet atmospheres with mid-IR observations and strong near-IR constraints on the H_2O abundance. SO_2 is one of the most prominent sulphur gases in the atmosphere of Venus, having substantial effect on its radiative balance (Vandaele et al. 2017). Therefore, investigating the possibility of SO_2 detection, can increase our understanding of the sulphur cycle in giant planetary atmospheres.

4.3.3 The impact of changing C/O

The effects of varying the carbon-to-oxygen (C/O) ratio are shown in Fig. 4.1 and 4.2 (bottom row) for a clear atmosphere at an equilibrium temperature of 1500 K, solar metallicity and gravity of $10\,\mathrm{ms}^{-2}$. The C/O ratio primarily dictates the dominance of various carbon and oxygen bearing molecular species in the atmosphere and thereby the spectra. As seen in Fig. 4.2 bottom row, for C/O ratios less than equal to solar values, atmosphere is dominated by CO, H_2O and CO_2. However, for C/O ratios greater than solar, the abundances of molecules with carbon but without oxygen such as CH_4, HCN, and C_2H_2 start increasing rapidly. This effect is visible in the transmission spectra as shown in Fig. 4.1 (bottom row), where the infrared spectra is primarily dominated by H_2O features upto solar C/O ratio (0.56), 0.7 being the transitional value and 1 being the C/O ratio at which the infrared spectra is primarily dominated by CH_4 and HCN features. Choice of condensation also has an effect on spectral features, especially for C/O ratios greater than solar. It can be seen in Fig. 4.1 that at C/O ratio of 1, spectral features are different between rainout and local condensation cases. This is because the rainout case has a slighly larger abundance of CH_4, HCN and C_2H_2, as compared to local condensation case seen in Fig. 4.2. It can also be seen from this figure that the abundances of spectrally important molecules such as H_2O, C_2H_2 etc. are more strongly dependent on the C/O ratio in the rainout case, compared to local condensation case.

4.3.4 The presence of VO without TiO

Recent observations have shown the possibility of VO with the absence of TiO in the atmosphere of extremely irradiated hot Jupiter WASP-121b (Equilibrium temperature $(T_{\mathrm{eq}}) = 2358\,\mathrm{K}$) (Evans et al. 2017). The calculations presented here suggest that this may only be possible across a narrow range of temperatures, namely $\sim$ 1200–1400 K, under the assumption of local condensation as seen in Fig. 4.2 (top row). In this rather narrow temperature regime, the abundance of VO is higher than that of TiO and sufficient enough to impart its features in the transmission spectrum. This is because the primary Ti condensate Ti_3O_5 is more abundant than the V condensate V_2O_3, thereby locking more Ti in condensates than V at these temperatures. For temperatures higher than 1400 K TiO starts dominating the optical spectrum. However, for the rainout condensation case, this narrow range where VO is present without TiO, is $\sim$ 1700–1800 K. Therefore, presence of VO features in the spectrum without TiO can help constrain the limb temperature of the planet's atmosphere, if the rainout and local condensation processes in the planetary limb are constrained. Additionally, if the planetary limb temperature is constrained using the Rayleigh scattering slope, TiO or VO features can reveal which process is dominant in these atmospheres (rainout or local condensation).

4.4 Working with the Grid

The generic exoplanet `ATMO` model grid has been produced such that it can be scaled to a wide range of planet/star combinations and can be applied as an interpretive tool as well as a preparation tool for exoplanet atmospheric studies. Temperature and gravity are two of the most important parameters shaping the transmission spectrum of giant exoplanets as they effectively control the scale height of the atmosphere. The temperature also governs the chemical state of the atmosphere, where different temperatures can lead to different chemical properties (see Fig. 4.2). As such, the parameter space of the temperature (400-2600 K) is broken down into fine bins (of $\sim$100 K). The gravity, however, can be represented over fewer values and scaled to a more precise value. The amplitude of features in the transmission spectra are strongly tied to the scale height of the planet's atmosphere, which is inversely proportional to the planet's gravity as shown in Fig. 4.3. In short, all else remaining equal, as the gravity increases, the amplitude of spectral features decrease.

To demonstrate the scalability of the gravity, for each gravity parameter in the grid (5, 10, 20, 50 $\mathrm{ms^{-2}}$) the model has been scaled to a variety of different planetary gravities and compared to a model specifically generated for that gravity. In Fig. 4.4 and 4.5, we demonstrate the accuracy associated with scaling the four gravities supplied in the grid to a finer parameter space between 3–100 $\mathrm{ms^{-2}}$. The residuals are well below half the scale height of the atmosphere, when scaled from the 5, 10, 20 or 50 $\mathrm{ms^{-2}}$ models as seen in Fig. 4.4 and 4.5. It can be noticed that the residuals are maximum between 0.5 and 1 µm, specifically around Na and K absorption bands at 0.58 and 0.76 µm respectively. This is because when transmission spectra is computed for a specific value of gravity it corresponds to specific value of pressure and therefore specific pressure broadening of opacities. However, scaling to a different gravity changes the pressure level probed by transmission spectra, since it varies as square root of g (see Equation 4.2) and therefore ideally requires pressure broadened opacities at this new pressure levels. But while scaling generic models

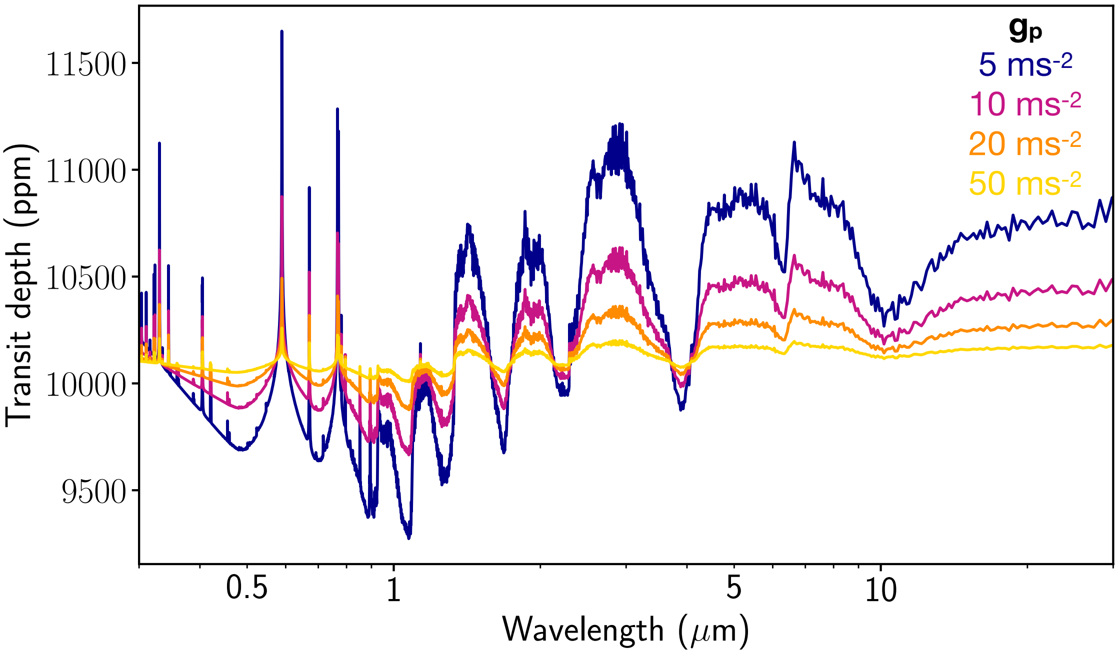

Figure 4.3: Figure showing how changing the gravity changes the size of the absorption features in the transmission spectrum, due to a change in the scale height, for each of the gravities represented in the grid ($5\,\mathrm{ms}^{-2}$, $10\,\mathrm{ms}^{-2}$, $20\,\mathrm{ms}^{-2}$, $50\,\mathrm{ms}^{-2}$). Each model is for a clear solar metallicity ans solar C/O ratio atmosphere with $\mathrm{T}_{eq} = 1500\,\mathrm{K}$.

between different gravities, we don't alter the opacities, leading to largest residuals for Na and K bands which are very strongly affected by pressure broadening.

The other parameters covered by the grid represent different scaling parameters applied to either the chemistry (e.g. metallicity, C/O ratio) via a scaling of the abundances, or in the opacity (e.g. haze and cloud, via scaling factors with and without wavelength dependence; see Goyal et al. 2018 for details).

4.4.1 Scaling to Specific Planetary Parameters

In order for these models to be applied to the desired exoplanet they will have to be scaled based on the planetary radius, stellar radius, surface gravity, and planetary equilibrium temperature.

The wavelength-dependent observed (apparent) radius of the planet $R_p(\lambda)$ can be seen as a combination of the wavelength-independent bulk planet radius $R_{p,bulk}$ and a wavelength-dependent contribution from the atmosphere $z(\lambda)$,

$$R_p(\lambda) = z(\lambda) + R_{p,bulk}, \tag{4.1}$$

where the term $z(\lambda)$ is dependent on the physical and chemical properties of the atmosphere.

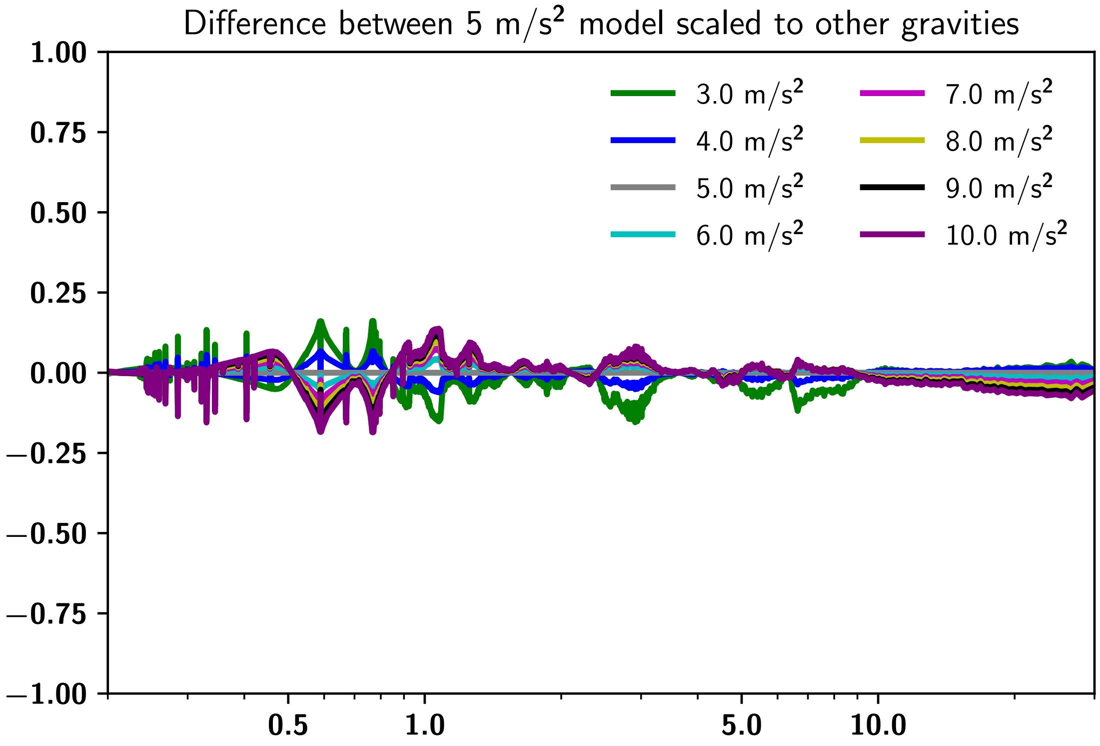

(a)

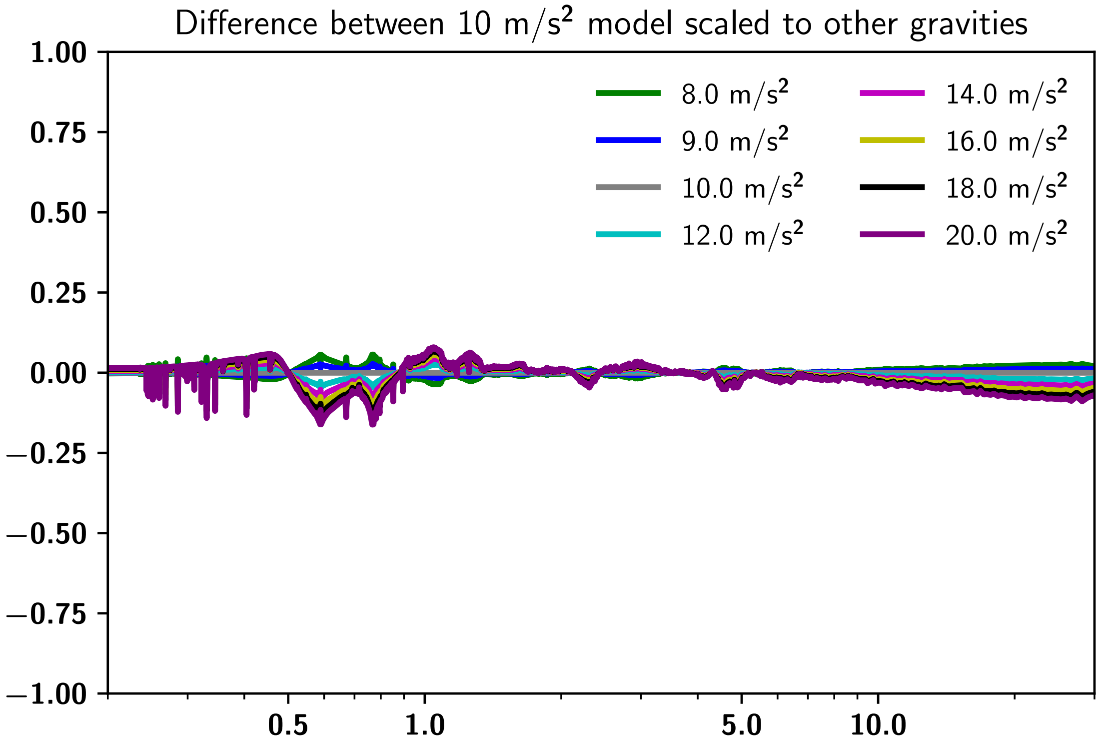

(b)

Figure 4.4: Figure showing the residual comparison of the generic model scaled to different planetary gravities to models computed at the specific gravities, for each of the planetary gravity parameters in the grid ($5\,\mathrm{ms}^{-2}$ top, $10\,\mathrm{ms}^{-2}$ bottom).

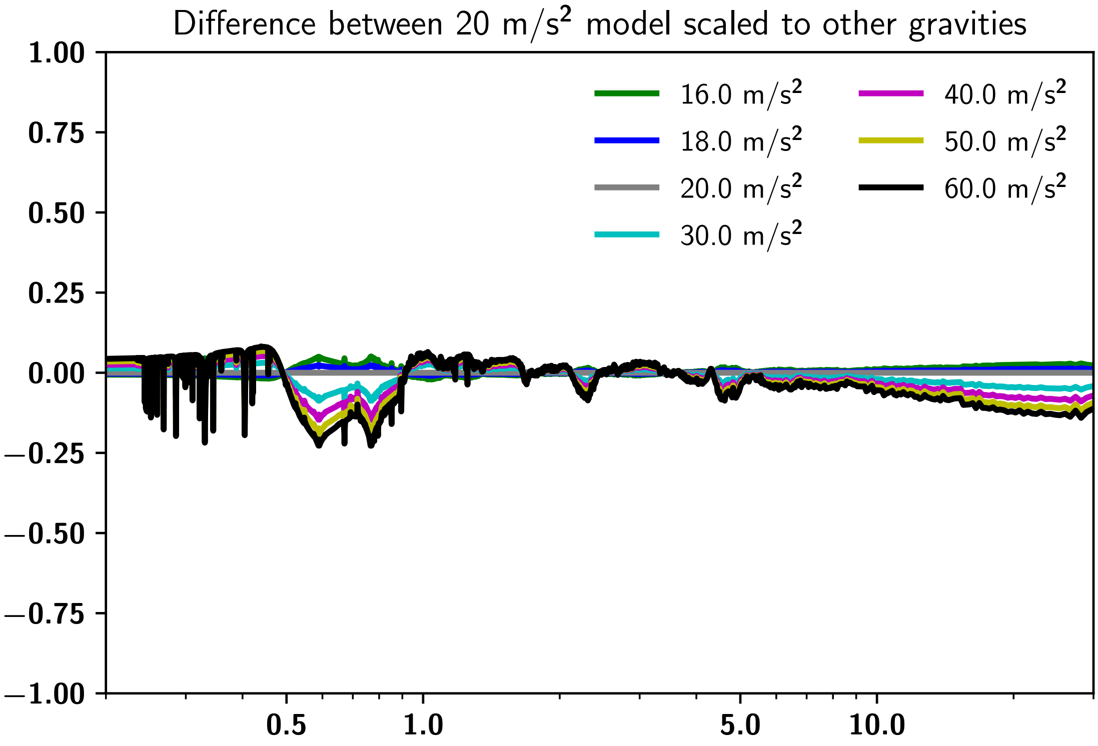

(a)

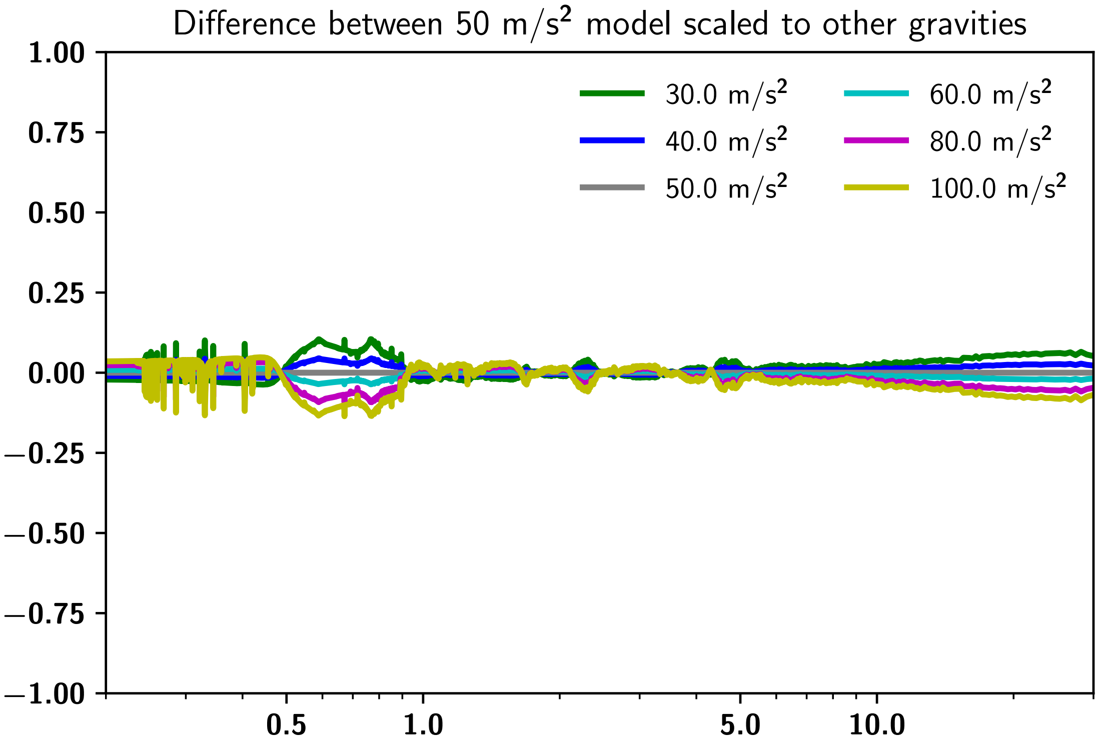

(b)

Figure 4.5: Same as Figure 4.4 but for gravity values of 20 ms^{-2} (top) and 50 ms^{-2} (bottom).

Lecavelier Des Etangs et al. (2008) provide an approximate analytic solution for $z(\lambda)$,

$$z(\lambda) = H \ln \left(\frac{\xi_{abs} P_{z=0} \sigma_{abs}(\lambda)}{\tau_{eq}} \sqrt{\frac{2\pi R_{p,bulk}}{k_b T \mu g}} \right) = H \ln \alpha, \tag{4.2}$$

where T is temperature, μ is the mean molecular weight, g is gravity, k_b is the Boltzmann constant and $H = (k_b T)/(\mu g)$ is the atmospheric scale height. $\sigma_{abs}(\lambda)$ and ξ_{abs} are the absorption cross section and mole fraction of the dominant absorbing species, respectively. $P_{z=0}$ is the pressure at the effective altitude(z) of 0 (i.e at the base of the atmosphere). Optical depth, τ_{eq}, is set to 0.56 (Lecavelier Des Etangs et al. 2008). We note that we do not use Eq. 4.2 to calculate the transmission spectra in our model grid, but use the numerical approach detailed in Amundsen (2015) and Goyal et al. (2018).

In this model grid a large number of transmission spectra are included for specific sets of model parameters, where, $R_p^{grid}(\lambda) = z^{grid}(\lambda) + R_{p,bulk}^{grid}$, as shown in Eq. 4.1. However, we derive a scaling relation by solving Eq. 4.2 simultaneously for grid and planet parameters, to fine-tune a particular model from the grid to a specific set of planetary parameters,

$$\frac{z^{grid}(\lambda)}{H^{grid}} - \frac{z^{planet}(\lambda)}{H^{planet}} = \ln \alpha^{grid} - \ln \alpha^{planet} \tag{4.3}$$

where terms denoted “grid” are values from the model grid and terms denoted “planet” are the new parameters for a specific case. Rearranging Eq. 4.3 and canceling constants we obtain the scaling relation,

$$z^{planet}(\lambda) = z^{grid}(\lambda) \frac{T^{planet} g^{grid}}{T^{grid} g^{planet}} - 0.5 \ln \frac{R_{p,bulk}^{grid} T^{planet} g^{planet}}{R_{p,bulk}^{planet} T^{grid} g^{grid}}. \tag{4.4}$$

Importantly, the assumption that σ_{abs}, ξ_{abs} and μ are constants has been made while scaling from the nearest grid to planetary parameter, which is a reasonable assumption given the fine variation of parameters in the grid, as demonstrated in Section 4.4.2

The wavelength dependent planetary radius ($R_p(\lambda)$) scaled to the parameters of a specific planet can then be found using Eq. 4.1 and Eq. 4.4. The transmission spectrum $\left(\frac{R_p(\lambda)}{R_*}\right)$ can then be obtained simply by including the relevant stellar radius R_*. We provide a python code on GitHub and the grid on the google drive to scale these models[2,3].

---

[2] https://github.com/hrwakeford/Generic_Grid

[3] https://drive.google.com/open?id=1ZFbkPdqg37_Om7ECSspSpEp5QrUMfA9J

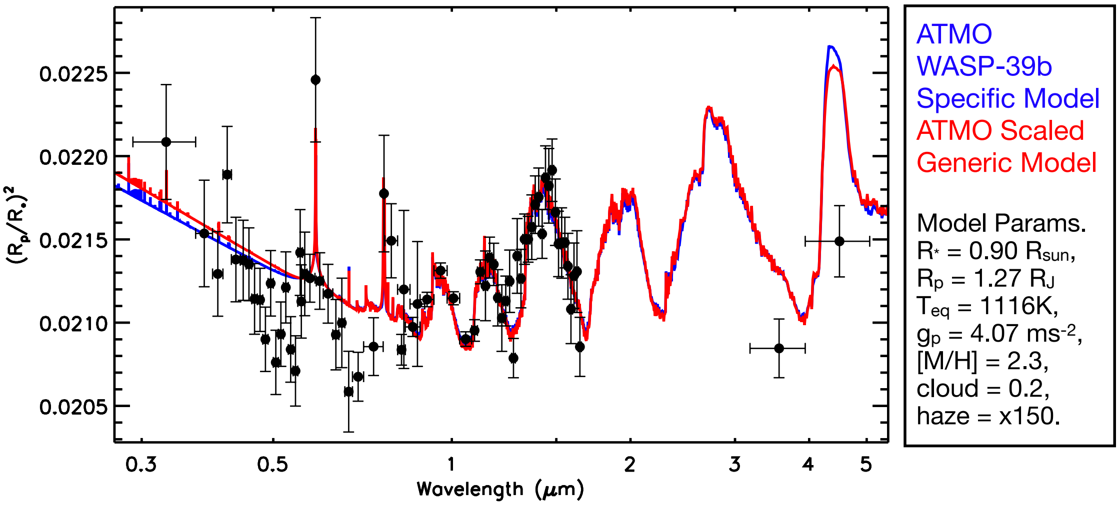

Figure 4.6: Figure showing the use of the generic grid (red) to fit atmospheric data (black points, Wakeford et al. 2018), in comparison to the planetary forward model grid (blue) presented in Goyal et al. (2018). In both cases we use the grid for local condensation only.

4.4.2 Comparison to Planetary Specific Grid

To test this new scalable `ATMO` grid it has been compared to the previously published planetary specific transmission spectra (Goyal et al. 2018)[4]. WASP-39b has $T_{eq} = 1116\,K$, $g_p = 4.07\,ms^{-2}$, $R_p = 1.27\,R_J$, and $R_* = 0.90\,R_{sun}$ adopted from TEPCAT database (Southworth 2011b). As shown in Wakeford et al. (2018), the best fit model for WASP-39b data from the Goyal et al. (2018) grid has a metallicity of 100× solar, uniform cloud = 0.2, and scattering haze = 150×. To demonstrate the applicability of this generic model spectra grid for different planetary systems, it is scaled to the planetary parameters of WASP-39b, and compared to this best fit model in Fig. 4.6. From the generic grid we scale the $T_{eq} = 1100\,K$, $g_p = 5.0\,ms^{-2}$, 200× solar, uniform cloud = 0.2, and scattering haze = 150× model to the best fit model parameters for WASP-39b. For this temperature range the spectrum is relatively independent of the treatment of the condensation, so for clarity we only show the local condensation spectrum in Fig. 4.6.

This test demonstrates the flexibility of this grid of models to be adapted to specific planetary parameters. There are minor differences, ~100ppm, in the IR near 4.5 microns with the scaled CO/CO_2 feature, however, these do not significantly affect the fit to the data. In the rest of the spectra, the differences between the models average 50 ppm, which is well below the data uncertainties. The minor differences in the Rayleigh scattering slope can be attributed to differences in adopted pressure broadening profiles for Na in this work and that in (Goyal et al. 2018), explained in detail in Section 4.1.

---

[4] `https://bd-server.astro.ex.ac.uk/exoplanets/`

This test also demonstrates that differences shown in Fig. 4.4 when scaling the 5 ms^{-2} model to new planetary parameters are negligible between specifically generated models and our re-scaled generic models, where differences are well within the constraints of the current observational measurements.

Compared to the planetary specific grid presented in (Goyal et al. 2018) this grid can be applied to a wide range of H_2/He dominated exoplanet atmospheres and is not limited to the 117 well studied planets. This grid is applicable to targets detected using TESS, NGTS, HATS and any number of other H_2/He dominated planets discovered in the future over a wide parameter space. Due to the scalable nature of the grid it can also be implemented within a retrieval framework, for which the planetary specific grid is not suitable.

4.4.3 Comparison to other Forward Models

Figure 4.7 shows the "scaled" simulated spectrum from the generic exoplanet `ATMO` forward model grid, with similar generic forward model simulations from Fortney et al. (2008) and Fortney et al. (2010) and Exo-transmit from Kempton et al. (2017). Each simulation is computed for isothermal P-T profiles assuming thermochemical equilibrium. The simulations in Fig. 4.7 are computed for solar metallicity atmospheres without cloud opacities and $T_{eq} = 600$ K (top), $T_{eq} = 1500$ K (bottom), with $g_p = 10\,ms^{-2}$, $R_p = 1\,R_J$, and $R_* = 1\,R_{sun}$. Both Exo-transmit (Kempton et al. 2017) and the models based on Fortney et al. (2008) and Fortney et al. (2010), included thermochemical equilibrium scheme which account for condensation (Lodders 1999; Lodders et al. 2002b; Lodders et al. 2006a; Lodders et al. 2002a; Lodders et al. 2006b; Visscher et al. 2006; Freedman et al. 2008).

We see that all three models agree well at low temperature ($T_{eq} = 600$ K) (with a slight difference in the ExoTransmit model between 1–2 µm). The difference in the relative radius ratio in the optical slopes at $T_{eq} = 1500$ K between models from Fortney et al. (2010) and `ATMO`, can be attributed to raining out of TiO/VO in `ATMO` at these temperatures.

Here some of the potential reasons for differences between these models as seen in Fig. 4.7 are discussed. Both Exo-transmit (Kempton et al. 2017) and the models based on Fortney et al. (2008) and Fortney et al. (2010) use elemental abundances from Lodders (2003). However, `ATMO` uses elemental abundances from Asplund et al. (2009). The major difference between these two sources is in Helium abundance which is greater in Lodders (2003) compared to Asplund et al. (2009). This can lead to some differences in equilibrium chemical abundances. The differences in adopted polynomial coefficients for chemical equilibrium calculations can also lead to differences. In Fortney et al. (2010) the base radius is either at 10 or 100 bar,

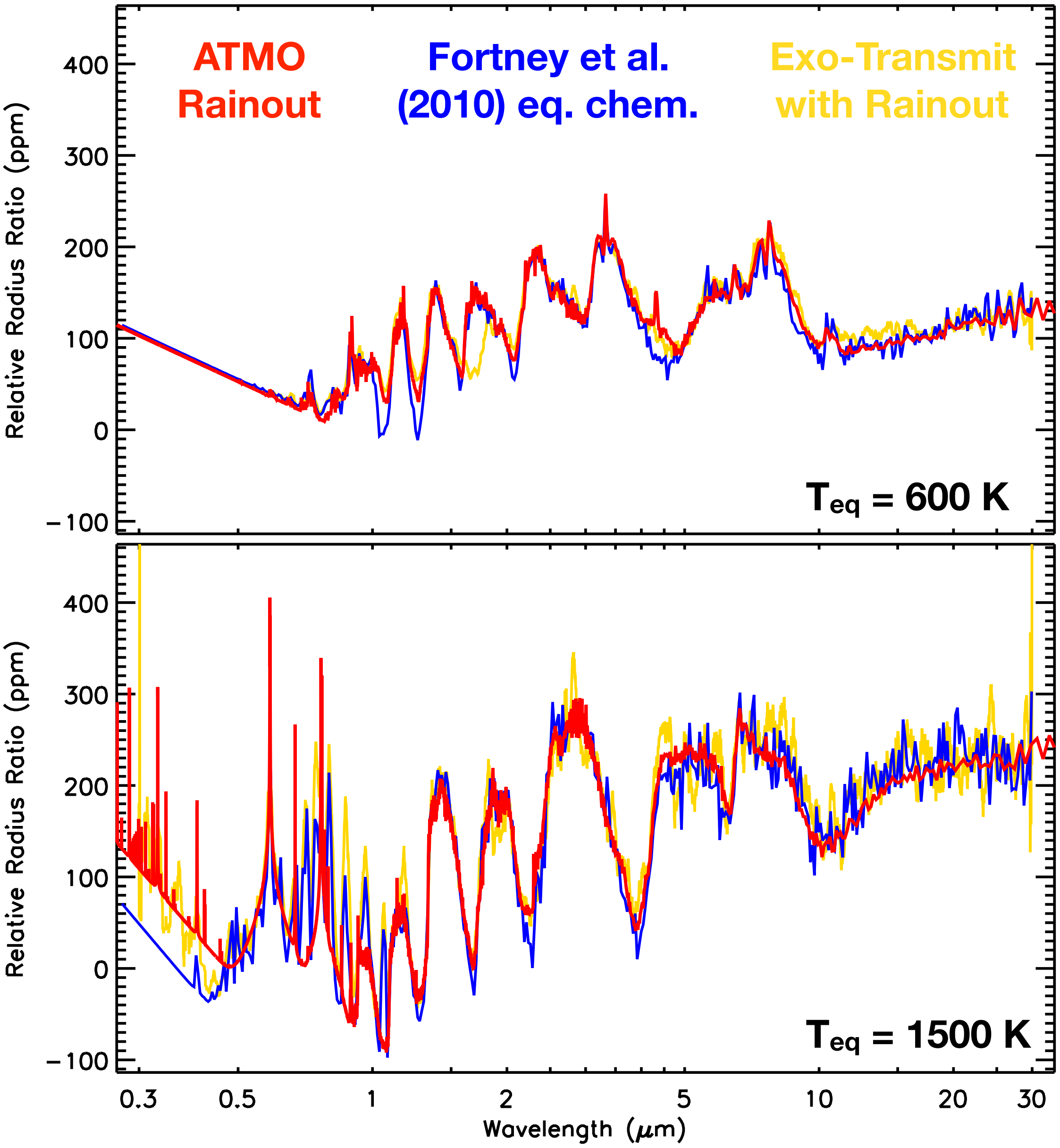

Figure 4.7: Figure showing comparison of `ATMO` rainout condensation model (red) to the Fortney et al. (2010) equilibrium model with TiO/VO (blue), and Exo-transmit with condensation and rainout (yellow). Each are isothermal models for g_p=25 ms^{-2}, R_p/R_*=0.1, and T_{eq}= 600 K (top) and 1500 K (bottom). We show the spectra aligned in the infrared 1.4 μm. The main differences in the infrared are due to the opacity database used for H_2O and CH_4. Bottom: In the optical, Exo-transmit and the Fortney et al. (2010) show evidence for VO absorption while this is removed in the rainout process in `ATMO`.

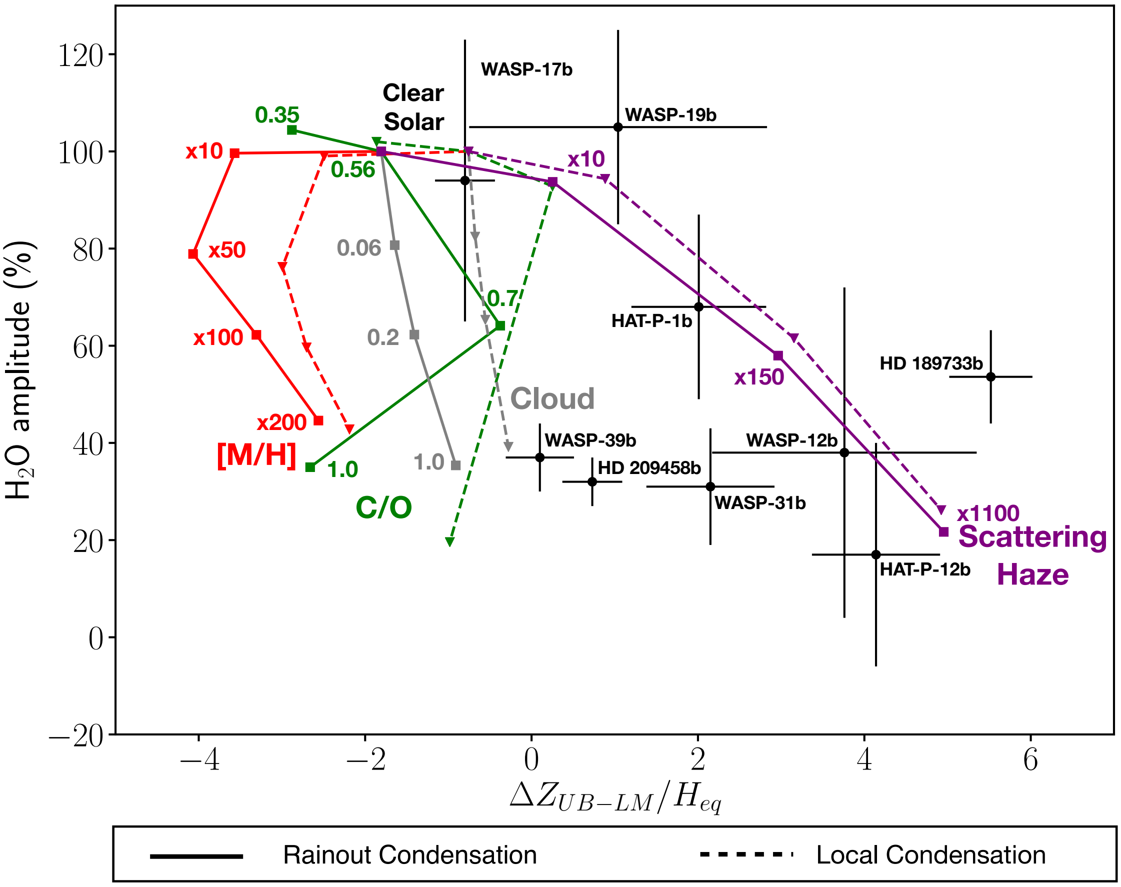

Figure 4.8: Figure showing `ATMO` grid based transmission spectral index tracks first (e.g. Sing et al. (2016)). We show the H_2O amplitude versus the Δz_{UB-LM} index for [M/H] (red), C/O (green), uniform cloud (grey), and scattering haze (purple) parameters. We show the tracks for both the grid with rainout condensation (solid lines) and local condensation (dashed lines). Planetary data points are taken from Sing et al. (2016) and Wakeford et al. (2018).

while in this work a value of 10 bar is adopted. The grid generated using ATMO uses high temperature line-lists primarily from Exomol with H_2/He pressure broadening applied wherever possible. In comparison, Fortney et al. (2010) and Kempton et al. (2017) models primarily use HITRAN line-lists. This can lead to differences in spectral features.

4.5 Transmission Spectral Index

To evaluate the impact that changing individual scaling parameters has on the atmospheric transmission spectrum, the grid of generic models has been used to compute the different transmission spectral indices as detailed in (Sing et al. 2016). Spectral indices for both local condensation and rainout condensation grids are computed, and the difference in the radius ratio with an increase in atmospheric metallicity, uniform cloud scattering, and wavelength dependent haze scattering is measured. The H_2O amplitude versus $\Delta Z_{UB-LM}/H_{eq}$ index for both the grids are computed and the model trends are shown in Fig. 4.8.

For each model, the H_2O amplitude is computed based on the radius ratio of each model between 1.34–1.49 μm relative to the standard solar model over the same wavelength range. The relative change in the radius ratio for each model is then converted to a percentage amplitude of the H_2O feature compared to solar. The $\Delta z_{UB-LM}/H_{eq}$ index represents the measured radius ratio of the model in the blue-optical UB-band (0.3–0.57 µm) compared to the mid-infrared LM-band (3–5 μm) in terms of atmospheric scale height. A negative number here indicates that the blue-optical is lower in altitude than the mid-IR, with the opposite true for positive numbers. The model trends for the uniform cloud, scattering haze, and super solar metallicity parameters covered by both grids are shown in Fig. 4.8.

The transmission spectral indices show that the differences between local condensation and rainout condensation are predominantly in the $\Delta z_{UB-LM}/H_{eq}$ index, where $\Delta z_{UB-LM}/H_{eq} =$ -0.8 and -1.75 for the clear solar model for local condensation and rainout condensation respectively. In all model cases the H_2O amplitude is decreased, with the exception of the 10× solar model which would require the optical and mid-IR data to distinguish from a clear solar case. There is a distinct separation between each of the model tracks. Increasing the metallicity decreases the amplitude of the water feature while increasing the radius ratio in the mid-IR compared to the optical, mainly due to the presence of CO_2 at higher metallicities (see Fig. 4.1). Increasing the uniform cloud parameter decreases the H_2O amplitude with little change to the relative radius ratio between the optical and mid-IR. Increasing the wavelength dependent scattering haze decreases the amplitude of the H_2O feature while increasing the relative radius ratio between the optical and mid-IR.

Note that these computed transmission spectral tracks show the trend of the individual parameters compared to a clear solar abundance atmosphere and for example, do not depict the combined impact of scattering haze and high metallicity. However, these are a useful indication of dominant factors in the transmission spectra of exoplanets and have successfully been used to make predictions for atmospheric measurements (Sing et al. 2016; Wakeford et al. 2018). Each of the measurements shown on the diagram are from Sing et al. (2016) with the addition of WASP-39b from Wakeford et al. (2018). A majority of the currently measured transmission spectra from the optical to the mid-IR follow the track of increased scattering haze with a majority of measured H_2O amplitudes between 20–50% of the clear solar model. These indices demonstrate the importance of the optical and mid-IR data to distinguish between different model parameters, in this case the cloud, haze, and enhanced metallicity trends.

4.6 Summary

A publicly available[5] generic forward model grid of exoplanet transmission spectra is presented in this chapter, computed using the `ATMO` code, based on both local condensation and rainout condensation conditions. This grid can be scaled to a wide range of H_2/He dominated planetary atmospheres. The entire grid consists of 56,320 model simulations across 22 isothermal temperatures, four planetary gravities, five atmospheric metallicities, four C/O ratios, four uniform cloud parameters, four scattering haze parameters, and two chemical condensation scenarios. Sensitivity analysis is performed to explain the reasoning behind selection of different grid parameters and their values. Furthermore, scaling relations have been derived allowing the grid to be used over a wide range of planet-star combinations. This grid of forward models is validated against published models of Fortney et al. (2010), Kempton et al. (2017) and Goyal et al. (2018).

Degeneracies are known to exist in the interpretation of various characteristics of planetary atmospheres from observations. The grid of atmospheric models presented here allows us to decouple and better understand the thermochemical processes shaping observable spectra. Changes in temperature and chemical abundances have been demonstrated to cause different trends in the spectra, and the following major factors that can effect interpretation of observations have been identified:

- Adopting different condensation processes (rainout and local) can lead to different interpretation of observations.

- SO_2 features at 6–8µm, along with H_2O, can be used to constrain the metallicity of the exoplanet atmosphere, since the SO_2 spectral feature only appears for metallcities greater than 100x solar.

- The presence of VO without TiO can help constrain the temperature of the atmospheric limb, and that both TiO/VO features can reveal dominant physical process (rainout or local condensation) in the planet's atmosphere.

- At high C/O ratios ($\sim$1), spectral features in the infrared are different between the rainout and local condensation case, because rainout case has higher abundance of carbon bearing species without oxygen such as CH_4, C_2H_2 and HCN.

- The difference in solar elemental abundances between Asplund et al. (2009) and Lodders (2003) used for model initialisation, can lead to differences in equilibrium chemical abundances and therefore the spectral features.

---

[5] https://drive.google.com/open?id=1ZFbkPdqg37_Om7ECSspSpEp5QrUMfA9J

This grid can be used to interpret the observations of H_2/He dominated hot Jupiter exoplanet atmospheres, as well as to plan future observations using the HST, VLT, JWST and various other telescopes. It can be used directly with the HST and JWST simulator `PandExo` (Batalha et al. 2017) for planning observations. The scaling flexibility provided by this grid for a wide range of planet-star combinations will be extremely valuable to efficiently choose and plan observations, for soon to be discovered TESS targets.The fine variation of parameters in the grid also allows it to be incorporated in a retrieval framework with various machine learning techniques, as demonstrated in Marquez-Neila et al. (2018).

Chapter 5

Library of Self-consistent Simulated Exoplanet Atmospheres

> “To explain all nature is too difficult a task for any one man or even for any one age. ’Tis much better to do a little with certainty & leave the rest for others that come after you.”
>
> — Issac Newton

The weather, climate and dynamics of a planetary atmosphere are governed by its pressure-temperature (P-T) structure. The P-T structure of the planetary atmosphere also governs its spectral signatures, when remotely observed using telescopes, spacecrafts or satellites. Therefore, it is necessary to constrain the P-T structure of a planet’s atmosphere, to understand the various physical processes occurring within them. Constraining the 3D P-T structure of the planetary atmosphere is ideally required, but the complexity and the computational limitations of such a model, especially for a library of model simulations, motivates us to restrict our current analysis to 1D P-T profiles. 1D P-T profiles of an irradiated H_2/He dominated planetary atmospheres with sufficiently high equilibrium temperatures are expected to reach a radiative-convective equilibrium condition in the lower pressure regions ($< \sim$100 bar) (Iro et al. 2005; Madhusudhan et al. 2016b), but not in the higher pressure regions (e.g Mayne et al. 2014). This is primarily a result of extremely large heating rates provided by strong irradiation from the host star, that rapidly forces any perturbations in P-T profiles back to radiative-convective equilibrium, termed, RCE, hereafter. Using equilibrium chemistry, to model hot Jupiter atmospheres is also a reasonable assumption, due to high temperature of these planets, especially for atmospheric temperatures larger than $\sim$2000 K, and a good starting point to constrain main atmospheric constituents for lower temperatures (Madhusudhan et al. 2016b). However, RCE *P*-*T* profiles for different planets can vary depending on their gravity, host star distance and spectral type, circulation in the planet's atmosphere, chemical composition of the atmosphere and the presence of haze or clouds. This can then lead to a wide range of possible spectra for a given planet, governed by its *P*-*T* profile. Therefore, a library of RCE *P*-*T* profiles and the corresponding chemical abundances and simulated spectra is required to interpret the observations of exoplanet atmospheres and constrain the important physical processes in them.

In the previous chapters, we used isothermal *P*-*T* profiles for computing transmission spectra for a wide range of exoplanet atmospheres. This library of models was made publicly available and has proved to be very useful in interpreting observations of various exoplanets (see for e.g Wakeford et al. 2018; Alam et al. 2018). However, the assumption of an isothermal *P*-*T* profiles is only accurate for a small region of the atmosphere, namely the high-altitude, low-pressure regions probed by transmission spectra. In fact, the atmosphere in this region may rarely be exactly isothermal, but current transmission spectra observations cannot differentiate between such small temperature changes in *P*-*T* profiles. However, future high resolution observations might permit this. Additionally, isothermal *P*-*T* profiles would give rise to a simple black body emission spectrum, devoid of spectral features. Furthermore, the emission spectrum is much more strongly directly dependent on the temperature than the transmission spectrum (Emission Flux $\propto$ Temperature^4). Therefore, to identify features in the emission as well as constrain the *P*-*T* profile using these features, we require computation of a more accurate non-isothermal *P*-*T* profile. Therefore, in this work we compute *P*-*T* profiles in radiative - convective equilibrium for various observationally significant exoplanets, along with their corresponding equilibrium chemical abundances, simulated transmission and emission spectra, and contribution functions.

Computing RCE *P*-*T* profiles consistent with equilibrium chemistry is not a trivial task. The *P*-*T* profile and the chemistry are intricately linked as they depend on each other. Chemistry is largely dependent on temperature, and temperature is largely dependent on composition (via opacities). Moreover, the *P*-*T* profile as well as the chemical abundance profile continuously evolve as the simulation progresses towards the solution. In such a scenario a large number of temperature and pressure points are encountered. Therefore, it is extremely difficult to obtain converged (satisfying all constraints) RCE *P*-*T* profiles for values across a large parameter space. There are always the regions of the parameter space where the simulations tend not to reach a converged solution due to many factors such as the boundary conditions, numerical instabilities, non-convergence of equilibrium chemistry especially with condensation and many more. We deal with such problems by tweaking the numerical setup for some of the failed model simulations as described in the next section.

In this chapter we first start by introducing the details of the numerical setup of this grid with RCE *P*-*T* profiles in Section 5.1, including the chemistry and opacity setup. This is followed by the implementation and validation of the recently included H- opacity in ATMO in Section 5.2. In Section 5.3 we describe the parameter space of the grid. In Section 5.4 we show the sensitivity of model simulations to different model choices by comparing RCE *P*-*T* profiles, equilibrium chemical abundances and the spectra, using two planets WASP-017b or WASP-121b as test cases. These model sensitivity tests include, comparison due to rainout and local condensation approaches in Section 5.4.1, comparison when adopting different Na and K line wing profiles in Section 5.4.2, comparison when adopting different VO line-lists in Section 5.4.3 and comparison with and without including convection in the model simulations in Section 5.4.4. Furthermore, comparison of model simulations varying O/H (Oxygen to Hydrogen ratio) with those varying C/H (Carbon to Hydrogen ratio), to vary C/O ratio is discussed in Section 5.4.5. In Section 5.5 we show decoupled model emission spectra for WASP-17b and WASP-121b for a particular combination of parameters from the grid, mainly to help identify major spectral features in the emission spectrum. In Section 5.6 we show the effects caused by high levels of irradiation by using extremely irradiated hot Jupiter WASP-121b as the test case. This includes the effect of thermal ionisation in Section 5.6.1, followed by the implications of recently added H- and Fe opacities in Section 5.6.2 and 5.6.3, respectively, and formation of inversion due to additional grey opacity or Fe opacity without any TiO/VO opacities, in Section 5.6.4. This is followed by sensitivity to grid parameters in Section 5.7. This includes the effect of varying the recirculation factor on the *P*-*T* profiles and the spectra using WASP-121b as the test case in Section 5.7.1, followed by the effect of varying metallicity and varying C/O ratio by varying O/H, on the *P*-*T* profiles and the spectra in Section 5.7.2 and 5.7.3, respectively, using both planets WASP-017b and WASP-121b as the test case. In Section 5.8, transmission and emission spectrum observations of WASP-121b are interpreted using the grid of models presented in this chapter. Finally, we summarise this chapter in Section 5.9.

5.1 Numerical setup for the Grid

We use 50 vertical model levels with a maximum optical depth of 5×10^5 at 1 µm. Since ATMO calculates quantities on the optical depth grid, the minimum and maximum optical depths govern the pressure domain (extent of the atmosphere). An increase in the maximum optical depth leads to an increase in the pressure domain of the P-T profile, for a given set of parameters. The model stability when solving for radiative-convective equilibrium, consistently with equilibrium chemistry, is very sensitive to the selected top of the atmosphere (minimum) optical depth boundary condition, as the atmosphere can become very sparse (less dense) in this region. Therefore, the top of the atmosphere optical depth is varied to achieve convergence. The typical values used for top of the atmosphere optical depth are 10^{-2}, 10^{-5}, 10^{-10} and 10^{-13} at 1 µm. Although this is a wide range for top of the atmosphere optical depth, these extremely low optical depth regions are outside the domains of the region probed by either transmission or emission spectra. Moreover, we find that the value of 10^{-5} is sufficient for most of the model simulations. The top of the atmosphere pressure is restricted to 10^{-6} bar, which corresponds to the top of the atmosphere minimum optical depth. Even though we vary the minimum optical depth to achieve convergence, the pressure is always set at 10^{-6} bar for this minimum optical depth, serving as a reference for the atmospheric P-T profile. We use 32 band correlated-k cross-sections for generating consistent RCE P-T profiles and 5000 bands to generate transmission spectra, emission spectra and contribution functions, as explained in detail in Chapter 2. We adopt a mixing length constant $\alpha = 1.5$ for calculating convective flux (Baraffe et al. 2015), as used in previous ATMO simulations (e.g Drummond et al. 2016).To standardise the comparison of transmission spectra for a range of variables, we set the pressure at which the radius of the planet is defined at 1 millibar (Lecavelier Des Etangs et al. 2008), only while computing the transmission spectra. We note that there exists a degeneracy between reference transit radius and associated reference pressure as highlighted by Lecavelier Des Etangs et al. (2008) and Heng et al. (2017). The input stellar spectra for each planetary model grid are taken from the BT-Settl[1] models (Allard et al. 2012; Rajpurohit et al. 2013). These stellar spectra are selected according to closest obtained host star temperature, gravity and metallicity from the TEPCAT database (Southworth 2011a). All the parameters required for model initialisation like stellar radius, planetary radius, planetary equilibrium temperature, surface gravity and semi-major axis are also adopted from the TEPCAT[2] database. The minimum and maximum step size while iterating the P-T profiles to obtain a converged solution is typically 0.1 and 0.9, respectively. This step size is basically the multiplying factor to the temperature perturbation while the model is iterating to obtain a converged solution. The minimum value of accuracy to achieve convergence is typically set to 10^{-3}, which corresponds to error in flux balance. The angle of incidence of the incoming beam of radiation as explained in Chapter 2 Section 2.2.3 and shown in Fig. 2.3 is taken as 60°, representing the dayside average, giving $\cos 60^\circ = 0.5$. The

---

[1] `https://phoenix.ens-lyon.fr/Grids/BT-Settl/AGSS2009/SPECTRA/`

[2] `http://www.astro.keele.ac.uk/jkt/tepcat/allplanets-ascii.txt`

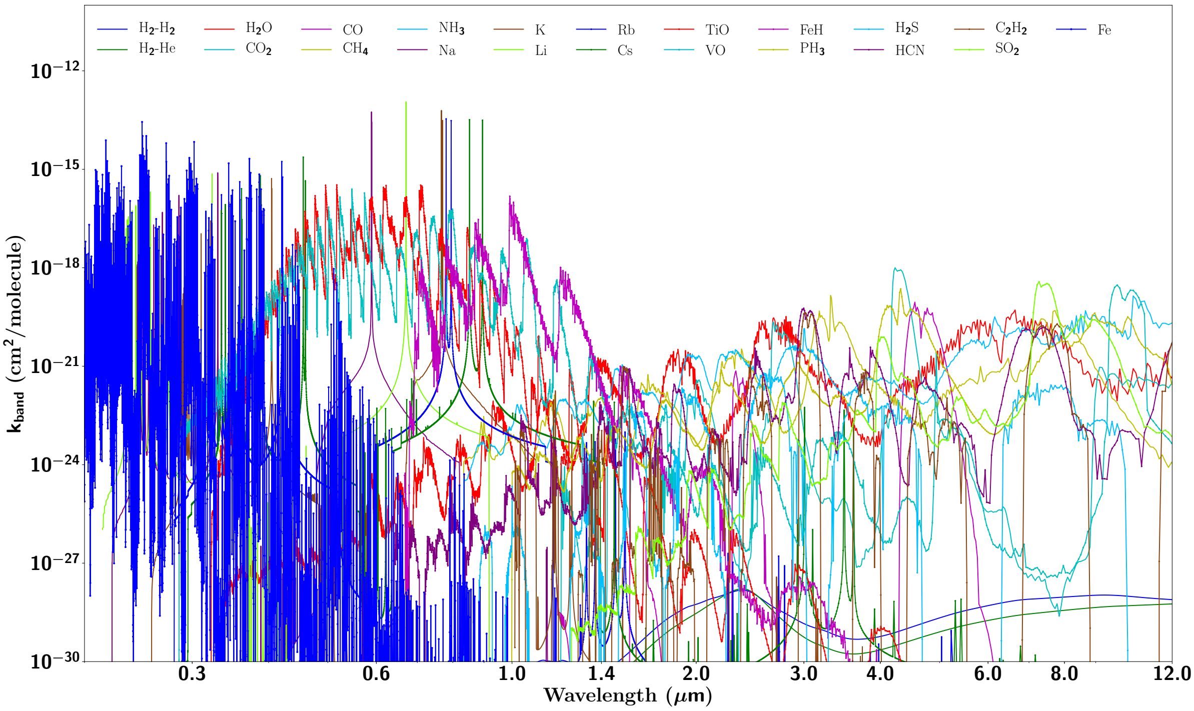

Figure 5.1: Absorption cross-sections (k_{band}) of all species used in ATMO in each of the 5000 correlated-k bands at 1 millibar and 1000 K. These are absolute cross-sections without any dependance on chemical abundances.

equation for contribution function is described in Chapter 2 Section 2.11. However, for plotting we compute Normalised Contribution Function (NCF), by normalising using the largest value of contribution function along the P-T profile.

5.1.1 Chemistry Setup

The chemistry for the calculations presented in this chapter are also restricted to equilibrium chemistry, as in Goyal et al. (2018) and Goyal et al. (2019b) (i.e in Chapters 3 and 4). However, the major addition to those previous works in terms of chemistry is the inclusion of ionization in the equilibrium chemistry computation. Therefore, in addition to 258 species as used in Goyal et al. (2018) and Goyal et al. (2019b) and listed in Chapter 3 Section 3.1.2, the list of species for equilibrium computation now also includes H+, H-, Na+, K+, e-, C+, He+, Ca+ and Si+ ions along with additional gaseous species NaF, KF, SiO, SiS, CaH, CaOH and condensate species Na_3AlF_6 in three different forms and LiF in the crystalline form. Thus the total number of species used in equilibrium chemistry calculation adds up to 277 for simulations presented here.

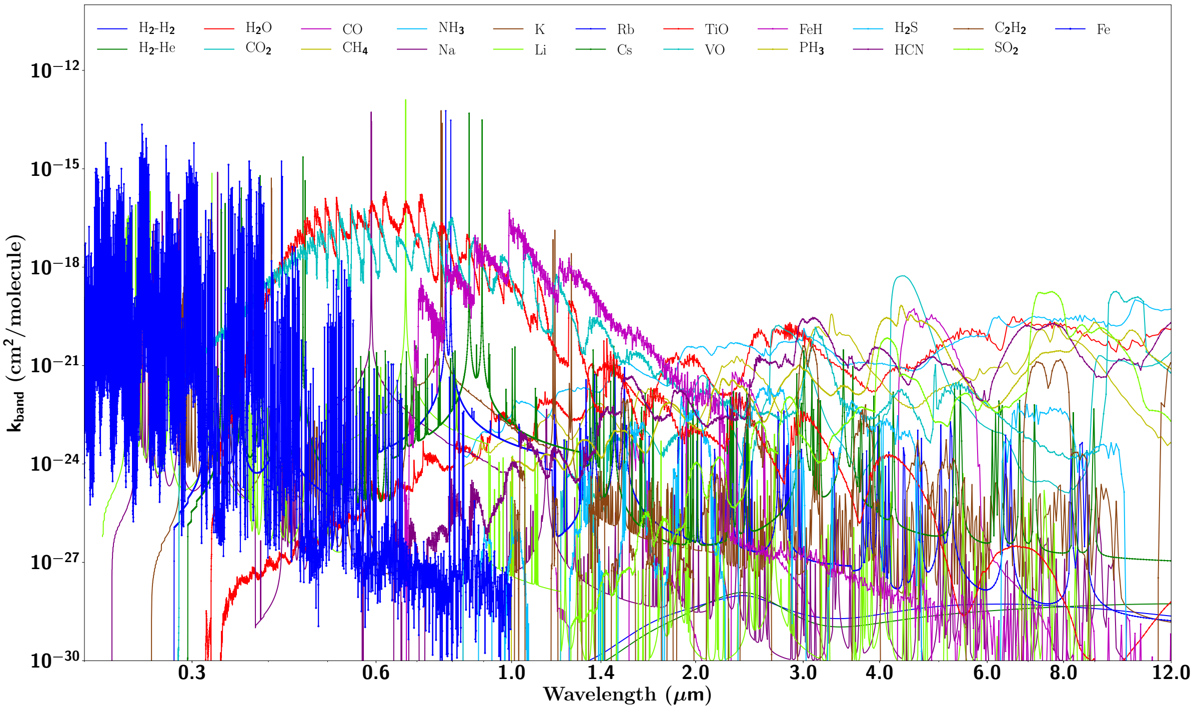

Figure 5.2: Same as Figure 5.1 but at 1 millibar and 2000 K.

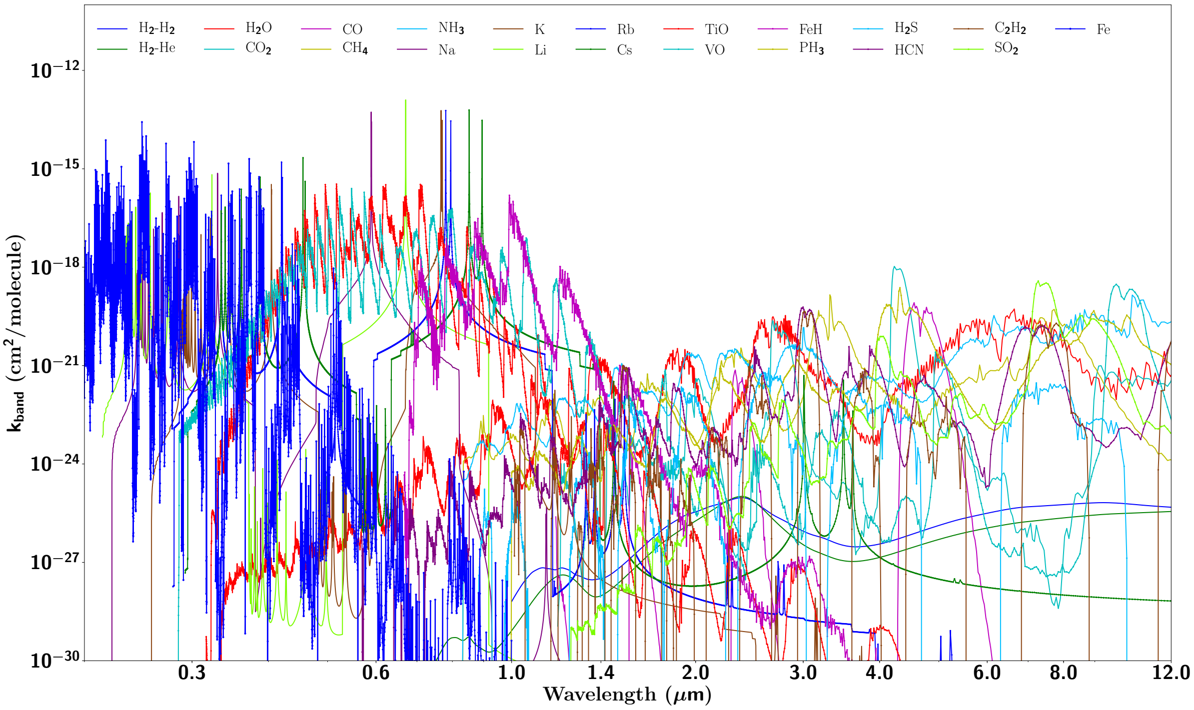

Figure 5.3: Same as Figure 5.1 but at 1 bar and 1000 K.

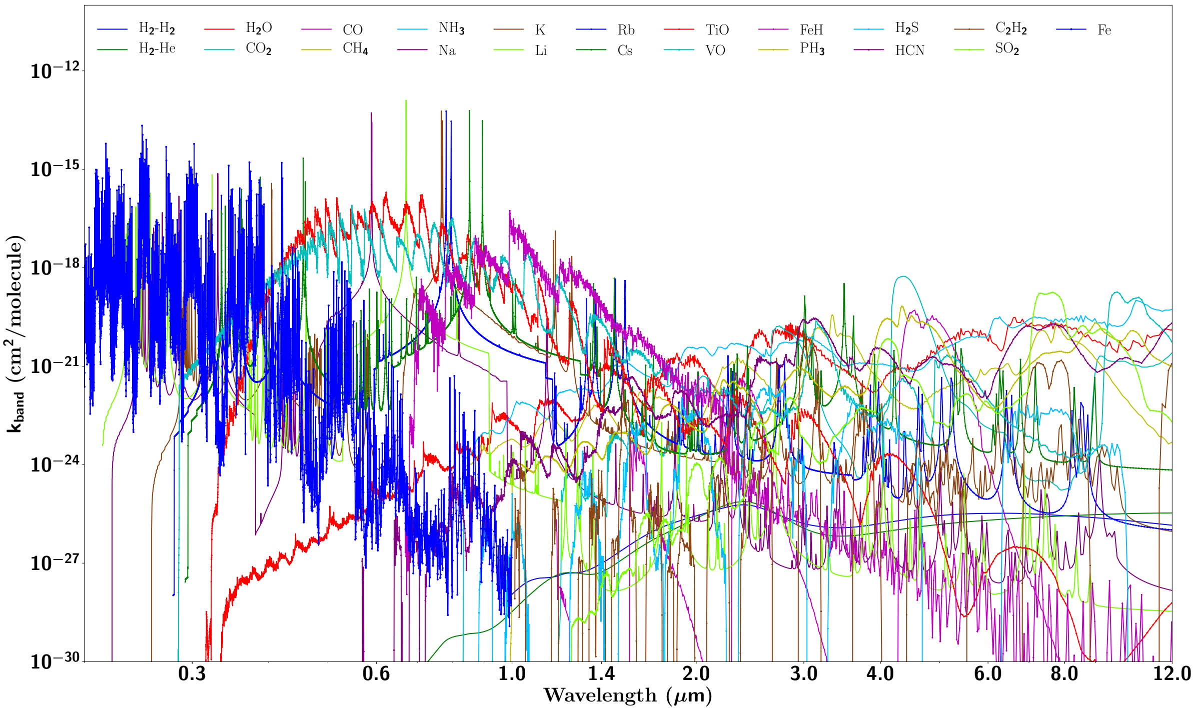

Figure 5.4: Same as Figure 5.1 but at 1 bar and 2000 K.

5.1.2 Opacity Setup

As described in Chapter 2 the potential of a particular species to absorb/emit radiation at a particular wavelength/wavenumber is governed by its absorption cross-sections. These cross-sections are then binned into various bands for computational efficiency, using the correlated-k technique, as described in Chapter 2. Compared to the simulations presented in Chapter 3 and 4, the opacities due to H- and Fe have been newly included in this work, in addition to H_2-H_2 and H_2-He collision induced absorption (CIA) opacities, and opacities due to H_2O, CO_2, CO, CH_4, NH_3, Na, K, Li, Rb, Cs, TiO, VO, FeH, CrH, PH_3, HCN, C_2H_2, H_2S and SO_2. The implementation of H- opacity is described in Section 5.2. The effect of these newly added opacities, H- and Fe on the P-T profiles and thereby the spectra is discussed in Section 5.6.2 and 5.6.3, respectively.

Absorption cross-sections for all the species included in ATMO in each of the 5000 correlated-k bands at 1 millibar and 1000 K, 1 millibar and 2000 K, 1 bar and 1000 K and, 1 bar and 2000 K are shown in Figures 5.1, 5.2, 5.3 and 5.4, respectively. These plots will help in identifying major absorbing species in various parts of the spectrum. However, it must be noted that the final opacities are the product of absorption cross-sections and chemical abundances. Therefore, although species such as TiO,VO, FeH, Fe have strong absorption cross-sections in the optical their contribution to total absorption will be zero if they condense or don't form at any given temperature.

5.2 Implementation and Validation of H- opacity

Recently, a series of publications highlighted the importance of H- opacity in the atmospheres of extremely irradiated hot Jupiters (Arcangeli et al. 2018; Mansfield et al. 2018; Kreidberg et al. 2018; Parmentier et al. 2018). Therefore, we also included H- opacities in `ATMO` and investigated its effects on the P-T profiles and thereby the spectra. The H- opacity was implemented using the analytical equations of John (1988). The formation of species H- (hydrogen anion) is basically a result of electron attachment, driven by presence of abundant hydrogen (H) and low energy electrons in the ionised atmospheres of stars or hot Jupiters (Rau 1996). The absorption of electromagnetic radiation by H- is driven by photo-detachment (bound-free) and free-free transition processes. These are computed using analytical equations from John (1988) derived from the original derivation of free-free transition in Bell et al. (1987).

The photo-detachment process of H- absorption is given by

$$h\nu + \mathrm{H}^- \longrightarrow \mathrm{H} + \mathrm{e}^-, \tag{5.1}$$

where h is the Planck's constant and ν is the frequency of radiation. In this process H- ions absorbs radiation of frequency ν, to form atomic hydrogen and an electron. As shown in John (1988) for wavelengths (λ) less than the ionisation threshold λ of H- ($\lambda < 1.6419$ µm) this is computed using,

$$k_{bf}(\lambda) = 10^{-18}\lambda^3\left(\frac{1}{\lambda} - \frac{1}{\lambda_0}\right)^{3/2} f(\lambda), \tag{5.2}$$

$$where,$$

$$f(\lambda) = \sum_{n=1}^{6} C_n \left[\frac{1}{\lambda} - \frac{1}{\lambda_0}\right]^{(n-1)/2},$$

where $k_{bf}(\lambda)$ is the bound-free cross-section of H- in units of cm^2, λ is the wavelength, $\lambda_0 = 1.6419$ µm is the threshold wavelength, C_n are the coefficients for n different values given in the Table 2 of John (1988). The bound-free absorption cross-section above the threshold λ of 1.6419 µm is zero. The total opacity due to bound-free absorption is then computed using,

$$\kappa_{bf} = k_{bf}(\lambda, T)A[H^-]\frac{n_d}{\rho} \tag{5.3}$$

where κ_{bf} is the total bound-free opacity, $A[H^-]$ is the abundance of H- (mixing ratio), n_d is the atmospheric number density (cm^{-3}) and ρ is the atmospheric mass density (g/cm^3).

The free-free transition process of H- is given by

$$h\nu + \mathrm{e}^- + \mathrm{H} \longrightarrow \mathrm{H} + \mathrm{e}^-. \tag{5.4}$$

In this reaction photons can be absorbed by electrons interacting with neutral hydrogen atom across the whole spectral range ($0 < \lambda < \infty$). This process is solely responsible for H- opacity beyond the ionisation threshold wavelength (1.6419 µm). This is computed using

$$k_{ff}(\lambda, T) = 10^{-29} \sum_{n=1}^{6} \left(\frac{5040}{T}\right)^{(n+1)/2} (\lambda^2 A_n + B_n + C_n/\lambda + D_n/\lambda^2 + E_n/\lambda^3 + F_n/\lambda^4) \tag{5.5}$$

where $k_{ff}(\lambda, T)$ is the free-free cross-section of H- in units of cm^4/$dyne$ and T is the temperature. A$_n$, B$_n$, C$_n$, D$_n$, E$_n$ and F$_n$ are coefficients as given in table 3a and 3b of John (1988) for $\lambda > 0.3645$ µm and $0.1823 < \lambda < 0.3645$ µm, respectively. By multiplying by Boltzmann's constant (1.38×10^{-16} erg/s) and temperature, $k_{ff}(\lambda, T)$ is obtained in the units of cm^5. The total opacity due to free-free absorption is then computed using,

$$\kappa_{ff} = k_{ff}(\lambda, T) A[H] \frac{n_d}{\rho} A[e^-] n_d \tag{5.6}$$

where κ_{ff} is the total free-free opacity, $A[H]$ is the abundance of neutral hydrogen (mixing ratio) and $A[e^-]$ is the abundance of electron (mixing ratio). The total opacity of the H- ion (κ_{tot}) due to bound-free and free-free transitions is then given by $\kappa_{tot} = \kappa_{bf} + \kappa_{ff}$.

5.2.1 Validating H- Opacity

We validate the abundance weighted H- opacity by comparing with the results from Parmentier et al. (2018) and Mansfield et al. (2018). Figure 4 of Parmentier et al. (2018) shows the abundance weighted absorption cross-section of H- (cm^2/molecule) as a function of wavelength at the P-T point of 0.042 bar and 3100 K. We also compute the abundance weighted absorption cross-section of H- at this P-T point within ATMO using $\kappa_{tot} \times \frac{\mu_{mean}}{N_A}$, where κ_{tot} is the total opacity of the H- ion computed as shown in the previous section, μ_{mean} is the mean molecular weight of the atmosphere and N$_A$ is the Avogadro's constant. The comparison

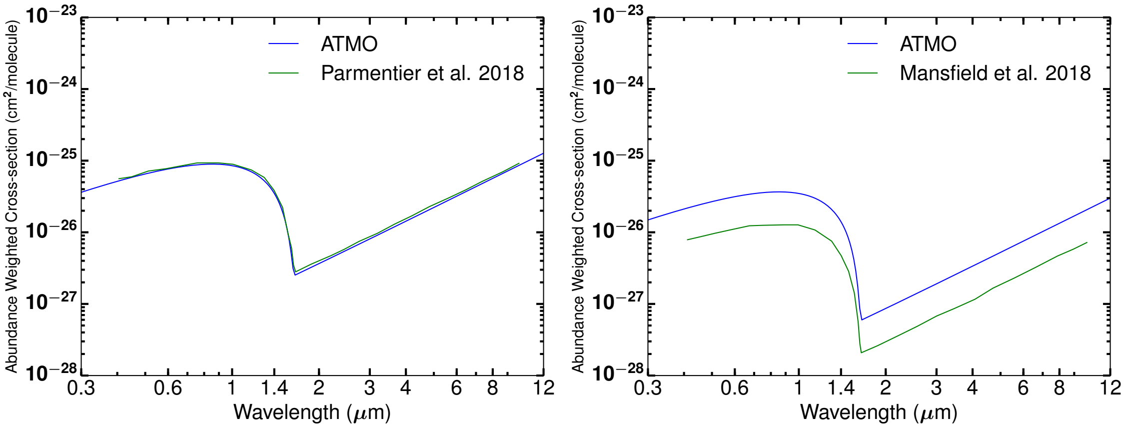

(a) (b)

Figure 5.5: **(a)** Figure showing abundance weighted cross-section of H- at 0.042 bar and 3100 K from Figure 4 of Parmentier et al. (2018) (green) and from ATMO (blue). **(b)** Figure showing abundance weighted cross-section of H- at 0.084 bar and 2756 K from Figure 7 of Mansfield et al. (2018) (green) and from ATMO (blue).

is shown in Figure 5.5a. Figure 5.5a shows that the agreement is quite good and even the equilibrium chemical abundances at this *P*-*T* point are similar in ATMO and Parmentier et al. (2018) (from Figure 3 in their paper), thus validating the implementation of H- opacity in ATMO.

Figure 7 of Mansfield et al. (2018) shows the abundance weighted absorption cross-section of H- at a *P*-*T* point of 0.084 bar and 2756 K. When compared with this, there is a substantial difference between the abundance weighted absorption cross-section of H- as shown in Figure 5.5a. The primary reason being the difference in equilibrium chemical abundances at this *P*-*T* point, which is ∼3.4 times larger in ATMO as compared to Mansfield et al. (2018). However, when this factor of 3.4 is taken into consideration while comparing the abundance weighted absorption cross-section of H- from both models, there is a good agreement (not shown here). The reason for differences in equilibrium chemical abundances is still unclear and can be due to many factors, such as the differences in input elemental abundances, polynomial coefficients etc. as shown in Goyal et al. (2019a). We note that the equilibrium chemistry scheme used in ATMO has been validated by comparing to various numerical and analytical equilibrium chemistry models, with local and rainout condensation (Drummond et al. 2016; Goyal et al. 2019a).

5.3 Grid Parameter Space

In Chapter 2, we defined the recirculation factor, metallicity and C/ O ratio. The library of models with RCE *P*-*T* profiles and corresponding equilibrium chemical abundances, transmission spectra, emission spectra and contribution functions for various planets are computed at four different recirculation factors (0.25, 0.5, 0.75, 1.0), six metallicities (0.1, 1, 10, 50, 100, 200; all in × solar) and six C/O ratios (0.35, 0.56, 0.7, 0.75 1.0,1.5), giving a total of 144 model RCE *P*-*T* profiles and spectra per planet. However, as mentioned earlier, not all models in the parameter space achieve convergence, thus leading to absence of some models in the library ($\sim$5-10%) which varies for different planets.

The choice of recirculation factor (RCF) covers all possible scenarios from no recirculation (1.0) to extremely fast winds (0.25). We do not extend the grid to metallicities greater than 200× solar, because above this metallicity the atmosphere becomes abundant in species other that H_2 and He, such as CO_2, H_2O, CO etc. This would require the inclusion of pressure broadening effects due to these species, and no existing studies have solved this problem due to lack of lab-based observational data (Fortney et al. 2016). The choice of C/O ratios in the grid is guided by important transition regimes as found by previous studies (Madhusudhan 2012; Mollière et al. 2015; Goyal et al. 2018).

As discussed in Chapters 3 and Chapter 4, there are two approaches to treat condensation in our library of models, rainout and local condensation. While computing equilibrium chemical abundances to obtain RCE *P*-*T* profiles with rainout condensation, each layer is dependent on other layers, specifically only on layers that lie at higher pressures, in contrast to the local condensation approach where each layer is independent. This makes the assumption of rainout with RCE *P*-*T* profiles more likely to resemble a real planetary atmosphere as compared to just local condensation. Therefore, we generate RCE *P*-*T* profiles with rainout condensation for the library of models presented in this chapter. However, we show the differences in the *P*-*T* profiles and the spectra due to both approaches in the next section.

The structure of the pressure broadened line wings of Na and K can have a substantial effect on the *P*-*T* profiles and thereby the emission spectrum of Brown dwarfs and hot Jupiter exoplanet atmospheres (Burrows et al. 2000; Allard et al. 2003). Even with their high resolution measurements, the shape of the pressure broadened wings are still a matter of debate for Brown dwarfs (Burrows et al. 2002; Burgasser et al. 2003; Allard et al. 2003). For hot Jupiters we have very recently started to observationally probe the line wings of Na/K (Nikolov et al. 2018). In Section 5.4.2 we show the differences in the *P*-*T* profiles and the spectra due to these two line wing profiles for Na and K. The differences are negligible and unlikely to be detectable by observations. We adopt the Na and K line wing profiles from (Allard et al. 2003) for the library of models presented in this chapter, which includes detailed quantum mechanical calculations while computing these profiles (Amundsen 2015).

Although convection plays an important role in determining the P-T profile of brown dwarfs, we see for hot Jupiter exoplanet atmospheres the effect of convection on the P-T structure is negligible. The P-T profile comparison with and without including convection is discussed in Section 5.4.4, which shows negligible differences. This is because of the strong irradiation on these planets from their host stars, which reduces the radiative time scale, thus making the atmospheric P-T profile entirely dependant on the top of the atmosphere irradiation (along with the atmospheric pressure, temperature and heat capacity), at-least in the region where observations can probe the atmosphere. Therefore, we conclude that it is not necessary to include convection while computing RCE P-T profiles for irradiated hot Jupiter exoplanet atmospheres. However, in this chapter all the P-T profiles (except in Section 5.4.4) include convection for testing, as it is computationally inexpensive, but will not be included for the entire library of models.

5.4 Sensitivity to Model Choices

5.4.1 Comparing model simulations with rainout and local condensation

Rainout and local condensation approaches result in the differences in transmission spectra with isothermal P-T profiles, as shown in Chapters 3 and 4. Here, we investigate the effects of these two condensation approaches on the RCE P-T profiles and thereby the equilibrium chemical abundances, and transmission and emission spectra. Fig. 5.6a, 5.6b, 5.6c, 5.6d and 5.6e, show the RCE P-T profiles, equilibrium chemical abundances, transmission spectra, emission spectra and Normalised Contribution Functions (NCF), respectively, for WASP-017b at 0.25 RCF, solar metallicity and solar C/O ratio, with rainout and local condensation . A difference of ∼100-300 K can be seen between the 1 and 100 mbar pressure levels in Fig. 5.6a, with the P-T profile adopting the local condensation approach having higher temperatures. However, in the deeper atmosphere (∼ 0.1-1000 bar) the P-T profile with rainout condensation is hotter by ∼200 K. This difference in temperature leads to lower abundance of Na and K in the upper atmosphere and a higher abundance of TiO/VO in the local condensation case, as compared to rainout condensation case, shown in Fig. 5.6b. This higher TiO/VO abundance can also be noticed in the transmission spectra shown in Figure 5.6c where the spectra with local condensation show TiO/VO features in the optical, missing in the rainout condensation case. This also strengthens the findings of Goyal et al. (2019b), that TiO/VO features can reveal dominant physical process (rainout or local condensation) in the planet's atmosphere.

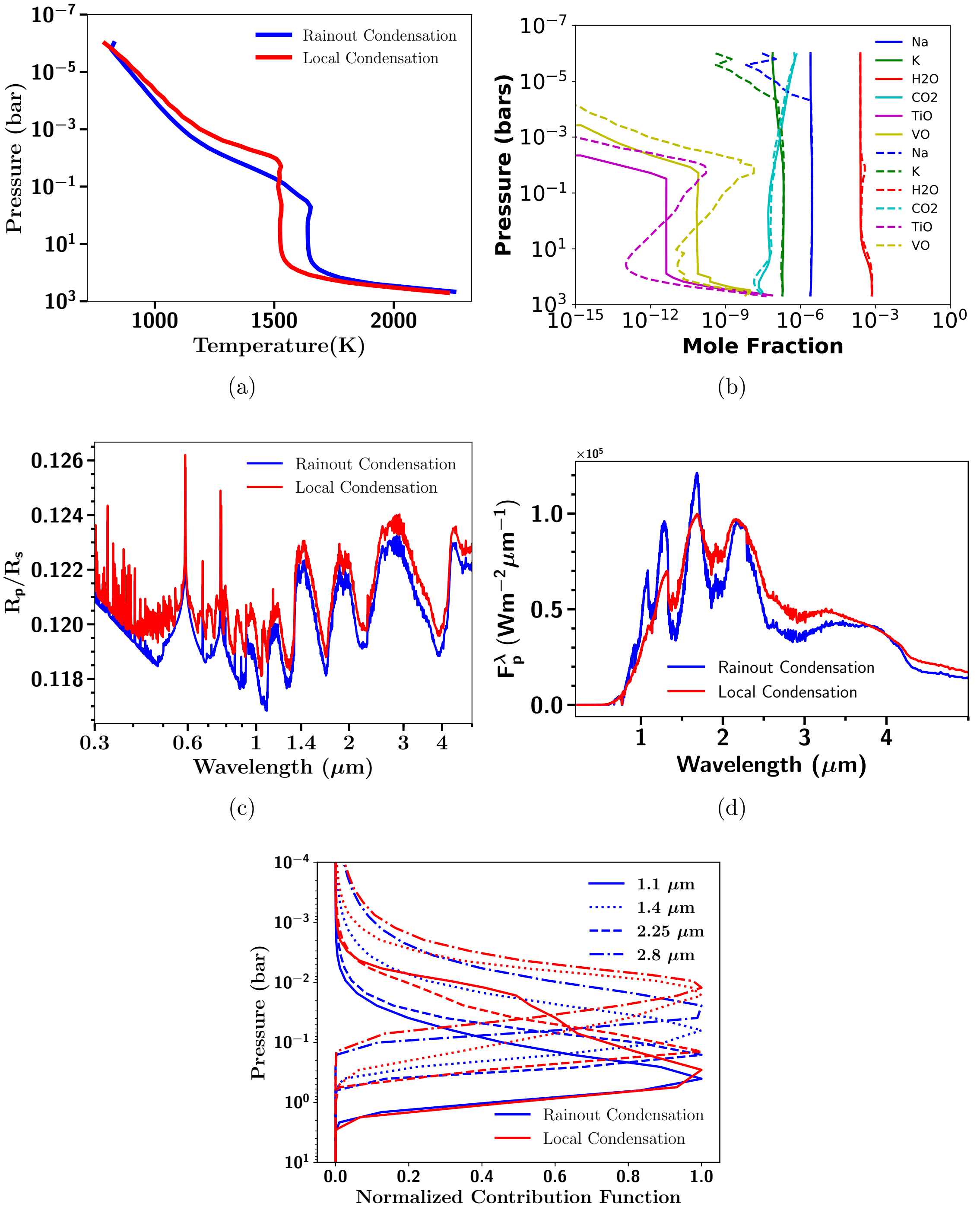

(a) (b) (c) (d) (e)

Figure 5.6: **(a)** Figure showing RCE *P*-*T* profiles for WASP-017b at 0.25 recirculation factor (RCF) and solar metallicity and solar C/O ratio, with rainout (blue) and local condensation (red). **(b)** Figure showing equilibrium chemical abundances of important species using *P*-*T* profiles shown in Figure 5.6a, with rainout (solid) and local condensation (dashed). **(c)** Figure showing transmission spectra using *P*-*T* profiles shown in Fig. 5.6a and chemical abundances shown in Figure 5.6b, with rainout (blue) and local condensation (red). **(d)** Figure showing emission spectra using *P*-*T* profiles shown in Fig. 5.6a and chemical abundances shown in Figure 5.6b, with rainout (blue) and local condensation (red) .**(e)** Figure showing contribution function for emission spectra shown in Fig. 5.6d, with rainout (blue) and local condensation (red) at 1.1 (solid), 1.4 (doted), 2.25 (dashed) and 2.8 (dot-dash) μm.

The differences in the emission spectra shown in Fig. 5.6d are substantial, primarily due to the differences in the *P*-*T* structure. At 1.1 μm deeper parts of the atmosphere (~1 bar) are being probed as seen in the NCF shown in Fig. 5.6e, mainly because none of the species have a strong opacity to absorb in this region. Therefore, it can be seen in the emission spectra that the flux is higher for rainout condensation as compared to local condensation, since the temperature at ~1 bar is higher for the simulation adopting rainout condensation. At 1.4 μm the wavelength of one of the strongest water opacity bands, we see the NCF moves to the upper atmosphere and the difference between the pressure levels being probed by observations of emission in the case of the rainout (0.1 bar) and local condensation (0.01bar) simulations are also substantially different. This is mainly due to the large difference in the temperatures between the rainout and local condensation simulations between 0.1 and 0.01bar. However, in the emission spectra the difference in the flux between both condensation approaches is very low. This is because the differences in the pressure level probed leads to almost similar emission temperatures (~1500 K) for both as can be noticed from *P*-*T* profiles in Fig. 5.6a. These simulations reveal an important result that even though the emission spectrum of two different *P*-*T* structure are similar, the pressure level of the atmosphere that they probe can be substantially different. The difference in the peak pressure level of the NCF as observed between 1.1 and 1.4 μm, the wing and core of water band, respectively, can be observed more strongly at 2.25 and 2.8 μm, since this is the region of peak emission for body with temperature similar to the equilibrium temperature of WASP-017b. It might be possible to distinguish between emission spectra due to rainout and local condensation, and therefore constrain the *P*-*T* profiles and thereby the condensation processes using JWST.

5.4.2 Comparing model simulations with different Na and K line wing profiles

Figure 5.7a shows the Na and K cross-sections at 1000 K and 1 mbar with line profiles from Burrows et al. (2000) which is primarily Lorentzian and from Allard et al. (2003) which uses more detailed quantum mechanical calculations. It can be noticed from this figure that the differences are primarily in the pressure broadened wings.

The effect of these line profiles on the RCE *P*-*T* profiles, transmission and emission spectra are shown in Figure 5.7b, 5.7c and 5.7d, respectively, for WASP-017b at 0.25 RCF, solar metallicity and solar C/O ratio. The differences are negligible and likely not detectable with current observations, in all cases.

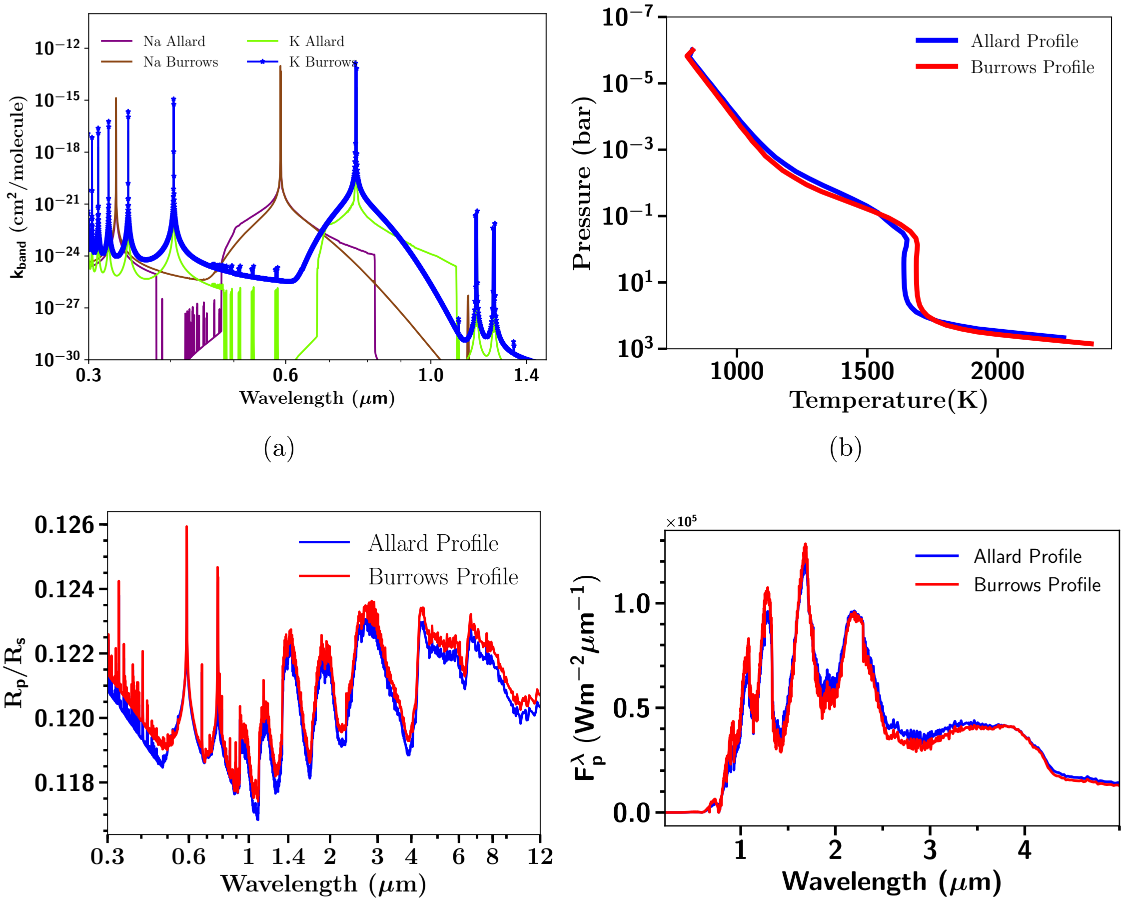

(a) (b)

(c) (d)

Figure 5.7: **(a)** Figure showing absorption cross-sections (cm^2/molecule) of Na and K using two different pressure broadening treatments from Allard et al. (2003) and Burrows et al. (2000) **(b)** Figure showing RCE *P*-*T* profiles using two different pressure broadening profiles (Allard and Burrows) for Na and K, shown in Figure 5.7a, for WASP-017b at solar metallicity and solar C/O ratio with 0.25 RCF. **(c)** Transmission spectra for WASP-017b using *P*-*T* profiles shown in Figure 5.7b, and two different pressure broadening profiles, namely, Allard and Burrows. **(d)** Emission spectra for WASP-017b using *P*-*T* profiles shown in Figure 5.7b, and two different pressure broadening profiles, namely, Allard and Burrows.

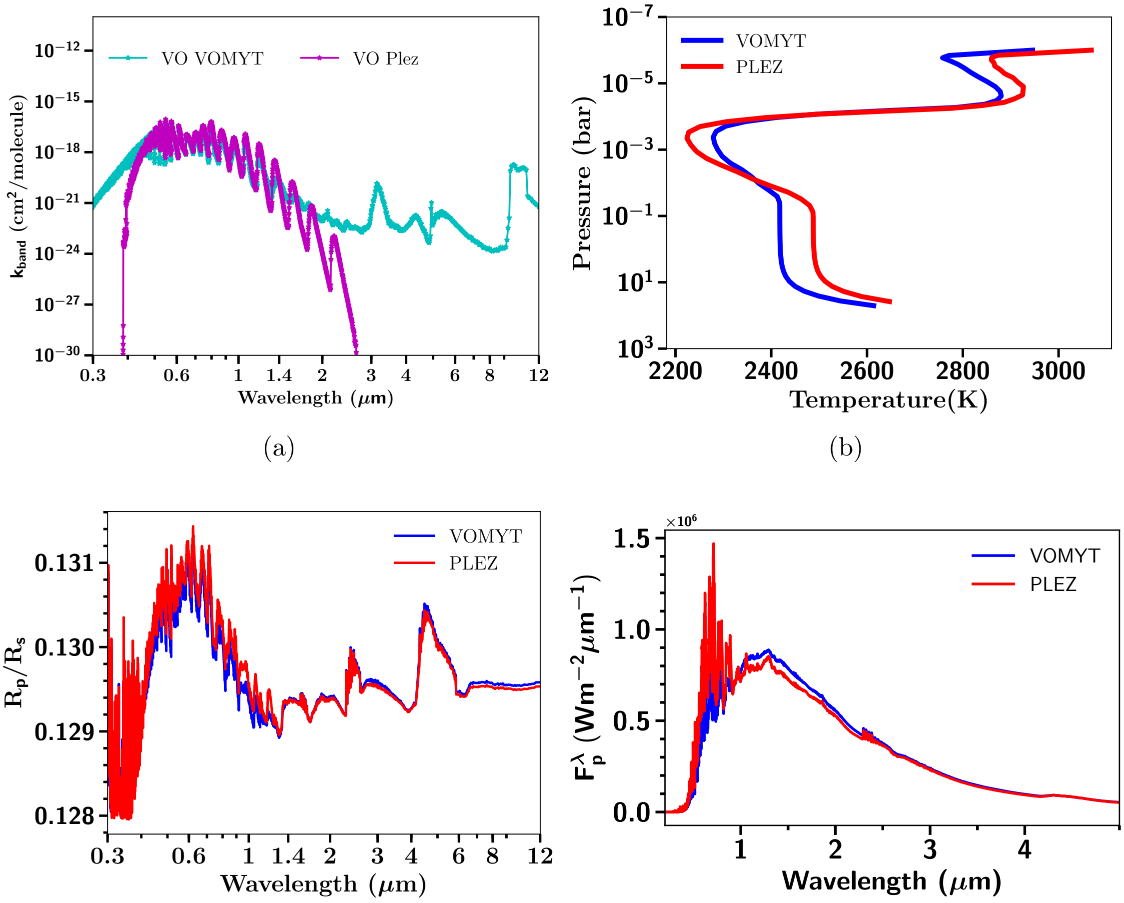

(a)

(b)

(c)

(d)

Figure 5.8: **(a)** Figure showing absorption cross-sections (cm^2/molecule) of VO using different two different line-lists VOMYT (McKemmish et al. 2016) and PLEZ (Plez 1999) **(b)** Figure showing RCE *P*-*T* profiles using different VO line-list named PLEZ and VOMYT for WASP-121b at 200x solar metallicity and solar C/O ratio with 0.5 RCF. **(c)** Transmission spectra for WASP-121b using *P*-*T* profiles shown in Figure 5.8b, and two different VO line-lists. **(d)** Emission spectra for WASP-121b using *P*-*T* profiles shown in Figure 5.8b, and two different VO line-lists.

5.4.3 Comparing model simulations with different VO line-list sources

Vanadium Oxide (VO) has been predicted to be the major absorber in the atmosphere of WASP-121b leading to an inversion, with the hints of VO features detected in the transmission and emission spectrum of WASP-121b (Evans et al. 2017; Evans et al. 2018). In ATMO we initially included the VO line-list from Plez (1999), this was updated to new high temperature VO line-list from Exomol named as VOMYT (McKemmish et al. 2016). Figure 5.8a show the differences in the cross-sections computed using both line-lists. It can be seen that the new line-list (VOMYT) is more complete, especially in the infrared. Surprisingly, there is also a strong VO absorption band in the infrared between 10-12 μm in the new VO line list (McKemmish et al. 2016) in comparison to the old line-list. There are two important peaks one near 3 μm and other a broad band peak between 10-12 μm, offering a potential wavelength region to detect VO using JWST. The effect of using different line-lists on the RCE P-T profiles is shown in Figures 5.8b at 200 times solar metallicity for WASP-121b. At solar metallicity and solar C/O ratio with 0.5 RCF, there is no difference in the RCE P-T profiles generated using the two different line-lists (not shown here), due to comparatively low abundance of VO. However, when the metallicity is increased to 200x solar, the abundance of VO increases, (see Figure 3.21b in Chapter 3) rising to $\sim$1000 times than that at solar metallicity. These enhanced abundances are then sufficient to create differences between the P-T profiles obtained using the two different line-lists. Moreover, retrieval models have also predicted the presence of substantially large abundances of VO ($\sim$ 1000x solar abundance), required to produce an inversion in the atmosphere of WASP-121b (Evans et al. 2017). At 200× solar metallicity, the P-T profile obtained using the VOMYT line-list is hotter by $\sim$ 50 K around 1 millibar region, but this absorption of radiation in the upper atmosphere leads to cooling in the deeper atmosphere from 0.1 to 10 bar by about 100 K.

The effect of different VO line-lists on the transmission and emission spectra of WASP-121b are shown in Figure 5.8c and 5.8d, respectively. In the transmission spectra the differences are only in the size of the features which is a combination of difference in P-T profiles, abundances and small differences in line-lists. In the emission spectra, the difference is a result of differences in the P-T profile. As the temperature in the region of the inversion which is probed by emission spectra is higher for VOMYT than PLEZ, it leads to higher value of F_p^λ (planetary flux) in the near infrared wavelengths ($> 1\,\mu$m), thus producing differences.

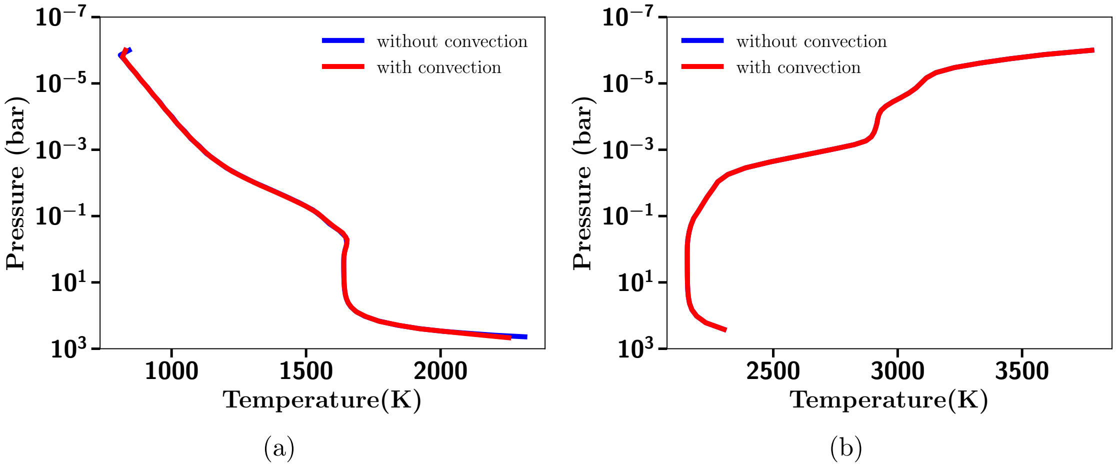

Figure 5.9: **(a)** Figure showing RCE *P*-*T* profiles for WASP-017b at 0.25 RCF and solar metallicity and solar C/O ratio, without (blue) and with (red) convection. **(b)** Same as Figure 5.9a but for WASP-121b at 0.5 RCF and solar metallicity and solar C/O ratio.

5.4.4 Comparing model simulations with and without convection

Figure 5.9a and 5.9b show *P*-*T* profiles for simulations of WASP-017b and WASP-121b, respectively, with and without convection. It can be seen that the differences in the *P*-*T* profiles for both planets are negligible, implying that convection plays no role in determining the *P*-*T* structure across the pressures we simulate for irradiated hot Jupiters with sufficiently high temperatures.

5.4.5 Comparing model simulations varying O/H with those varying C/H to vary C/O ratio.

As mentioned earlier in Chapter 2 there are three different methodologies to vary C/O ratio relative to solar C/O ratio of 0.55. In Chapters 3 and 4 we varied C/O ratio by varying O/H as adopted in (Goyal et al. 2019b, 2019b). However, varying C/O by varying C/H can lead to differences in *P*-*T* profiles and equilibrium chemical abundances as shown by Drummond et al. (2019). Therefore, here we show the differences in the *P*-*T* profiles and the spectra between the simulations, varying C/O ratio by varying O/H and those by varying C/H, using WASP-017b and WASP-121b as the test cases. We note that when we vary C/H or O/H we keep the abundances of other species to their solar value or to a metallicity scaled value.

WASP-017b Figures 5.10a shows the *P*-*T* profiles at a C/O ratio of 0.35 resulting from varying O/H and C/H for WASP-017b. We can see there are differences of

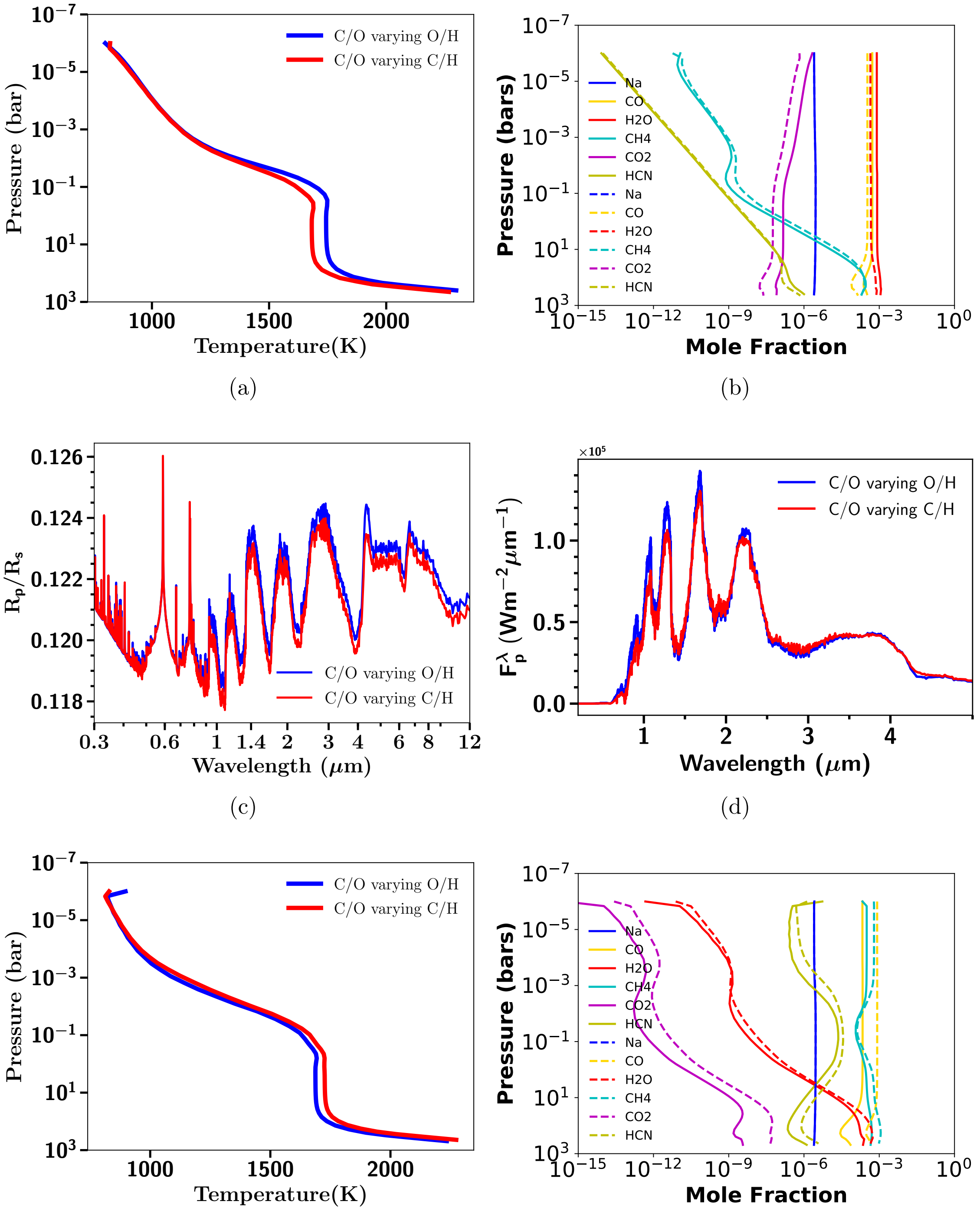

(a) (b)

(c) (d)

(e) (f)

Figure 5.10: **(a)** Figure showing *P*-*T* profiles with C/O ratio of 0.35 by varying C/H (red) and O/H (blue) relative to solar C/O ratio (0.55) at 0.25 RCF and solar metallicity for WASP-017b. **(b)** Figure showing equilibrium chemical abundances for *P*-*T* profiles shown in Fig. 5.10a by varying C/H (solid) and O/H (dashed)**(c)** Figure showing transmission spectra using *P*-*T* profiles shown in Fig. 5.10a and chemical abundances shown in Fig. 5.10b **(d)** Figure showing emission spectra using *P*-*T* profiles shown in Fig. 5.10a and chemical abundances shown in Fig. 5.10b **(e)** Same as Fig. 5.10a but for C/O ratio of 1.5. **(f)** Same as Fig. 5.10b but for C/O ratio of 1.5.

the order of 50 K between the two profiles. The differences can also be seen in the equilibrium chemical abundances shown in 5.10b. The abundances of H_2O, CO and CO_2 are slightly larger when O/H is varied, compared to the same C/O ratio model where C/H is varied. This is because for C/O ratios less than 1, abundances of these species are limited by the carbon abundance (more so for CO as it is the dominant molecule), therefore when O/H is varied to reach a C/O ratio of 0.35, O/H is increased thus favouring an increase in oxygen bearing species. On the contrary if C/H is varied, it has to be decreased (keeping O/H constant) to reach a C/O ratio of 0.35 thus limiting (decreasing) the formation of carbon bearing species. There is also an effect caused by the changing of P-T profile which can be seen for CH_4 as its abundances are mainly different in the region where there are larger differences in P-T profiles, between simulations varying either O/H or C/H, at the same C/O ratio. The changing P-T profile will also have an effect on other species. These differences can also be seen in the transmission and emission spectra shown in Fig. 5.10c and 5.10d, respectively, primarily at 4.5 μm due to CO.

Figures 5.10e and Figures 5.10f show the P-T profiles and equilibrium chemical abundances similar to Fig. 5.10a and 5.10b, respectively, but at a C/O ratio of 1.5. At a C/O ratio of 1.5 differences can again be seen in the P-T profiles and abundances. However, in this case since the C/O ratio is greater than 1, the abundances are limited by the O/H abundance. Therefore, the abundance of carbon bearing species is larger when C/H is varied as compared to when O/H is varied at C/O ratios > 1. However, it must be noted that the effect of changing P-T profiles is also embedded in this difference.

WASP-121b Figures 5.11a shows the P-T profiles at a C/O ratio of 0.35 obtained from simulations varying O/H and C/H for WASP-121b. Similar to WASP-017b there are differences in the P-T profile and the chemical abundances shown in Fig. 5.11b. Similarly, the abundance of H_2O, CO and CO_2 are also slightly larger when O/H is varied. The differences in the transmission spectra shown in Fig. 5.11c are basically due to differences in the size of the features due to differences in abundances. The differences in the emission spectra shown in Fig. 5.11c are negligible, as the RCE P-T profile adjusts itself to maintain energy balance.

Figures 5.11e and Figures 5.11f show the P-T profiles and equilibrium chemical abundances similar to Fig. 5.11a and 5.11b, respectively, but at a C/O ratio of 1.5. In this case a similar trend as observed for WASP-017b is seen, since for C/O ratios > 1, abundances are limited by the O/H abundance. Therefore, the abundance of carbon bearing species is larger when C/H is varied, as opposed to when O/H is varied, at C/O ratios > 1.

In this section we presented the differences in the P-T profiles and the spec-

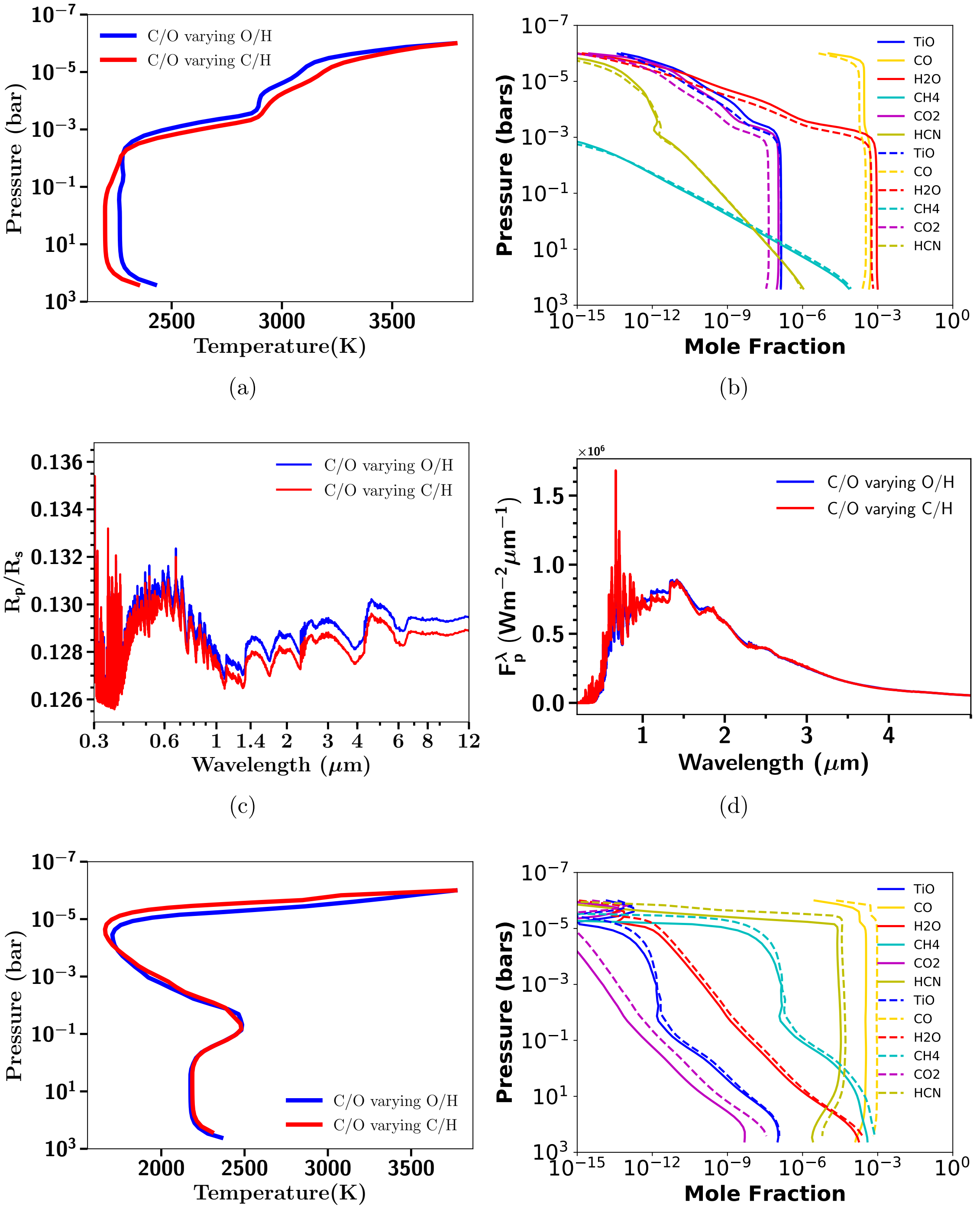

(a) (b) (c) (d) (e) (f)

Figure 5.11: **(a)** Figure showing *P*-*T* profiles with C/O ratio of 0.35 by varying C/H (red) and O/H (blue) relative to solar C/O ratio (0.55) at 0.5 RCF and solar metallicity for WASP-121b. **(b)** Figure showing equilibrium chemical abundances for *P*-*T* profiles shown in Fig. 5.11a by varying C/H (solid) and O/H (dashed)**(c)** Figure showing transmission spectra using *P*-*T* profiles shown in Fig. 5.11a and chemical abundances shown in Fig. 5.11b **(d)** Figure showing emission spectra using *P*-*T* profiles shown in Fig. 5.11a and chemical abundances shown in Fig. 5.11b **(e)** Same as Fig. 5.11a but for C/O ratio of 1.5. **(f)** Same as Fig. 5.11b but for C/O ratio of 1.5.

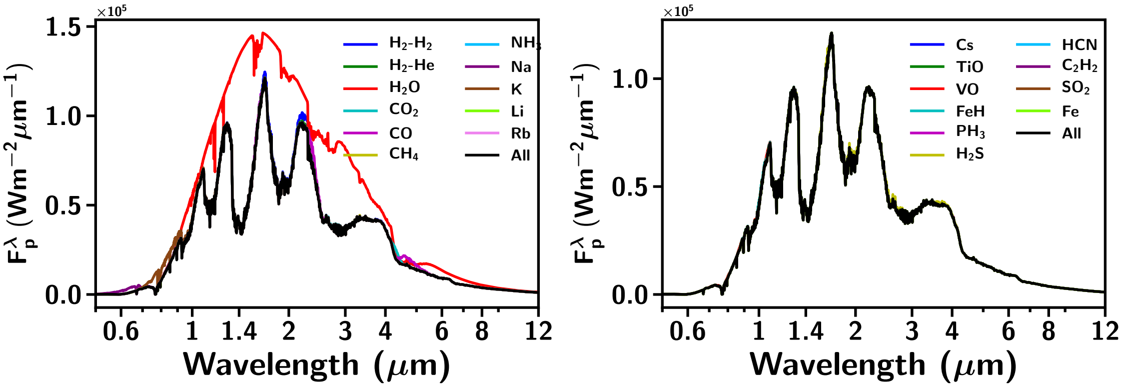

(a) (b)

Figure 5.12: Figure showing WASP-017b emission spectrum with 0.25 RCF, solar metallicity and solar C/O ratio, when removing opacity contributions of single species at a time from the calculation, shown by their respective colours. Emission spectrum including all 21 opacities is shown in black. **(a)** Emission Spectrum when removing opacity due to species H_2-H_2 (blue), H_2-He (green), H_2O (red), CO_2 (cyan), CO (magenta), CH_4 (yellow), NH_3 (lightblue), Na (purple), K (brown), Li (lightgreen) and Rb (violet). **(b)** Same as 5.12a but when removing opacity due to species Cs (blue), TiO (green), VO (red), FeH (cyan), PH_3 (magenta), H_2S (yellow), HCN (lightblue), C_2H_2 (purple), SO_2 (brown) and Fe (lightgreen)

tra, at extreme values of C/O ratio parameter space in the grid (0.35 and 1.5) by adopting two different approaches, one by varying O/H and other by varying C/H. Although there are some differences in the results obtained using these two different methodologies, in the parameter space we consider, they are smaller compared to the effects of other parameters in the grid and other model choices (for e.g. local or rainout condensation). Therefore, to avail fair comparison between the model spectra generated in the previous chapters and keep the library of models consistent with our previous works (Goyal et al. 2018; Goyal et al. 2019b), we again in this work adopt the methodology varying C/O ratio by varying O/H. The effects of varying C/O ratio using this methodology across the parameter space is described in detail in Section 5.7.3. Ideally, we could use O/H and C/H as separate parameters in the grid, however, that increases the size of the grid substantially and makes it computationally expensive for a large number of exoplanets. Therefore, we select one methodology over the other.

5.5 Decoupled emission spectrum

To identify the features of various absorbing/emitting species in the emission spectrum, we compute the spectrum by removing opacity contribution due to one species

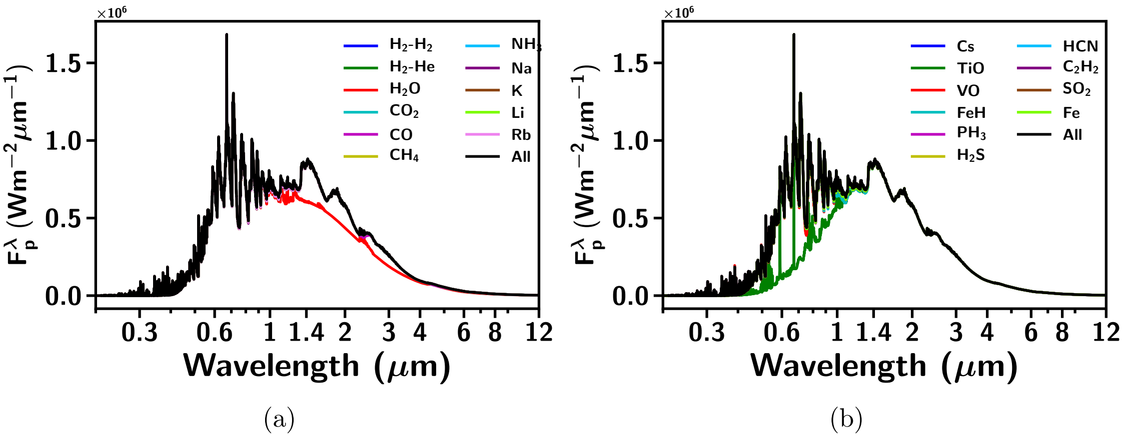

(a) (b)

Figure 5.13: **(a)** Same as Figure 5.12a but for WASP-121b, at solar metallicity and solar C/O ratio with 0.5 RCF. **(b)** Same as 5.12b but for WASP-121b, at solar metallicity and solar C/O ratio with 0.5 RCF.

at a time, which we term the decoupled emission spectrum. In the emission spectrum as the radiation travelling radially outward from the planetary atmosphere is measured, spectral features are indicated by a dip due to absorption as opposed to in a transmission spectrum, unless there is an inversion, in which case it shows an emission feature (bump). We show decoupled spectra for two planets, first is WASP-017b, a hot Jupiter with $T_{eq} = \sim 1750\,K$ in Fig. 5.12a and 5.12a. Second an extremely irradiated hot Jupiter WASP-121b, with $T_{eq} = \sim 2400\,K$ and a strong evidence of an inversion layer in its atmosphere (Evans et al. 2017) in Fig. 5.12a and 5.12b. For WASP-017b it can be seen that most of the contribution to the emission spectrum is from H_2O , since when H_2O is removed while computing the emission spectrum as shown in Figure 5.12a most of the absorption features vanish as compared to where all opacities sources are included (black). The absence of H_2O also allows probing the hotter deeper atmospheres, as can be seen from higher flux for model without H_2O opacity. There is also a strong CO absorption feature at 4.5 μm. The *P*-*T* profile used to generate the spectrum for WASP-017b is shown in Figure 5.19a.

Figure 5.13a and 5.13b show the decoupled spectra for WASP-121b with the corresponding *P*-*T* profile shown in Figure 5.19a. For WASP-121b also it can be seen that most of the contribution to the emission spectrum is from H_2O since when the opacity of H_2O is removed, shown in Figure 5.12a most of the emission features vanish when compared to the spectrum including all opacity sources (black). However, it is interesting to note that due to the temperature inversion in the simulated atmosphere of Wasp-121b the H_2O features are seen in emission, as opposed to absorption as in the case of Wasp-017b. There is also a decrease in the overall flux after removal of H_2O opacity as emission is now from the cooler deeper atmosphere. The emission from CO can also be noticed near $\sim$4.5 μm. The optical spectrum is dominated by emission features of TiO as seen in Figure 5.13b. It must be noted here that we remove TiO only while computing emission spectra for this test shown in Figure 5.13b, not while computing RCE P-T profile used to generate the emission spectrum.

5.6 Effects caused by high levels of irradiation

5.6.1 Effect of Thermal Ionisation

Thermal ionisation of certain species can have a substantial effect on the chemistry of the planetary atmospheres, depending on the atmospheric temperature. Figure 5.14a shows the equilibrium chemical abundances of certain important species for a extremely irradiated hot Jupiter WASP-121b, with (dashed line) and without (solid line) thermal ionisation. The abundance of Na decreases by about 3 orders of magnitude in the upper atmosphere (transmission spectra probed region) when thermal ionisation is included, as Na is ionised to form Na^+. Figure 5.14a shows that the abundance of Na^+ becomes almost equal to Na without thermal ionisation in the upper atmosphere (Pressures $< 10^{-3}$ bar). Similar behaviour can be observed for K and K^+ ions. The thermal ionisation also has effects on the transmission spectra, where the narrow Na and K features (cores) seen in the model spectra without thermal ionisation, disappear in the model spectra with thermal ionisation as shown in Figure 5.14b.

At higher C/O ratios (C/O = 1.5) as shown in Figure 5.14d, the abundance of Na and Na^+, and K and K^+ are similar, as the P-T profiles shown in Figure 5.14c is about 1000 K cooler than for a solar C/O ratio at 1 mbar pressure, inhibiting thermal ionisation of Na and K. Also at such high values of the C/O, the abundance of TiO and VO is low enough to have any effect on the transmission spectra. Therefore, Na and K features can be seen in the transmission spectra if the C/O ratio of the extremely irradiated planet similar to WASP-121b is very high (see Figure 5.22c). However, when compared with the observations of Evans et al. (2018) we can rule out a high C/O ratio for this planet, as there is no evidence of either Na or K in the atmosphere of WASP-121b and there is a strong evidence of an inversion (Evans et al. 2017), potentially due to VO.

5.6.2 Effect of H- opacity

H- opacity contributes to the absorption of radiation in hot Jupiters via bound-free and free-free cross-sections as explained in section 5.2. To understand the effect of

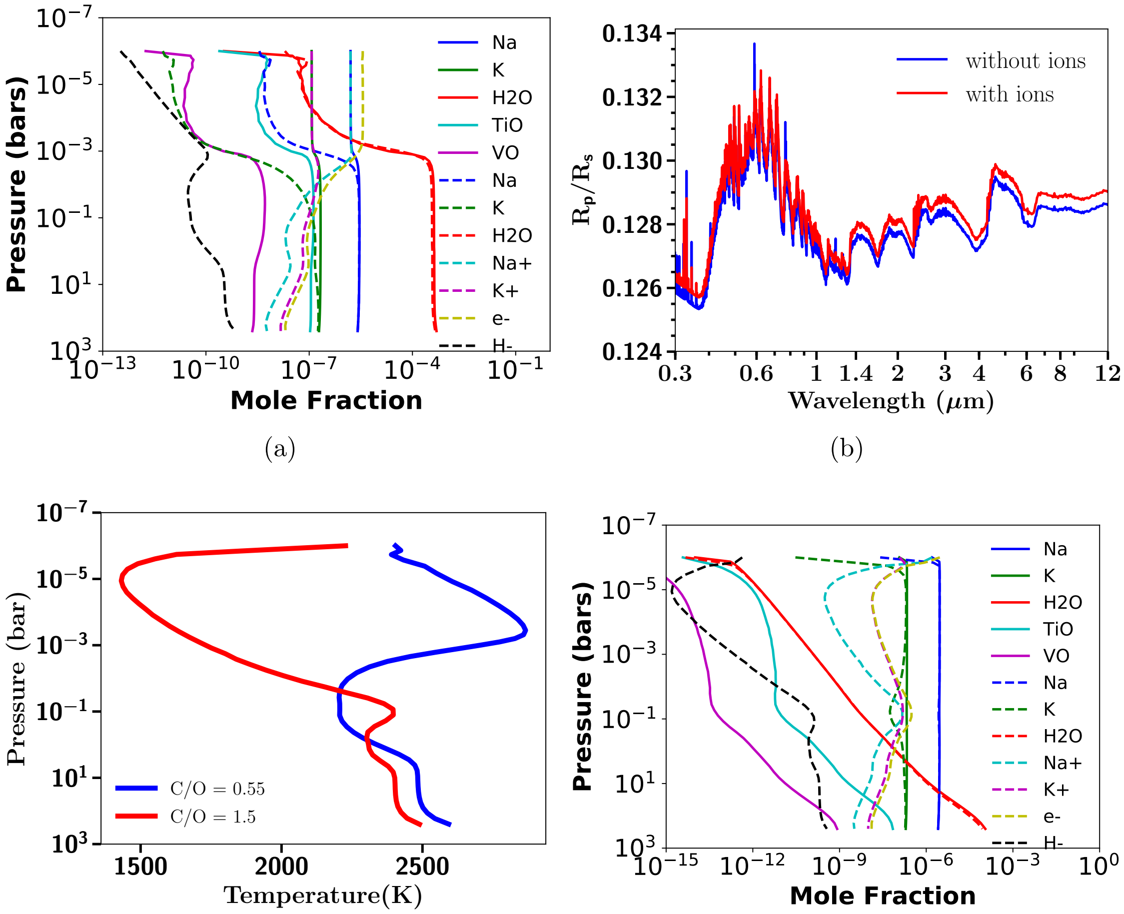

(a) (b)

(c) (d)

Figure 5.14: **(a)** Figure showing equilibrium chemical abundances of various species without (solid) and with (dashed) thermal ionisation included in the model for WASP-121b at solar metallicity, solar C/O ratio and 0.5 RCF. **(b)** Figure showing transmission spectra models, with and without thermal ionisation at solar metallicity, solar C/O ratio and 0.5 RCF. **(c)** Figure showing *P*-*T* profile with C/O ratio of 0.55 (solar) and 1.5, solar metallicity and 0.5 RCF, with thermal ionisation included in chemistry. **(d)** Figure showing equilibrium chemical abundances of various species without (solid) and with (dashed) thermal ionisation included in the model for WASP-121b at solar metallicity, C/O ratio of 1.5 and 0.5 RCF.

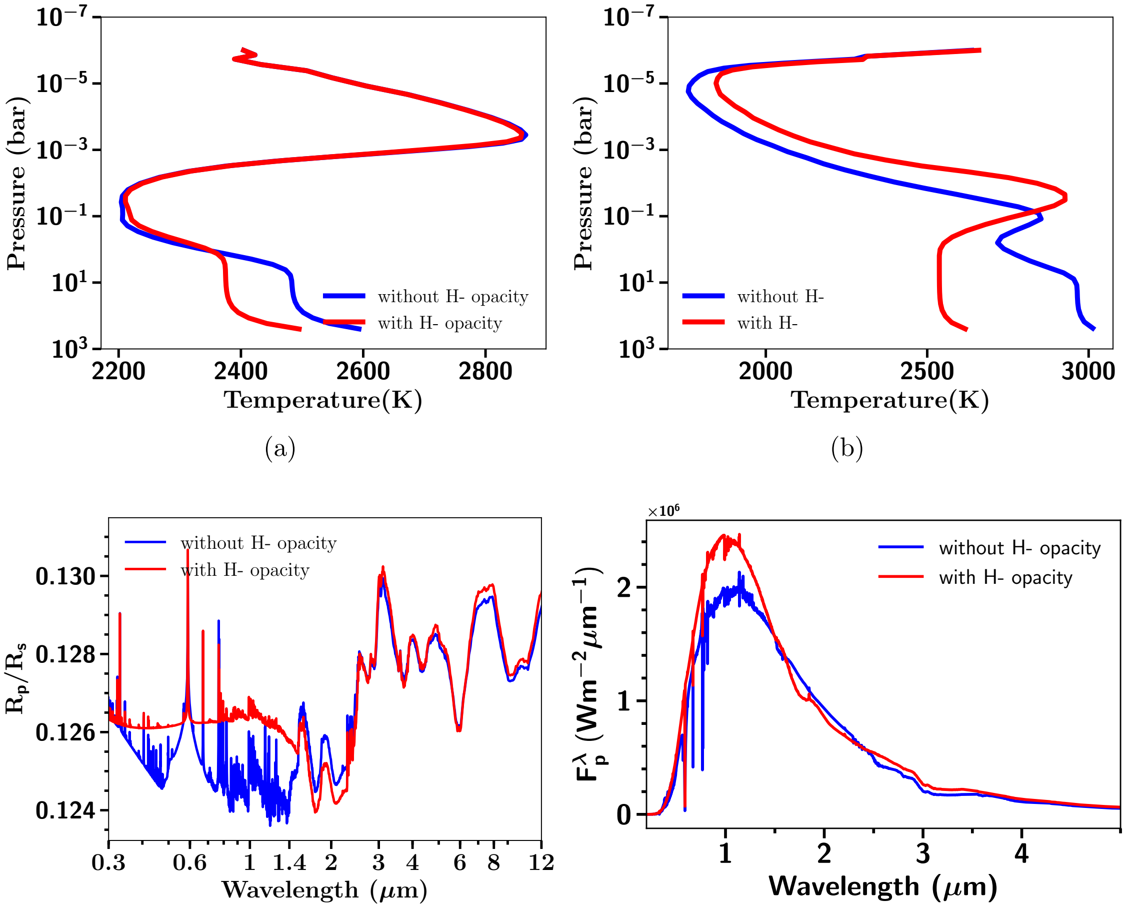

(a) (b)

(c) (d)

Figure 5.15: **(a)** Figure showing RCE *P*-*T* profiles without (blue) and with (red) H- opacity included in the model for WASP-121b at solar metallicity, solar C/O ratio and 0.5 RCF. **(b)** Same as Figure 5.15a but at C/O ratio of 1.5 and 1.0 RCF. **(c)** Figure showing transmission spectra using *P*-*T* profiles shown in Figure 5.15b and corresponding chemical abundances with and without H- opacity. **(d)** Figure showing emission spectra using *P*-*T* profiles shown in Figure 5.15b and corresponding chemical abundances with and without H- opacity.

H- opacity we compute *P*-*T* profiles with and without H- opacities included in the model. Figure 5.15a show these *P*-*T* profiles at 0.5 RCF with solar metallicity and C/O ratio for WASP-121b. It can be noticed from the *P*-*T* profiles that H- opacity tends to cool the deeper atmosphere ($>$ 1 bar) by about 100 K which increases to 400 K with an RCF value of 1 (not shown here). This can be attributed to an increase in H- abundance in the lower atmosphere ($>$ 1 bar), with a higher RCF value, as the temperature increases. In Figure 5.15b the *P*-*T* profile obtained using a RCF value of 1.0, solar metallicity and a C/ O ratio of 1.5 is shown. This has been particularly chosen to show the extreme effects due to H- opacity. Figure 5.15b shows that there is a substantial difference in *P*-*T* profiles with and without H- opacity. Without H- opacity there is a weak temperature inversion as compared to that with H- opacity. This is mainly because at high C/O ratios (1 or 1.5) as shown in Figure 5.25b, the abundance of TiO/VO decreases dramatically, the major absorbers likely to cause an inversion in extremely irradiated hot Jupiters like WASP-121b. Therefore, without H- opacity the strong inversion is not sustained but there is a weak inversion due to Na and K discussed in detail in Section 5.7.3. With H- opacity the strength of inversion increases dramatically at 1.0 RCF as H- abundance reaches levels where the opacity can create an inversion similar to TiO/VO.

The effect of H- opacity on the transmission spectrum is also substantial as shown in the Figure 5.15c where it tends to obstruct the deeper atmosphere due to its high opacity as shown for a high C/O ratio case for WASP-121b. In this case it tends to mute the wings of Na and K mimicking the effect of cloud at optical wavelengths. Figure 5.15d shows the emission spectrum for WASP-121b with and without H- opacity using the *P*-*T* profile shown in Figure 5.15b. Figure 5.15d shows that there is a substantial difference in the emission spectrum with and without H- opacity, due to difference in *P*-*T* profiles. The flux in the peak region of the emission spectrum is more with H- opacity as compared to that without H- opacity, due to consistently high temperature with H- opacity above 0.1 bar pressure level, as seen in Figure 5.15b.

5.6.3 Effect of Fe opacity

Gaseous iron (Fe) opacity dramatically effects the *P*-*T* profiles of extremely irradiated hot Jupiters. It tends to heat the upper, lower pressure, atmosphere as shown in the Fig. 5.16a and cool the lower, high pressure, atmosphere. Fe cross-section is quite strong in the optical leading to strong absorption and therefore the heating in the upper atmosphere. This blocking of radiation higher up in the atmosphere is one of the causes of the cooling in the deeper atmosphere similar to H-. As seen in the emission spectrum with and without Fe opacity, it can be seen that the strength

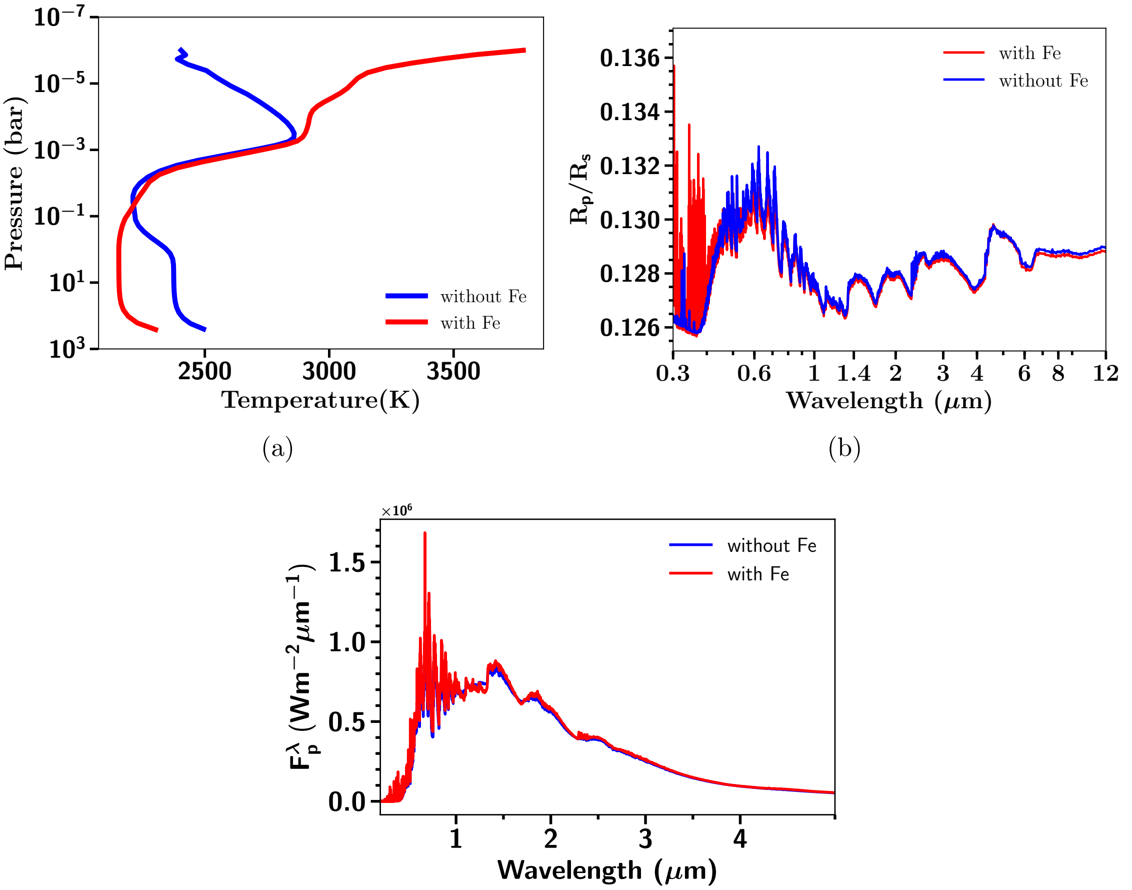

(a)

(b)

(c)

Figure 5.16: **(a)** Figure showing RCE P-T profiles without (blue) and with (red) Fe opacity included in the model for WASP-121b at solar metallicity, solar C/O ratio and 0.5 RCF. **(b)** Figure showing transmission spectra using P-T profiles shown in Figure 5.16a and corresponding chemical abundances with and without Fe opacity. **(c)** Figure showing emission spectra using P-T profiles shown in Figure 5.16a and corresponding chemical abundances with and without Fe opacity.

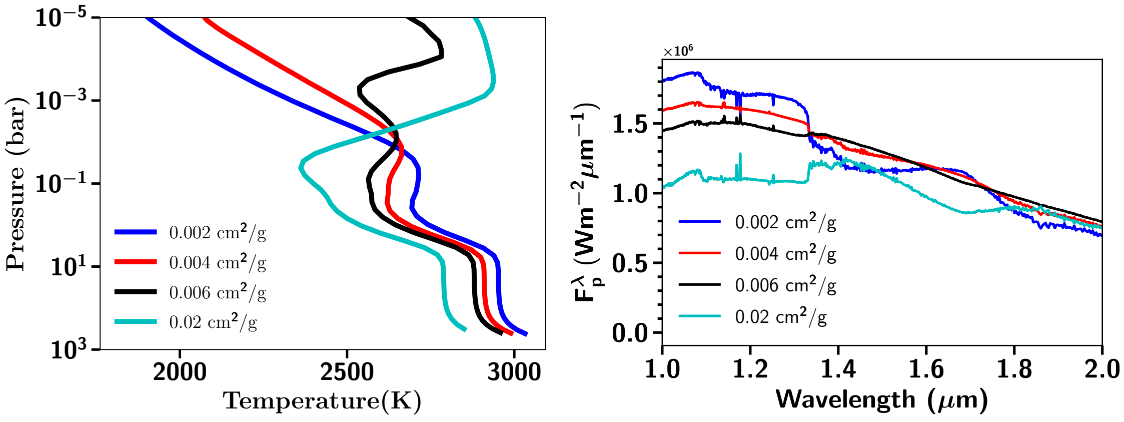

(a) (b)

Figure 5.17: **(a)** Figure showing *P-T* profiles for WASP-121b with 0.8 RCF, solar metallicity and solar C/O ratio, with different amount of optical grey opacity added throughout the atmosphere. **(b)** Figure showing emission spectra with different amount of optical grey opacity using *P-T* profiles shown in Figure 5.17a.

of the inversion in the emission increases after adding Fe opacity. Thus Fe opacity along with TiO/VO opacity can play an important role in creating inversions. In the transmission spectra as shown in Figure 5.16c, it can be seen that Fe opacity is important in the optical part of the spectrum, generally dominated by Rayleigh scattering slope. The differences in the emission spectrum shown in Figure 5.16c are negligible because the *P-T* profile for both cases, with and without Fe, only differ in the region which is not probed by the emission spectrum, which are the deep and the uppermost part (optically thin) of the atmosphere, as described in Figure 2.6 in Chapter 2.

5.6.4 Inversions in hot Jupiters without TiO/VO

Temperature inversions with grey opacity Although a temperature inversion has been suggested in the atmosphere of WASP-121b (Evans et al. 2017), it is unclear what the opacity source is to create the extra flux absorption required to generate a temperature inversion. Therefore, in this section the opacity required to produce an inversion, the impact on the *P-T* profile and thereby the emission spectra is investigated. Following Burrows et al. (2008) and Spiegel et al. (2009), we add an arbitrary grey absorbing opacity across the optical wavelengths (0.44 - 1 μm) throughout the atmosphere (all model layers) of WASP-121b with 0.8 RCF, solar metallicity and C/O ratio. Varying the magnitude of this opacity then allows us to explore the evolution of the *P-T* profile from being non-inverted to being inverted as a function of opacity, along with the evolution of the emission spectrum for these different atmospheric structures. The value of 0.8 RCF is chosen as the best fit value

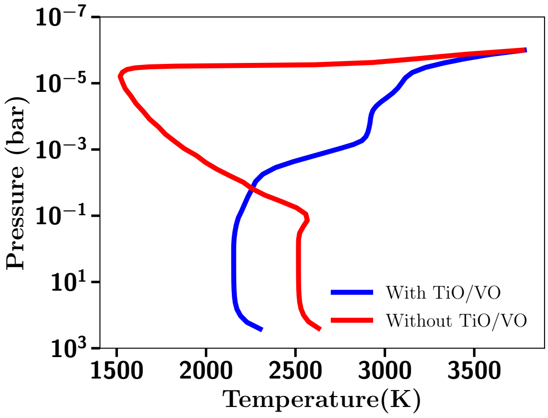

Figure 5.18: Figure showing RCE *P*-*T* profiles with all opacities (blue) and without TiO/VO opacities (red), at solar metallicity and solar C/O ratio with 0.5 RCF for WASP-121b.

to observations in Evans et al. (2017). For this particular test along with a grey absorbing opacity in the optical, only the H_2-H_2 and H_2-He CIA, and H_2O, CO_2, CO, CH_4, NH_3, Na, K, Li, Rb, Cs opacities were used for simplicity. Figure 5.17a and 5.17b show the *P*-*T* profile and emission spectra, respectively, for varying levels of grey opacity for WASP-121b. We note that we have omitted TiO/VO opacity in this model simulation. It can be seen that as the grey opacity increases from 0.002 to 0.02 cm^2/g the *P*-*T* profile evolves from being non-inverted to inverted. The evolution in the emission spectrum is more interesting where the H_2O absorption feature at 1.4 μm gradually changes into an emission feature, as the amount of grey opacity is increased. Moreover, with 0.006 cm^2/g grey opacity the spectrum almost resembles a blackbody spectrum indicating an isothermal atmosphere, which can be seen in Figure 5.17a.

Can Fe without TiO/VO lead to inversion ? Iron (Fe) has very strong opacity in the UV and the optical part of the spectrum. Therefore, we tested whether Fe can lead to inversions without TiO/VO in extremely irradiated hot Jupiter such as WASP-121b. For this we removed TiO/VO opacities from the model while computing RCE *P*-*T* profiles. We found that Fe is unable to produce inversion like TiO/VO at solar metallicity as shown in Figure 5.18. It however, leads to a sharp increase in the temperature at lower pressures (like a thermosphere inversion). Even if we increase the metallicity to 200x solar, although the Fe abundance increases to $\sim 30\times$ than that at solar metallicity, it does not lead to an inversion.

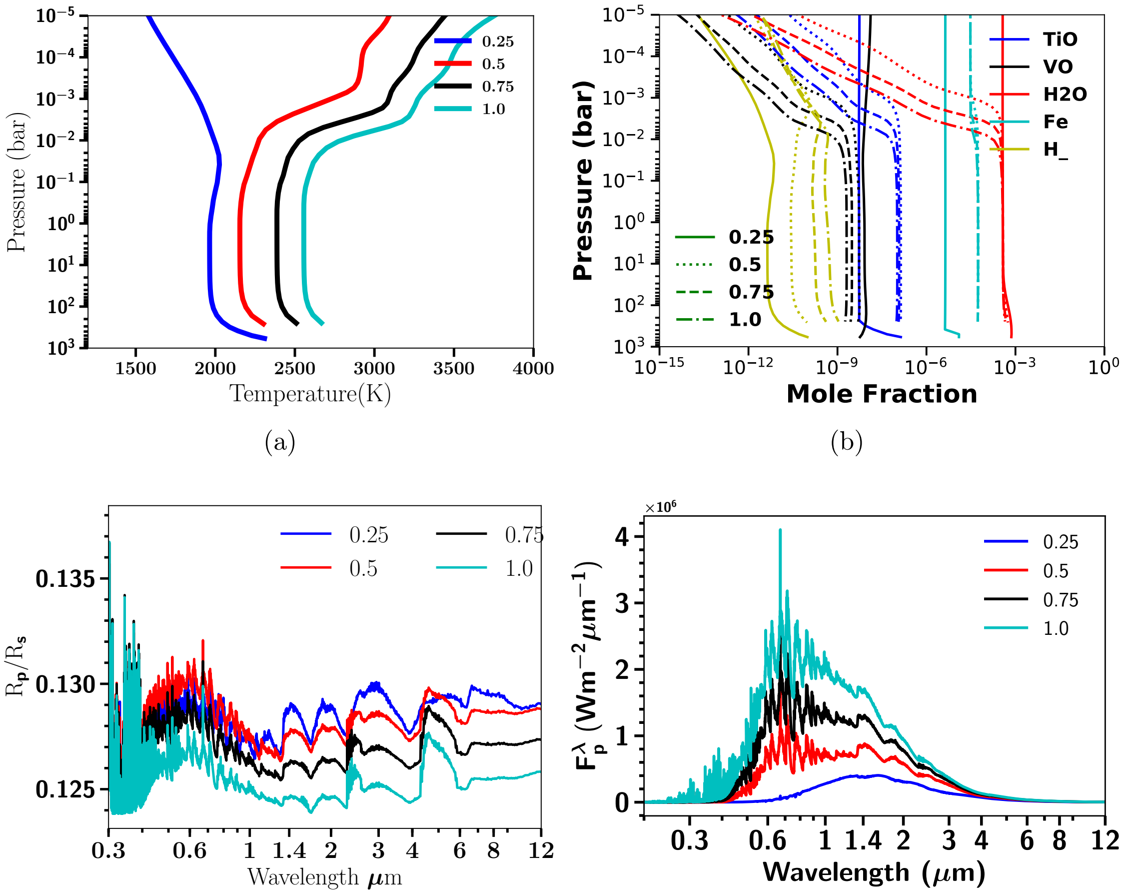

(a) (b) (c) (d)

Figure 5.19: **(a)** Figure showing *P*-*T* profiles for a range of RCF values (0.25, 0.5, 0.75 and 1) at solar metallicity and solar C/O ratio (0.56) for WASP-121b **(b)** Figure showing equilibrium chemical abundances for some important species for various RCF values obtained using *P*-*T* profiles shown in Figure 5.19a. **(c)** Figure showing transmission spectra for various RCF values obtained using *P*-*T* profiles shown in Figure 5.19a and corresponding equilibrium chemical abundances. **(d)** Figure showing planetary emission spectra for various RCF values obtained using *P*-*T* profiles shown in Figure 5.19a and corresponding equilibrium chemical abundances.

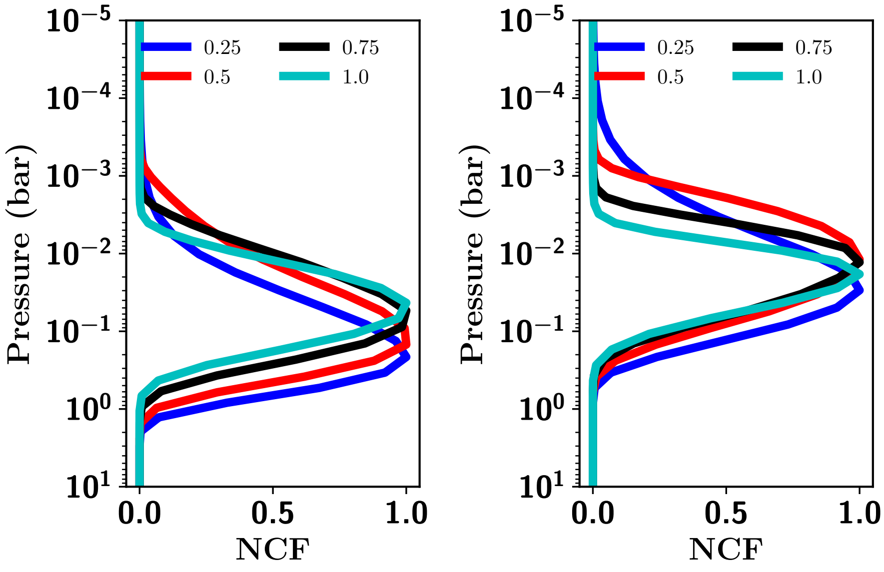

(a) (b)

Figure 5.20: **(a)** Figure showing normalized contribution function at 1.7 μm for a range of RCF values for emission spectra as shown in Figure 5.19d. **(b)** Same as Figure 5.20a but for 1.4 μm.

5.7 Sensitivity to Grid Parameters

In this section we show the sensitivity of the model simulation, i.e *P-T* profiles and the spectra, to all the grid parameters, namely recirculation factor, metallicity and C/O ratio across their full range used in this library, using WASP-017b and WASP-121b as the test case.

5.7.1 Effect of recirculation factor

The recirculation factor (RCF) described in Section 2.3 governs the efficiency of redistribution of energy (by winds) received from the host star in a column. The value of 1 corresponds to no-redistribution, with increase in redistribution as this factor decreases. Here, we show the effect of varying the recirculation factor on the *P-T* profiles and thereby the chemical abundances and spectra, using extremely irradiated hot Jupiter WASP-121b as an example. As can in seen in the *P-T* profiles in Figure 5.19a for WASP-121b, the strength of the atmospheric temperature inversion increases with RCF as expected, since more energy is available to create an inversion at higher values of RCF. At 0.25 RCF the inversion is absent in the *P-T* structure due to reduced irradiation. Absorption due to TiO/VO is the primary reason for the inversion, but surprisingly the abundance of TiO/VO starts decreasing, as the inversion is formed and increases in strength, as can be seen in Figure 5.19b for increasing RCF. However, the abundance of H- and Fe increases with increasing RCF. This increase in H- maintains the temperature inversion even though the abundance of TiO/VO decreases, as described in in Section 5.6.2 and also Section 5.7.3.

In the transmission spectrum of WASP-121b as shown in Figure 5.19c, it can be seen that the strength of the H_2O features decreases with increasing RCF as H_2O abundance decreases in the region where transmission spectra probes ($\sim$ 1mbar), since H_2O starts becoming thermally unstable with increasing temperatures. However, CO features start appearing near $\sim$2.5 μm and broadband CO features between 4 to 6 μm. The strength of these CO features increases with increasing RCF. As expected, the flux in the planetary emission spectrum shown in Figure 5.19d increases with increasing RCF as the temperature of emission increases. The P-T profile at 0.25 RCF is very close to isothermal structure, therefore its emission spectrum also resembles a blackbody curve, with small dips in the strong water vapour absorption bands at 1.4, 2 and 3 μm. In contrast, P-T profiles at other RCF values have temperature inversions, thus leading to a bump instead of dip in the strong H_2O and CO absorption bands.

The normalised contribution functions (NCF) at 1.7 and 1.4 μm are shown in Figure 5.20a and 5.20b, respectively. At 1.7 μm, the NCF peaks deeper in the atmosphere as compared to that at 1.4 μm, indicating emission at 1.7 μm is from comparatively deeper parts of the atmosphere, since 1.7 μm is at the edge of strong water absorption band centred at 1.4 μm. For the profiles with a temperature inversion (RCF $=$ 0.5, 0.75, 1.0), the deeper and cooler isothermal part (not the inversion) is primarily probed at 1.7 μm as compared to 1.4 μm which probes the inversion layer, thus leading to a emission feature (bump) instead of a absorption feature (dip) in the emission spectrum from 1.2 to 1.7 μm. This also happens for other strong water absorption bands as shown in the emission spectra. The 1.4 μm emission feature has been detected in the atmosphere of WASP-121b (Evans et al. 2017), but other such potential emission features indicative of inversion for wavelengths $>$ 2 μm are still to be detected for WASP-121b and can only be possible with JWST.

At 0.25 RCF the inversion is absent as we reduce the irradiation received from the host star to 25% of its original value, mimicking the transport of energy by advection (strong winds). This also motivates accurate 3D modelling of extremely irradiated hot Jupiter exoplanets to predict inversions as well as to infer wind velocities based on the presence or absence of inversions.

5.7.2 Effect of Metallicity

Metallicity fundamentally effects the chemistry of the atmosphere and thereby its P-T structure and observed spectrum. The effect of metallicity on the P-T structure, chemistry, transmission and emission spectra for two different planets is discussed here.

WASP-017b WASP-017b is a hot Jupiter planet with an equilibrium temperature of 1755 K. Adopting a value of 0.5 for the RCF the transmission spectra for this planet shows TiO/VO features due to hotter P-T structure as compared to that using 0.25 RCF. However, observations from Sing et al. (2016) shows the absence of TiO/VO features, therefore we restrict the following analysis to simulations adopting an RCF of 0.25 (although all values are available in the model grid). The C/O ratio is fixed to solar value and the metallicity varied from across the grid range to investigate the effect of metallicity. For this planet, an increasing metallicity leads to an increase in the temperature throughout the atmosphere as shown in Figure 5.21a. This is a result of increased absorption of radiation at lower pressures, due to increased opacity, as the mean molecular weight of the atmosphere increases, driven by an increase in the abundances of species heavier than H_2 and He, namely H_2O, CO_2 and Na as shown in Figure 5.21b. A sharp increase in temperature for sub-solar metallicity can be seen at pressures less than $\sim 10^{-5}$ bar, but it is observationally insignificant either in transmission or emission spectra, due to the low atmospheric density at these pressures.

The effect of varying the metallicity on the transmission and emission spectra of WASP-017b is shown in Figure 5.21c and 5.21d, respectively. The transmission spectra are primarily dominated by Na, K and narrow Li features in the optical for all metallicities, with weaker TiO/VO features as metallicity increases. The infrared part of the spectrum is primarily dominated by H_2O features for all metallicities. The size of the H_2O features initially increase in size with increase in metallicity as H_2O abundance increases shown in Figure 5.21b, but then again decreases with increasing metallicity. This is caused by the increase in the mean molecular weight of the atmosphere, leading to a decrease of the atmospheric scale height, which, in turn, shrinks the spectral features in transmission. Pressure broadened wings of Na and K are also effected by change in metallicity. Due to decreasing scale height associated with increasing metallicity, transmission spectra probes high pressure levels of the atmosphere, resulting in enhanced broadening of Na and K line wings with increasing metallicity. The CO_2 feature near 4.5 μm and 2.5 - 3 μm increases in amplitude, which can also be seen in the emission spectrum, primarily due to a rapid increase in the CO_2 abundances. This shows that even under chemical equilibrium conditions the atmosphere rapidly tends to migrate towards a CO_2 abundant atmosphere with

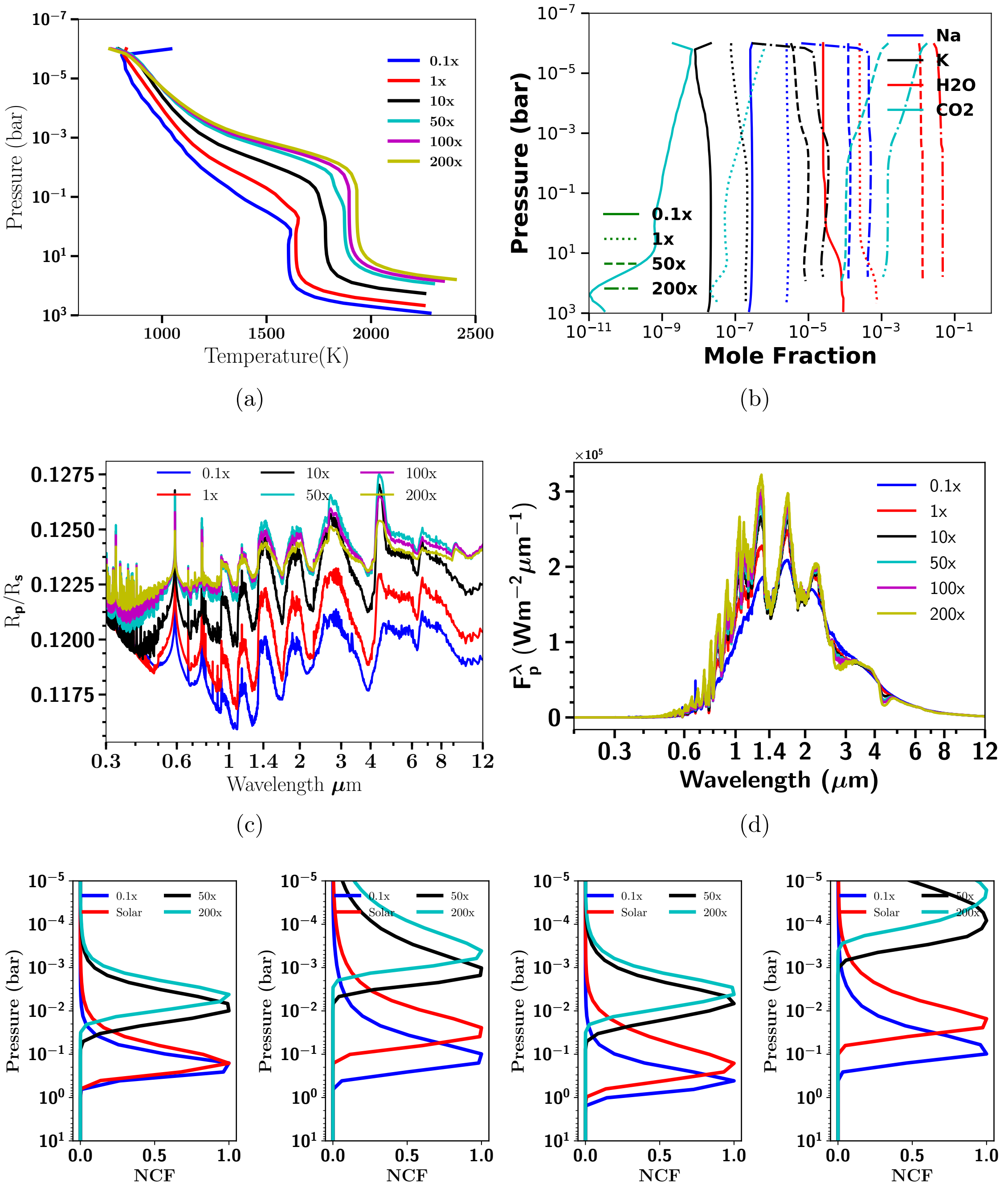

(a) (b)

(c) (d)

(e) (f) (g) (h)

Figure 5.21: **(a)** Figure showing *P*-*T* profiles for a range of metallicities at 0.25 RCF and a solar C/O ratio (0.56) for WASP-017b. **(b)** Figure showing equilibrium chemical abundances for some important species for various metallicity values obtained using *P*-*T* profiles shown in Figure 5.21b. **(c)** Figure showing transmission spectra for WASP-017b for different values of metallicity obtained using *P*-*T* profiles shown in Figure 5.21a and corresponding equilibrium chemical abundances shown in Fig. 5.21b. **(d)** Figure showing emission spectra for WASP-017b for different values of metallicity obtained using *P*-*T* profiles shown in Figure 5.21a and corresponding equilibrium chemical abundances shown in Fig. 5.21b. **(e, f, g, h)** Figures e, f, g, h showing normalised contribution function at 2.25, 2.8, 3.8 and 4.5 μm for a range of metallicity values for emission spectra as shown in Figure 5.21d.

increasing metallicity (Moses et al. 2013a), offering potential reasons for the CO_2 dominated compositions of Mars and Venus in our Solar system. Even Earth in the past may have had a CO_2 dominated atmosphere, currently captured in the oceans and rocks by various geological processes (Zahnle et al. 2010). The transmission spectra can also be compared with Figure 3.20a of Chapter 3 which uses isothermal P-T profiles. The comparison might not be completely accurate as the RCE P-T profiles shown here are overall cooler than the equilibrium temperature of WASP-017b (1755 K) in the transmission spectra probed region (∼1mbar).

The emission spectra of WASP-017b with varying metallicity is shown in Figure 5.21d. The blackbody emission flux increases with increase in metallicity, since the overall temperature of P-T profiles shown in Fig. 5.21a increases with increasing metallicity. This increase in temperature combined with the increase in abundances of species such as H_2O and CO_2, with increasing metallicity, leads to deeper absorption features. Similar to transmission spectrum, emission spectrum is also dominated by water absorption features for WASP-017b in the infrared with CO_2 features around 4.5 and 2.5 - 3 μm region for metallicities greater than 10 times solar value. The atmospheric level which contributes most to the emission at different wavelengths can be found using the normalised contribution function (NCF). The increase in the overall temperature of the P-T profile causes NCF to consistently shifts towards lower pressure with increase in metallicity as shown in Figures 5.21e, 5.21f, 5.21g and 5.21h. The NCF at core of the CO_2 absorption band at 4.5 μm shown in the Fig. 5.21h, peaks at low pressures ($>\sim$ 1 mbar) in the atmosphere (low pressures), for metallicities greater than 50 times solar, as compared to the wing of the band at 3.8 μm as shown in the Figure 5.21g. The dramatic drop in the emission flux between these two wavelengths can also be noticed in the emission spectra for metallicities greater than 50 times solar. The NCF for the 2.8 μm H_2O absorption band also shows similar effect as 4.5 μm CO_2 absorption band, shown in Figures 5.21e and 5.21f, for 2.25 and 2.8 μm, respectively.

WASP-121b WASP-121b is an extremely irradiated hot Jupiter planet with an equilibrium temperature of 2358 K (Southworth 2011a). This is the first planet with definitive evidence of an inversion layer in its atmosphere, potentially created due to VO (Evans et al. 2017; Evans et al. 2018). Figures 5.22a, 5.22b, 5.22c and 5.22d show the P-T structure, chemical abundances, transmission and emission spectra, respectively for WASP-121b at 0.5 RCF and solar C/O ratio. Figures 5.22e, 5.22f, 5.22g and 5.22h show the contribution function at 2.25, 2.8, 3.8 and 4.5 μm, respectively.

For WASP-121b we see a temperature inversion in the P-T profile, which moves towards higher pressure levels with increasing metallicity, primarily driven

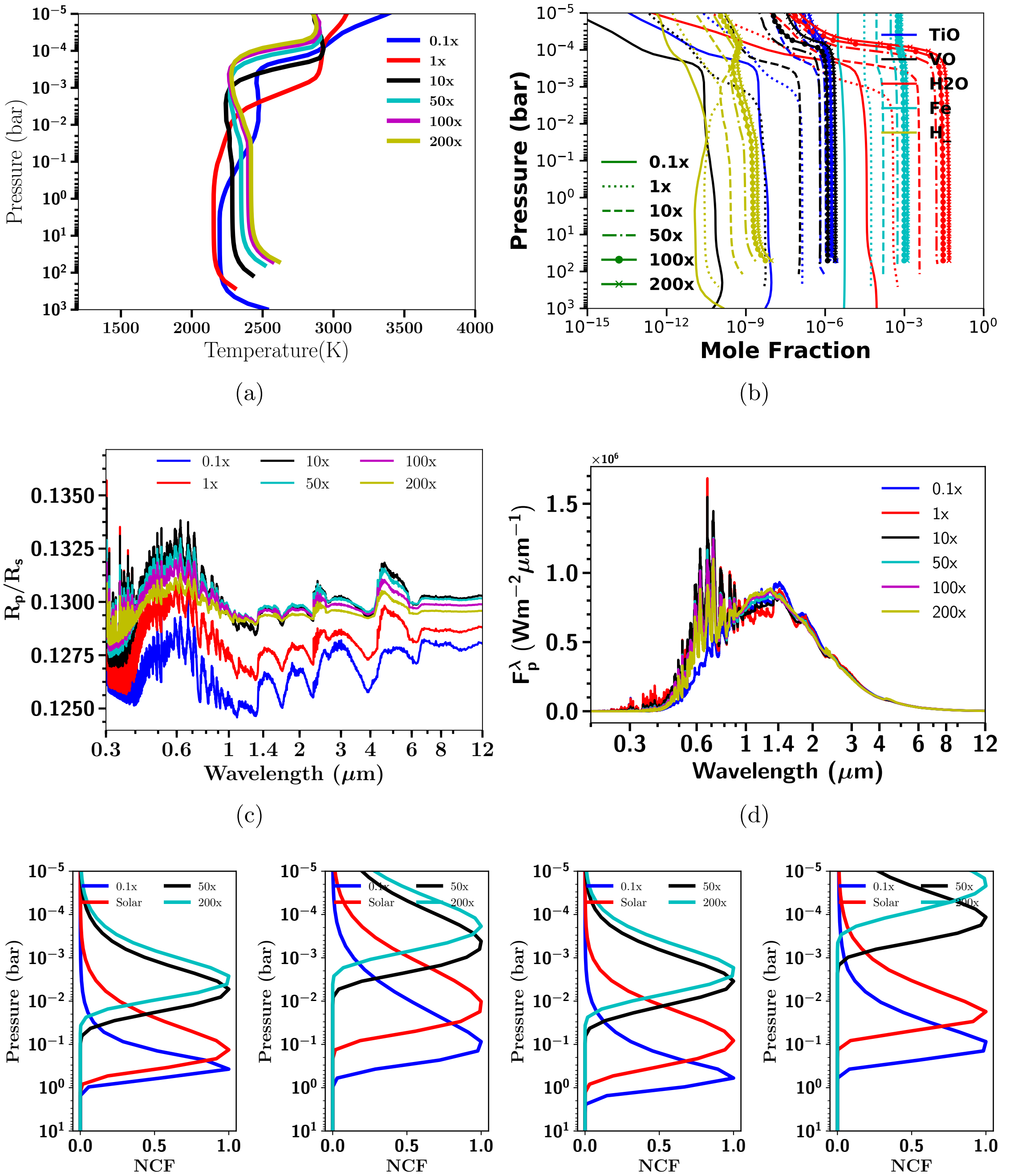

(a) (b)

(c) (d)

(e) (f) (g) (h)

Figure 5.22: **(a)** Figure showing *P*-*T* profiles for a range of metallicity at 0.5 RCF and a solar C/O ratio (0.56) for WASP-121b. **(b)** Figure showing equilibrium chemical abundances for some important species for various metallicity values obtained using *P*-*T* profiles shown in Figure 5.22a. **(c)** Figure showing transmission spectra for WASP-121b for different values of metallicity obtained using *P*-*T* profiles shown in Figure 5.22a and corresponding equilibrium chemical abundances shown in Fig. 5.22b. **(d)** Figure showing emission spectra for WASP-121b for different values of metallicity obtained using *P*-*T* profiles shown in Figure 5.22a and corresponding equilibrium chemical abundances shown in Fig. 5.22b. **(e, f, g, h)** Figures e, f, g, h showing normalised contribution function at 2.25, 2.8, 3.8 and 4.5 μm for a range of metallicity values for emission spectra as shown in Figure 5.22d.

by TiO/VO absorption. At sub-solar metallicity the inversion is very weak, due to the low abundance of TiO/VO, seen in Figure 5.22b. The Fe abundance is also substantial, mainly contributing to upper atmosphere heating, as the Fe absorption cross-sections are largest in the UV-Optical spectrum. This upper atmosphere heating leads to formation of second inversion layer but this inversion does not have any observational signature due to the very low density of the atmosphere in this region.

The transmission spectra shown in Figure 5.22c is dominated by TiO/VO features in the optical, the size of which deceases with increasing metallicity due to a reduction in the atmospheric scale height. Sharp Fe features dominate the optical spectrum short-ward of ~0.4 μm with H_2O features in the infrared. The CO features are also seen in the transmission spectrum particularly around 2.5 and 4-6 μm, which can also be seen in the emission spectrum in Fig. 5.22d.

In the emission spectra shown in Figure 5.22d for WASP-121b, due to an inversion layer in the P-T profile, most of the molecular features are seen as emission features as opposed to the absorption features seen for WASP-017b. The amplitude of the CO features increases with increasing metallicity. The TiO/VO features can also be seen as emission features in the emission spectra in the optical. The H_2O emission features dominate the infrared, where the 1.4 μm feature has led to the detection of an inversion layer for the first time in an exoplanet atmosphere (Evans et al. 2017). It can also be noticed from the NCF that the wings of strong absorption bands at 2.25 (H_2O) and 3.8 μm (CO) shown in Fig. 5.22e and 5.22g, respectively, mainly probe the region below the inversion layer, while the cores of absorption bands at 2.8 and 4.5 μm shown in Fig. 5.22f and 5.22h probe the inversion layer.

5.7.3 Effect of C/O ratio

WASP-017b The P-T profiles for WASP-017b for a range of C/O ratios are shown in Fig. 5.23a at 0.5 RCF and solar metallicity. We choose to show simulations with 0.5 RCF instead of 0.25 RCF as one of the models with 0.25 RCF and a C/O ratio of 1.0 failed to converge in the grid. It can be seen that with increasing C/O ratio the P-T structure consistently cools for pressure (P)$\leq 10^{-1}$ bar. However, for P$\geq 10^{-1}$ bar the P-T structure first cools up-to C/O ratio of 0.75 and then the temperature increases for a C/O ratio of 1 and 1.5. The sharp heating at around 10^{-6} bar is due to Fe opacity as explained earlier.

The change in the equilibrium chemical abundances due to the change in the C/O ratio is drastic, as it effects all the major carbon and oxygen bearing molecules. As expected the abundances of H_2O drop with increasing C/O ratio. Although CO_2 bears a carbon atom it needs two oxygen atoms per carbon atom, therefore the equilibrium abundance of CO_2 also drops with increasing C/O ratio, but in smaller

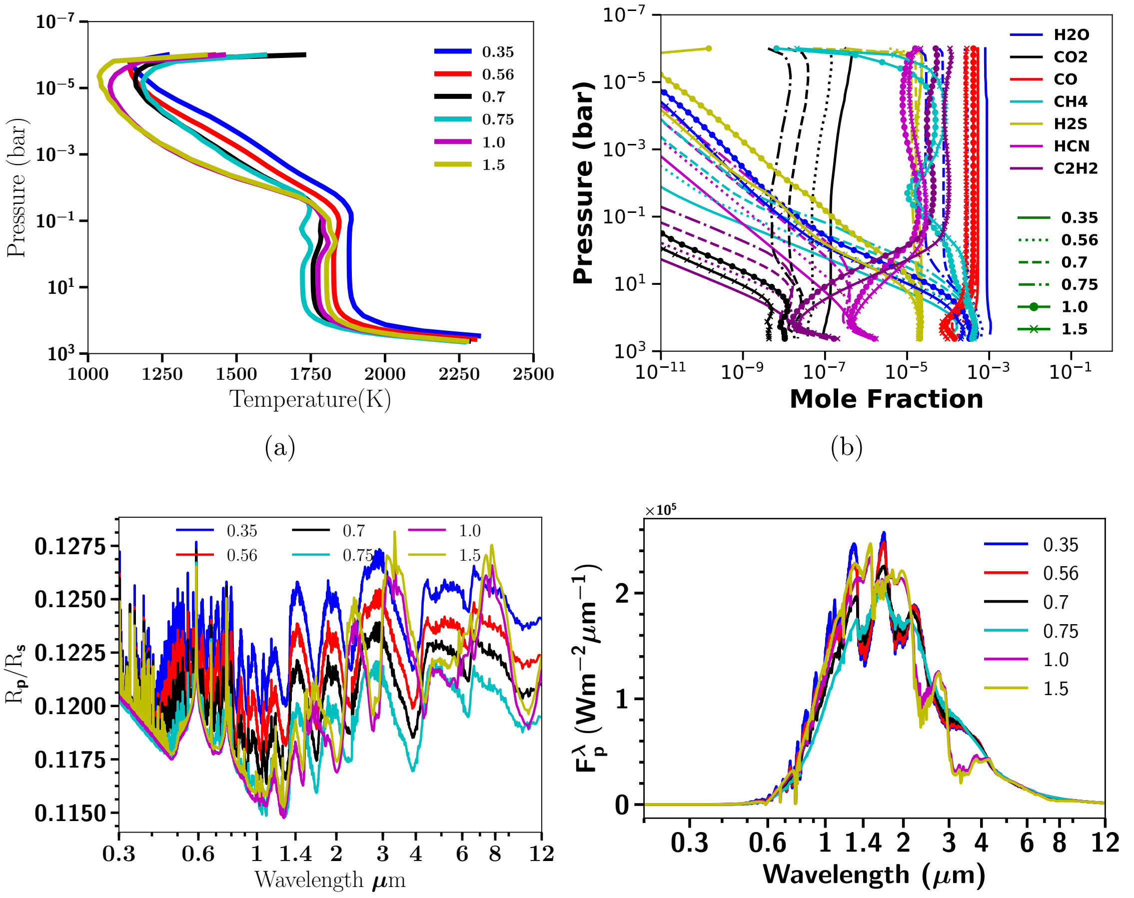

(a) (b)

(c) (d)

Figure 5.23: **(a)** Figure showing *P*-*T* profiles for a range of C/O ratios at 0.5 RCF and solar metallicity (0.56) for WASP-017b. **(b)** Figure showing equilibrium chemical abundances for some important species for various C/O values obtained using *P*-*T* profiles shown in Figure 5.23a. **(c)** Figure showing transmission spectra for WASP-017b for different values of C/O ratios obtained using *P*-*T* profiles shown in Figure 5.23a and corresponding equilibrium chemical abundances shown in Fig. 5.23b. **(d)** Figure showing emission spectra for WASP-017b for different values of C/O ratios obtained using *P*-*T* profiles shown in Figure 5.23a and corresponding equilibrium chemical abundances shown in Fig. 5.23b.

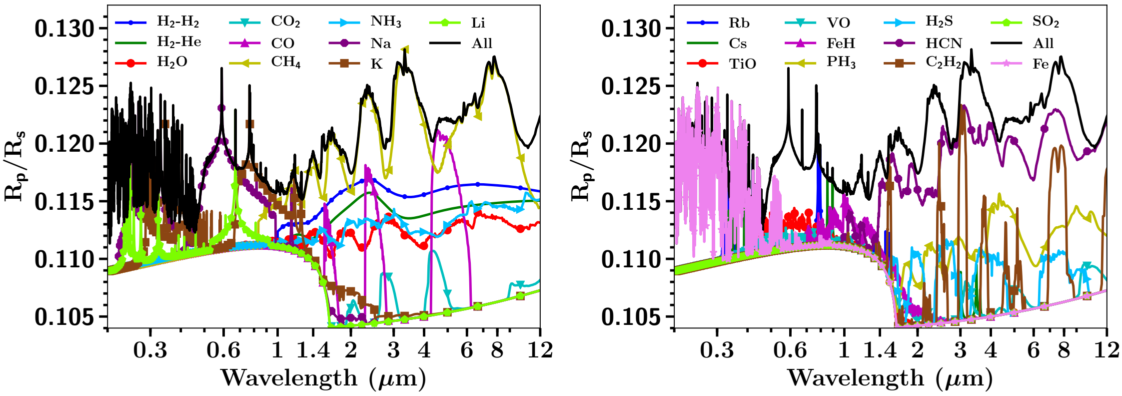

(a) (b)

Figure 5.24: **(a)** Figure showing transmission spectra features of each individual molecule used in `ATMO` (1 to 10) for WASP-017b transmission spectra shown in Fig. 5.23c. H_2-H_2 (blue), H_2-He (green), H_2O (red), CO_2 (cyan), CO (magenta), CH_4 (yellow), NH_3 (lightblue), Na (purple), K (brown), Li (lightgreen) and all 21 opacities (black). No $R_\mathrm{p}/R_\star$ offset was applied while plotting. Individual simulations are divided into blocks of 10 while plotting for clarity. **(b)** Same as Figure 5.24a but for Rb (blue), Cs (green), TiO (red), VO (cyan), FeH (magenta), PH_3 (yellow), H_2S (lightblue), HCN (purple), C_2H_2 (brown), SO_2 (lightgreen), Fe (violet) and all 21 opacities (black).

increments as compared to H_2O. The abundance of carbon bearing species such as CH_4, HCN, C_2H_2 increases with increasing C/O ratio, while the abundance of CO is almost constant, since it has one atom of carbon and oxygen each. This transition between H_2O dominated spectra, to spectra dominated by various carbon bearing species occurs between C/O ratios of 0.75 and 1, slightly higher than that found with isothermal P-T profiles where it was between 0.7 -0.75 as shown in Goyal et al. (2018). However, this value might change with change in RCF value as the C/O transition point is a strong function of temperature (Mollière et al. 2016; Goyal et al. 2018).

This C/O transition is also seen in the transmission spectrum shown in Fig. 5.23c, where the spectra transitions from being H_2O dominated to being dominated by CH_4, HCN and C_2H_2 between a C/O ratio of 0.75 and 1. Fig. 5.24a and 5.24b show this transmission spectrum at a C/O ratio of 1.5 decoupled into various molecules. It can be seen that at a C/O ratio of 1.5, the transmission spectrum is dominated by CH_4 features in the infrared, with contributions from CO, HCN and C_2H_2. There is a strong HCN and C_2H_2 feature at ∼1.6 μm and the most common CO feature at 4.5 μm. The emission spectrum shown in Fig. 5.23d also shows this C/O transition between 0.75-1, from deep H_2O absorption features to more deeper CH_4 absorption features, in the peak region of emission around ∼3 μm

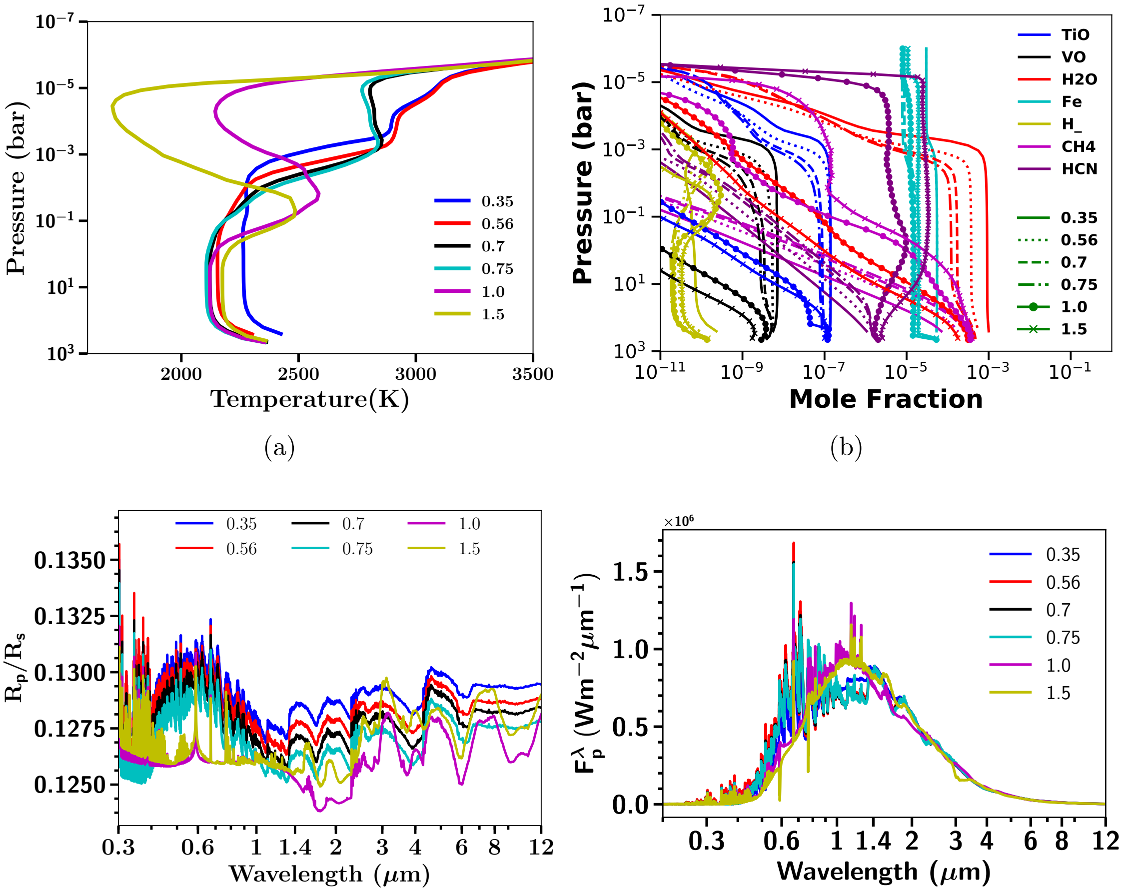

(a) (b)

(c) (d)

Figure 5.25: **(a)** Figure showing *P*-*T* profiles for a range of C/O ratios at 0.5 RCF and solar metallicity (0.56) for WASP-121b. **(b)** Figure showing equilibrium chemical abundances for some important species for various C/O values obtained using *P*-*T* profiles shown in Figure 5.25a. **(c)** Figure showing transmission spectra for WASP-121b for different values of C/O ratios obtained using *P*-*T* profiles shown in Figure 5.25a and corresponding equilibrium chemical abundances shown in Fig. 5.25b. **(d)** Figure showing emission spectra for WASP-121b for different values of C/O ratios obtained using *P*-*T* profiles shown in Figure 5.25a and corresponding equilibrium chemical abundances shown in Fig. 5.25b.

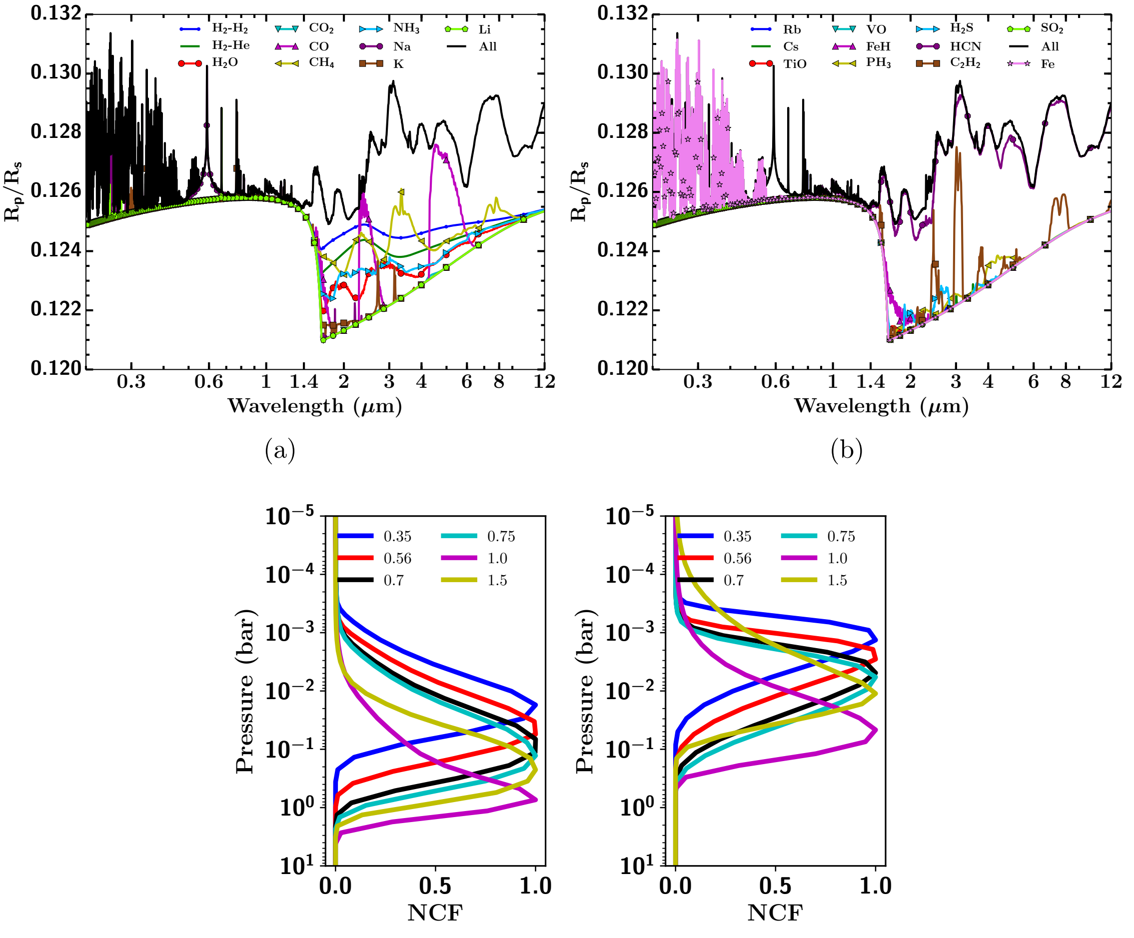

(a) (b)

(c) (d)

Figure 5.26: **(a)** Same as Fig. 5.24a but for WASP-121b. **(b)** Same as Fig. 5.24b but for WASP-121b. **(c,d)** Figures c, d showing normalised contribution function at 1.6 and 3.1 μm for a range of C/O ratios for emission spectra as shown in Figure 5.25d.

WASP-121b The *P-T* profiles for WASP-121b for a range of C/O ratios are shown in Fig. 5.25a. With increasing C/O ratio the major temperature inversion shifts to higher pressures. The major temperature inversion refers to the inversion that has a potential observational signature unlike the inversion due to Fe opacity at extremely low pressures ($\sim 10^{-5}$ bar) seen in Fig. 5.25a. The absence of H_2O due to thermal dissociation also contributes to an inversion at extremely low pressures, as there is no strong infrared emitting species available to re-emit the energy absorbed by Fe.

The abundance of TiO/VO species which are the primary absorbers for forming the temperature inversion layer, decrease with increasing C/O ratio. Their abundance at a C/O ratio of 1.0 and 1.5 is low, still the inversion layer is maintained, albeit not as hot as at other low C/O ratios. We investigated this phenomenon by using two tests, first removing TiO/VO opacities and second removing Na, K, TiO and VO opacities. We found that this inversion at high C/O ratio can be maintained due to Na and K opacities in the absence of TiO/VO opacities or their low abundance, as found by Mollière et al. (2015). Moreover, surprisingly H- opacity also contributes to this inversion at high C/O ratio and high value of RCF (1.0) as discussed in Section 5.6.2. It is interesting to see that the HCN abundance at high C/O ratios is substantial even in the low pressure regions ($P > \sim 1$ mbar). This can also be noticed in the transmission spectrum shown in Fig. 5.25c and decoupled transmission spectrum shown in Fig. 5.26a and 5.26b, which is dominated by HCN features in the infrared at a C/O ratio of 1 and 1.5, as opposed to CH_4 for WASP-017b. This shows an important result that at high temperatures HCN dominates over CH_4 in the atmosphere at high C/O ratios. Therefore, HCN features provide a very strong signature to constrain high C/O ratios in exoplanet atmospheres. The transition from an H_2O dominated spectra to that dominated by HCN happens between C/O ratio of 0.75-1.0. Therefore, the temperature dependence of the C/O transition as seen in Mollière et al. (2015) and Goyal et al. (2018) does not seem to be holding in this case, as the transition for WASP-017b also happens in this C/O regime (0.75-1.0). The transmission spectrum also shows FeH features between 0.8 and 1.2 μm at a C/O ratio of 1.0 and 1.5. The absence of TiO/VO features makes it possible for FeH to appear, without being masked.

In the emission spectrum shown in Fig. 5.25d most of the molecular features are seen in emission due to the presence of an inversion layer, as explained before. However, between a C/O ratio of 1 and 1.5 surprising difference can be seen, especially at 3.1 μm which is the wavelength of a strong HCN absorption band. At a C/O ratio of 1 it is an emission feature, however it transforms to an absorption feature at a C/O ratio of 1.5. This is because at a C/O ratio of 1.5 slightly cooler upper atmosphere is being probed as can be seen in the NCF at 3.1 μm in Fig. 5.26d

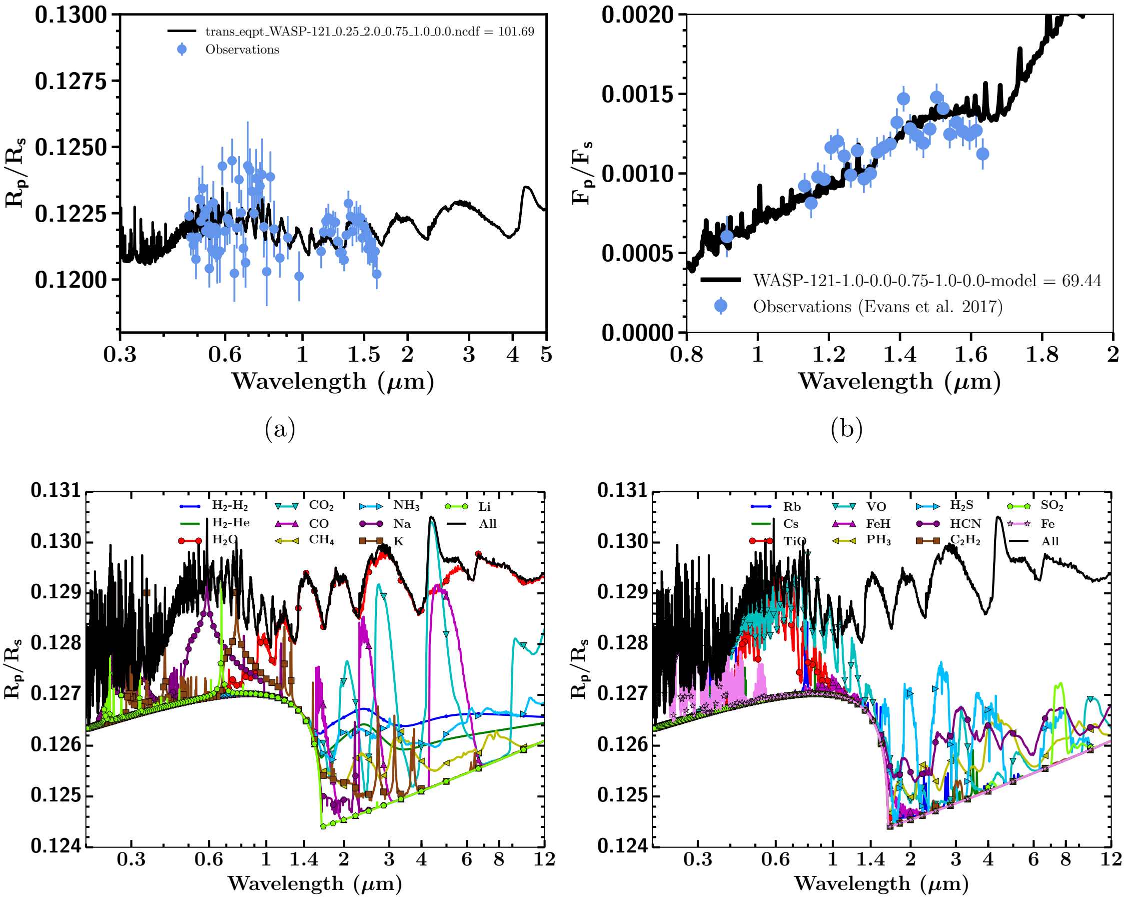

(a) (b)

(c) (d)

Figure 5.27: **(a)** Figure showing best fit model transmission spectra using the grid of model transmission spectra for WASP-121b and observations from Evans et al. (2018) with χ^2 value of 101.68. **(b)** Figure showing best fit model emission spectra using the grid of model emission spectra for WASP-121b and observations from Evans et al. (2017) with χ^2 value of 69.44. **(c)** Decoupled transmission spectra similar to Figure 5.24a. **(d)** Decoupled transmission spectra similar to Figure 5.24b.

as compared to a C/O ratio of 1. Therefore, at a C/O ratio of 1.5, HCN absorbs the radiation from the lower (high pressure atmosphere) in comparison to for a C/O ratio of 1.0, which probes deeper atmosphere where it has an inversion and leads to HCN emission. Interestingly, at 1.6 μm HCN leads to an emission feature both at a C/O ratio of 1 and 1.5, since at 1.6 μm the inversion layer is being probed at both C/O ratios as seen in the NCF in Fig. 5.26c and *P*-*T* profile in Fig. 5.25a. Therefore, HCN can be observed in emission as well as absorption at high C/O ratios (1.5) for extremely irradiated planets such as WASP-121b.

5.8 Interpreting the observations of WASP-121b

WASP-121b is not expected to be cloudy due to its extremely high temperature. Moreover, Evans et al. (2018) showed that the extremely steep slope in the optical is not due to enhanced Rayleigh scattering from a haze. In Evans et al. (2018) observations were interpreted using isothermal P-T profiles (see Fig. 11 and 12 in Evans et al. 2018) and resulting in detection of H_2O, evidence of VO and the possibility of SH causing significant absorption in the UV and optical. Therefore, here we use our grid of model transmission spectra with RCE P-T profiles and additional H- and Fe opacity, without grey clouds and enhanced scattering, to fit the WASP-121b data from Evans et al. (2018). Similar to Chapter 3, we have excluded the data short-ward of 0.47 μm while performing the fitting, since the steep slope in this region is not explained by Rayleigh scattering and is potentially due to SH molecule (Evans et al. 2018), currently not included in the ATMO model. Fig. 5.27a shows the best fit model transmission spectra for observations from Evans et al. (2018). It shows the clear H_2O feature at 1.4 μm and features in the optical resembling TiO/VO features. The decoupled spectra in Figure 5.27c and 5.27d shows that the optical spectra is dominated by VO features. This strengthens the argument that VO leads to temperature inversion in WASP-121b and the P-T structure of this planet is in that narrow temperature regime where VO abundance dominates the TiO abundance as discussed in Chapter 4. This fitting result is very surprising in a sense that it confirms the result using isothermal P-T profiles discussed in Section 3.7.12 in Chapter 3 and Evans et al. (2018). This result also strengthens the evidence of VO in the atmosphere of WASP-121b.

The best fit model gives a reduced χ^2 value of 1.37 with 74 DOF (75 data points minus 1). The best fit model with RCE P-T profiles gives super-solar metallicity and super-solar C/O ratio (both when varying O/H and C/H). The best fit model with isothermal P-T profile and without H- and Fe opacity also has a super-solar metallicity with rainout condensation and sub-solar with local condensation, however they both have a sub-solar C/O ratio. Fig. 5.27b shows the best fit model emission spectra for observations from Evans et al. (2017). It shows a 1.4 μm H_2O emission feature, indicative of inversion layer, as explained in previous sections. However, the emission feature at 1.2 μm is still a mystery, similar to transmission feature at 1.2 μm in Figure 5.27a.

5.9 Summary

The approximation of an isothermal P-T profile has many limitations for a real planetary atmosphere and is a reasonable approximation only to generate model transmission spectra, which probes a very small part of the overall atmosphere.Therefore, a grid of radiative-convective equilibrium *P*-*T* profiles and corresponding equilibrium chemical abundances, transmission spectra, emission spectra and contribution functions was created, for a range of observationally significant exoplanets. This grid of models also included H- and Fe opacity, in addition to the previous grid of models in Goyal et al. (2018) and Goyal et al. (2019b), presented in Chapters 3 and 4, respectively. Some of the major contributors to opacities in different temperature and pressure ranges were identified. The sensitivity of model simulations to model choices was investigated. The differences in RCE *P*-*T* profiles with local and rain-out condensation were investigated, showing that adopting different condensation approaches can result in substantial differences in the resulting *P*-*T* profiles and thereby the model spectra, for a typical hot Jupiter planet like WASP-017b. Adopting different line wing profiles of Na and K, led to differences of ∼50-100 K in the deeper atmosphere temperature, thus leading to some differences in the emission spectra, which may be detectable with future observations. The effect of differences in VO line-lists on the *P*-*T* profiles and the spectra were investigated. It was found to have some differences on the *P*-*T* profiles and spectra, which can even be larger in certain regions of the grid parameter space where VO becomes more dominant than TiO as shown in Chapter 4. The differences in the derived RCE *P*-*T* profiles with and without convection were also investigated, concluding that convection plays a negligible role in determining the RCE *P*-*T* profiles of highly irradiated hot Jupiter exoplanets. The differences in the derived *P*-*T* profiles and the spectra between the simulations, varying C/O ratio by varying O/H and those by varying C/H are investigated, which reveals some differences within the range of C/O ratio adopted in the library, but to a lesser extent compared to other parameters in the library and other model choices.

Decoupled emission spectra for WASP-017b and WASP-121b enabled us to identify major spectral features in the emission spectrum. The effect of thermal ionisation was investigated for the high temperature planet WASP-121b, revealing that Na and K are ionized between 10^{-1} to 10^{-5} bar (with an atmospheric temperature inversion) at a solar C/O ratio, solar metallicity and 0.5 RCF. However, at a C/O ratio of 1.5 there is no temperature inversion with overall lower temperatures, thus inhibiting the thermal ionisation of Na and K. The effect of recently added opacities H- and Fe were investigated. It was found that Fe leads to very sharp inversion at the top of the model atmosphere (∼10^{-5} - 10^{-6} bar). Moreover, Fe opacity tends to cool the *P*-*T* profile for $P > 0.1$ bar, due to absorption of radiation in the upper atmosphere. It also imparts narrow spectral features in the UV-optical part of the transmission spectrum short-ward of ∼0.4 μm. The effect of H- opacity was investigated for the high temperature planet WASP-121b. At 0.5 RCF and a solar C/O ratio, H- opacity tends to cool the deeper atmosphere (P $>$ 0.1 bar), similar to Fe. However, the more extreme effect of H- opacity is apparent at 1.0 RCF and a C/O ratio of 1.5, due to increasing abundance of H- with increased temperature (due to higher RCF) and decreased TiO/VO abundance at this C/O ratio. There is a substantial difference in the P-T profile with and without H- opacity, with $\sim$200 K difference for P $<$ 0.1 bar and $\sim$500 K for P $>$ 0.1 bar. In the transmission spectrum H- opacity tends to mute the line wings of Na, K and all features up-to 1.6 μm (limit of H- bound free absorption) mimicking the effect of grey cloud deck opacity. The differences in the P-T profile with and without H- opacity also leads to substantial differences in the emission spectrum.

Since a temperature inversion has been detected in the atmosphere of WASP-121b (Evans et al. 2017), we investigated different mechanisms other than TiO/VO that can produce such a temperature inversion. At first the amount of opacity needed to form an inversion was investigated by adding varying levels of optical grey opacity throughout the atmosphere for WASP-121b, showing that an optical grey opacity of 0.02 cm^2/g is needed to form an inversion. This test also showed how the emission spectrum evolves when the derived P-T profile evolves from an atmosphere without a temperature inversion to one with such an inversion, also revealing the transformation of the 1.4 μm H_2O absorption feature to an emission feature, as detected in WASP-121b (Evans et al. 2017). Since the Fe absorption cross-section is very high in the UV-Optical region of the spectrum, its potential to form a temperature inversion was investigated, which revealed that Fe is unable to produce a temperature inversion in the dense atmosphere (1 bar to 0.01 mbar) even at 200× solar metallicity.

The library of simulations presented in this chapter was developed for four different recirculation factors, six metallicities and six C/O ratios. The effect of varying the recirculation factor was investigated for WASP-121b, showing the variation of the P-T profile, equilibrium chemical abundances and thereby the transmission and the emission spectrum. The 0.25 RCF P-T profile almost resembles an isothermal atmosphere which is also reflected in the emission spectrum, with an increase in size of the spectral features both in transmission and emission spectrum as RCF increases and the appearance of a temperature inversion in the P-T profiles.The effect of varying metallicity was investigated for WASP-017b and WASP-121b. For WASP-017b the P-T profile becomes hotter throughout the atmosphere with increasing metallicity because of increasing opacity due to absorption by heavier molecules such as H_2O, CO_2 etc., as their abundance increases with increasing metallicity. The size of the spectral features of H_2O, CO_2 etc. at first increases with metallicity (up to 10× solar metallicity) due to higher abundances but then decreases again as the scale height of the atmosphere decreases with increased metallicity. Increased metallicity leads to deeper absorption features in the emission spectra for WASP-017b. For WASP-121b, the observationally significant temperature inversion shifts to lower pressures with increasing metallicity. The transmission spectra variation with metallicity is similar to that for WASP-017b. However, in contrast to WASP-017b there are many emission features in the emission spectrum of WASP-121b due to presence of a temperature inversion and some of them (for e.g., the CO feature) become larger with increasing metallicity.

The effect of varying the C/O ratio by varying O/H was investigated for WASP-017b and WASP-121b, across the entire range of C/O ratios adopted in the grid (0.35 to 1.5). For WASP-017b when O/H is varied, the resulting *P*-*T* profile cools with increasing C/O ratio and a transition can be seen from a H_2O dominated spectra to a spectra dominated by carbon bearing species (primarily CH_4) between a C/O ratio of 0.75 and 1. This leads to drastic changes in the transmission and emission spectra with C/O ratio variation. For WASP-121b when O/H is varied, the strength of the temperature inversion decreases as the abundance of TiO/VO decreases with increasing C/O ratio. At a C/O ratio greater than 1 even though TiO/VO abundances are low, a temperature inversion is maintained in the atmosphere due to Na and K at RCF value of 0.5. Whereas, for a RCF value of 1 (hotter *P*-*T* profile) H- opacity contributes substantially to develop inversion as discussed in Section 5.6.2. Interestingly, extremely irradiated exoplanet atmospheres like WASP-121b show a spectra dominated by HCN features at infrared wavelengths for high C/O ratios (> 1) in comparison to comparatively cooler planets like WASP-017b which are dominated by CH_4 features.

Finally, the transmission and emission observations of WASP-121b were interpreted using the library of models with RCE *P*-*T* profiles. The observational transmission spectra probing the planetary atmospheric limb reveal H_2O features in the infrared with evidence of VO in the optical. The best fit model indicates super-solar metallicity and surprisingly greater than solar C/O ratio. The observational emission spectra probing the dayside of the planetary atmosphere reveals a H_2O feature in emission giving evidence of a potential temperature inversion.

Chapter 6

Conclusions and Future Work

> "Nothing in life is to be feared, it is only to be understood. Now is the the time to understand more, so that we may fear less"
>
> — Marie Curie

We are entering an era of comparative studies, with regards to observations of exoplanet atmospheres, from atmospheric studies of a few handful of hot Jupiters some time ago, to a plethora of different types of exoplanets. This has motivated development of atmospheric models for a range of exoplanet atmospheres, that could be used not only to interpret their observations, but to understand the different physical and chemical processes that shape these far away worlds. Therefore, in this thesis we take the first step of developing a library of 1D model atmospheres for a range of hot Jupiter and warm Neptune exoplanets. This allows to explore different types of atmospheres these planets could form or have, based on the distance from their host stars and its spectral type, planetary atmospheric temperature structure and composition, planetary gravity, and many other factors. Furthermore, it provides a tool to identify various observational signatures, that could be used to characterise these atmospheres and constrain their properties. Simulated observations using theoretical forward models also aid predicting scientifically important targets for characterisation, to use precious telescope time most efficiently. The launch of the James Webb Space Telescope (JWST) will enable probing exoplanet atmospheres from wavelengths of 0.6 all the way up-to 28 µm. Therefore, a library of models will be extremely valuable to select the best targets for characterisation using JWST.

6.1 Conclusions

In this thesis we first describe various ingredients to construct a one dimensional radiative-convective-chemical equilibrium model for planetary atmospheres in Chapter 2. We derive the radiative transfer equation to compute the radiative flux in a plane-parallel atmosphere with isotropic and coherent scattering. We detail the computation of high temperature absorption cross-sections of various gases and describe the correlated-k technique used to increase the computational efficiency, while including absorption cross-sections in atmospheric models. We describe the computation of equilibrium chemical abundances and treatment of rainout condensation, along with definitions of metallicity and C/O ratio. We also detail the parameterisations used for multi-gas Rayleigh scattering, haze, clouds and convective flux in the ATMO model. Finally in this chapter, we describe the computation of transmission spectra and the contribution function in ATMO.

We then present a library of model spectra, pressure-temperature profiles and equilibrium chemical abundances, for a range of hot Jupiter and warm Neptune exoplanet atmospheres, altogether termed the "Atmospheric Library of Far Away Worlds" using our 1D radiative-convective equilibrium model ATMO in subsequent Chapters 3, 4 and 5.

In Chapter 3, we started by validating the equilibrium condensation scheme with local and rainout condensation by comparing with different published models in the literature. We highlighted the reasons for differences in various models and their potential to effect interpretation of observations due to differences in adopted thermodynamic data, list of chemical species used for computation of equilibrium chemical abundances and approach for rainout condensation (constant pressure or temperature) with isothermal P-T profiles. We demonstrated that the difference in the transmission spectra between the isothermal and consistent P-T profile were small in most cases, except in the temperature regime where spectrally important species condense and potentially rain out of the atmosphere (for example, Na). We developed a methodology to select the best exoplanet candidates for transmission spectroscopy observations, using the planetary scale height and the host star's V and K magnitude. Following this, a library of model transmission spectra and equilibrium chemical abundances was developed for 117 selected exoplanets. We term this library focused on specific planets as "planet specific library". The simulated spectra and abundances were produced using our 1D radiative–convective–chemical equilibrium model ATMO, under the assumption of an isothermal P-T profile and including local and rainout condensation, varying temperature, metallicity, C/O ratio, haziness and cloudiness. This resulted in a grid of approximately 1 million simulated spectra. We highlighted spectral features of various chemical species across a range of wavelengths, useful for identifying their signatures in JWST or HST transmission spectra. We find that CO remains the most abundant chemical species between $\sim$0.1 to 100 millibar, apart from H, H_2 and He in all the temperature regimes, except below 800 K, where H_2O and CH_4 are more abundant than CO. CO also remains the most abundant chemical species apart from H, H_2 and He in all the metallicity regimes. CO abundances also increase substantially with increasing metallicity. There are changes in the spectral features with change in metallicity, first due to change in the chemical composition and second due to change in the atmospheric scale height, which decreases with increasing metallicity for a given temperature. We find the transition C/O ratio, from H_2O to CH_4 (carbon species) dominated spectra increases with increasing temperature in agreement with previous studies, but spanning a larger range, with values as low as $\sim$0.7 for low equilibrium temperature (960 K) planets like HAT-P-12b and $\sim$1-1.3 for very high equilibrium temperature (2580 K) planets like WASP-12b, where even HCN and C_2H_2 can become more abundant than CH_4.

We used our set of simulations to interpret observations of the ten exoplanet atmospheres from Sing et al. (2016). We see a continuum from clear to hazy/cloudy atmospheres as found by Sing et al. (2016). The data for all the ten planets are consistent with sub-solar to solar C/O ratio, 0.005 to 10 times solar metallicity and a water, rather than a methane dominated atmosphere. The data for WASP-17b, HAT-P-1b and WASP-6b are consistent with the lowest C/O ratio in out parameter space (0.15), implying the current observations of these planets do not show any clear features, indicative of carbon bearing species. The data for HAT-P-12b and WASP-6b are consistent with extremely high haziness, but without any grey clouds. The data for WASP-12b show extremely muted H_2O features leading to the most hazy and cloudy planet of all, while the data for WASP-17b, WASP-39b, WASP-19b and WASP-31b are consistent with a comparatively clear atmosphere. The χ^2 map for WASP-31b also highlighted the degeneracy existing between the effect of metallicity and clouds/haze on spectral features. The χ^2 map for HD 209458b revealed a bimodal structure in metallicity, again highlighting the degeneracy between metallicity and all other considered parameters. We also interpreted the observations of WASP-96b and WASP-121b from Nikolov et al. (2018) and (Evans et al. 2018), respectively. WASP-96b showed the first detection of Na line wings in an exoplanet atmosphere, which allowed us to constrain its Na abundance using retrieval techniques. The spectra of WASP-121b showed a H_2O feature along with strong evidence of VO and a steep slope in the UV-optical wavelengths, possibly due to SH. We also demonstrated the application of our set of model simulations in conjunction with JWST simulator `PandExo`, as a predictive tool to plan future observations.

Planet specific library included simulations with fixed gravity for a a particular planet. Moreover, the measured gravity values of a planet can change due to changes in stellar/planetary radius derived from new observations (for e.g., GAIA mission). Therefore, to make the library of models flexible enough to be adapted to any gravity values and also to their updated values in the future we developed a generic library of transmission spectra, which can be scaled to a range of H_2/He dominated exoplanet atmospheres, described in detail in Chapter 4. The entire generic library consists of 56,320 model simulations across 22 isothermal temperatures, four planetary gravities, five atmospheric metallicities, four C/O ratios, four uniform cloud parameters, four scattering haze parameters, and two chemical condensation scenarios. This library of atmospheric models allowed us to decouple and better understand the thermochemical processes shaping observable spectra. We found that SO_2 features at 6–8µm, along with H_2O, can be used to constrain the metallicity of the exoplanet atmosphere, since the SO_2 spectral feature only appears for metallicities greater than 100x solar. We also found that the presence of VO without TiO can help constrain the temperature of the atmospheric limb, and that both TiO/VO features can reveal dominant physical processes (rainout or local condensation) in the planet's atmosphere. It was seen that at high C/O ratios ($\sim$1), spectral features in the infrared are different between the rainout and local condensation case, as the rainout case has a higher abundance of carbon bearing species without any oxygen, such as CH_4, C_2H_2 and HCN. We also concluded that the differences in solar elemental abundances used for model initialisation, can lead to differences in equilibrium chemical abundances and therefore the spectral features.

Finally, to overcome the limitations due to adopting an isothermal P-T profiles and also to generate planetary emission spectra, a library of radiative-convective equilibrium (rce) P-T profiles and corresponding equilibrium chemical abundances, transmission and emission spectra, and contribution functions was developed, described in detail in Chapter 5. We showed that adopting different condensation approaches (local or rainout) can result in substantial differences in the rce P-T profiles and thereby the spectra. Adopting different line wing profiles for Na and K and different line-list sources for VO resulted in differences in the P-T profiles but the differences in the transmission and emission spectra were negligible in terms of potential detection with current observations. The difference between simulations with and without convection was found to be negligible for irradiated hot Jupiter exoplanet atmospheres, indicating that convection plays no role in shaping the P-T structure of the hot Jupiter exoplanets, at-least in the observable region of the atmosphere. The model simulations, varying C/O ratio by varying O/H and those by varying C/H revealed some differences within the range of C/O ratio adopted in the library, but to a lesser extent compared to other parameters in the library and other model choices.

Including ionisation in the model has a substantial effect of the Na and K abundances at temperatures greater than 2000 K, where they tend to ionise into Na+ and K+ ions and are therefore are absent from the transmission spectra. Ionisation also leads to formation of H- ions. The abundance of H- increases with increasing temperature (or RCF) and contributes greatly to absorption of radiation and thereby altering the *P*-*T* profile. At some extreme values of our parameter space such as at a C/O ratio of 1.5 where TiO/VO abundance is low, H- opacity even contributes to a temperature inversion and thereby leads to cooling of the deeper atmosphere. The transmission spectra features of H- can also be noticed at a high C/O ratio or when TiO/VO are absent, as it tends to mute the features in the optical to near infrared wavelengths (up-to 1.6 μm), mimicking the effect of cloud. The differences in *P*-*T* profiles due to the additional H- opacity also leads to differences in the emission spectra. The strong UV-optical absorption of Fe leads to a sharp temperature inversion at the top the atmosphere but this feature does not have any observational signature due to the low density of the atmosphere in that region. However, sharp Fe features can be seen in UV-Optical wavelength region of the transmission spectra. Without TiO/VO opacity an additional grey opacity of 0.02 cm^2/g and higher, in the optical wavelengths, throughout the atmosphere can lead to formation of a temperature inversion. Moreover, even though Fe has strong opacity in the the UV-optical wavelength region, it is not sufficient to produce a temperature inversion in the dense observable region of the atmosphere.

Adoption of an increasing recirculation factor (decrease in actual energy redistribution) leads to hotter *P*-*T* profile throughput the atmosphere. The *P*-*T* profile throughout the atmosphere also becomes hotter with increasing metallicity, due to an increase in the abundances of species heavier than H_2 and He. This also leads to an increase in the size of the spectral features up-to $\sim$10× solar metallicity due to an increase in the abundances of heavier species, but the features again start becoming smaller due to a decrease in atmospheric scale height. Changing the C/O ratio drastically changes the transmission and emission spectra, due to a transition from H_2O dominated spectra at a low C/O ratio to spectra dominated by carbon bearing species such as CH_4, HCN, C_2H_2 etc. at a high C/O ratio. The C/O ratio of this transition also increases with increasing temperature (hotter planets). For extremely irradiated exoplanet atmospheres like WASP-121, at high C/O ratio and low RCF value, Na and K opacity contributes to produce a temperature inversion, however at high C/O ratio and high RCF value, even H- contributes substantially to produce this inversion. Moreover, WASP-121b shows a spectra dominated by HCN features in the infrared at high C/O ratios (> 1) in comparison to comparatively cooler planets like WASP-017b which are dominated by CH_4 features.

The observational transmission spectra of WASP-121b from Evans et al. (2018)

probing the planetary atmospheric limb, when interpreted using this library of models with rce P-T profiles, reveal H_2O features in the infrared with evidence of VO in the optical. This strengthens the argument that VO opacity is the cause of the temperature inversion in WASP-121b, and the P-T structure of this planet is in that narrow temperature regime where the VO abundance dominates the TiO abundance as predicted initially using the generic grid in Chapter 5. The best fit model indicates super-solar metallicity and, surprisingly, a greater than solar C/O ratio. The observational emission spectra probing the dayside of the planetary atmosphere reveals a H_2O feature in emission giving an evidence of a P-T profile with a temperature inversion.

The planet specific and generic library of models is publicly available here[1], with the web interface for generic grid on the Space Telescope Science Institute (STScI) EXOCTK portal[2]. We encourage the community to use it as a tool to assist them in planning future observations, such as with JWST, HST and various ground based telescopes, along-with interpreting existing datasets. It can provide a useful complement for interpretation, alongside atmospheric retrieval analysis.

6.2 Future Work

We recently coupled the Eddysed cloud code (Ackerman et al. 2001) fully consistently with ATMO. This means that the radiative effects of clouds/condensates are fed back into the radiative transfer computation, thus the final radiative-convective equilibrium P-T profile includes the radiative effect of clouds as in a real planetary atmosphere. This allows us to explore the clouds formation and its effects on the P-T profiles and thereby the spectra, in exoplanet atmospheres. Therefore, a future version of the library of model simulations will also include this more realistic cloud treatment. This development will also pave the way for development of a cloudy retrieval model for hot Jupiter exoplanet atmospheres similar to Burningham et al. (2017), developed for Brown dwarfs.

In this thesis we mainly focused on hot Jupiter and warm Neptune exoplanet atmospheres. However, a surprisingly large number of mini-Neptune and super-Earth sized planets were detected by Kepler (Fressin et al. 2013; Dressing et al. 2015). The Transiting Exoplanet Survey Satellite (TESS) yield calculations also predict that a large number of its detected planets ($\sim$50%) will be in the mini-Neptune to super-Earth planetary regime (Barclay et al. 2018). Therefore, we plan to extend the capability of ATMO to be able to model mini-Neptune, terrestrial super-Earth and Earth size planets. As a first step, a surface parameterisation will

---

[1] `https://drive.google.com/drive/folders/1Yz94usAAiXtnLR0yoq-qkuhegRrI4u4B`

[2] `https://exoctk.stsci.edu/`

be added in the model, to enable modelling terrestrial planets, including the radiative properties of surfaces, which can also act as a source or sink of atmospheric gases as in Hu et al. (2012). We also plan to use a more flexible chemistry scheme as shown in Rimmer et al. (2016) which will allow modelling chemistry across a range of planetary atmospheres. Informed by chemistry, we plan to include opacities of many more species important for cooler planets, beyond those included for this work. Including the effect of pressure broadening while computing opacity databases for different planetary atmospheres is one of the unsolved problems in the exoplanet modelling community and a major bottleneck for accurately modelling high metallicity (>200x solar) exoplanet atmospheres as expected for mini-Neptune, super-Earth and Earth size planets (see Section 2.2 from Goyal et al. 2018, for details). Therefore, there is scope to develop a flexible pressure broadening scheme that can be applicable to a range of planetary atmospheres.

In this thesis we focused mainly on equilibrium chemistry for hot Jupiter and warm Neptune exoplanet atmospheres. However, there are many non-equilibrium processes like vertical mixing and photochemistry that are important in hot Jupiter atmospheres as shown in Drummond et al. (2016). Furthermore, non-equilibrium processes play more important role in governing the chemical abundances of cooler mini-Neptune, super-Earth and Earth size planets, where the assumption of equilibrium chemistry, can become very inaccurate (Madhusudhan et al. 2016b). Therefore, we aim to compute non-equilibrium chemical abundances as we expand our library of models to cooler and terrestrial exoplanet atmospheres.

The colour of any planet is determined by its wavelength dependent albedo, which is a function of the scattering and absorption properties of the species in the atmosphere, clouds and the surface properties for terrestrial planets. For example, Earth has a bluish colour when observed from space mainly due to its water oceans and also to some extent due to Rayleigh scattering by N_2 and O_2 in earth's atmosphere. Thus the wavelength dependant albedo of the planet can be an important measure to constrain its atmospheric and surface properties. We plan to develop ATMO to compute the albedo or couple an existing albedo code to ATMO (e.g Lewis et al. 2014). This will allow generation of a grid of albedo maps and expected colours for a range of exoplanets.

As nature is always full of surprises, this library will evolve as we get more observations and our understanding of these worlds evolve, hopefully someday allowing us to answer one of the most fundamental questions of humanity, Are we alone in this Universe?

Appendix A

A.1 χ^2 Maps

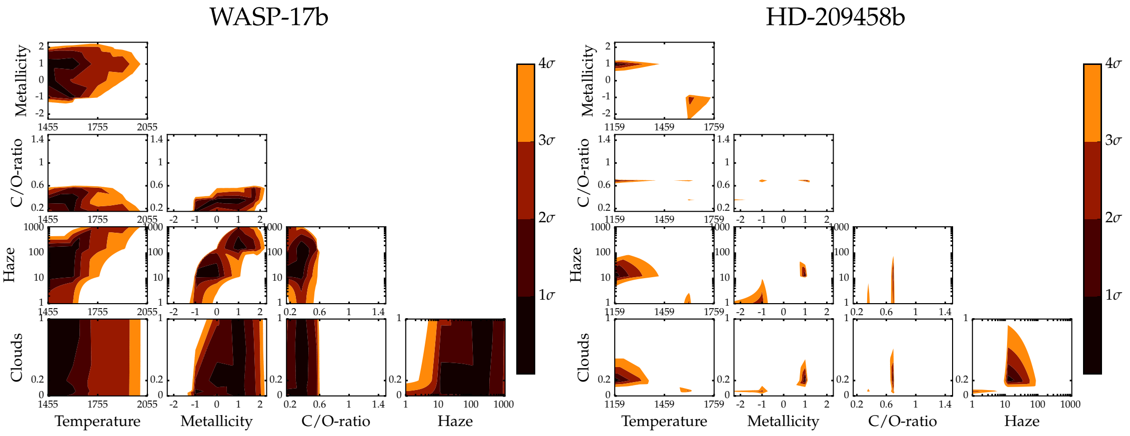

(a) (b)

Figure A.1: **(a)** Figure showing WASP-17b χ^2 Map, with same format as Figure 3.30 **(b)** Figure showing HD 209458b χ^2 Map.

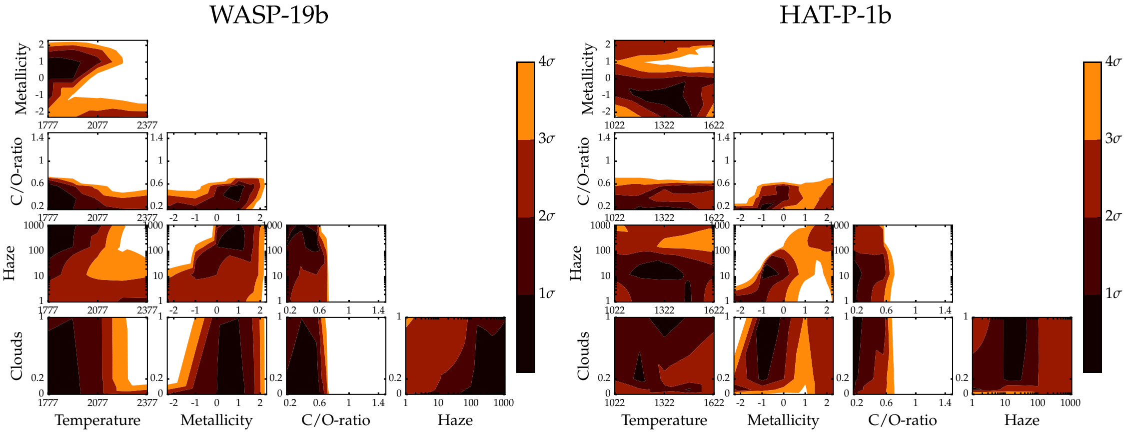

(a) (b)

Figure A.2: **(a)** Figure showing WASP-19b χ^2 Map. **(b)** Figure showing HAT-P-01b χ^2 Map.

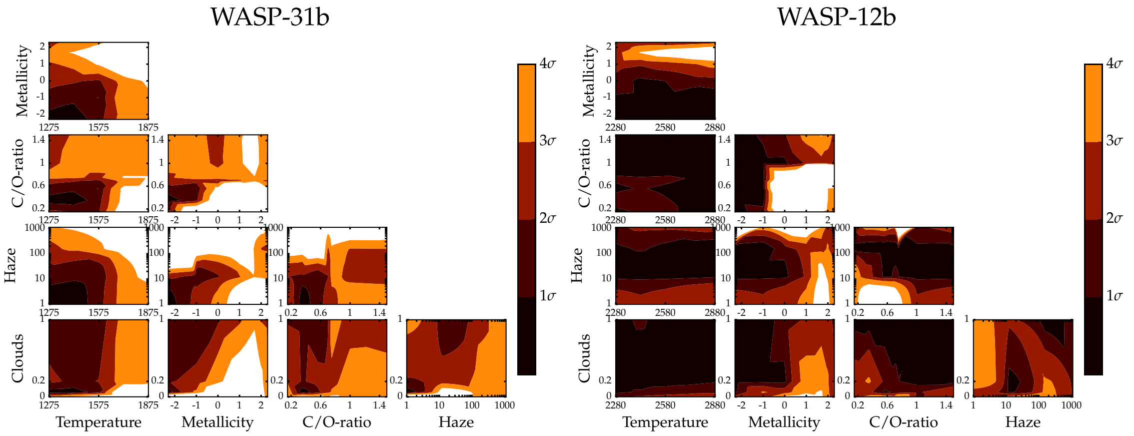

(a) (b)

Figure A.3: **(a)** Figure showing WASP-31b χ^2 Map. **(b)** Figure showing WASP-12b χ^2 Map.

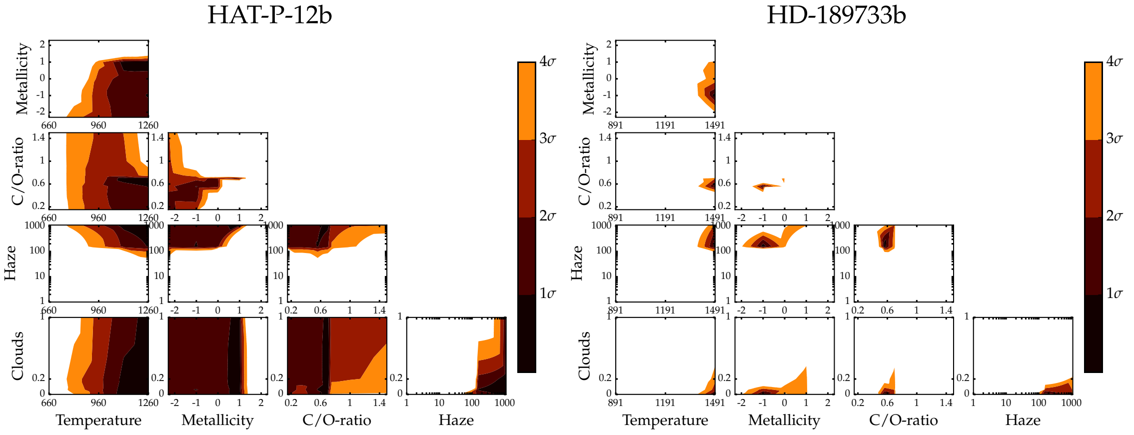

(a) (b)

Figure A.4: **(a)** Figure showing HAT-P-12b χ^2 Map. **(b)** Figure showing HD 189733b χ^2 Map.

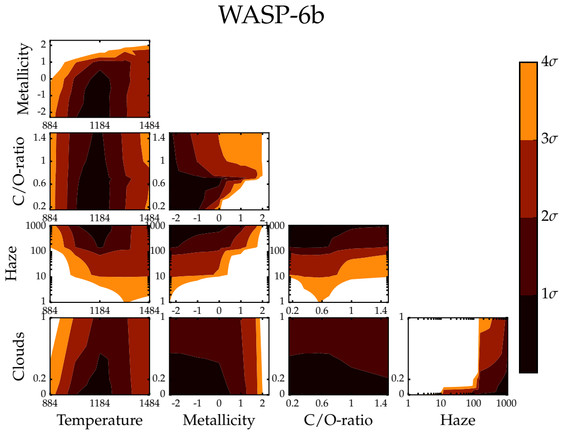

(a) (b)

Figure A.5: **(a)** Figure showing WASP-6b χ^2 Map.

Appendix B

B.1 Planets and their parameters in the Grid

All the stellar and planetary parameters adopted from TEPCAT (Southworth 2011a) database, for the model simulations of 117 exoplanets in the grid are listed here. First column shows planet names with 'b' omitted indicating first planet of the stellar system as in TEPCAT database. Subsequent columns show, stellar temperature ($\mathrm{T_s}$) in Kelvin, stellar metallicity ($\mathrm{[Fe/H]_s}$), stellar mass ($\mathrm{M_s}$) in units of solar mass, stellar radius ($\mathrm{R_s}$) in units of solar radius, logarithmic (base 10) stellar gravity ($\mathrm{logg_s}$) in m/s^2, semi-major axis (a) in AU, planetary mass ($\mathrm{M_p}$) in units of Jupiter mass, planetary radius ($\mathrm{R_p}$) in units of Jupiter radius, planetary surface gravity ($\mathrm{g_p}$) in m/s^2, planetary equilibrium temperature ($\mathrm{Teq_p}$) in Kelvin assuming 0 albedo and efficient redistribution, V magnitude ($\mathrm{V_{mag}}$) of the host star, discovery paper reference (Discovery Paper) and finally the most updated reference.

System	T_s	$[Fe/H]_s$	M_s	R_s	$\log g_s$	a	M_p	R_p	g_p	Teq_p	V_{mag}	Discovery Paper	Updated Reference
	(K)		(M_{sun})	(R_{sun})	(m/s^2)	(AU)	(M_{jup})	(R_{jup})	(m/s^2)	(K)			
55-Cnc-e	5196	0.31	0.91	0.94	4.43	0.02	0.03	0.17	21.40	2349	5.95	Winn et al. (2011)	Demory et al. (2016)
GJ-436	3416	-0.03	0.51	0.46	4.83	0.03	0.08	0.37	13.00	669	10.68	Gillon et al. (2007)	Lanotte et al. (2014)
GJ-1214	3026	0.39	0.15	0.22	4.94	0.01	0.02	0.25	7.60	547	14.67	Charbonneau et al. (2009)	Harpsøe et al. (2013)
GJ-3470	3652	0.17	0.51	0.48	4.78	0.04	0.04	0.35	6.80	604	12.27	Bonfils et al. (2012)	Biddle et al. (2014)
HAT-P-1	5975	0.13	1.15	1.17	4.36	0.06	0.53	1.32	7.46	1322	10.40	Bakos et al. (2007)	Nikolov et al. (2014)
HAT-P-3	5185	0.27	0.90	0.87	4.51	0.04	0.58	0.95	16.14	1189	11.86	Torres et al. (2007)	Southworth (2012)
HAT-P-4	5860	0.24	1.27	1.60	4.13	0.04	0.68	1.34	9.42	1691	11.00	Kovács et al. (2007)	Southworth (2011b)
HAT-P-6	6570	-0.13	1.29	1.52	4.19	0.05	1.06	1.40	13.50	1704	10.54	Noyes et al. (2008)	Southworth (2012)
HAT-P-11	4780	0.31	0.81	0.69	4.66	0.05	0.08	0.40	13.20	838	9.47	Bakos et al. (2010)	Southworth (2011b)
HAT-P-12	4650	-0.29	0.73	0.70	4.61	0.04	0.21	0.94	6.37	960	12.80	Hartman et al. (2009)	Lee et al. (2012b)
HAT-P-13	5653	0.41	1.32	1.76	4.07	0.04	0.91	1.49	10.15	1725	10.62	Bakos et al. (2009)	Southworth et al. (2012b)
HAT-P-17	5246	0.00	0.86	0.84	4.52	0.09	0.53	1.01	12.90	792	10.54	Howard et al. (2012a)	Howard et al. (2012a)
HAT-P-18	4870	0.10	0.77	0.72	4.61	0.06	0.20	0.95	5.42	841	12.76	Hartman et al. (2011a)	Esposito et al. (2014)
HAT-P-19	4990	0.23	0.84	0.82	4.54	0.05	0.29	1.13	5.62	1010	12.90	Hartman et al. (2011a)	Hartman et al. (2011a)
HAT-P-25	5500	0.31	1.01	0.96	4.48	0.05	0.57	1.19	10.00	1202	13.19	Quinn et al. (2012)	Quinn et al. (2012)
HAT-P-26	5011	0.01	0.82	0.79	4.56	0.05	0.06	0.56	4.47	1001	11.74	Hartman et al. (2011b)	Hartman et al. (2011b)
HAT-P-30	6338	0.12	1.24	1.22	4.36	0.04	0.71	1.34	9.80	1630	10.36	Johnson et al. (2011)	Johnson et al. (2011)
HAT-P-32	6207	-0.04	1.16	1.22	4.33	0.03	0.86	1.79	6.60	1786	11.29	Hartman et al. (2011c)	Hartman et al. (2011c)
HAT-P-33	6446	0.07	1.38	1.64	4.15	0.05	0.76	1.69	6.60	1782	11.19	Hartman et al. (2011c)	Hartman et al. (2011c)
HAT-P-39	6340	0.19	1.40	1.63	4.16	0.05	0.60	1.57	5.90	1752	12.42	Hartman et al. (2012)	Hartman et al. (2012)
HAT-P-40	6080	0.22	1.51	2.21	3.93	0.06	0.61	1.73	5.13	1770	11.34	Winn et al. (2011)	Winn et al. (2011)
HAT-P-41	6390	0.21	1.42	1.68	4.14	0.04	0.80	1.69	6.90	1941	11.36	Hartman et al. (2012)	Hartman et al. (2012)

System	T_s	$[Fe/H]_s$	M_s	R_s	$\log g_s$	a	M_p	R_p	g_p	Teq_p	V_{mag}	Discovery Paper	Updated Reference
	(K)		(M_{sun})	(R_{sun})	(m/s^2)	(AU)	(M_{jup})	(R_{jup})	(m/s^2)	(K)			
HAT-P-44	5295	0.33	0.94	0.95	4.46	0.05	0.35	1.24	5.62	1108	13.21	Hartman et al. (2014)	Hartman et al. (2014)
HAT-P-45	6330	0.07	1.26	1.32	4.30	0.05	0.89	1.43	10.70	1652	12.79	Hartman et al. (2014)	Hartman et al. (2014)
HAT-P-46	6120	0.30	1.28	1.40	4.25	0.06	0.49	1.28	7.30	1458	11.94	Hartman et al. (2014)	Hartman et al. (2014)
HAT-P-47	6703	0.00	1.39	1.51	4.22	0.06	0.21	1.31	2.95	1605	10.69	Bakos et al. (2016)	Bakos et al. (2016)
HAT-P-48	5946	0.02	1.10	1.22	4.30	0.05	0.17	1.13	3.24	1361	12.16	Bakos et al. (2016)	Bakos et al. (2016)
HAT-P-51	5449	0.27	0.98	1.04	4.39	0.05	0.31	1.29	4.58	1192	13.44	Hartman et al. (2015a)	Hartman et al. (2015a)
HAT-P-65	5835	0.10	1.21	1.86	3.98	0.04	0.53	1.89	3.63	1930	13.15	Hartman et al. (2016)	Hartman et al. (2016)
HATS-5	5304	0.19	0.94	0.87	4.53	0.05	0.24	0.91	7.08	1025	12.63	Zhou et al. (2014)	Zhou et al. (2014)
HATS-6	3770	0.20	0.57	0.57	4.68	0.04	0.32	1.00	7.90	713	15.16	Hartman et al. (2015b)	Hartman et al. (2015b)
HATS-19	5896	0.24	1.30	1.75	4.07	0.06	0.43	1.66	3.80	1570	13.03	Bhatti et al. (2016)	Bhatti et al. (2016)
HATS-21	5695	0.30	1.08	1.02	4.45	0.05	0.33	1.12	6.50	1284	12.19	Bhatti et al. (2016)	Bhatti et al. (2016)
HD-097658	5170	-0.23	0.77	0.74	4.58	0.08	0.02	0.20	14.70	757	7.71	Dragomir et al. (2013)	Van Grootel et al. (2014)
HD-149026	6147	0.36	1.34	1.54	4.19	0.04	0.37	0.81	13.55	1634	8.16	Sato et al. (2005)	Carter et al. (2009)
HD-189733	5050	-0.03	0.84	0.75	4.61	0.03	1.15	1.15	21.50	1191	7.68	Bouchy et al. (2005)	Southworth (2010)
HD-209458	6117	0.02	1.15	1.16	4.37	0.05	0.71	1.38	9.30	1459	7.65	Henry et al. (2000)	Southworth (2010)
KELT-4	6206	-0.12	1.20	1.60	4.11	0.04	0.90	1.70	7.74	1823	10.47	Eastman et al. (2016)	Eastman et al. (2016)
KELT-6	6102	-0.28	1.08	1.58	4.07	0.08	0.43	1.19	7.40	1313	10.42	Collins et al. (2015)	Collins et al. (2015)
KELT-7	6789	0.14	1.53	1.73	4.15	0.04	1.28	1.53	13.50	2048	8.54	Bieryla et al. (2015)	Bieryla et al. (2015)
KELT-8	5754	0.27	1.21	1.67	4.08	0.05	0.87	1.86	6.20	1675	10.83	Fulton et al. (2015)	Fulton et al. (2015)
KELT-10	5948	0.09	1.11	1.21	4.32	0.05	0.68	1.40	8.57	1377	10.70	Kuhn et al. (2016)	Kuhn et al. (2016)
KELT-11	5370	0.18	1.44	2.72	3.73	0.06	0.20	1.37	2.55	1712	8.03	Pepper et al. (2017)	Pepper et al. (2017)
KELT-12	6278	0.19	1.59	2.37	3.89	0.07	0.95	1.79	7.40	1800	10.64	Stevens et al. (2017)	Stevens et al. (2017)

System	T_s	$[Fe/H]_s$	M_s	R_s	$\log g_s$	a	M_p	R_p	g_p	Teq_p	V_{mag}	Discovery Paper	Updated Reference
	(K)		(M_{sun})	(R_{sun})	(m/s^2)	(AU)	(M_{jup})	(R_{jup})	(m/s^2)	(K)			
KELT-15	6003	0.05	1.18	1.48	4.23	0.05	1.20	1.52	12.80	1904	11.44	Rodriguez et al. (2016)	Rodriguez et al. (2016)
KELT-17	7454	-0.02	1.64	1.65	4.22	0.05	1.31	1.52	13.90	2087	9.29	Zhou et al. (2016)	Zhou et al. (2016)
Kepler-12	5947	0.07	1.16	1.49	4.16	0.06	0.43	1.71	3.66	1485	13.53	Fortney et al. (2011)	Southworth (2012)
TrES-1	5226	0.06	0.89	0.82	4.56	0.04	0.76	1.10	15.60	1147	11.79	Alonso et al. (2004)	Southworth (2010)
TrES-4	6295	0.28	1.45	1.83	4.09	0.05	0.49	1.84	2.82	1795	11.59	Mandushev et al. (2007)	Sozzetti et al. (2015)
WASP-1	6160	0.14	1.24	1.47	4.20	0.04	0.85	1.48	9.80	1830	11.31	Collier Cameron et al. (2007)	Maciejewski et al. (2014)
WASP-2	5170	0.04	0.85	0.82	4.54	0.03	0.88	1.06	19.31	1286	11.98	Collier Cameron et al. (2007)	Southworth (2012)
WASP-4	5540	-0.03	0.93	0.91	4.49	0.02	1.25	1.36	16.64	1673	12.46	Wilson et al. (2008)	Southworth (2012)
WASP-6	5375	-0.20	0.84	0.86	4.49	0.04	0.48	1.23	7.96	1184	11.90	Gillon et al. (2009)	Tregloan-Reed et al. (2015)
WASP-7	6520	0.00	1.32	1.48	4.22	0.06	0.98	1.37	12.90	1530	9.48	Hellier et al. (2009)	Southworth (2012)
WASP-11	4900	0.12	0.81	0.77	4.57	0.04	0.49	0.99	12.45	992	11.89	West et al. (2009b)	Mancini et al. (2015)
WASP-12	6313	0.21	1.43	1.66	4.16	0.02	1.47	1.90	10.09	2580	11.69	Hebb et al. (2009)	Collins et al. (2015)
WASP-13	6025	0.11	1.22	1.66	4.09	0.06	0.51	1.53	5.44	1531	10.51	Skillen et al. (2009)	Southworth (2012)
WASP-15	6573	0.09	1.30	1.52	4.19	0.05	0.59	1.41	7.39	1676	10.92	West et al. (2009a)	Southworth et al. (2013)
WASP-16	5630	0.07	0.98	1.09	4.36	0.04	0.83	1.22	13.92	1389	11.31	Lister et al. (2009)	Southworth et al. (2013)
WASP-17	6550	-0.25	1.29	1.58	4.15	0.05	0.48	1.93	3.16	1755	11.50	Anderson et al. (2010)	Southworth et al. (2012a)
WASP-19	5460	0.14	0.94	1.02	4.39	0.02	1.14	1.41	14.21	2077	12.31	Hebb et al. (2010)	Mancini et al. (2013)
WASP-20	6000	-0.01	1.09	1.14	4.36	0.06	0.38	1.28	5.80	1282	10.68	Anderson et al. (2015b)	Evans et al. (2016a)
WASP-21	5924	-0.22	0.89	1.14	4.28	0.05	0.28	1.16	5.07	1333	11.50	Bouchy et al. (2010)	Ciceri et al. (2013)

System	T_s	$[Fe/H]_s$	M_s	R_s	$\log g_s$	a	M_p	R_p	g_p	Teq_p	V_{mag}	Discovery Paper	Updated Reference
	(K)		(M_{sun})	(R_{sun})	(m/s^2)	(AU)	(M_{jup})	(R_{jup})	(m/s^2)	(K)			
WASP-25	5736	0.06	1.05	0.92	4.53	0.05	0.60	1.25	9.54	1210	11.85	Enoch et al. (2011a)	Southworth et al. (2014)
WASP-29	4875	0.11	0.82	0.81	4.54	0.05	0.24	0.78	10.00	970	11.21	Hellier et al. (2010)	Gibson et al. (2013)
WASP-31	6175	-0.20	1.16	1.25	4.31	0.05	0.48	1.55	4.56	1575	11.94	Anderson et al. (2011)	Anderson et al. (2011)
WASP-33	7430	0.10	1.56	1.51	4.27	0.03	2.16	1.68	19.00	2710	8.30	Collier Cameron et al. (2010)	Lehmann et al. (2015)
WASP-34	5704	0.08	1.01	0.93	4.50	0.05	0.59	1.22	9.10	1250	10.37	Smalley et al. (2011)	Smalley et al. (2011)
WASP-35	6072	-0.05	1.07	1.09	4.40	0.04	0.72	1.32	9.50	1450	10.95	Enoch et al. (2011b)	Enoch et al. (2011b)
WASP-39	5460	-0.12	0.93	0.90	4.50	0.05	0.28	1.27	4.07	1116	12.10	Faedi et al. (2011)	Faedi et al. (2011)
WASP-41	5546	0.06	0.99	0.89	4.54	0.04	0.98	1.18	17.45	1242	11.64	Maxted et al. (2011)	Southworth et al. (2016b)
WASP-42	5315	0.29	0.95	0.89	4.51	0.06	0.53	1.12	10.38	1021	12.57	Lendl et al. (2012)	Southworth et al. (2016b)
WASP-43	4520	-0.01	0.72	0.67	4.64	0.02	2.03	1.04	47.00	1440	12.37	Hellier et al. (2011)	Gillon et al. (2012)
WASP-49	5600	-0.23	1.00	1.04	4.41	0.04	0.40	1.20	7.13	1399	11.36	Lendl et al. (2012)	Lendl et al. (2016)
WASP-52	5000	0.03	0.80	0.79	4.55	0.03	0.43	1.25	6.85	1315	12.20	Hébrard et al. (2013)	Mancini et al. (2017)
WASP-54	6296	0.00	1.21	1.83	4.00	0.05	0.64	1.65	5.32	1759	10.42	Faedi et al. (2013)	Faedi et al. (2013)
WASP-55	6070	0.09	1.16	1.10	4.42	0.06	0.63	1.33	8.73	1300	11.76	Hellier et al. (2012)	Southworth et al. (2016b)
WASP-58	5800	-0.45	0.94	1.17	4.27	0.06	0.89	1.37	10.70	1270	11.66	Hébrard et al. (2013)	Hébrard et al. (2013)
WASP-62	6230	0.04	1.25	1.28	4.32	0.06	0.57	1.39	6.76	1440	10.22	Hellier et al. (2012)	Hellier et al. (2012)
WASP-63	5715	0.28	1.32	1.88	4.01	0.06	0.38	1.43	4.17	1540	11.16	Hellier et al. (2012)	Hellier et al. (2012)
WASP-67	5417	0.18	0.83	0.82	4.53	0.05	0.41	1.09	8.45	1003	12.54	Hellier et al. (2012)	Mancini et al. (2014b)
WASP-69	4700	0.15	0.83	0.81	4.54	0.05	0.26	1.06	5.32	963	9.87	Anderson et al. (2014b)	Anderson et al. (2014b)
WASP-70	5700	-0.01	1.11	1.22	4.31	0.05	0.59	1.16	10.00	1387	10.79	Anderson et al. (2014b)	Anderson et al. (2014b)
WASP-74	5990	0.39	1.48	1.64	4.18	0.04	0.95	1.56	8.91	1910	9.76	Hellier et al. (2015)	Hellier et al. (2015)
WASP-76	6250	0.23	1.46	1.73	4.13	0.03	0.92	1.83	6.31	2160	9.53	West et al. (2016)	West et al. (2016)

System	T_s	$[Fe/H]_s$	M_s	R_s	$\log g_s$	a	M_p	R_p	g_p	Teq_p	V_{mag}	Discovery Paper	Updated Reference
	(K)		(M_{sun})	(R_{sun})	(m/s^2)	(AU)	(M_{jup})	(R_{jup})	(m/s^2)	(K)			
WASP-79	6600	0.03	1.52	1.91	4.06	0.05	0.90	2.09	4.70	1900	10.04	Smalley et al. (2012)	Smalley et al. (2012)
WASP-80	4145	-0.14	0.60	0.59	4.67	0.03	0.56	0.99	14.34	825	11.87	Triaud et al. (2013)	Mancini et al. (2014a)
WASP-82	6500	0.12	1.64	2.22	3.96	0.04	1.25	1.71	9.75	2202	10.08	West et al. (2016)	Smith (2015)
WASP-83	5480	0.29	1.11	1.05	4.44	0.06	0.30	1.04	6.17	1120	12.87	Hellier et al. (2015)	Hellier et al. (2015)
WASP-84	5280	0.09	0.85	0.77	4.60	0.08	0.69	0.98	16.52	833	10.83	Anderson et al. (2014b)	Anderson et al. (2015a)
WASP-88	6430	-0.08	1.45	2.08	3.96	0.06	0.56	1.70	4.68	1772	11.39	Delrez et al. (2014)	Delrez et al. (2014)
WASP-90	6440	0.11	1.55	1.98	4.03	0.06	0.63	1.63	5.37	1840	11.69	West et al. (2016)	West et al. (2016)
WASP-93	6700	0.07	1.33	1.52	4.20	0.04	1.47	1.60	13.20	1942	10.97	Hay et al. (2016)	Hay et al. (2016)
WASP-94	6170	0.26	1.45	1.62	4.18	0.06	0.45	1.72	3.48	1604	10.06	Neveu-VanMalle et al. (2014)	Neveu-VanMalle et al. (2014)
WASP-95	5830	0.14	1.11	1.13	4.38	0.03	1.13	1.21	21.80	1570	10.09	Hellier et al. (2014)	Hellier et al. (2014)
WASP-96	5500	0.14	1.06	1.05	4.42	0.05	0.48	1.20	7.59	1285	12.19	Hellier et al. (2014)	Hellier et al. (2014)
WASP-97	5670	0.23	1.12	1.06	4.43	0.03	1.32	1.13	23.40	1555	10.58	Hellier et al. (2014)	Hellier et al. (2014)
WASP-101	6380	0.20	1.34	1.29	4.34	0.05	0.50	1.41	5.75	1560	10.34	Hellier et al. (2014)	Hellier et al. (2014)
WASP-103	6110	0.06	1.21	1.41	4.22	0.02	1.47	1.65	14.34	2489	12.50	Gillon et al. (2014)	Southworth et al. (2016a)
WASP-108	6000	0.05	1.17	1.22	4.34	0.04	0.89	1.28	12.39	1590	11.22	Anderson et al. (2014a)	Anderson et al. (2014a)
WASP-109	6520	-0.22	1.20	1.35	4.26	0.05	0.91	1.44	10.00	1685	11.44	Anderson et al. (2014a)	Anderson et al. (2014a)
WASP-110	5400	-0.06	0.89	0.88	4.50	0.05	0.51	1.24	7.60	1134	12.27	Anderson et al. (2014a)	Anderson et al. (2014a)
WASP-113	5890	0.10	1.32	1.61	4.20	0.06	0.47	1.41	5.50	1496	11.77	Barros et al. (2016)	Barros et al. (2016)
WASP-117	6040	-0.11	1.13	1.17	4.28	0.09	0.28	1.02	6.56	1024	10.15	Lendl et al. (2014)	Lendl et al. (2014)
WASP-118	6410	0.16	1.32	1.70	4.10	0.05	0.51	1.44	5.71	1729	11.02	Hay et al. (2016)	Hay et al. (2016)
WASP-121	6460	0.13	1.35	1.46	4.24	0.03	1.18	1.86	9.40	2358	10.52	Delrez et al. (2016)	Delrez et al. (2016)

System	T_s	$[Fe/H]_s$	M_s	R_s	$\log g_s$	a	M_p	R_p	g_p	Teq_p	V_{mag}	Discovery Paper	Updated Reference
	(K)		(M_{sun})	(R_{sun})	(m/s^2)	(AU)	(M_{jup})	(R_{jup})	(m/s^2)	(K)			
WASP-122	5720	0.32	1.24	1.52	4.17	0.03	1.28	1.74	9.66	1970	11.00	Turner et al. (2016)	Turner et al. (2016)
WASP-123	5740	0.18	1.17	1.28	4.29	0.04	0.90	1.32	11.70	1520	11.03	Turner et al. (2016)	Turner et al. (2016)
WASP-124	6050	-0.02	1.07	1.02	4.44	0.04	0.60	1.24	8.90	1400	12.70	Maxted et al. (2016)	Maxted et al. (2016)
WASP-126	5800	0.17	1.12	1.27	4.28	0.04	0.28	0.96	6.80	1480	10.80	Maxted et al. (2016)	Maxted et al. (2016)
WASP-127	5750	-0.18	1.08	1.39	4.18	0.05	0.18	1.37	2.14	1400	10.16	Lam et al. (2017)	Lam et al. (2017)
WASP-131	5950	-0.18	1.06	1.53	4.09	0.06	0.27	1.22	4.17	1460	10.08	Hellier et al. (2017)	Hellier et al. (2017)
WASP-132	4750	0.22	0.80	0.74	4.61	0.07	0.41	0.87	12.60	763	12.40	Hellier et al. (2017)	Hellier et al. (2017)
WASP-139	5300	0.20	0.92	0.80	4.59	0.06	0.12	0.80	4.17	910	12.39	Hellier et al. (2017)	Hellier et al. (2017)
WASP-140	5300	0.12	0.90	0.87	4.51	0.03	2.44	1.44	25.00	1320	11.13	Hellier et al. (2017)	Hellier et al. (2017)
XO-1	5750	0.02	1.04	0.94	4.51	0.05	0.92	1.21	15.80	1210	11.14	McCullough et al. (2006)	Southworth (2010)
XO-2	5332	0.43	0.96	1.00	4.44	0.04	0.60	1.02	14.13	1328	11.25	Burke et al. (2007)	Damasso et al. (2015)

Table B.1: All the stellar and planetary parameters adopted from TEPCAT (Southworth 2011a) database, for the model simulations of 117 exoplanets in the grid are listed here. First column shows planet names with 'b' omitted indicating first planet of the stellar system as in TEPCAT database. Subsequent columns show, stellar temperature (T_s) in Kelvin, stellar metallicity ($[Fe/H]_s$), stellar mass (M_s) in units of solar mass, stellar radius (R_s) in units of solar radius, logarithmic (base 10) stellar gravity ($\log g_s$) in m/s^2, semi-major axis (a) in AU, planetary mass (M_p) in units of Jupiter mass, planetary radius (R_p) in units of Jupiter radius, planetary surface gravity (g_p) in m/s^2, planetary equilibrium temperature (Teq_p) in Kelvin assuming 0 albedo and efficient redistribution, V magnitude (V_{mag}) of the host star, discovery paper reference (Discovery Paper) and finally the most updated reference.

Bibliography

Ackerman, Andrew S., et al. 2001. "Precipitating Condensation Clouds in Substellar Atmospheres". ApJ 556 (): 872–884. doi:10.1086/321540. arXiv: astro-ph/0103423 [astro-ph].

Agúndez, M., et al. 2014. "Pseudo 2D chemical model of hot-Jupiter atmospheres: application to HD 209458b and HD 189733b". A&A 564, A73 (): A73. doi:10.1051/0004-6361/201322895. arXiv: 1403.0121 [astro-ph.EP].

Alam, Munazza K., et al. 2018. "The HST PanCET Program: Hints of Na I and Evidence of a Cloudy Atmosphere for the Inflated Hot Jupiter WASP-52b". AJ 156, 298:298. doi:10.3847/1538-3881/aaee89. arXiv: 1811.00935 [astro-ph.EP].

Allard, F., et al. 2012. "Models of very-low-mass stars, brown dwarfs and exoplanets". *Philosophical Transactions of the Royal Society of London Series A* 370 (): 2765–2777. doi:10.1098/rsta.2011.0269. arXiv: 1112.3591 [astro-ph.SR].

Allard, France, et al. 1996. "Synthetic Spectra and Mass Determination of the Brown Dwarf GI 229B". ApJ 465:L123. doi:10.1086/310143.

Allard, N. F., et al. 2003. "A new model for brown dwarf spectra including accurate unified line shape theory for the Na I and K I resonance line profiles". A&A 411 (): L473–L476. doi:10.1051/0004-6361:20031299.

Allard, N. F., et al. 1999. "Effect of the variation of electric-dipole moments on the shape of pressure-broadened atomic spectral lines". Phys. Rev. A 60 (): 1021–1033. doi:10.1103/PhysRevA.60.1021.

Allard, N. F., et al. 2007. "Study of the K-H{_2} quasi-molecular line satellite in the potassium resonance line". A&A 465 (): 1085–1091. doi:10.1051/0004-6361:20066616.

Alonso, R., et al. 2004. "TrES-1: The Transiting Planet of a Bright K0 V Star". ApJ 613 (): L153–L156. doi:10.1086/425256. eprint: astro-ph/0408421.

Amundsen, D. S. 2015. "Climate Simulations of Hot Jupiters". *PhD Thesis*.

Amundsen, D. S., et al. 2014. "Accuracy tests of radiation schemes used in hot Jupiter global circulation models". A&A 564, A59 (): A59. doi:10.1051/0004-6361/201323169. arXiv: 1402.0814 [astro-ph.EP].

Amundsen, D. S., et al. 2017. "Treatment of overlapping gaseous absorption with the correlated-k method in hot Jupiter and brown dwarf atmosphere models". A&A 598, A97 (): A97. doi:10.1051/0004-6361/201629322. arXiv: 1610.01389 [astro-ph.EP].

Anderson, D. R., et al. 2014a. "Six newly-discovered hot Jupiters transiting F/G stars: WASP-87b, WASP-108b, WASP-109b, WASP-110b, WASP-111b & WASP-112b". *ArXiv e-prints* (). arXiv: 1410.3449 [astro-ph.EP].

Anderson, D. R., et al. 2015a. "The Well-aligned Orbit of Wasp-84b: Evidence for Disk Migration of a Hot Jupiter". ApJ 800, L9 (): L9. doi:10.1088/2041-8205/800/1/L9. arXiv: 1409.6335 [astro-ph.EP].

Anderson, D. R., et al. 2014b. "Three newly discovered sub-Jupiter-mass planets: WASP-69b and WASP-84b transit active K dwarfs and WASP-70Ab transits the evolved primary of a G4+K3 binary". MNRAS 445 (): 1114–1129. doi:10.1093/mnras/stu1737. arXiv: 1310.5654 [astro-ph.EP].

Anderson, D. R., et al. 2010. "WASP-17b: An Ultra-Low Density Planet in a Probable Retrograde Orbit". ApJ 709 (): 159–167. doi:10.1088/0004-637X/709/1/159. arXiv: 0908.1553 [astro-ph.EP].

Anderson, D. R., et al. 2015b. "WASP-20b and WASP-28b: a hot Saturn and a hot Jupiter in near-aligned orbits around solar-type stars". A&A 575, A61 (): A61. doi:10.1051/0004-6361/201423591. arXiv: 1402.1482 [astro-ph.EP].

Anderson, D. R., et al. 2011. "WASP-31b: a low-density planet transiting a metal-poor, late-F-type dwarf star". A&A 531, A60 (): A60. doi:10.1051/0004-6361/201016208. arXiv: 1011.5882 [astro-ph.EP].

Arcangeli, Jacob, et al. 2018. "H^- Opacity and Water Dissociation in the Dayside Atmosphere of the Very Hot Gas Giant WASP-18b". ApJ 855, L30:L30. doi:10.3847/2041-8213/aab272. arXiv: 1801.02489 [astro-ph.EP].

Asplund, M., et al. 2009. "The Chemical Composition of the Sun". ARA&A 47 (): 481–522. doi:10.1146/annurev.astro.46.060407.145222. arXiv: 0909.0948 [astro-ph.SR].

Bakos, G. Á., et al. 2010. "HAT-P-11b: A Super-Neptune Planet Transiting a Bright K Star in the Kepler Field". ApJ 710 (): 1724–1745. doi:10.1088/0004-637X/710/2/1724. arXiv: 0901.0282 [astro-ph.EP].

Bakos, G. Á., et al. 2009. "HAT-P-13b,c: A Transiting Hot Jupiter with a Massive Outer Companion on an Eccentric Orbit". ApJ 707 (): 446–456. doi:10.1088/0004-637X/707/1/446. arXiv: 0907.3525 [astro-ph.EP].

Bakos, G. Á., et al. 2007. "HAT-P-1b: A Large-Radius, Low-Density Exoplanet Transiting One Member of a Stellar Binary". ApJ 656 (): 552–559. doi:10.1086/509874. eprint: astro-ph/0609369.

Bakos, G. Á., et al. 2016. "HAT-P-47b AND HAT-P-48b: Two Low Density Sub-Saturn-Mass Transiting Planets on the Edge of the Period–Mass Desert". *ArXiv e-prints* (). arXiv: 1606.04556 [astro-ph.EP].

Baraffe, I., et al. 2015. "New evolutionary models for pre-main sequence and main sequence low-mass stars down to the hydrogen-burning limit". A&A 577, A42 (): A42. doi:10.1051/0004-6361/201425481. arXiv: 1503.04107 [astro-ph.SR].

Barber, R. J., et al. 2006. "A high-accuracy computed water line list". MNRAS 368 (): 1087–1094. doi:10.1111/j.1365-2966.2006.10184.x. eprint: astro-ph/0601236.

Barber, R. J., et al. 2014. "ExoMol line lists - III. An improved hot rotation-vibration line list for HCN and HNC". MNRAS 437 (): 1828–1835. doi:10.1093/mnras/stt2011. arXiv: 1311.1328 [astro-ph.SR].

Barclay, Thomas, et al. 2018. "A Revised Exoplanet Yield from the Transiting Exoplanet Survey Satellite (TESS)". *ArXiv e-prints*, arXiv:1804.05050 (): arXiv:1804.05050. arXiv: 1804.05050 [astro-ph.EP].

Barklem, P. S., et al. 2016. "Partition functions and equilibrium constants for diatomic molecules and atoms of astrophysical interest". A&A 588, A96 (): A96. doi:10.1051/0004-6361/201526961. arXiv: 1602.03304 [astro-ph.IM].

Barnes, Jason W. 2007. "Effects of Orbital Eccentricity on Extrasolar Planet Transit Detectability and Light Curves". *Publications of the Astronomical Society of the Pacific* 119:986–993. doi:10.1086/522039. arXiv: 0708.0243 [astro-ph].

Barros, S. C. C., et al. 2016. "WASP-113b and WASP-114b, two inflated hot Jupiters with contrasting densities". A&A 593, A113 (): A113. doi:10.1051/0004-6361/201526517. arXiv: 1607.02341 [astro-ph.EP].

Barshay, S. S., et al. 1978. "Chemical structure of the deep atmosphere of Jupiter". Icarus 33 (): 593–611. doi:10.1016/0019-1035(78)90192-6.

Barstow, J. K., et al. 2017. "A Consistent Retrieval Analysis of 10 Hot Jupiters Observed in Transmission". ApJ 834, 50 (): 50. doi:10.3847/1538-4357/834/1/50. arXiv: 1610.01841 [astro-ph.EP].

Batalha, N. E., et al. 2017. "PandExo: A Community Tool for Transiting Exoplanet Science with JWST & HST". *ArXiv e-prints* (). arXiv: 1702.01820 [astro-ph.IM].

Beaulieu, J. P., et al. 2006. “Discovery of a cool planet of 5.5 Earth masses through gravitational microlensing”. Nature 439 (): 437–440. doi:10.1038/nature04441. arXiv: astro-ph/0601563 [astro-ph].

Beichman, C., et al. 2014. “Observations of Transiting Exoplanets with the James Webb Space Telescope (JWST)”. PASP 126 (): 1134. doi:10.1086/679566.

BelBruno, J. J., et al. 1982. “Helium and self-broadening in the first and second overtone bands of ^{12}C ^{16}O”. *Journal of Molecular Spectroscopy* 94 (): 336–342. doi:10.1016/0022-2852(82)90009-1.

Bell, K. L., et al. 1987. “Free-free absorption coefficient of the negative hydrogen ion”. *Journal of Physics B Atomic Molecular Physics* 20 (): 801–806. doi:10.1088/0022-3700/20/4/019.

Benneke, B., et al. 2012. “Atmospheric Retrieval for Super-Earths: Uniquely Constraining the Atmospheric Composition with Transmission Spectroscopy”. ApJ 753, 100 (): 100. doi:10.1088/0004-637X/753/2/100. arXiv: 1203.4018 [astro-ph.EP].

Benneke, Björn, et al. 2013. “How to Distinguish between Cloudy Mini-Neptunes and Water/Volatile-dominated Super-Earths”. ApJ 778, 153:153. doi:10.1088/0004-637X/778/2/153. arXiv: 1306.6325 [astro-ph.EP].

Bhatti, W., et al. 2016. “HATS-19b, HATS-20b, HATS-21b: Three Transiting Hot-Saturns Discovered by the HATSouth Survey”. *ArXiv e-prints* (). arXiv: 1607.00322 [astro-ph.EP].

Biddle, L. I., et al. 2014. “Warm ice giant GJ 3470b - II. Revised planetary and stellar parameters from optical to near-infrared transit photometry”. MNRAS 443 (): 1810–1820. doi:10.1093/mnras/stu1199. arXiv: 1406.6437 [astro-ph.EP].

Bieryla, Allyson, et al. 2015. “KELT-7b: A Hot Jupiter Transiting a Bright V = 8.54 Rapidly Rotating F-star”. AJ 150, 12 (1): 12. doi:10.1088/0004-6256/150/1/12. arXiv: 1501.05565 [astro-ph.EP].

Birkby, J. L. 2018. “Exoplanet Atmospheres at High Spectral Resolution”. *arXiv e-prints*, arXiv:1806.04617: arXiv:1806.04617. arXiv: 1806.04617 [astro-ph.EP].

Bonfils, X., et al. 2012. “A hot Uranus transiting the nearby M dwarf GJ 3470. Detected with HARPS velocimetry. Captured in transit with TRAPPIST photometry”. A&A 546, A27 (): A27. doi:10.1051/0004-6361/201219623. arXiv: 1206.5307 [astro-ph.EP].

Borucki, W. J., et al. 1984. “The photometric method of detecting other planetary systems”. Icarus 58:121–134. doi:10.1016/0019-1035(84)90102-7.

Borucki, William J., et al. 2011. "Characteristics of Planetary Candidates Observed by Kepler. II. Analysis of the First Four Months of Data". ApJ 736, 19:19. doi:`10.1088/0004-637X/736/1/19`. arXiv: `1102.0541 [astro-ph.EP]`.

Bouanich, J.-P., et al. 2004. "H“2-broadening coefficients in the @n”2 and @n“4 bands of PH”3". J. Quant. Spec. Radiat. Transf. 84 (): 195–205. doi:`10.1016/S0022-4073(03)00143-2`.

Bouchy, F., et al. 2005. "ELODIE metallicity-biased search for transiting Hot Jupiters. II. A very hot Jupiter transiting the bright K star HD 189733". A&A 444 (): L15–L19. doi:`10.1051/0004-6361:200500201`. eprint: `astro-ph/0510119`.

Bouchy, F., et al. 2010. "WASP-21b: a hot-Saturn exoplanet transiting a thick disc star". A&A 519, A98 (): A98. doi:`10.1051/0004-6361/201014817`. arXiv: `1006.2605 [astro-ph.EP]`.

Brogi, Matteo, et al. 2012. "The signature of orbital motion from the dayside of the planet τ Boötis b". Nature 486:502–504. doi:`10.1038/nature11161`. arXiv: `1206.6109 [astro-ph.EP]`.

Brown, T. M. 2001. "Transmission Spectra as Diagnostics of Extrasolar Giant Planet Atmospheres". ApJ 553 (): 1006–1026. doi:`10.1086/320950`. eprint: `astro-ph/0101307`.

Burgasser, Adam J., et al. 2003. "The Spectra of T Dwarfs. II. Red Optical Data". ApJ 594 (1): 510–524. doi:`10.1086/376756`. arXiv: `astro-ph/0305139 [astro-ph]`.

Burke, C. J., et al. 2007. "XO-2b: Transiting Hot Jupiter in a Metal-rich Common Proper Motion Binary". ApJ 671 (): 2115–2128. doi:`10.1086/523087`. arXiv: `0705.0003`.

Burningham, Ben, et al. 2017. "Retrieval of atmospheric properties of cloudy L dwarfs". MNRAS 470 (1): 1177–1197. doi:`10.1093/mnras/stx1246`. arXiv: `1701.01257 [astro-ph.SR]`.

Burrows, A., et al. 1997. "A Nongray Theory of Extrasolar Giant Planets and Brown Dwarfs". ApJ 491 (): 856–875. doi:`10.1086/305002`. eprint: `astro-ph/9705201`.

Burrows, A., et al. 1999. "Chemical Equilibrium Abundances in Brown Dwarf and Extrasolar Giant Planet Atmospheres". ApJ 512 (): 843–863. doi:`10.1086/306811`. eprint: `astro-ph/9807055`.

Burrows, A., et al. 2002. "New CrH Opacities for the Study of L and Brown Dwarf Atmospheres". ApJ 577 (): 986–992. doi:`10.1086/342242`. eprint: `astro-ph/0206159`.

Burrows, A., et al. 2008. “Theoretical Spectra and Light Curves of Close-in Extrasolar Giant Planets and Comparison with Data”. ApJ 678 (2): 1436–1457. doi:`10.1086/533518`. arXiv: `0709.4080 [astro-ph]`.

Burrows, Adam, et al. 2000. “The Near-Infrared and Optical Spectra of Methane Dwarfs and Brown Dwarfs”. ApJ 531 (): 438–446. doi:`10.1086/308462`. arXiv: `astro-ph/9908078`.

Caffau, E., et al. 2011. “Solar Chemical Abundances Determined with a CO5BOLD 3D Model Atmosphere”. Sol. Phys. 268 (): 255–269. doi:`10.1007/s11207-010-9541-4`. arXiv: `1003.1190 [astro-ph.SR]`.

Carter, J. A., et al. 2009. “Near-Infrared Transit Photometry of the Exoplanet HD 149026b”. ApJ 696 (): 241–253. doi:`10.1088/0004-637X/696/1/241`. arXiv: `0902.1542 [astro-ph.EP]`.

Chabrier, G., et al. 2014. “Giant Planet and Brown Dwarf Formation”. In *Protostars and Planets VI*, ed. by Henrik Beuther et al., 619. doi:`10.2458/azu_uapress_9780816531240-ch027`. arXiv: `1401.7559 [astro-ph.SR]`.

Chamberlain, J. W., et al. 1987. *Theory of planetary atmospheres. An introduction to their physics andchemistry.* Vol. 36.

Chandrasekhar, Subrahmanyan. 1960. *Radiative transfer.*

Charbonneau, D., et al. 2009. “A super-Earth transiting a nearby low-mass star”. Nature 462 (): 891–894. doi:`10.1038/nature08679`. arXiv: `0912.3229 [astro-ph.EP]`.

Charbonneau, D., et al. 2002. “Detection of an Extrasolar Planet Atmosphere”. ApJ 568 (): 377–384. doi:`10.1086/338770`. eprint: `astro-ph/0111544`.

Chase, M. W. 1986. *JANAF thermochemical tables.*

Ciceri, S., et al. 2013. “Simultaneous follow-up of planetary transits: revised physical properties for the planetary systems HAT-P-16 and WASP-21”. A&A 557, A30 (): A30. doi:`10.1051/0004-6361/201321669`. arXiv: `1307.5874 [astro-ph.EP]`.

Collier Cameron, A., et al. 2010. “Line-profile tomography of exoplanet transits - II. A gas-giant planet transiting a rapidly rotating A5 star”. MNRAS 407 (): 507–514. doi:`10.1111/j.1365-2966.2010.16922.x`. arXiv: `1004.4551 [astro-ph.EP]`.

Collier Cameron, A., et al. 2007. “WASP-1b and WASP-2b: two new transiting exoplanets detected with SuperWASP and SOPHIE”. MNRAS 375 (): 951–957. doi:`10.1111/j.1365-2966.2006.11350.x`. eprint: `astro-ph/0609688`.

Collins, K. A., et al. 2015. “Transit Timing Variation Measurements of WASP-12b and Qatar-1b: No Evidence for Additional Planets”. *ArXiv e-prints* (). arXiv: `1512.00464 [astro-ph.EP]`.

Cox, A. N. 2000. *Allen's astrophysical quantities.*

Currie, Thayne, et al. 2013. "A Combined Very Large Telescope and Gemini Study of the Atmosphere of the Directly Imaged Planet, β Pictoris b". ApJ 776, 15 (1): 15. doi:10.1088/0004-637X/776/1/15. arXiv: 1306.0610 [astro-ph.EP].

Damasso, M., et al. 2015. "The GAPS programme with HARPS-N at TNG. V. A comprehensive analysis of the XO-2 stellar and planetary systems". A&A 575, A111 (): A111. doi:10.1051/0004-6361/201425332. arXiv: 1501.01424 [astro-ph.SR].

Delrez, L., et al. 2014. "Transiting planets from WASP-South, Euler, and TRAPPIST. WASP-68 b, WASP-73 b, and WASP-88 b, three hot Jupiters transiting evolved solar-type stars". A&A 563, A143 (): A143. doi:10.1051/0004-6361/201323204. arXiv: 1312.1827 [astro-ph.EP].

Delrez, L., et al. 2016. "WASP-121 b: a hot Jupiter close to tidal disruption transiting an active F star". MNRAS 458 (): 4025–4043. doi:10.1093/mnras/stw522. arXiv: 1506.02471 [astro-ph.EP].

Deming, D., et al. 2013. "Infrared Transmission Spectroscopy of the Exoplanets HD 209458b and XO-1b Using the Wide Field Camera-3 on the Hubble Space Telescope". ApJ 774, 95 (): 95. doi:10.1088/0004-637X/774/2/95. arXiv: 1302.1141 [astro-ph.EP].

Demory, B.-O., et al. 2016. "A map of the large day-night temperature gradient of a super-Earth exoplanet". Nature 532 (): 207–209. doi:10.1038/nature17169. arXiv: 1604.05725 [astro-ph.EP].

Demory, Brice-Olivier, et al. 2013. "Inference of Inhomogeneous Clouds in an Exoplanet Atmosphere". ApJ 776, L25:L25. doi:10.1088/2041-8205/776/2/L25. arXiv: 1309.7894 [astro-ph.EP].

Dragomir, D., et al. 2013. "MOST Detects Transits of HD 97658b, a Warm, Likely Volatile-rich Super-Earth". ApJ 772, L2 (): L2. doi:10.1088/2041-8205/772/1/L2. arXiv: 1305.7260 [astro-ph.EP].

Dressing, Courtney D., et al. 2015. "The Occurrence of Potentially Habitable Planets Orbiting M Dwarfs Estimated from the Full Kepler Dataset and an Empirical Measurement of the Detection Sensitivity". ApJ 807, 45 (): 45. doi:10.1088/0004-637X/807/1/45.

Drummond, B., et al. 2018a. "The effect of metallicity on the atmospheres of exoplanets with fully coupled 3D hydrodynamics, equilibrium chemistry, and radiative transfer". A&A 612, A105:A105. doi:10.1051/0004-6361/201732010. arXiv: 1801.01045 [astro-ph.EP].

Drummond, B., et al. 2016. “The effects of consistent chemical kinetics calculations on the pressure-temperature profiles and emission spectra of hot Jupiters”. A&A 594, A69 (): A69. doi:10.1051/0004-6361/201628799. arXiv: 1607.04062 [astro-ph.EP].

Drummond, Benjamin, et al. 2018b. “The 3D Thermal, Dynamical, and Chemical Structure of the Atmosphere of HD 189733b: Implications of Wind-driven Chemistry for the Emission Phase Curve”. ApJ 869, 28 (1): 28. doi:10.3847/1538-4357/aaeb28. arXiv: 1810.09724 [astro-ph.EP].

Drummond, Benjamin, et al. 2019. “The carbon-to-oxygen ratio: implications for the spectra of hydrogen-dominated exoplanet atmospheres”. MNRAS 486 (1): 1123–1137. doi:10.1093/mnras/stz909. arXiv: 1903.10997 [astro-ph.EP].

Eastman, J. D., et al. 2016. “KELT-4Ab: An Inflated Hot Jupiter Transiting the Bright (V 10) Component of a Hierarchical Triple”. AJ 151, 45 (): 45. doi:10.3847/0004-6256/151/2/45. arXiv: 1510.00015 [astro-ph.EP].

Edwards, J. M., et al. 1996. “Studies with a flexible new radiation code. I: Choosing a configuration for a large-scale model”. *Quarterly Journal of the Royal Meteorological Society* 122 (): 689–719. doi:10.1002/qj.49712253107.

Enoch, B., et al. 2011a. “WASP-25b: a 0.6 M_J planet in the Southern hemisphere”. MNRAS 410 (): 1631–1636. doi:10.1111/j.1365-2966.2010.17550.x. arXiv: 1009.5917 [astro-ph.EP].

Enoch, B., et al. 2011b. “WASP-35b, WASP-48b, and HAT-P-30b/WASP-51b: Two New Planets and an Independent Discovery of a Hat Planet”. AJ 142, 86 (): 86. doi:10.1088/0004-6256/142/3/86. arXiv: 1104.2827 [astro-ph.EP].

Esposito, M., et al. 2014. “The GAPS Programme with HARPS-N at TNG. III: The retrograde orbit of HAT-P-18b”. A&A 564, L13 (): L13. doi:10.1051/0004-6361/201423735. arXiv: 1403.6728 [astro-ph.EP].

Evans, D. F., et al. 2016a. “WASP-20 Is a Close Visual Binary with a Transiting Hot Jupiter”. ApJ 833, L19 (): L19. doi:10.3847/2041-8213/833/2/L19. arXiv: 1611.08735 [astro-ph.EP].

Evans, T. M., et al. 2017. “An ultrahot gas-giant exoplanet with a stratosphere”. Nature 548 (): 58–61. doi:10.1038/nature23266. arXiv: 1708.01076 [astro-ph.EP].

Evans, T. M., et al. 2016b. “Detection of $\mathrm{H_2O}$ and Evidence for TiO/VO in an Ultra-hot Exoplanet Atmosphere”. ApJ 822, L4 (): L4. doi:10.3847/2041-8205/822/1/L4. arXiv: 1604.02310 [astro-ph.EP].

Evans, Thomas M., et al. 2018. "An Optical Transmission Spectrum for the Ultra-hot Jupiter WASP-121b Measured with the Hubble Space Telescope". AJ 156, 283:283. doi:`10.3847/1538-3881/aaebff`. arXiv: `1810.10969 [astro-ph.EP]`.

Faedi, F., et al. 2011. "WASP-39b: a highly inflated Saturn-mass planet orbiting a late G-type star". A&A 531, A40 (): A40. doi:`10.1051/0004-6361/201116671`. arXiv: `1102.1375 [astro-ph.EP]`.

Faedi, F., et al. 2013. "WASP-54b, WASP-56b, and WASP-57b: Three new sub-Jupiter mass planets from SuperWASP". A&A 551, A73 (): A73. doi:`10.1051/0004-6361/201220520`. arXiv: `1210.2329 [astro-ph.EP]`.

Feroz, F., et al. 2009. "MULTINEST: an efficient and robust Bayesian inference tool for cosmology and particle physics". MNRAS 398:1601–1614. doi:`10.1111/j.1365-2966.2009.14548.x`. arXiv: `0809.3437 [astro-ph]`.

Fischer, P. D., et al. 2016. "HST Hot-Jupiter Transmission Spectral Survey: Clear Skies for Cool Saturn WASP-39b". ApJ 827, 19 (): 19. doi:`10.3847/0004-637X/827/1/19`. arXiv: `1601.04761 [astro-ph.EP]`.

Fortney, J. J. 2005. "The effect of condensates on the characterization of transiting planet atmospheres with transmission spectroscopy". MNRAS 364 (): 649–653. doi:`10.1111/j.1365-2966.2005.09587.x`. eprint: `astro-ph/0509292`.

Fortney, J. J., et al. 2008. "A Unified Theory for the Atmospheres of the Hot and Very Hot Jupiters: Two Classes of Irradiated Atmospheres". ApJ 678, 1419-1435 (): 1419–1435. doi:`10.1086/528370`. arXiv: `0710.2558`.

Fortney, J. J., et al. 2007. "Analysis of Spitzer Spectra of Irradiated Planets: Evidence for Water Vapor?" ApJ 666 (): L45–L48. doi:`10.1086/521603`. arXiv: `0705.2457`.

Fortney, J. J., et al. 2011. "Discovery and Atmospheric Characterization of Giant Planet Kepler-12b: An Inflated Radius Outlier". ApJS 197, 9 (): 9. doi:`10.1088/0067-0049/197/1/9`. arXiv: `1109.1611 [astro-ph.EP]`.

Fortney, J. J., et al. 2016. "The Need for Laboratory Work to Aid in The Understanding of Exoplanetary Atmospheres". *ArXiv e-prints* (). arXiv: `1602.06305 [astro-ph.EP]`.

Fortney, J. J., et al. 2010. "Transmission Spectra of Three-Dimensional Hot Jupiter Model Atmospheres". ApJ 709 (): 1396–1406. doi:`10.1088/0004-637X/709/2/1396`. arXiv: `0912.2350 [astro-ph.EP]`.

Freedman, R. S., et al. 2008. "Line and Mean Opacities for Ultracool Dwarfs and Extrasolar Planets". ApJS 174, 504-513 (): 504–513. doi:`10.1086/521793`. arXiv: `0706.2374`.

Fressin, François, et al. 2013. "The False Positive Rate of Kepler and the Occurrence of Planets". ApJ 766, 81 (): 81. doi:10.1088/0004-637X/766/2/81. arXiv: 1301.0842 [astro-ph.EP].

Fulton, B. J., et al. 2015. "KELT-8b: A Highly Inflated Transiting Hot Jupiter and a New Technique for Extracting High-precision Radial Velocities from Noisy Spectra". ApJ 810, 30 (): 30. doi:10.1088/0004-637X/810/1/30. arXiv: 1505.06738 [astro-ph.EP].

Gaia Collaboration et al. 2016. "The Gaia mission". A&A 595, A1:A1. doi:10.1051/0004-6361/201629272. arXiv: 1609.04153 [astro-ph.IM].

Gamache, R. R., et al. 1996. "Theoretical calculations of pressure broadening coefficients for H_2O perturbed by hydrogen or helium gas." J. Quant. Spec. Radiat. Transf. 56 (): 471–487. doi:10.1016/0022-4073(96)00098-2.

Gandhi, Siddharth, et al. 2017. "GENESIS: new self-consistent models of exoplanetary spectra". MNRAS 472:2334–2355. doi:10.1093/mnras/stx1601. arXiv: 1706.02302 [astro-ph.EP].

Garland, R., et al. 2019. "Effectively Calculating Gaseous Absorption in Radiative Transfer Models of Exoplanetary and Brown Dwarf Atmospheres". *arXiv e-prints*, arXiv:1903.03997: arXiv:1903.03997. arXiv: 1903.03997 [astro-ph.EP].

Gibson, N. P., et al. 2013. "A Gemini ground-based transmission spectrum of WASP-29b: a featureless spectrum from 515 to 720 nm". MNRAS 428 (): 3680–3692. doi:10.1093/mnras/sts307. arXiv: 1210.7798 [astro-ph.EP].

Gillon, M., et al. 2007. "Detection of transits of the nearby hot Neptune GJ 436 b". A&A 472 (): L13–L16. doi:10.1051/0004-6361:20077799. arXiv: 0705.2219.

Gillon, M., et al. 2009. "Discovery and characterization of WASP-6b, an inflated sub-Jupiter mass planet transiting a solar-type star". A&A 501 (): 785–792. doi:10.1051/0004-6361/200911749. arXiv: 0901.4705 [astro-ph.EP].

Gillon, M., et al. 2012. "The TRAPPIST survey of southern transiting planets. I. Thirty eclipses of the ultra-short period planet WASP-43 b". A&A 542, A4 (): A4. doi:10.1051/0004-6361/201218817. arXiv: 1201.2789 [astro-ph.EP].

Gillon, M., et al. 2014. "WASP-103 b: a new planet at the edge of tidal disruption". A&A 562, L3 (): L3. doi:10.1051/0004-6361/201323014. arXiv: 1401.2784 [astro-ph.EP].

Gillon, Michaël, et al. 2017. "Seven temperate terrestrial planets around the nearby ultracool dwarf star TRAPPIST-1". Nature 542:456–460. doi:10.1038/nature21360. arXiv: 1703.01424 [astro-ph.EP].

Goody, R., et al. 1989. “The correlated-k method for radiation calculations in nonhomogeneous atmospheres”. J. Quant. Spec. Radiat. Transf. 42 (): 539–550. doi:10.1016/0022-4073(89)90044-7.

Gordon, S., et al. 1994. “Computer Program for Calculation of Complex Chemical Equilibrium Compositions and Applications”. *NASA Reference Publication* 1311.

Goyal, Jayesh M., et al. 2018. “A library of ATMO forward model transmission spectra for hot Jupiter exoplanets”. MNRAS 474 (): 5158–5185. doi:10.1093/mnras/stx3015.

— . 2019a. “Erratum: A library of ATMO forward model transmission spectra for hot Jupiter exoplanets”. MNRAS: 722. doi:10.1093/mnras/stz755.

Goyal, Jayesh M., et al. 2019b. “Fully scalable forward model grid of exoplanet transmission spectra”. MNRAS 482 (4): 4503–4513. doi:10.1093/mnras/sty3001. arXiv: 1810.12971 [astro-ph.EP].

Greene, T. P., et al. 2016. “Characterizing Transiting Exoplanet Atmospheres with JWST”. ApJ 817, 17 (): 17. doi:10.3847/0004-637X/817/1/17. arXiv: 1511.05528 [astro-ph.EP].

Gustafsson, B., et al. 2008. “A grid of MARCS model atmospheres for late-type stars. I. Methods and general properties”. A&A 486 (): 951–970. doi:10.1051/0004-6361:200809724. arXiv: 0805.0554.

Hadded, S., et al. 2001. “Line Broadening and Mixing in NH $_3$ Inversion Doublets Perturbed by NH $_3$, He, Ar, and H $_2$”. *Journal of Molecular Spectroscopy* 210 (): 275–283. doi:10.1006/jmsp.2001.8452.

Harpsøe, K. B. W., et al. 2013. “The transiting system GJ1214: high-precision defocused transit observations and a search for evidence of transit timing variation”. A&A 549, A10 (): A10. doi:10.1051/0004-6361/201219996. arXiv: 1207.3064 [astro-ph.EP].

Harris, G. J., et al. 2006. “Improved HCN/HNC linelist, model atmospheres and synthetic spectra for WZ Cas”. MNRAS 367 (): 400–406. doi:10.1111/j.1365-2966.2005.09960.x. eprint: astro-ph/0512363.

Hartman, J. D., et al. 2009. “HAT-P-12b: A Low-Density Sub-Saturn Mass Planet Transiting a Metal-Poor K Dwarf”. ApJ 706 (): 785–796. doi:10.1088/0004-637X/706/1/785. arXiv: 0904.4704 [astro-ph.EP].

Hartman, J. D., et al. 2011a. “HAT-P-18b and HAT-P-19b: Two Low-density Saturn-mass Planets Transiting Metal-rich K Stars”. ApJ 726, 52 (): 52. doi:10.1088/0004-637X/726/1/52. arXiv: 1007.4850 [astro-ph.EP].

Hartman, J. D., et al. 2011b. “HAT-P-26b: A Low-density Neptune-mass Planet Transiting a K Star”. ApJ 728, 138 (): 138. doi:10.1088/0004-637X/728/2/138. arXiv: 1010.1008 [astro-ph.EP].

Hartman, J. D., et al. 2011c. “HAT-P-32b and HAT-P-33b: Two Highly Inflated Hot Jupiters Transiting High-jitter Stars”. ApJ 742, 59 (): 59. doi:10.1088/0004-637X/742/1/59. arXiv: 1106.1212 [astro-ph.EP].

Hartman, J. D., et al. 2012. “HAT-P-39b-HAT-P-41b: Three Highly Inflated Transiting Hot Jupiters”. AJ 144, 139 (): 139. doi:10.1088/0004-6256/144/5/139. arXiv: 1207.3344 [astro-ph.EP].

Hartman, J. D., et al. 2014. “HAT-P-44b, HAT-P-45b, and HAT-P-46b: Three Transiting Hot Jupiters in Possible Multi-planet Systems”. AJ 147, 128 (): 128. doi:10.1088/0004-6256/147/6/128. arXiv: 1308.2937 [astro-ph.EP].

Hartman, J. D., et al. 2015a. “HAT-P-50b, HAT-P-51b, HAT-P-52b, and HAT-P-53b: Three Transiting Hot Jupiters and a Transiting Hot Saturn From the HATNet Survey”. AJ 150, 168 (): 168. doi:10.1088/0004-6256/150/6/168. arXiv: 1503.04149 [astro-ph.EP].

Hartman, J. D., et al. 2016. “HAT-P-65b and HAT-P-66b: Two Transiting Inflated Hot Jupiters and Observational Evidence for the Reinflation of Close-in Giant Planets”. AJ 152, 182 (): 182. doi:10.3847/0004-6256/152/6/182. arXiv: 1609.02767 [astro-ph.EP].

Hartman, J. D., et al. 2015b. “HATS-6b: A Warm Saturn Transiting an Early M Dwarf Star, and a Set of Empirical Relations for Characterizing K and M Dwarf Planet Hosts”. AJ 149, 166 (): 166. doi:10.1088/0004-6256/149/5/166. arXiv: 1408.1758 [astro-ph.EP].

Hatzes, Artie P., et al. 2015. “A Definition for Giant Planets Based on the Mass-Density Relationship”. ApJ 810, L25:L25. doi:10.1088/2041-8205/810/2/L25. arXiv: 1506.05097 [astro-ph.EP].

Hay, K. L., et al. 2016. “WASP-92b, WASP-93b and WASP-118b: three new transiting close-in giant planets”. MNRAS 463 (): 3276–3289. doi:10.1093/mnras/stw2090. arXiv: 1607.00774 [astro-ph.EP].

Hebb, L., et al. 2009. “WASP-12b: The Hottest Transiting Extrasolar Planet Yet Discovered”. ApJ 693 (): 1920–1928. doi:10.1088/0004-637X/693/2/1920. arXiv: 0812.3240.

Hebb, L., et al. 2010. “WASP-19b: The Shortest Period Transiting Exoplanet Yet Discovered”. ApJ 708 (): 224–231. doi:10.1088/0004-637X/708/1/224. arXiv: 1001.0403 [astro-ph.EP].

Hébrard, G., et al. 2013. "WASP-52b, WASP-58b, WASP-59b, and WASP-60b: Four new transiting close-in giant planets". A&A 549, A134 (): A134. doi:`10.1051/0004-6361/201220363`. arXiv: `1211.0810 [astro-ph.EP]`.

Hedges, C., et al. 2016. "Effect of pressure broadening on molecular absorption cross sections in exoplanetary atmospheres". MNRAS 458 (): 1427–1449. doi:`10.1093/mnras/stw278`. arXiv: `1602.00751 [astro-ph.EP]`.

Heiter, U., et al. 2008. "VALD — an atomic and molecular database for astrophysics". In *Journal of Physics Conference Series*, 130:012011. Journal of Physics Conference Series. doi:`10.1088/1742-6596/130/1/012011`.

Hellier, C., et al. 2012. "Seven transiting hot Jupiters from WASP-South, Euler and TRAPPIST: WASP-47b, WASP-55b, WASP-61b, WASP-62b, WASP-63b, WASP-66b and WASP-67b". MNRAS 426 (): 739–750. doi:`10.1111/j.1365-2966.2012.21780.x`. arXiv: `1204.5095 [astro-ph.EP]`.

Hellier, C., et al. 2015. "Three WASP-South Transiting Exoplanets: WASP-74b, WASP-83b, and WASP-89b". AJ 150, 18 (): 18. doi:`10.1088/0004-6256/150/1/18`. arXiv: `1410.6358 [astro-ph.EP]`.

Hellier, C., et al. 2014. "Transiting hot Jupiters from WASP-South, Euler and TRAPPIST: WASP-95b to WASP-101b". MNRAS 440 (): 1982–1992. doi:`10.1093/mnras/stu410`. arXiv: `1310.5630 [astro-ph.EP]`.

Hellier, C., et al. 2010. "WASP-29b: A Saturn-sized Transiting Exoplanet". ApJ 723 (): L60–L63. doi:`10.1088/2041-8205/723/1/L60`. arXiv: `1009.5318 [astro-ph.EP]`.

Hellier, C., et al. 2011. "WASP-43b: the closest-orbiting hot Jupiter". A&A 535, L7 (): L7. doi:`10.1051/0004-6361/201117081`. arXiv: `1104.2823 [astro-ph.EP]`.

Hellier, C., et al. 2009. "Wasp-7: A Bright Transiting-Exoplanet System in the Southern Hemisphere". ApJ 690 (): L89–L91. doi:`10.1088/0004-637X/690/1/L89`. arXiv: `0805.2600`.

Hellier, C., et al. 2017. "WASP-South transiting exoplanets: WASP-130b, WASP-131b, WASP-132b, WASP-139b, WASP-140b, WASP-141b and WASP-142b". MNRAS 465 (): 3693–3707. doi:`10.1093/mnras/stw3005`. arXiv: `1604.04195 [astro-ph.EP]`.

Heng, K., et al. 2016. "Analytical Models of Exoplanetary Atmospheres. III. Gaseous C-H-O-N Chemistry with Nine Molecules". ApJ 829, 104 (): 104. doi:`10.3847/0004-637X/829/2/104`. arXiv: `1603.05418 [astro-ph.EP]`.

Heng, K., et al. 2017. “The theory of transmission spectra revisited: a fast method for analyzing WFC3 data and an unresolved challenge”. *ArXiv e-prints* (). arXiv: `1702.02051 [astro-ph.EP]`.

Heng, Kevin, et al. 2011. “Atmospheric circulation of tidally locked exoplanets: II. Dual-band radiative transfer and convective adjustment”. MNRAS 418:2669–2696. doi:`10.1111/j.1365-2966.2011.19658.x`. arXiv: `1105.4065 [astro-ph.EP]`.

Henry, G. W., et al. 2000. “A Transiting “51 Peg-like” Planet”. ApJ 529 (): L41–L44. doi:`10.1086/312458`.

Henyey, L., et al. 1965. “Studies in Stellar Evolution. III. The Calculation of Model Envelopes.” ApJ 142 (): 841. doi:`10.1086/148357`.

Howard, A. W., et al. 2012a. “HAT-P-17b,c: A Transiting, Eccentric, Hot Saturn and a Long-period, Cold Jupiter”. ApJ 749, 134 (): 134. doi:`10.1088/0004-637X/749/2/134`. arXiv: `1008.3898 [astro-ph.EP]`.

Howard, Andrew W., et al. 2012b. “Planet Occurrence within 0.25 AU of Solar-type Stars from Kepler”. *The Astrophysical Journal Supplement Series* 201, 15:15. doi:`10.1088/0067-0049/201/2/15`. arXiv: `1103.2541 [astro-ph.EP]`.

Hu, Renyu, et al. 2012. “Photochemistry in Terrestrial Exoplanet Atmospheres. I. Photochemistry Model and Benchmark Cases”. ApJ 761, 166 (): 166. doi:`10.1088/0004-637X/761/2/166`. arXiv: `1210.6885 [Astrophysics - Earth and Planetary Astrophysics]`.

Hubbard, W. B., et al. 2001. “Theory of Extrasolar Giant Planet Transits”. ApJ 560 (): 413–419. doi:`10.1086/322490`. eprint: `astro-ph/0101024`.

Hubeny, Ivan, et al. 2014. *Theory of Stellar Atmospheres.*

Huitson, C. M., et al. 2013. “An HST optical-to-near-IR transmission spectrum of the hot Jupiter WASP-19b: detection of atmospheric water and likely absence of TiO”. MNRAS 434 (): 3252–3274. doi:`10.1093/mnras/stt1243`. arXiv: `1307.2083 [astro-ph.EP]`.

Huitson, C. M., et al. 2012. “Temperature-pressure profile of the hot Jupiter HD 189733b from HST sodium observations: detection of upper atmospheric heating”. MNRAS 422 (): 2477–2488. doi:`10.1111/j.1365-2966.2012.20805.x`. arXiv: `1202.4721 [astro-ph.EP]`.

Iro, N., et al. 2005. “A time-dependent radiative model of HD 209458b”. A&A 436 (2): 719–727. doi:`10.1051/0004-6361:20048344`. arXiv: `astro-ph/0409468 [astro-ph]`.

Irwin, P. G. J., et al. 2008. “The NEMESIS planetary atmosphere radiative transfer and retrieval tool”. J. Quant. Spec. Radiat. Transf. 109 (): 1136–1150. doi:10.1016/j.jqsrt.2007.11.006.

John, T. L. 1988. “Continuous absorption by the negative hydrogen ion reconsidered”. A&A 193 (): 189–192.

Johnson, J. A., et al. 2011. “HAT-P-30b: A Transiting Hot Jupiter on a Highly Oblique Orbit”. ApJ 735, 24 (): 24. doi:10.1088/0004-637X/735/1/24. arXiv: 1103.3825 [astro-ph.EP].

Kataria, T., et al. 2016. “The Atmospheric Circulation of a Nine-hot-Jupiter Sample: Probing Circulation and Chemistry over a Wide Phase Space”. ApJ 821, 9 (): 9. doi:10.3847/0004-637X/821/1/9. arXiv: 1602.06733 [astro-ph.EP].

Kempton, E. M.-R., et al. 2017. “Exo-Transmit: An Open-Source Code for Calculating Transmission Spectra for Exoplanet Atmospheres of Varied Composition”. PASP 129, no. 4 (): 044402. doi:10.1088/1538-3873/aa61ef. arXiv: 1611.03871 [astro-ph.EP].

Knutson, H. A., et al. 2009. “Multiwavelength Constraints on the Day-Night Circulation Patterns of HD 189733b”. ApJ 690 (): 822–836. doi:10.1088/0004-637X/690/1/822. arXiv: 0802.1705.

Knutson, Heather A., et al. 2007. “A map of the day-night contrast of the extrasolar planet HD 189733b”. Nature 447:183–186. doi:10.1038/nature05782. arXiv: 0705.0993 [astro-ph].

Kopparapu, R. k., et al. 2012. “A Photochemical Model for the Carbon-rich Planet WASP-12b”. ApJ 745, 77 (): 77. doi:10.1088/0004-637X/745/1/77. arXiv: 1110.2793 [astro-ph.EP].

Kovács, G., et al. 2007. “HAT-P-4b: A Metal-rich Low-Density Transiting Hot Jupiter”. ApJ 670 (): L41–L44. doi:10.1086/524058. arXiv: 0710.0602.

Kreidberg, L., et al. 2015. “A Detection of Water in the Transmission Spectrum of the Hot Jupiter WASP-12b and Implications for Its Atmospheric Composition”. ApJ 814, 66 (): 66. doi:10.1088/0004-637X/814/1/66. arXiv: 1504.05586 [astro-ph.EP].

Kreidberg, L., et al. 2014. “A Precise Water Abundance Measurement for the Hot Jupiter WASP-43b”. ApJ 793, L27 (): L27. doi:10.1088/2041-8205/793/2/L27. arXiv: 1410.2255 [astro-ph.EP].

Kreidberg, Laura, et al. 2018. “Global Climate and Atmospheric Composition of the Ultra-hot Jupiter WASP-103b from HST and Spitzer Phase Curve Observations”. AJ 156, 17:17. doi:10.3847/1538-3881/aac3df. arXiv: 1805.00029 [astro-ph.EP].

Kuhn, R. B., et al. 2016. “KELT-10b: the first transiting exoplanet from the KELT-South survey - a hot sub-Jupiter transiting a V = 10.7 early G-star”. MNRAS 459 (): 4281–4298. doi:10.1093/mnras/stw880. arXiv: 1509.02323 [astro-ph.EP].

Lacis, A. A., et al. 1991. “A description of the correlated-k distribution method for modelling nongray gaseous absorption, thermal emission, and multiple scattering in vertically inhomogeneous atmospheres”. J. Geophys. Res. 96 (): 9027–9064. doi:10.1029/90JD01945.

Lam, K. W. F., et al. 2017. “From dense hot Jupiter to low-density Neptune: The discovery of WASP-127b, WASP-136b, and WASP-138b”. A&A 599, A3 (): A3. doi:10.1051/0004-6361/201629403. arXiv: 1607.07859 [astro-ph.EP].

Landrain, V., et al. 1997. “Diode-Laser Measurements of H $_2$-Broadening Coefficients in the ν $_2$Band of HCN”. *Journal of Molecular Spectroscopy* 182 (): 184–188. doi:10.1006/jmsp.1996.7223.

Lanotte, A. A., et al. 2014. “A global analysis of Spitzer and new HARPS data confirms the loneliness and metal-richness of GJ 436 b”. A&A 572, A73 (): A73. doi:10.1051/0004-6361/201424373. arXiv: 1409.4038 [astro-ph.EP].

Le Moal, M. F., et al. 1986. “N_2 and H_2 broadening parameters in the fundamental band of CO.” J. Quant. Spec. Radiat. Transf. 35 (): 145–152.

Lecavelier Des Etangs, A., et al. 2008. “Rayleigh scattering in the transit spectrum of HD 189733b”. A&A 481 (): L83–L86. doi:10.1051/0004-6361:200809388. arXiv: 0802.3228.

Lee, J.-M., et al. 2012a. “Optimal estimation retrievals of the atmospheric structure and composition of HD 189733b from secondary eclipse spectroscopy”. MNRAS 420 (): 170–182. doi:10.1111/j.1365-2966.2011.20013.x. arXiv: 1110.2934 [astro-ph.EP].

Lee, J. W., et al. 2012b. “The Sub-Saturn Mass Transiting Planet HAT-P-12b”. AJ 143, 95 (): 95. doi:10.1088/0004-6256/143/4/95. arXiv: 1201.6419 [astro-ph.EP].

Lehmann, H., et al. 2015. “Mass of WASP-33b”. A&A 578, L4 (): L4. doi:10.1051/0004-6361/201526176.

Lendl, M., et al. 2016. "FORS2 observes a multi-epoch transmission spectrum of the hot Saturn-mass exoplanet WASP-49b". A&A 587, A67 (): A67. doi:`10.1051/0004-6361/201527594`. arXiv: `1512.06698 [astro-ph.EP]`.

Lendl, M., et al. 2014. "WASP-117b: a 10-day-period Saturn in an eccentric and misaligned orbit". A&A 568, A81 (): A81. doi:`10.1051/0004-6361/201424481`. arXiv: `1406.6942 [astro-ph.EP]`.

Lendl, M., et al. 2012. "WASP-42 b and WASP-49 b: two new transiting sub-Jupiters". A&A 544, A72 (): A72. doi:`10.1051/0004-6361/201219585`. arXiv: `1205.2757 [astro-ph.EP]`.

Leonard, P. J. 1974. "Refractive Indices, Verdet Constants, and Polarizabilities of the Inert Gases". *Atomic Data and Nuclear Data Tables* 14:21. doi:`10.1016/S0092-640X(74)80028-8`.

Levy, A., et al. 1994. "Temperature Dependence of Collision-Broadened Lines of Phosphine". *Journal of Molecular Spectroscopy* 166 (): 20–31. doi:`10.1006/jmsp.1994.1168`.

Lewis, Nikole, et al. 2014. "Theoretical Albedo Spectra of Exoplanet Direct Imaging Targets". In *American Astronomical Society Meeting Abstracts #224*, 224:201.05.

Line, M. R., et al. 2013. "A Systematic Retrieval Analysis of Secondary Eclipse Spectra. I. A Comparison of Atmospheric Retrieval Techniques". ApJ 775, 137 (): 137. doi:`10.1088/0004-637X/775/2/137`. arXiv: `1304.5561 [astro-ph.EP]`.

Line, M. R., et al. 2016. "The Influence of Nonuniform Cloud Cover on Transit Transmission Spectra". ApJ 820, 78 (): 78. doi:`10.3847/0004-637X/820/1/78`. arXiv: `1511.09443 [astro-ph.EP]`.

Line, Michael R., et al. 2015. "Uniform Atmospheric Retrieval Analysis of Ultracool Dwarfs. I. Characterizing Benchmarks, Gl 570D and HD 3651B". ApJ 807, 183:183. doi:`10.1088/0004-637X/807/2/183`. arXiv: `1504.06670 [astro-ph.SR]`.

Lines, S., et al. 2018a. "Exonephology: transmission spectra from a 3D simulated cloudy atmosphere of HD 209458b". MNRAS 481 (): 194–205. doi:`10.1093/mnras/sty2275`.

Lines, S., et al. 2018b. "Simulating the cloudy atmospheres of HD 209458 b and HD 189733 b with the 3D Met Office Unified Model". A&A 615, A97 (): A97. doi:`10.1051/0004-6361/201732278`.

Liou, K. N. 1980. *An introduction to atmospheric radiation.*

Lister, T. A., et al. 2009. "WASP-16b: A New Jupiter-Like Planet Transiting a Southern Solar Analog". ApJ 703 (): 752–756. doi:`10.1088/0004-637X/703/1/752`. arXiv: `0908.0297 [astro-ph.EP]`.

Lodders, K. 1999. “Alkali Element Chemistry in Cool Dwarf Atmospheres”. ApJ 519 (): 793–801. doi:10.1086/307387.

Lodders, K., et al. 2002a. “Atmospheric Chemistry in Giant Planets, Brown Dwarfs, and Low-Mass Dwarf Stars. I. Carbon, Nitrogen, and Oxygen”. Icarus 155 (): 393–424. doi:10.1006/icar.2001.6740.

Lodders, K., et al. 2006a. “Chemistry of Low Mass Substellar Objects”. In *Astrophysics Update 2*, ed. by J. W. Mason, 1. doi:10.1007/3-540-30313-8_1.

— . 2006b. “Chemistry of Low Mass Substellar Objects”. In *Astrophysics Update 2*, ed. by J. W. Mason, 1. doi:10.1007/3-540-30313-8_1.

Lodders, Katharina. 2003. “Solar System Abundances and Condensation Temperatures of the Elements”. ApJ 591 (): 1220–1247. doi:10.1086/375492.

Lodders, Katharina, et al. 2002b. “Atmospheric Chemistry in Giant Planets, Brown Dwarfs, and Low-Mass Dwarf Stars. I. Carbon, Nitrogen, and Oxygen”. Icarus 155 (): 393–424. doi:10.1006/icar.2001.6740.

MacDonald, Ryan J., et al. 2017. “HD 209458b in new light: evidence of nitrogen chemistry, patchy clouds and sub-solar water”. MNRAS 469 (2): 1979–1996. doi:10.1093/mnras/stx804. arXiv: 1701.01113 [astro-ph.EP].

Maciejewski, G., et al. 2014. “Revisiting Parameters for the WASP-1 Planetary System”. Acta Astron. 64 (): 11–26. arXiv: 1402.6518 [astro-ph.EP].

Macintosh, B., et al. 2015. “Discovery and spectroscopy of the young jovian planet 51 Eri b with the Gemini Planet Imager”. *Science* 350:64–67. doi:10.1126/science.aac5891. arXiv: 1508.03084 [astro-ph.EP].

Madhusudhan, N. 2012. “C/O Ratio as a Dimension for Characterizing Exoplanetary Atmospheres”. ApJ 758, 36 (): 36. doi:10.1088/0004-637X/758/1/36. arXiv: 1209.2412 [astro-ph.EP].

Madhusudhan, N., et al. 2011. “A high C/O ratio and weak thermal inversion in the atmosphere of exoplanet WASP-12b”. Nature 469 (): 64–67. doi:10.1038/nature09602. arXiv: 1012.1603 [astro-ph.EP].

Madhusudhan, N., et al. 2009. “A Temperature and Abundance Retrieval Method for Exoplanet Atmospheres”. ApJ 707 (): 24–39. doi:10.1088/0004-637X/707/1/24. arXiv: 0910.1347 [astro-ph.EP].

Madhusudhan, N., et al. 2016a. “Atmospheric Signatures of Giant Exoplanet Formation by Pebble Accretion”. *ArXiv e-prints* (). arXiv: 1611.03083 [astro-ph.EP].

Madhusudhan, Nikku. 2018. "Atmospheric Retrieval of Exoplanets". In *Handbook of Exoplanets, ISBN 978-3-319-55332-0. Springer International Publishing AG, part of Springer Nature, 2018, id.104*, 104. doi:10.1007/978-3-319-55333-7_104.

Madhusudhan, Nikku, et al. 2016b. "Exoplanetary Atmospheres—Chemistry, Formation Conditions, and Habitability". Space Sci. Rev. 205 (): 285–348. doi:10.1007/s11214-016-0254-3.

Malik, M., et al. 2017. "HELIOS: An Open-source, GPU-accelerated Radiative Transfer Code for Self-consistent Exoplanetary Atmospheres". AJ 153, 56 (): 56. doi:10.3847/1538-3881/153/2/56. arXiv: 1606.05474 [astro-ph.EP].

Mancini, L., et al. 2017. "Orbital alignment and star-spot properties in the WASP-52 planetary system". MNRAS 465 (): 843–857. doi:10.1093/mnras/stw1987. arXiv: 1608.02001 [astro-ph.EP].

Mancini, L., et al. 2014a. "Physical properties and transmission spectrum of the WASP-80 planetary system from multi-colour photometry". A&A 562, A126 (): A126. doi:10.1051/0004-6361/201323265. arXiv: 1312.4982 [astro-ph.EP].

Mancini, L., et al. 2014b. "Physical properties of the WASP-67 planetary system from multi-colour photometry". A&A 568, A127 (): A127. doi:10.1051/0004-6361/201424106. arXiv: 1406.7448 [astro-ph.EP].

Mancini, L., et al. 2013. "Physical properties, transmission and emission spectra of the WASP-19 planetary system from multi-colour photometry". MNRAS 436 (): 2–18. doi:10.1093/mnras/stt1394. arXiv: 1306.6384 [astro-ph.EP].

Mancini, L., et al. 2015. "The GAPS Programme with HARPS-N at TNG. VIII. Observations of the Rossiter-McLaughlin effect and characterisation of the transiting planetary systems HAT-P-36 and WASP-11/HAT-P-10". A&A 579, A136 (): A136. doi:10.1051/0004-6361/201526030. arXiv: 1503.01787 [astro-ph.EP].

Mandell, A. M., et al. 2013. "Exoplanet Transit Spectroscopy Using WFC3: WASP-12 b, WASP-17 b, and WASP-19 b". ApJ 779, 128 (): 128. doi:10.1088/0004-637X/779/2/128. arXiv: 1310.2949 [astro-ph.EP].

Mandushev, G., et al. 2007. "TrES-4: A Transiting Hot Jupiter of Very Low Density". ApJ 667 (): L195–L198. doi:10.1086/522115. arXiv: 0708.0834.

Mansfield, C. R., et al. 1969. "Dispersion of Helium". *Journal of the Optical Society of America (1917-1983)* 59 (): 199.

Mansfield, Megan, et al. 2018. "An HST/WFC3 Thermal Emission Spectrum of the Hot Jupiter HAT-P-7b". AJ 156, 10:10. doi:10.3847/1538-3881/aac497. arXiv: 1805.00424 [astro-ph.EP].

Mantz, A. W., et al. 2005. "A multispectrum analysis of widths and shifts in the 2010-2260 cm $^{-1}$ region of ^{12}C ^{16}O broadened by Helium at temperatures between 80 and 297 K". *Journal of Molecular Structure* 742 (): 99–110. doi:10.1016/j.molstruc.2004.11.094.

Margolis, J. S. 1993. "Measurement of hydrogen-broadened methane lines in the ν_4 band at 296 and 200K." J. Quant. Spec. Radiat. Transf. 50 (): 431–441. doi:10.1016/0022-4073(93)90073-Q.

Marley, M. S., et al. 1996. "Atmospheric, Evolutionary, and Spectral Models of the Brown Dwarf Gliese 229 B". *Science* 272 (5270): 1919–1921. doi:10.1126/science.272.5270.1919. arXiv: astro-ph/9606036 [astro-ph].

Marois, Christian, et al. 2010. "Images of a fourth planet orbiting HR 8799". Nature 468 (7327): 1080–1083. doi:10.1038/nature09684. arXiv: 1011.4918 [astro-ph.EP].

Marquez-Neila, Pablo, et al. 2018. "Supervised Machine Learning for Analysing Spectra of Exoplanetary Atmospheres". *ArXiv e-prints*, arXiv:1806.03944 (): arXiv:1806.03944. arXiv: 1806.03944.

Maxted, P. F. L., et al. 2016. "Five transiting hot Jupiters discovered using WASP-South, Euler, and TRAPPIST: WASP-119 b, WASP-124 b, WASP-126 b, WASP-129 b, and WASP-133 b". A&A 591, A55 (): A55. doi:10.1051/0004-6361/201628250. arXiv: 1602.01740 [astro-ph.EP].

Maxted, P. F. L., et al. 2011. "WASP-41b: A Transiting Hot Jupiter Planet Orbiting a Magnetically Active G8V Star". PASP 123 (): 547. doi:10.1086/660007. arXiv: 1012.2977 [astro-ph.EP].

Mayne, N. J., et al. 2013. "The UM, a fully–compressible, non–hydrostatic, deep atmosphere GCM, applied to hot Jupiters". *ArXiv e-prints* (). arXiv: 1311.2083 [astro-ph.EP].

— . 2014. "The unified model, a fully-compressible, non-hydrostatic, deep atmosphere global circulation model, applied to hot Jupiters. ENDGame for a HD 209458b test case". A&A 561, A1 (): A1. doi:10.1051/0004-6361/201322174.

Mayor, M., et al. 1995. "A Jupiter-mass companion to a solar-type star". Nature 378 (): 355–359. doi:10.1038/378355a0.

Mayor, M., et al. 2003. "Setting New Standards with HARPS". *The Messenger* 114:20–24.

Mbarek, R., et al. 2016. "Clouds in Super-Earth Atmospheres: Chemical Equilibrium Calculations". ApJ 827, 121 (): 121. doi:10.3847/0004-637X/827/2/121. arXiv: 1602.02759 [astro-ph.EP].

McBride, B. J., et al. 1993. “Coefficients for Calculating Thermodynamic and Transport Properties of Individual Species”. *NASA Technical Memorandum* 4513.

McBride, B. J., et al. 2002. “NASA Glenn Coefficients for Calculating Thermodynamic Properties of Individual Species”. *NASA/TP* 2002-211556.

McCullough, P. R., et al. 2006. “A Transiting Planet of a Sun-like Star”. ApJ 648 (): 1228–1238. doi:`10.1086/505651`. eprint: `astro-ph/0605414`.

McCullough, P. R., et al. 2014. “Water Vapor in the Spectrum of the Extrasolar Planet HD 189733b. I. The Transit”. ApJ 791, 55 (): 55. doi:`10.1088/0004-637X/791/1/55`. arXiv: `1407.2462 [astro-ph.SR]`.

McKemmish, L. K., et al. 2016. “ExoMol line lists - XVIII. The high-temperature spectrum of VO”. MNRAS 463 (): 771–793. doi:`10.1093/mnras/stw1969`. arXiv: `1609.06120 [astro-ph.SR]`.

Menou, Kristen, et al. 2009. “Atmospheric Circulation of Hot Jupiters: A Shallow Three-Dimensional Model”. ApJ 700:887–897. doi:`10.1088/0004-637X/700/1/887`. arXiv: `0809.1671 [astro-ph]`.

Mollière, P., et al. 2015. “Model Atmospheres of Irradiated Exoplanets: The Influence of Stellar Parameters, Metallicity, and the C/O Ratio”. ApJ 813, 47 (): 47. doi:`10.1088/0004-637X/813/1/47`. arXiv: `1509.07523 [astro-ph.EP]`.

Mollière, P., et al. 2016. “Observing transiting planets with JWST – Prime targets and their synthetic spectral observations”. *ArXiv e-prints* (). arXiv: `1611.08608 [astro-ph.EP]`.

Morley, C. V., et al. 2015. “Thermal Emission and Reflected Light Spectra of Super Earths with Flat Transmission Spectra”. ApJ 815, 110 (): 110. doi:`10.1088/0004-637X/815/2/110`. arXiv: `1511.01492 [astro-ph.EP]`.

Moses, J. I. 2014. “Chemical kinetics on extrasolar planets”. *Philosophical Transactions of the Royal Society of London Series A* 372 (2014): 20130073–20130073. doi:`10.1098/rsta.2013.0073`. arXiv: `1307.5450 [astro-ph.EP]`.

Moses, J. I., et al. 2013a. “Chemical Consequences of the C/O Ratio on Hot Jupiters: Examples from WASP-12b, CoRoT-2b, XO-1b, and HD 189733b”. ApJ 763, 25 (): 25. doi:`10.1088/0004-637X/763/1/25`. arXiv: `1211.2996 [astro-ph.EP]`.

Moses, J. I., et al. 2013b. “Compositional Diversity in the Atmospheres of Hot Neptunes, with Application to GJ 436b”. ApJ 777, 34 (): 34. doi:`10.1088/0004-637X/777/1/34`. arXiv: `1306.5178 [astro-ph.EP]`.

Moses, J. I., et al. 2011. “Disequilibrium Carbon, Oxygen, and Nitrogen Chemistry in the Atmospheres of HD 189733b and HD 209458b”. ApJ 737, 15 (): 15. doi:`10.1088/0004-637X/737/1/15`. arXiv: `1102.0063 [astro-ph.EP]`.

Neveu-VanMalle, M., et al. 2014. "WASP-94 A and B planets: hot-Jupiter cousins in a twin-star system". A&A 572, A49 (): A49. doi:10.1051/0004-6361/201424744. arXiv: 1409.7566 [astro-ph.EP].

Niemann, H. B., et al. 1998. "The composition of the Jovian atmosphere as determined by the Galileo probe mass spectrometer". J. Geophys. Res. 103 (): 22831–22846. doi:10.1029/98JE01050.

Nikolov, N., et al. 2018. "An absolute sodium abundance for a cloud-free 'hot Saturn' exoplanet". Nature 557 (): 526–529. doi:10.1038/s41586-018-0101-7.

Nikolov, N., et al. 2015. "HST hot-Jupiter transmission spectral survey: haze in the atmosphere of WASP-6b". MNRAS 447 (): 463–478. doi:10.1093/mnras/stu2433. arXiv: 1411.4567 [astro-ph.SR].

Nikolov, N., et al. 2014. "Hubble Space Telescope hot Jupiter transmission spectral survey: a detection of Na and strong optical absorption in HAT-P-1b". MNRAS 437 (): 46–66. doi:10.1093/mnras/stt1859. arXiv: 1310.0083 [astro-ph.SR].

Nouri, S., et al. 2004. "Temperature dependence of pressure broadening of NH $_3$ perturbed by H $_2$ and N $_2$". *Journal of Molecular Spectroscopy* 227 (): 60–66. doi:10.1016/j.jms.2004.05.009.

Noyes, R. W., et al. 2008. "HAT-P-6b: A Hot Jupiter Transiting a Bright F Star". ApJ 673, L79 (): L79. doi:10.1086/527358. arXiv: 0710.2894.

Öberg, K. I., et al. 2011. "The Effects of Snowlines on C/O in Planetary Atmospheres". ApJ 743, L16 (): L16. doi:10.1088/2041-8205/743/1/L16. arXiv: 1110.5567.

Padmanabhan, A., et al. 2014. "Study of pressure broadening effects of H_2 on CO_2 and CO in the near infrared region between 6317 and 6335 cm^{-1} at room temperature". J. Quant. Spec. Radiat. Transf. 133 (): 81–90. doi:10.1016/j.jqsrt.2013.07.016.

Parmentier, Vivien, et al. 2018. "From thermal dissociation to condensation in the atmospheres of ultra hot Jupiters: WASP-121b in context". A&A 617, A110:A110. doi:10.1051/0004-6361/201833059. arXiv: 1805.00096 [astro-ph.EP].

Penndorf, R. 1957. "Tables of the Refractive Index for standard Air and the Rayleigh Scattering Coefficient for the Spectral Region between 0.2 and 20.0 mgr and Their Application to Atmospheric Optics". *Journal of the Optical Society of America (1917-1983)* 47 (): 176.

Pepper, J., et al. 2017. "KELT-11b: A Highly Inflated Sub-Saturn Exoplanet Transiting the V = 8 Subgiant HD 93396". AJ 153, 215 (): 215. doi:10.3847/1538-3881/aa6572. arXiv: 1607.01755 [astro-ph.EP].

Perryman, Michael. 2014. *The Exoplanet Handbook.*

Petigura, Erik A., et al. 2013. "Prevalence of Earth-size planets orbiting Sun-like stars". *Proceedings of the National Academy of Science* 110:19273–19278. doi:10.1073/pnas.1319909110. arXiv: 1311.6806 [astro-ph.EP].

Pine, A. S. 1992. "Self-, N2, O2, H2, Ar, and He broadening in the nu3 band Q branch of CH4". J. Chem. Phys. 97 (): 773–785. doi:10.1063/1.463943.

Pine, A. S., et al. 1993. "N_2, O_2, H_2, Ar and He broadening in the ν_1 band of NH_3." J. Quant. Spec. Radiat. Transf. 50 (): 337–348. doi:10.1016/0022-4073(93)90069-T.

Plez, B. 1998. "A new TiO line list". A&A 337 (): 495–500.

— . 1999. "The modelling of M-giant spectra". In *Asymptotic Giant Branch Stars*, ed. by T. Le Bertre et al., 191:75. IAU Symposium.

Pollacco, D. L., et al. 2006. "The WASP Project and the SuperWASP Cameras". *Publications of the Astronomical Society of the Pacific* 118 (): 1407–1418. doi:10.1086/508556. arXiv: astro-ph/0608454 [astro-ph].

Pont, F., et al. 2013. "The prevalence of dust on the exoplanet HD 189733b from Hubble and Spitzer observations". MNRAS 432 (): 2917–2944. doi:10.1093/mnras/stt651. arXiv: 1210.4163 [astro-ph.EP].

Quinn, S. N., et al. 2012. "HAT-P-25b: A Hot-Jupiter Transiting a Moderately Faint G Star". ApJ 745, 80 (): 80. doi:10.1088/0004-637X/745/1/80. arXiv: 1008.3565 [astro-ph.EP].

Rajpurohit, A. S., et al. 2013. "The effective temperature scale of M dwarfs". A&A 556, A15 (): A15. doi:10.1051/0004-6361/201321346. arXiv: 1304.4072 [astro-ph.SR].

Rau, A. R. P. 1996. "The Negative Ion of Hydrogen". *Journal of Astrophysics and Astronomy* 17:113. doi:10.1007/BF02702300.

Rayleigh. 1919. "Scattering of Light by Resonating Molecules". Nature 104 (): 276. doi:10.1038/104276c0.

Redfield, S., et al. 2008. "Sodium Absorption from the Exoplanetary Atmosphere of HD 189733b Detected in the Optical Transmission Spectrum". ApJ 673, L87 (): L87. doi:10.1086/527475. arXiv: 0712.0761.

Régalia-Jarlot, L., et al. 2005. "Pressure-broadened line widths and pressure-induced line shifts coefficients of the (1-0) and (2-0) bands of 12CO". J. Quant. Spec. Radiat. Transf. 91 (): 121–131. doi:10.1016/j.jqsrt.2004.05.042.

Richard, C., et al. 2012. "New section of the HITRAN database: Collision-induced absorption (CIA)". J. Quant. Spec. Radiat. Transf. 113 (): 1276–1285. doi:10.1016/j.jqsrt.2011.11.004.

Ricker, G. R., et al. 2014. "Transiting Exoplanet Survey Satellite (TESS)". In *Space Telescopes and Instrumentation 2014: Optical, Infrared, and Millimeter Wave*, 9143:914320. Proc. SPIE. doi:10.1117/12.2063489. arXiv: 1406.0151 [astro-ph.EP].

Rimmer, P. B., et al. 2016. "A Chemical Kinetics Network for Lightning and Life in Planetary Atmospheres". *The Astrophysical Journal Supplement Series* 224, 9 (): 9. doi:10.3847/0067-0049/224/1/9.

Rodriguez, J. E., et al. 2016. "KELT-14b and KELT-15b: An Independent Discovery of WASP-122b and a New Hot Jupiter". AJ 151, 138 (): 138. doi:10.3847/0004-6256/151/6/138. arXiv: 1509.08953 [astro-ph.EP].

Rothman, L. S., et al. 2010. "HITEMP, the high-temperature molecular spectroscopic database". J. Quant. Spec. Radiat. Transf. 111 (): 2139–2150. doi:10.1016/j.jqsrt.2010.05.001.

Rothman, L. S., et al. 2009. "The HITRAN 2008 molecular spectroscopic database". J. Quant. Spec. Radiat. Transf. 110 (): 533–572. doi:10.1016/j.jqsrt.2009.02.013.

Rothman, L. S., et al. 2013. "The HITRAN2012 molecular spectroscopic database". J. Quant. Spec. Radiat. Transf. 130 (): 4–50. doi:10.1016/j.jqsrt.2013.07.002.

Rybicki, George B., et al. 1986. *Radiative Processes in Astrophysics.*

Salem, J., et al. 2005. "Helium- and argon-broadening coefficients of phosphine lines in the ν_2 and ν_4 bands". *Journal of Molecular Spectroscopy* 232 (): 247–254. doi:10.1016/j.jms.2005.04.014.

Sato, B., et al. 2005. "The N2K Consortium. II. A Transiting Hot Saturn around HD 149026 with a Large Dense Core". ApJ 633 (): 465–473. doi:10.1086/449306. eprint: astro-ph/0507009.

Sauval, A. J., et al. 1984. "A set of partition functions and equilibrium constants for 300 diatomic molecules of astrophysical interest". ApJS 56 (): 193–209. doi:10.1086/190980.

Seager, S., et al. 2005. "On the Dayside Thermal Emission of Hot Jupiters". ApJ 632 (): 1122–1131. doi:10.1086/444411. eprint: astro-ph/0504212.

Seager, S., et al. 2000. "Theoretical Transmission Spectra during Extrasolar Giant Planet Transits". ApJ 537 (): 916–921. doi:10.1086/309088. eprint: astro-ph/9912241.

Seager, Sara. 2010. *Exoplanet Atmospheres: Physical Processes.*

Sharp, C. M., et al. 2007. “Atomic and Molecular Opacities for Brown Dwarf and Giant Planet Atmospheres”. ApJS 168 (): 140–166. doi:`10.1086/508708`. eprint: `astro-ph/0607211`.

Showman, A. P., et al. 2002. “Atmospheric circulation and tides of “51 Pegasus b-like” planets”. A&A 385 (): 166–180. doi:`10.1051/0004-6361:20020101`. eprint: `astro-ph/0202236`.

Showman, Adam P., et al. 2009. “Atmospheric Circulation of Hot Jupiters: Coupled Radiative-Dynamical General Circulation Model Simulations of HD 189733b and HD 209458b”. ApJ 699:564–584. doi:`10.1088/0004-637X/699/1/564`. arXiv: `0809.2089 [astro-ph]`.

Shporer, Avi, et al. 2015. “Studying Atmosphere-dominated Hot Jupiter Kepler Phase Curves: Evidence that Inhomogeneous Atmospheric Reflection Is Common”. AJ 150, 112:112. doi:`10.1088/0004-6256/150/4/112`. arXiv: `1504.00498 [astro-ph.SR]`.

Sing, D. K., et al. 2016. “A continuum from clear to cloudy hot-Jupiter exoplanets without primordial water depletion”. Nature 529 (): 59–62. doi:`10.1038/nature16068`. arXiv: `1512.04341 [astro-ph.EP]`.

Sing, D. K., et al. 2008. “Determining Atmospheric Conditions at the Terminator of the Hot Jupiter HD 209458b”. ApJ 686, 667-673 (): 667–673. doi:`10.1086/590076`. arXiv: `0803.1054`.

Sing, D. K., et al. 2011. “Gran Telescopio Canarias OSIRIS transiting exoplanet atmospheric survey: detection of potassium in XO-2b from narrowband spectrophotometry”. A&A 527, A73 (): A73. doi:`10.1051/0004-6361/201015579`. arXiv: `1008.4795 [astro-ph.EP]`.

Sing, D. K., et al. 2015. “HST hot-Jupiter transmission spectral survey: detection of potassium in WASP-31b along with a cloud deck and Rayleigh scattering”. MNRAS 446 (): 2428–2443. doi:`10.1093/mnras/stu2279`. arXiv: `1410.7611 [astro-ph.EP]`.

Sing, D. K., et al. 2013. “HST hot-Jupiter transmission spectral survey: evidence for aerosols and lack of TiO in the atmosphere of WASP-12b”. MNRAS 436 (): 2956–2973. doi:`10.1093/mnras/stt1782`. arXiv: `1309.5261 [astro-ph.EP]`.

Skillen, I., et al. 2009. “The 0.5M_J transiting exoplanet WASP-13b”. A&A 502 (): 391–394. doi:`10.1051/0004-6361/200912018`. arXiv: `0905.3115 [astro-ph.EP]`.

Smalley, B., et al. 2011. “WASP-34b: a near-grazing transiting sub-Jupiter-mass exoplanet in a hierarchical triple system”. A&A 526, A130 (): A130. doi:10.1051/0004-6361/201015992. arXiv: 1012.2278 [astro-ph.EP].

Smalley, B., et al. 2012. “WASP-78b and WASP-79b: two highly-bloated hot Jupiter-mass exoplanets orbiting F-type stars in Eridanus”. A&A 547, A61 (): A61. doi:10.1051/0004-6361/201219731. arXiv: 1206.1177 [astro-ph.EP].

Smith, A. M. S. 2015. “The Properties of XO-5b and WASP-82b Redetermined Using New High-Precision Transit Photometry and Global Data Analyses”. Acta Astron. 65 (). arXiv: 1412.0451 [astro-ph.EP].

Sneep, M., et al. 2005. “Direct measurement of the Rayleigh scattering cross section in various gases”. J. Quant. Spec. Radiat. Transf. 92 (): 293–310. doi:10.1016/j.jqsrt.2004.07.025.

Snellen, I. A. G., et al. 2008. “Ground-based detection of sodium in the transmission spectrum of exoplanet HD 209458b”. A&A 487 (): 357–362. doi:10.1051/0004-6361:200809762. arXiv: 0805.0789.

Snellen, Ignas A. G., et al. 2010. “The orbital motion, absolute mass and high-altitude winds of exoplanet HD209458b”. Nature 465:1049–1051. doi:10.1038/nature09111. arXiv: 1006.4364 [astro-ph.EP].

Solodov, A. M., et al. 2009. “Helium-induced halfwidths and line shifts of water vapor transitions of the $\nu1 + \nu2$ and $\nu2 + \nu3$ bands”. *Molecular Physics* 107 (): 43–51. doi:10.1080/00268970802698655.

Soter, Steven. 2006. “What Is a Planet?” AJ 132:2513–2519. doi:10.1086/508861. arXiv: astro-ph/0608359 [astro-ph].

Sousa-Silva, C., et al. 2014. “VizieR Online Data Catalog: ExoMol line lists for phosphine (PH_3) (Sousa-Silva+,” *VizieR Online Data Catalog* 744 ().

Southworth, J. 2010. “Homogeneous studies of transiting extrasolar planets - III. Additional planets and stellar models”. MNRAS 408 (): 1689–1713. doi:10.1111/j.1365-2966.2010.17231.x. arXiv: 1006.4443 [astro-ph.EP].

— . 2011a. “Homogeneous studies of transiting extrasolar planets - IV. Thirty systems with space-based light curves”. MNRAS 417 (): 2166–2196. doi:10.1111/j.1365-2966.2011.19399.x. arXiv: 1107.1235 [astro-ph.EP].

— . 2011b. “Homogeneous studies of transiting extrasolar planets - IV. Thirty systems with space-based light curves”. MNRAS 417 (): 2166–2196. doi:10.1111/j.1365-2966.2011.19399.x. arXiv: 1107.1235 [astro-ph.EP].

— . 2012. “Homogeneous studies of transiting extrasolar planets - V. New results for 38 planets”. MNRAS 426 (): 1291–1323. doi:`10.1111/j.1365-2966.2012.21756.x`. arXiv: `1207.5796 [astro-ph.EP]`.

Southworth, J., et al. 2016a. “Contamination from a nearby star cannot explain the anomalous transmission spectrum of the ultrashort period giant planet WASP-103 b”. MNRAS 463 (): 37–44. doi:`10.1093/mnras/stw1943`. arXiv: `1608.00746 [astro-ph.EP]`.

Southworth, J., et al. 2012a. “High-precision photometry by telescope defocusing - IV. Confirmation of the huge radius of WASP-17 b”. MNRAS 426 (): 1338–1348. doi:`10.1111/j.1365-2966.2012.21781.x`. arXiv: `1207.5797 [astro-ph.EP]`.

Southworth, J., et al. 2013. “High-precision photometry by telescope defocusing - V. WASP-15 and WASP-16”. MNRAS 434 (): 1300–1308. doi:`10.1093/mnras/stt1089`. arXiv: `1306.3509 [astro-ph.EP]`.

Southworth, J., et al. 2014. “High-precision photometry by telescope defocussing - VI. WASP-24, WASP-25 and WASP-26”. MNRAS 444 (): 776–789. doi:`10.1093/mnras/stu1492`. arXiv: `1407.6253 [astro-ph.EP]`.

Southworth, J., et al. 2016b. “High-precision photometry by telescope defocussing - VIII. WASP-22, WASP-41, WASP-42 and WASP-55”. MNRAS 457 (): 4205–4217. doi:`10.1093/mnras/stw279`. arXiv: `1512.05549 [astro-ph.EP]`.

Southworth, J., et al. 2012b. “Refined physical properties of the HAT-P-13 planetary system”. MNRAS 420 (): 2580–2587. doi:`10.1111/j.1365-2966.2011.20230.x`. arXiv: `1111.5432 [astro-ph.EP]`.

Sozzetti, A., et al. 2015. “The GAPS programme with HARPS-N at TNG. VI. The curious case of TrES-4b”. A&A 575, L15 (): L15. doi:`10.1051/0004-6361/201425570`. arXiv: `1501.06403 [astro-ph.EP]`.

Spake, J. J., et al. 2018. “Helium in the eroding atmosphere of an exoplanet”. Nature 557:68–70. doi:`10.1038/s41586-018-0067-5`. arXiv: `1805.01298 [astro-ph.EP]`.

Spiegel, D. S., et al. 2009. “Can TiO Explain Thermal Inversions in the Upper Atmospheres of Irradiated Giant Planets?” ApJ 699 (): 1487–1500. doi:`10.1088/0004-637X/699/2/1487`. arXiv: `0902.3995 [astro-ph.EP]`.

Stevens, D. J., et al. 2017. “KELT-12b: A P 5 day, Highly Inflated Hot Jupiter Transiting a Mildly Evolved Hot Star”. AJ 153, 178 (): 178. doi:`10.3847/1538-3881/aa5ffb`. arXiv: `1608.04714 [astro-ph.EP]`.

Stevens, Daniel J., et al. 2013. “A Posteriori Transit Probabilities”. *Publications of the Astronomical Society of the Pacific* 125:933. doi:10.1086/672572. arXiv: 1305.1298 [astro-ph.EP].

Stevenson, K. B., et al. 2014. “Thermal structure of an exoplanet atmosphere from phase-resolved emission spectroscopy”. *Science* 346 (): 838–841. doi:10.1126/science.1256758. arXiv: 1410.2241 [astro-ph.EP].

Steyert, D. W., et al. 2004. “Hydrogen and helium pressure broadening of water transitions in the 380-600cmˆ-ˆ1 region”. J. Quant. Spec. Radiat. Transf. 83 (): 183–191. doi:10.1016/S0022-4073(02)00300-X.

Sudarsky, D., et al. 2003. “Theoretical Spectra and Atmospheres of Extrasolar Giant Planets”. ApJ 588 (): 1121–1148. doi:10.1086/374331. eprint: astro-ph/0210216.

Tashkun, S. A., et al. 2011. “CDSD-4000: High-resolution, high-temperature carbon dioxide spectroscopic databank”. J. Quant. Spec. Radiat. Transf. 112 (): 1403–1410. doi:10.1016/j.jqsrt.2011.03.005.

Tennyson, J., et al. 2012. “ExoMol: molecular line lists for exoplanet and other atmospheres”. MNRAS 425 (): 21–33. doi:10.1111/j.1365-2966.2012.21440.x. arXiv: 1204.0124 [astro-ph.EP].

Tennyson, J., et al. 2016. “The ExoMol database: Molecular line lists for exoplanet and other hot atmospheres”. *Journal of Molecular Spectroscopy* 327 (): 73–94. doi:10.1016/j.jms.2016.05.002. arXiv: 1603.05890.

Thibault, F., et al. 2000. “Experimental and theoretical CO2 He pressure broadening cross sections”. *Physical Chemistry Chemical Physics (Incorporating Faraday Transactions)* 2:5404–5410. doi:10.1039/B006224N.

Thibault, F., et al. 1992. “Pressure induced shifts of CO2 lines - Measurements in the 00(0)3-00(0)0 band and theoretical analysis”. J. Chem. Phys. 96 (): 4945–4953. doi:10.1063/1.462737.

Thomas, Gary E, et al. 2002. *Radiative transfer in the atmosphere and ocean*. Cambridge University Press.

Torres, G., et al. 2007. “HAT-P-3b: A Heavy-Element-rich Planet Transiting a K Dwarf Star”. ApJ 666 (): L121–L124. doi:10.1086/521792. arXiv: 0707.4268.

Tregloan-Reed, J., et al. 2015. “Transits and starspots in the WASP-6 planetary system”. MNRAS 450 (): 1760–1769. doi:10.1093/mnras/stv730. arXiv: 1503.09184 [astro-ph.EP].

Tremblin, P., et al. 2017. “Advection of Potential Temperature in the Atmosphere of Irradiated Exoplanets: A Robust Mechanism to Explain Radius Inflation”. ApJ 841, 30 (): 30. doi:10.3847/1538-4357/aa6e57.

Tremblin, P., et al. 2016. “Cloudless Atmospheres for L/T Dwarfs and Extrasolar Giant Planets”. ApJ 817, L19 (): L19. doi:10.3847/2041-8205/817/2/L19. arXiv: 1601.03652 [astro-ph.EP].

Tremblin, P., et al. 2015. “Fingering Convection and Cloudless Models for Cool Brown Dwarf Atmospheres”. ApJ 804, L17 (): L17. doi:10.1088/2041-8205/804/1/L17. arXiv: 1504.03334 [astro-ph.SR].

Triaud, A. H. M. J., et al. 2013. “WASP-80b: a gas giant transiting a cool dwarf”. A&A 551, A80 (): A80. doi:10.1051/0004-6361/201220900. arXiv: 1303.0254 [astro-ph.EP].

Trotta, Roberto. 2017. “Bayesian Methods in Cosmology”. *arXiv e-prints*, arXiv:1701.01467: arXiv:1701.01467. arXiv: 1701.01467 [astro-ph.CO].

Trujillo Bueno, J, et al. 1995. “A novel iterative scheme for the very fast and accurate solution of non-LTE radiative transfer problems”. *The Astrophysical Journal* 455:646.

Tsuji, T. 1973. “Molecular abundances in stellar atmospheres. II.” A&A 23 (): 411.

Turner, O. D., et al. 2016. “WASP-120 b, WASP-122 b, AND WASP-123 b: Three Newly Discovered Planets from the WASP-South Survey”. PASP 128, no. 6 (): 064401. doi:10.1088/1538-3873/128/964/064401. arXiv: 1509.02210 [astro-ph.EP].

Underwood, D. S., et al. 2016. “ExoMol molecular line lists - XIV. The rotation-vibration spectrum of hot SO_2”. MNRAS 459 (): 3890–3899. doi:10.1093/mnras/stw849. arXiv: 1603.04065 [astro-ph.EP].

Van Grootel, V., et al. 2014. “Transit Confirmation and Improved Stellar and Planet Parameters for the Super-Earth HD 97658 b and its Host Star”. ApJ 786, 2 (): 2. doi:10.1088/0004-637X/786/1/2. arXiv: 1402.5850 [astro-ph.EP].

Vandaele, A. C., et al. 2017. “Sulfur dioxide in the Venus Atmosphere: II. Spatial and temporal variability”. Icarus 295 (): 1–15. doi:10.1016/j.icarus.2017.05.001.

Varanasi, P., et al. 1990. “The temperature dependence of lineshifts, linewidths and line intensities of methane at low temperatures”. J. Quant. Spec. Radiat. Transf. 43 (): 1–11. doi:10.1016/0022-4073(90)90060-J.

Venot, O., et al. 2012. “A chemical model for the atmosphere of hot Jupiters”. A&A 546, A43 (): A43. doi:10.1051/0004-6361/201219310. arXiv: 1208.0560 [astro-ph.EP].

Venot, O., et al. 2015. “New chemical scheme for studying carbon-rich exoplanet atmospheres”. A&A 577, A33 (): A33. doi:10.1051/0004-6361/201425311. arXiv: 1502.03567 [astro-ph.EP].

Visscher, C., et al. 2006. “Atmospheric Chemistry in Giant Planets, Brown Dwarfs, and Low-Mass Dwarf Stars. II. Sulfur and Phosphorus”. ApJ 648 (): 1181–1195. doi:10.1086/506245. eprint: astro-ph/0511136.

Šimečková, Marie, et al. 2006. “Einstein A-coefficients and statistical weights for molecular absorption transitions in the HITRAN database”. *Journal of Quantitative Spectroscopy and Radiative Transfer* 98:130–155. doi:10.1016/j.jqsrt.2005.07.003.

Wakeford, H. R., et al. 2017. “HAT-P-26b: A Neptune-Mass Exoplanet with a Well Constrained Heavy Element Abundance”. *ArXiv e-prints* (). arXiv: 1705.04354 [astro-ph.EP].

Wakeford, H. R., et al. 2013. “HST hot Jupiter transmission spectral survey: detection of water in HAT-P-1b from WFC3 near-IR spatial scan observations”. MNRAS 435 (): 3481–3493. doi:10.1093/mnras/stt1536. arXiv: 1308.2106 [astro-ph.EP].

Wakeford, H. R., et al. 2016. “Marginalizing Instrument Systematics in HST WFC3 Transit Light Curves”. ApJ 819, 10 (): 10. doi:10.3847/0004-637X/819/1/10. arXiv: 1601.02587 [astro-ph.EP].

Wakeford, H. R., et al. 2018. “The Complete Transmission Spectrum of WASP-39b with a Precise Water Constraint”. AJ 155 (). doi:10.3847/1538-3881/aa9e4e.

Wakeford, H. R., et al. 2015. “Transmission spectral properties of clouds for hot Jupiter exoplanets”. A&A 573, A122 (): A122. doi:10.1051/0004-6361/201424207. arXiv: 1409.7594 [astro-ph.EP].

Wende, S., et al. 2010. “CRIRES spectroscopy and empirical line-by-line identification of FeH molecular absorption in an M dwarf”. A&A 523, A58 (): A58. doi:10.1051/0004-6361/201015220. arXiv: 1007.4116 [astro-ph.SR].

West, R. G., et al. 2009a. “The Low Density Transiting Exoplanet WASP-15b”. AJ 137 (): 4834–4836. doi:10.1088/0004-6256/137/6/4834. arXiv: 0902.2651 [astro-ph.EP].

West, R. G., et al. 2009b. “The sub-Jupiter mass transiting exoplanet WASP-11b”. A&A 502 (): 395–400. doi:10.1051/0004-6361/200810973. arXiv: 0809.4597.

West, R. G., et al. 2016. “Three irradiated and bloated hot Jupiters:. WASP-76b, WASP-82b, and WASP-90b”. A&A 585, A126 (): A126. doi:10.1051/0004-6361/201527276. arXiv: 1310.5607 [astro-ph.EP].

Wiedemann, G. 1996. “Science with the VLT: high-resolution infrared spectroscopy.” *The Messenger* 86:24–30.

Wilson, D. M., et al. 2008. “WASP-4b: A 12th Magnitude Transiting Hot Jupiter in the Southern Hemisphere”. ApJ 675, L113 (): L113. doi:10.1086/586735. arXiv: 0801.1509.

Winn, J. N. 2010. “Exoplanet Transits and Occultations”. In *Exoplanets*, ed. by S. Seager, 55–77. University of Arizona Press.

Winn, J. N., et al. 2011. “A Super-Earth Transiting a Naked-eye Star”. ApJ 737, L18 (): L18. doi:10.1088/2041-8205/737/1/L18. arXiv: 1104.5230 [astro-ph.EP].

Woitke, P., et al. 2018. “Equilibrium chemistry down to 100 K. Impact of silicates and phyllosilicates on the carbon to oxygen ratio”. A&A 614, A1 (): A1. doi:10.1051/0004-6361/201732193. arXiv: 1712.01010 [astro-ph.EP].

Wolszczan, A., et al. 1992. “A planetary system around the millisecond pulsar PSR1257 + 12”. Nature 355:145–147. doi:10.1038/355145a0.

Wong, Ian, et al. 2016. “3.6 and 4.5 μm Spitzer Phase Curves of the Highly Irradiated Hot Jupiters WASP-19b and HAT-P-7b”. ApJ 823, 122:122. doi:10.3847/0004-637X/823/2/122. arXiv: 1512.09342 [astro-ph.EP].

Wright, J. T., et al. 2012. “The Frequency of Hot Jupiters Orbiting nearby Solar-type Stars”. ApJ 753, 160:160. doi:10.1088/0004-637X/753/2/160. arXiv: 1205.2273 [astro-ph.EP].

Yung, Y., et al., eds. 1999. *Photochemistry of planetary atmospheres.*

Yurchenko, S. N., et al. 2011. “A variationally computed line list for hot NH_3”. MNRAS 413 (): 1828–1834. doi:10.1111/j.1365-2966.2011.18261.x. arXiv: 1011.1569 [astro-ph.EP].

Yurchenko, S. N., et al. 2014. “ExoMol line lists - IV. The rotation-vibration spectrum of methane up to 1500 K”. MNRAS 440 (): 1649–1661. doi:10.1093/mnras/stu326. arXiv: 1401.4852 [astro-ph.EP].

Zahnle, K., et al. 2009. “Atmospheric Sulfur Photochemistry on Hot Jupiters”. ApJ 701:L20–L24. doi:10.1088/0004-637X/701/1/L20. arXiv: 0903.1663 [astro-ph.EP].

Zahnle, Kevin, et al. 2010. “Earth’s earliest atmospheres.” [**inlang**eng]. *Cold Spring Harb Perspect Biol* (Space Science Division, NASA Ames Research Center.) 2 (10): a004895. ISSN: 1943-0264 (Electronic); 1943-0264 (Linking). doi:10.1101/cshperspect.a004895.

Zellem, R. T., et al. 2014. "The 4.5 μm Full-orbit Phase Curve of the Hot Jupiter HD 209458b". ApJ 790, 53 (): 53. doi:10.1088/0004-637X/790/1/53. arXiv: 1405.5923 [astro-ph.EP].

Zhou, G., et al. 2014. "HATS-5b: A Transiting Hot Saturn from the HATSouth Survey". AJ 147, 144 (): 144. doi:10.1088/0004-6256/147/6/144. arXiv: 1401.1582 [astro-ph.EP].

Zhou, G., et al. 2016. "KELT-17b: A Hot-Jupiter Transiting an A-star in a Misaligned Orbit Detected with Doppler Tomography". AJ 152, 136 (): 136. doi:10.3847/0004-6256/152/5/136. arXiv: 1607.03512 [astro-ph.EP].